Designing Organic A-site Cations for Emerging Optoelectronic Properties of Hybrid Halide Perovskites: Reversible Melting, Non-Centrosymmetry, and Chirality

विद्या वाचस्पति की
उपाधि की अपेक्षाओं की आंशिक पूर्ति में प्रस्तुत शोध प्रबंध

A thesis submitted in partial fulfillment of the requirements of the degree of Doctor of Philosophy

द्वारा / By

छात्र का नाम / Name of Student

परीक्षित कुमार राजपूत / Parikshit Kumar Rajput

पंजीकरण सं. / Registration No.: 20193682

शोध प्रबंध पर्यवेक्षक / Thesis Supervisor

प्रोफेसर अंशुमन नाग / Prof. Angshuman Nag

IISER PUNE

भारतीय विज्ञान शिक्षा एवं अनुसंधान संस्थान पुणे

INDIAN INSTITUTE OF SCIENCE EDUCATION AND RESEARCH PUNE

2024

This thesis is dedicated to the memory of my late grandfather

Declaration by Student

Name of Student: Parikshit Kumar Rajput

Reg. No.: 20193682

Thesis Supervisor: Prof. Angshuman Nag

Department: Chemistry

Date of joining program: 01/08/2019

Date of Pre-Synopsis Seminar: 06/09/2024

Title of Thesis: Designing Organic A-site Cations for Emerging Optoelectronic Properties of Hybrid Halide Perovskites: Reversible Melting, Non-Centrosymmetry, and Chirality

I declare that this written submission represents my idea in my own words and where others' ideas have been included; I have adequately cited and referenced the original sources. I declare that I have acknowledged collaborative work and discussions whenever such work has been included. I also declare that I have adhered to all principles of academic honesty and integrity and have not misrepresented or fabricated or falsified any idea/data/fact/source in my submission. I understand that violation of the above will be cause for disciplinary action by the institute and can evoke penal action from the sources which have thus not been properly cited or from whom proper permission has not been taken when needed.

The work reported in this thesis is the original work done by me under the guidance of Prof. Angshuman Nag.

Date: 13/12/2024

Signature of Student

CERTIFICATE

Certified that the work incorporated in the thesis entitled "Designing Organic A-site Cations for Emerging Optoelectronic Properties of Hybrid Halide Perovskites: Reversible Melting, Non-Centrosymmetry, and Chirality" submitted by Parikshit Kumar Rajput was carried out by the candidate, under my supervision. The work presented here or any part of it has not been included in any other thesis submitted previously for the award of any degree or diploma from any other University or institution.

Angshuman Nag

Prof. Angshuman Nag

(Thesis Supervisor)

Date: 13/12/2024

Acknowledgments

First and foremost, I express my deepest gratitude to my Ph.D. supervisor, Prof. Angshuman Nag, for his exceptional guidance, constant support, and encouragement throughout Ph.D. His immense knowledge and critical thinking have been invaluable in shaping my research skills and scientific outlook. He was always actively involved in my work and provided valuable support throughout my journey. I would always look up to him for his distinguished mentoring practices in my career.

I would like to acknowledge my research advisory committee (RAC) members, Prof. Nirmalaya Ballav (IISER Pune) and Prof. Arup Kumar Rath (NCL Pune), for their valuable comments and suggestions during my RAC meetings.

I would like to sincerely acknowledge our collaborators: Prof. K. V. Adarsh, Prof. Atikur Rahaman, Prof. Pankaj Mandal, Dr. Kadhiravan Shanmuganathan, Prof. Surajit Saha, Dr. Gokul M. A., Dr. Shabnum Maqbool, Ms. Meghasree Basu, Dr. Ajay Kumar Punia, Dr. Megha Shrivastava, Dr. Ranjan Das, Mr. Animesh Gopal, and Ms. Aprajita Joshi from IISER Pune, IISER Bhopal, NCL Pune, and IISc Bangalore. I had the privilege of visiting some of their labs and conducting experiments with their valuable assistance. These visits provided a wonderful opportunity to learn various experimental techniques and gain new insights through meaningful interactions with them.

I would like to express my gratitude to the Department of Chemistry, IISER Pune, for providing me the opportunity to pursue my PhD. I also extend my appreciation to the office and departmental staff at IISER Pune for their prompt assistance whenever needed. A special thanks to Mr. Ravindra Malothu for his invaluable help for the single-crystal data recording. I am also thankful to Dr. Pramod Pillai's group, Prof. Pankaj Mandal's group, and Prof. Nirmalya Ballav's group at IISER Pune for their support with various experimental measurements.

I sincerely express my heartfelt gratitude to all my teachers who have guided and supported me throughout my academic journey. Their dedication and encouragement have been significant in shaping my path and helping me reach this stage. I am particularly grateful to Dr. Suhas and Dr. R. K. Sukla from the Department of Chemistry, Gurukul Kangri University, Haridwar, for their motivation and guidance in helping me choose my research direction. I also extend my deep

appreciation to the faculty members of the Department of Chemistry at IISER Pune for their invaluable teachings during my coursework.

A heartfelt thanks to all my lab mates for such a wonderful and supportive environment in the lab. I gained invaluable research insights through our discussions and collaborations. Working with them was always enjoyable, and I value every moment shared with them, both in and outside the lab. All of them has contributed to my work in some way, directly or indirectly, and some of them are co-authors in my papers. I deeply appreciate their dedication and hard work in conducting experiments and helping me to complete projects on time.

A special thanks to my family for their unconditional trust and confidence, allowing me to stay away from home to pursue my goals. A big thanks to Umisha for always being there and supporting me throughout this journey. I am also grateful to my IISER Pune friends, my old friends (Deepanshu, Yugank, Vishnu), and my family members for their constant support whenever I needed it. On a lighter note, thanks to everyone who appreciated my cooking, I even managed to impress one non-vegetarian (Shankhajit) with my vegetarian dishes. I would like to thank to everyone who has helped me, both directly and indirectly, during this journey.

Lastly, I would like to express my gratitude to the University Grants Commission (UGC), India, for providing me the fellowship during my PhD. This support was significant in enabling me to carry out my research and sustain my journey here. Finally, I thank you, the readers, for taking the time to go through this thesis. I hope you find it insightful and enjoyable, and I sincerely apologize for any unintentional errors that may be present.

List of Abbreviations

0D: Zero dimensional

1D: One dimensional

2D: Two dimensional

3D: Three dimensional

3-APN: 3-amino propionitrile

AH: Alkali halides

BA: Butylammonium

CB: Conduction band

CBM: Conduction band minimum

CD: Circular dichroism

CISS: Chiral induced spin selectivity

DJ: Dion Jacobson

CPL: Circularly polarized emission

DMF: Dimethylformamide

DMSO: Dimethyl sulfoxide

DSC: Differential scanning calorimetry

EQE: External quantum efficiency

ETL: Electron transporting layer

FA: Formamidinum

FESEM: Field emission scanning electron microscopy

GABA: 3-amino butyric acid

List of Abbreviations

GBL: Gamma-butyrolactone

HTL: Hole transporting layer

IL: Ionic liquids

LED: Light emitting diodes

MA: Methylammonium

MBA: Methylbenzylammonium

MPEA: N-methyl phenethylammonium

NIR: Near infra-red

PCE: Power conversion efficiency

PEA: Phenethylammonium

PL: Photoluminescence

PXRD: Powder X-ray diffraction

RP: Ruddlesden popper

SCXRD: Single crystal X-ray diffraction

SHG: Second harmonic generation

TCSPC: Time-correlated single-photon counting

THG: Third harmonic generation

TGA: Thermogravimetric analysis

UV: Ultraviolet

VB: Valence band

VBM: Valance band maximum

Synopsis

Three-dimensional (3D) hybrid halide perovskites have received considerable attention over the past decade due to their outstanding semiconducting properties. Lower-dimensional (2D, 1D, and 0D) hybrid halide perovskites, are also being explored for their potential optical and optoelectronic applications. A key question in this area of study is whether the physical and chemical properties of lower-dimensional hybrid perovskites can be tuned by controlling A-site cation.

The primary objective of this thesis is to investigate the role of newly designed A-site organic ammonium cations, which not only stabilize the crystal structure but also enable the tuning of crucial properties such as melting temperature, molten-state synthesis, structural non-centrosymmetry, and chirality. These functionalities are introduced by the A-site organic ammonium cations at the organic-inorganic interfaces of hybrid halide perovskites. To achieve this, we explored the non-covalent bonding interactions, such as electrostatic interaction along with hydrogen and halogen bonding between the organic and inorganic sublattices. The nature of interactions was investigated by using single-crystal X-ray diffraction. Also, we have used differential scanning calorimetry, thermogravimetry analysis, photoluminescence, optical absorption, and circular dichroism spectroscopy. Then we established structure-property relationships providing insights into how these interactions influence the hybrid perovskite structures. This comprehensive study opens new pathways for the rational design of lower-dimensional perovskites with tailored physical and chemical properties. We have also fabricated photodetector devices based on single crystals and melt-pressed films of hybrid halide perovskites. This preliminary device fabrication enabled us to demonstrate the potential of specially designed hybrid perovskites, developed through our novel synthesis approaches, for optoelectronic applications.

Chapter 1: Introduction

This chapter introduces semiconductors, beginning with an overview of their fundamental principles and examples of traditional semiconductors like silicon, gallium arsenide etc. Following this, the focus shifts to halide hybrid perovskites, with an emphasis on their lower-dimensional forms (2D, 1D, and 0D) and their unique crystal structures. We discussed the possible A-site ammonium cations and a detailed discussion on the interactions between the organic-inorganic

and organic-organic sublattices at the organic-inorganic interfaces and within the inorganic sublattices. Also, we discussed strategies aimed at minimizing or eliminating the use of solvents during the synthesis of single crystals and film fabrication of lower dimensional hybrid halide perovskites. Furthermore, we have discussed the potential of lower dimensional hybrid halide perovskites for next generation optoelectronics. Particularly, photodetection is briefly discussed, including single crystal and thin film-based devices. Toward the end of the chapter, the scope of the thesis is outlined by introducing the effect of specially designed A-site ammonium cations on physical and chemical properties of lower dimensional perovskites.

Chapter 2: Entropy-Driven Reversible Melting and Recrystallization of Layered Hybrid Perovskites

2D layered hybrid halide perovskites, such as A_2PbX_4 (A: organic ammonium cation and X: Br, I), are an important class of semiconductors exhibiting interesting optoelectronic properties. Typical A_2PbX_4 compounds undergo irreversible decomposition with increasing temperature by forming volatile species. In this chapter we have rationally designed meltable 2D A_2PbX_4 layered hybrid halide perovskites by introducing specially designed A-site ammonium cations. We hypothesized that the A-site cations having functional groups at tail of cations like -I, -CN, -COOH etc. form hydrogen and halogen bonding non-covalent interactions, making the cation layer rigid in the solid form. This leads to reduce the entropy of crystal. Also, we hypothesized that the melt of A_2PbX_4 behave like an ionic liquid. We have also determined that which thermodynamic parameter entropy of fusion (ΔS_{fus}) or enthalpy of fusion (ΔH_{fus}) drive the melting of A_2PbX_4 perovskites. Then the meltable 2D perovskite converted into the films by melt-pressed films offering a solvent- and vacuum-free method. Finally developed a n-i-p based photodetector based on melt pressed film and checked its performance for future optoelectronics.

Chapter 3: Molten State Synthesis of Pb-I Hybrid Perovskite Derivative

Typically, the synthesis of hybrid halide perovskite involves the use of solvents like hydrohalic acids (HX, where X = I, Cl, Br), dimethylformamide (DMF), dimethyl sulfoxide (DMSO), and gamma-butyrolactone (GBL). However, reducing or eliminating these toxic solvents is essential for greener synthesis approaches. In this chapter, we introduced a novel method for synthesizing

Synopsis

Pb-I hybrid perovskite derivatives. Our alternative method involves melting the A-site organic ammonium cation precursor, N-methyl phenethyl ammonium iodide C_6H_5-$(CH_2)_2$-$NH_2^+(CH_3)I^-$ (MPEAI), which melts at approximately 100 °C. This molten precursor effectively dissolves lead iodide (PbI_2), forming a stable molten mixture. Upon cooling, the $(MPEA)_5Pb_3I_{11}$ perovskite derivative crystallizes. We propose that molten ammonium halide salts behave similarly to ionic liquids, as they consist of ammonium cations and halide anions. Finally, we compared the $(MPEA)_5Pb_3I_{11}$ structure obtained via the molten-state method with that synthesized through the acid precipitation method, demonstrating the viability of the molten-state synthesis as a less toxic alternative.

Chapter 4: Rational Design of Non-Centrosymmetric 1D Bi-I Hybrid Perovskite Derivative

Structural non-centrosymmetry in hybrid halide perovskites introduces unique and important functionalities like non-linear optical response, ferroelectricity and anomalous bulk photovoltaic effect. This chapter deals with the rational design of non-centrosymmetric, polar, and chiral one dimensional (1D) Bi-I-based hybrid halide perovskites. We employed achiral diammonium cation such as NH_3^+–$(CH_2)_3$–$NH(CH_3)_2^+$ (BMPA), where one end (-NH_3^+) is substituted by -$NH(CH_3)_2^+$. This substitution of two hydrogen atoms with methyl (-CH_3) groups reduces the rotational symmetry of BMPA at one end compared to unsubstituted cations. Asymmetric H---I interactions at the organic-inorganic interfaces in $(BMPA)BiI_5$ 1D perovskites disrupt the local inversion symmetry of Bi-I octahedra, causing $(BMPA)BiI_5$ to crystallize in the monoclinic $P2_1$ space group, which is non-centrosymmetric, chiral, and polar. Finally, $(BMPA)BiI_5$ crystals are employed for nonlinear optical properties, second and third harmonic generation. The single crystal also demonstrates the anomalous photovoltaic effect. Remarkably, $(BMPA)BiI_5$ films shows a chiral response despite the absence of a chiral organic component.

Chapter 5: Chirality Induction from Organic to Inorganic Sublattices in Chiral 0D Bi-I Hybrid Perovskite Derivative

Recently, the chiral organic sublattice has been shown to induce chirality in the achiral semiconducting inorganic sublattices for chiroptical, chiro optoelectronic, and spin-based properties in lower dimensional hybrid halide perovskites. In this chapter, we demonstrate how A-

site chiral organic ammonium cations interact with the achiral inorganic sublattices in hybrid halide perovskites. To achieve this, we first synthesized chiral 0D Bi-I hybrid perovskite derivatives (R-/S-MBA)$_4$Bi$_2$I$_{10}$, where MBA represents methylbenzyl ammonium. Structural analysis via single-crystal X-ray diffraction (SCXRD) offered mechanistic insights into how the chiral organic sublattice induces chirality in the inorganic sublattice, providing a deeper understanding of the structure-property relationships in these chiral hybrid perovskites. We confirmed the chirality in films of (R-/S-MBA)$_4$Bi$_2$I$_{10}$ using circular dichroism (CD) spectroscopy, where the films displayed positive and negative CD signals corresponding to their excitonic transitions. Additionally, temperature-dependent photoluminescence (PL) provided further insights into the excitonic photo physics of (R-/S-MBA)$_4$Bi$_2$I$_{10}$.

Thesis Summary and Future Outlook

In this section we have summarized the work discussed from chapter 2 to chapter 5 of this thesis. For future explorations, we are more inclined towards the molten hybrid perovskites and molten state synthesis of hybrid halide perovskites discussed in chapter 2 and chapter 3. We plan to carry out the systematic study on the molten perovskites or molten ammonium salts.

Table of Content

Table of Content

Table of Content

Table of Content

Table of Content

Chapter 1

Introduction

1.1 Semiconductors

Semiconductors form the foundation of modern technology, enabling the functioning of devices ranging from smartphones and computers to medical diagnostics equipment.[1] They are also critical for advancing emerging technologies such as solar cells, LEDs, and sensing devices, and play a vital role in the computing infrastructure that powers innovations like artificial intelligence. Semiconductors are known for its special ability it can conduct or resist electrical current depending on external influences. While as metals conduct electricity and insulators resist the flow of electrical current entirely. In metals, the valence and conduction bands are not separated by a band gap. Instead, the conduction band is partially filled, creating a sea of free electrons that enable efficient electrical conductivity. Insulators possess a large band gap, which prevents the flow of electrons from the valence band to the conduction band. Combined with low charge carrier mobility, this makes insulators poor conductors of electricity. While as semiconductors occupy an intermediate position, possessing a moderate band gap. In their pure form, semiconductors lack free charge carriers, making them non-conductive until external stimuli such as heat, light, or doping introduces charge carriers into the conduction band. This unique property enables semiconductors to act as controllable conductors in electronic devices. When this perturbation occurs, the semiconductor becomes highly conductive, entering what is referred to as the “on” state. This dual and contrasting behavior between insulating (“off” state) and conducting (“on” state) makes semiconductors an intriguing class of materials. The transition from the “off” to “on” state in semiconductors occurs due to their finite band gap and high carrier mobility.

When discussing semiconductors, certain names readily come to mind, such as silicon, gallium arsenide (GaAs), indium gallium arsenide (InGaAs) and many more.[2] These are often referred to as traditional semiconductors. Some of them are commercially available, silicon solar cells are available in market and gallium arsenide light emitting diodes are also available (emission at 850 nm).[3] In spite of this much attention, these star materials face several well-known challenges. One major issue is that their semiconducting properties are highly dependent on the quality of their crystals. The presence of defect states can trap charge carriers, severely impairing their semiconducting performance. To address this, methods like advanced epitaxial growth or high-temperature synthesis (above 1000 °C) are commonly employed to minimize defects and improve

crystallinity. While these methods improve crystal quality, they also substantially increase production and processing costs. Also, it is very difficult to modulate their physical and chemical properties for desired application. For example, it is difficult to introduce the desired functionalities like chirality, melting at lower temperature, and structural non-centrosymmetry in traditional semiconductors for advance optoelectronics. Hybrid halide perovskites have recently garnered significant attention as an alternative with the potential to overcome the limitations of traditional semiconductors. These materials can be synthesized with ease and at lower costs, making them ideal candidate. Unlike traditional semiconductors, halide perovskites naturally offer tunable electrical and optical properties due to their unique crystal structures and diverse compositional flexibility.

1.2 Hybrid Halide Perovskite Semiconductors

Hybrid halide perovskite semiconductors are materials composed of both insulating organic and semiconducting inorganic components. These semiconductors are primarily studied in their three-dimensional (3D) characterized by the general formula ABX_3, where A is an organic cation (MA, $CH_3NH_3^+$), B is a metal cation (Pb^{2+}, Sn^{2+}), and X is a halide anion (I^-, Br^-, Cl^-).[4-6] Depending on the structural arrangement of their inorganic frameworks and organic components, two-dimensional (2D), one-dimensional (1D), and zero-dimensional (0D) hybrid halide semiconductors can be achieved.[7-11]

Hybrid halide perovskite semiconductors come into picture because of their exceptional optical, optoelectronic and photovoltaic properties, including high absorption coefficients, long charge carrier diffusion lengths, low effective masses for electrons and holes, intense photoluminescence and narrow emission linewidths.[12-18] The first hybrid perovskite-based solar cell, utilizing methylammonium lead iodide ($MAPbI_3$), initially demonstrated a modest power conversion efficiency (PCE) of 3.8%.[19] Remarkably, within just two years, advancements pushed the PCE beyond 10%.[20] In less than a decade, perovskite solar cells have rapidly advanced to become formidable competitors to traditional solar technologies, often outperforming many of them. Today, perovskite solar cells boast a PCE exceeding 25%, rivaling the benchmark efficiency of single-crystalline silicon solar cells, which achieved 26.6% after over 40 years of development.[21, 22] Beyond solar cells, hybrid halide perovskite semiconductors have demonstrated their potential

in a wide range of applications, including sensors, light-emitting diodes (LEDs), photodetectors, lasers, and photocatalysts.[23-29] Their versatility and outstanding performance characteristics make them a focal point of research in next-generation optoelectronic materials.

1.2.1 3D Hybrid Pb Halide Perovskite

The 3D perovskite structure ABX_3, consists of $[BX_6]^{4-}$ (where B = Pb^{2+}) octahedra connected at their corners, forming an infinite three-dimensional (3D) framework as shown in Figure 1.1. The size, shape, and charge of A^+ cations ($CH_3NH_3^+$, $NH_2CHNH_2^+$) are essential for shaping and stabilizing the perovskite structure. The rules that govern perovskite formation were tackled by Goldschmidt,[30] who introduced the tolerance factor,

$$t = ((r_A + r_B))/(\sqrt{2}\,(r_B + r_X)) \qquad (1)$$

Here, the ionic radii of the A and B cations are r_A and r_B and the X anion is r_X, determine the tolerance factor (t), which should typically range between 0.71 and 1 for stability of a perovskite structure.[30, 31] In hybrid halide perovskites, cations like methylammonium (MA^+, $CH_3NH_3^+$), and formamidinium (FA^+, $NH_2CHNH_2^+$) are suitable for the A-site due to their ionic sizes, enabling the formation of stable structures.[32]

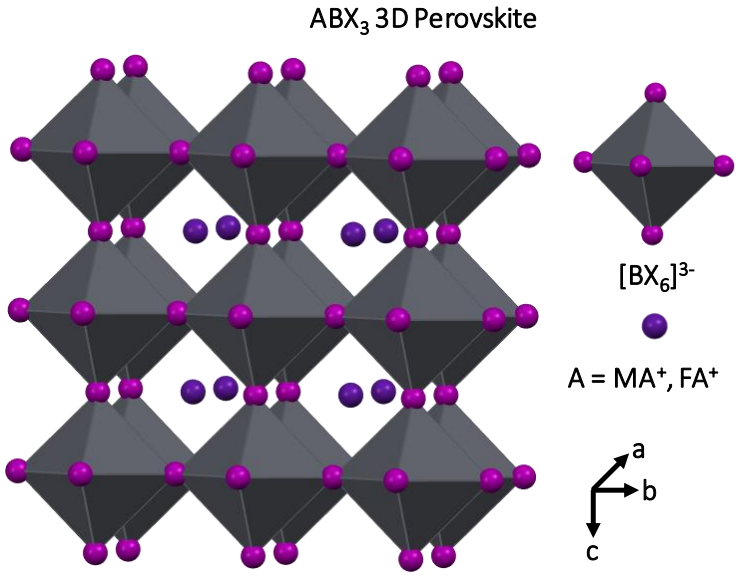

Figure 1.1: Schematic representation of the 3D perovskite structure, shows a corner-sharing $[BX_6]^{4-}$ octahedral network forming an infinite framework in all three directions. (where B = Pb^{2+}).

As the 3D perovskite compositions are limited because of the almost fixed sized void. In order to expand the material space researchers came across the larger A-site cations like butylammonium (CH_3-$(CH_2)_3$-NH_3^+). Incorporating large A-site cations reduces the 3D perovskite structure to lower-dimensional forms, such as 2D, 1D, and 0D perovskites, commonly termed "perovskitoids" or perovskite derivatives.[7] However, it is important to note that this reduction in dimensionality applies to the electronic connectivity only, as these materials remain three-dimensional in terms of their physical morphology.[7, 33] In these lower-dimensional perovskites, the inorganic octahedral framework loses its 3D connectivity. Unlike their 3D counterparts, the chemical composition of lower-dimensional perovskites is not constrained by the Goldschmidt tolerance factor.[30] This compositional flexibility allows for the integration of a broader range of organic and inorganic sub-lattices, opening up opportunities to introduce new functionalities.

1.2.2 2D Hybrid Pb Halide Perovskite

If the A-site cation is too large to fit within the cuboctahedral void of the 3D (ABX_3) perovskite structure, it causes the inorganic layers to separate (Figure 1.2).[33] This separation can occur along different crystallographic directions. When the splitting occurs along the (100) planes, the resulting structures are classified as (100) oriented layered perovskites. In this configuration, the 2D layers align with the (100) planes of the original 3D crystal, and the interlayer spacing defines the separation between consecutive (100) planes.[34-36] Most layered perovskites belong to this category. Layered perovskites sliced along other planes, such as (110) or (111), are also possible but are relatively rare.

The general formula for (100) oriented hybrid perovskites is either $(A')_2(A)_{n-1}B_nX_{3n+1}$ or $(A'')_2(A)_{n-1}B_nX_{3n+1}$. When the interlayer cation is a monocation (A'^+), such as a primary ammonium cation ($R{-}NH_3^+$), the organic cations in the interlayer space typically adopt a head-to-tail arrangement. This results in adjacent perovskite layers being staggered relative to one another see Figure 1.2. Due to their structural resemblance to the Ruddlesden-Popper (RP) phase, these are referred to as Ruddlesden-Popper layered hybrid perovskites.[37] Conversely, when the interlayer cation is a dication (A''^{2+}) such as a primary diammonium cation $(NH_3{-}R{-}NH_3)^{2+}$, dictations often favor an eclipsed configuration, where consecutive layers align directly on top of each other see Figure 1.2. These structures are called Dion-Jacobson layered hybrid perovskites, named for them

similarity to the Dion-Jacobson (DJ) phase.[38]

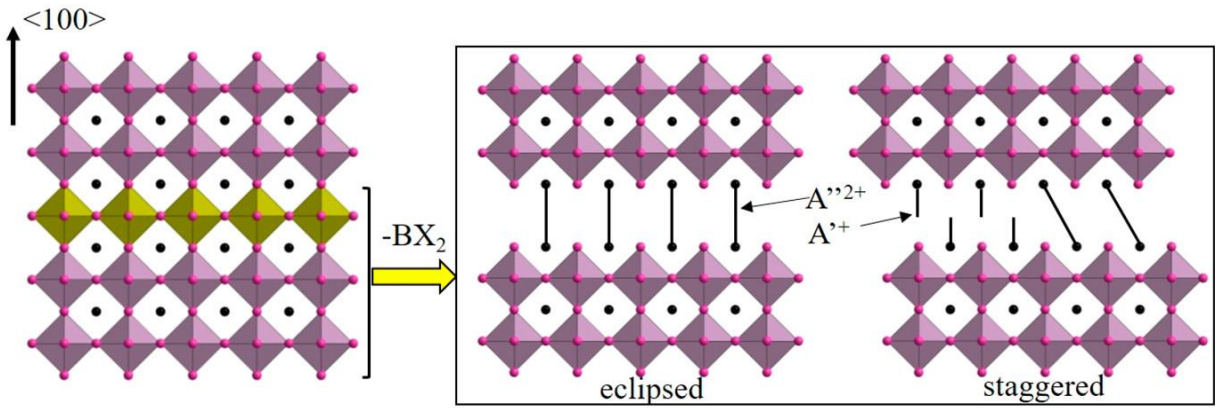

Figure 1.2: A schematic illustration depicting the structural evolution from ABX_3 3D perovskites (left) to 2D perovskites (right). In 2D perovskites, alternating organic and inorganic layers form a layered architecture, with the organic cations typically acting as spacers between the inorganic slabs. A'^{+} and A''^{2+} are monocations and dications, respectively. B^{2+} is a divalent metal ion (Pb^{2+}). Figure is reprinted from reference [33] with permission. Copyright © 2019, American Chemical Society.

In 2D layered hybrid perovskites, the positively charged ammonium groups of these cations are oriented toward the adjacent inorganic layers and form strong electrostatic and hydrogen bonding interactions to stabilize the structure.[34-36]

1.2.3 1D and 0D Pb and Bi Halide Hybrid Perovskite Derivatives

In previous section, we discussed how large A-site cations can reduce 3D perovskites to lower-dimensional 2D layered perovskites. However, this transformation does not always result in 2D structures. Some A-site cations instead lead to the formation of even lower-dimensional structures, such as 1D or 0D perovskites.[7, 8, 10, 11] The dimensionality of the resulting structure depends largely on the size, shape, and symmetry of the A-site cation. Generally linear chain A-site cations tend to form 2D layered perovskites, while large, bulky, or branched A-site cations are more likely to produce 1D or 0D perovskite structures as shown in Figure 1.3a and 1.3b.[8, 11, 39]

On the other hand, Bi^{3+} based hybrid halide perovskite commonly form zero-dimensional (0D) structures, such as $A_3Bi_2I_9$ (where A is Cs^+ or MA^+), which has face shared molecular dimers $[Bi_2I_9]^{3-}$ as shown in Figure 1.3c[40] and $A_4Bi_2I_{10}$ (where A = MBA^+), which have edge shared

molecular dimers $[Bi_2I_{10}]^{4-}$.[41, 42] They can also form one- dimensional (1D) chains like $ABiI_5$ (where A is an organic diammonium cation) as shown in Figure 1.3d.[43] The exploration of 1D $ABiI_5$ structures began in the late 1990s through the work of Mitzi et al[44] and Papavassiliou et al.[45] Low-dimensional structures often arise from edge-sharing or face-sharing PbI_6 and BiI_6 octahedra.

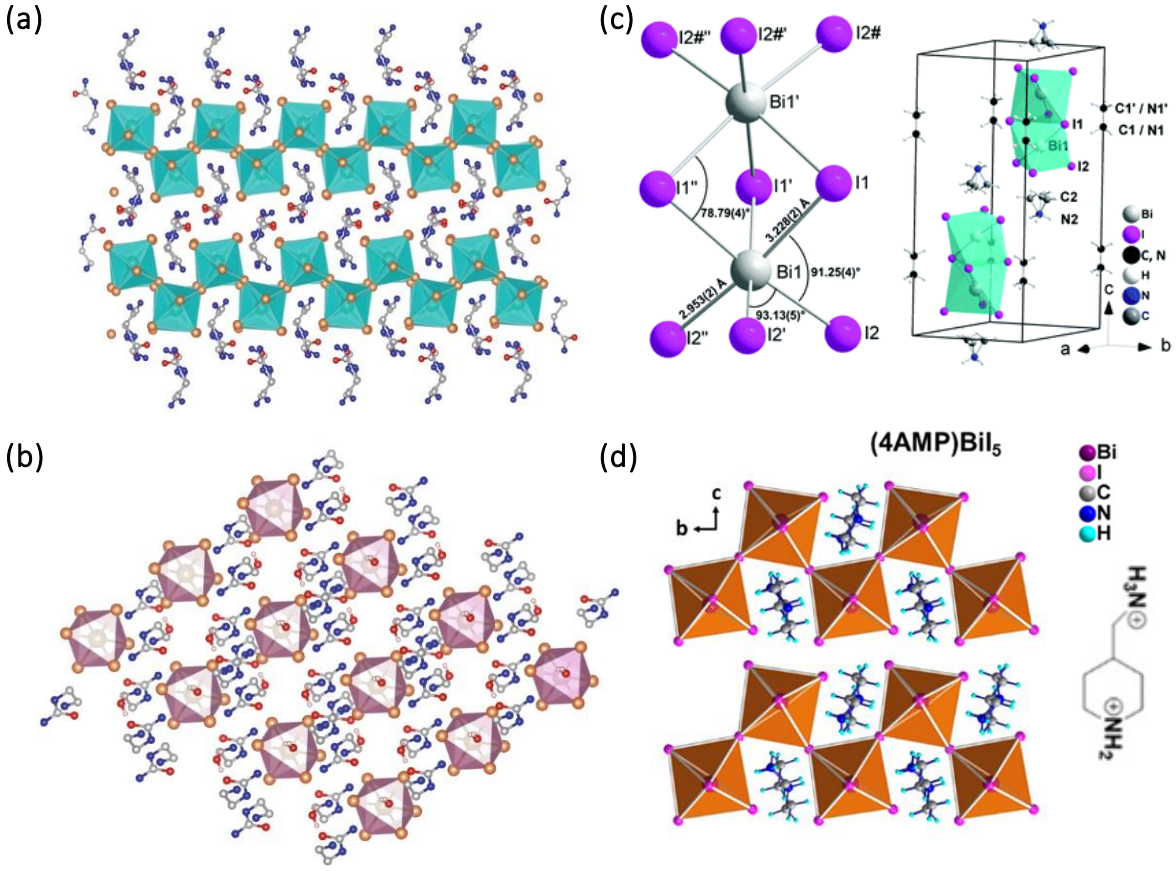

Figure 1.3: Crystal structures of (a) 1D $(C_3N_3H_{10}O)(C_3N_3H_{11}O)_2Pb_2Br_9$ and (b) 0D $(C_3N_3H_{11}O)_2PbBr_6{\cdot}4H_2O$, showing the arrangement of lead (brown spheres), bromine (orange spheres), nitrogen (blue spheres), and carbon (gray spheres) atoms. The $[PbBr_6]^{4-}$ octahedra are highlighted in indigo and pink for clarity. Hydrogen atoms are omitted for better visibility. (c) The crystal structure of $(CH_3NH_3)_3Bi_2I_9$ (MBI) consists of discrete $(Bi_2I_9)^{3-}$ anions, each composed of two face-sharing BiI_6 octahedra. These anions are surrounded by $CH_3NH_3^+$ (methylammonium) cations that occupy the voids within the structure. The unit cell contains both the $(Bi_2I_9)^{3-}$ anions and $CH_3NH_3^+$ cations. (d) The 1D chain structures of Bi-I in $(4AMPY)BiI_5$ consist of linear chains of corner-sharing BiI_6 octahedra. This structure is stabilized by diammonium A-site 4AMPY (4-aminopyridinium) cation. Figure d is reprinted from reference [43] with permission. Copyright © 2021, American Chemical Society.

1.3 Role of A-site Organic Ammonium Cations in Lower-Dimensional Hybrid Halide Perovskites

Though valence band maximum (VBM) and conduction band minimum (CBM) in hybrid halide perovskites are primarily derived from the orbitals of the metal and halide ions within the inorganic framework.[46-48] As a result, the optical and optoelectronic properties of hybrid halide perovskites are predominantly governed by the metal-halide framework. However, A-site cations, while not directly contributing to the electronic states near the band edges, play an indirect role in influencing optical and optoelectronic properties of hybrid halide perovskites. The indirect role of the A-site cations can be seen by the non-covalent bonding interactions at organic-inorganic interfaces of hybrid halide perovskites (see schematic Figure 1.4).[34, 49, 50] Hence, understanding the nature of A-site ammonium cations and their interactions at the organic-inorganic interface is crucial for investigating their role and impact on the physical and chemical properties of lower dimensional hybrid halide perovskites.

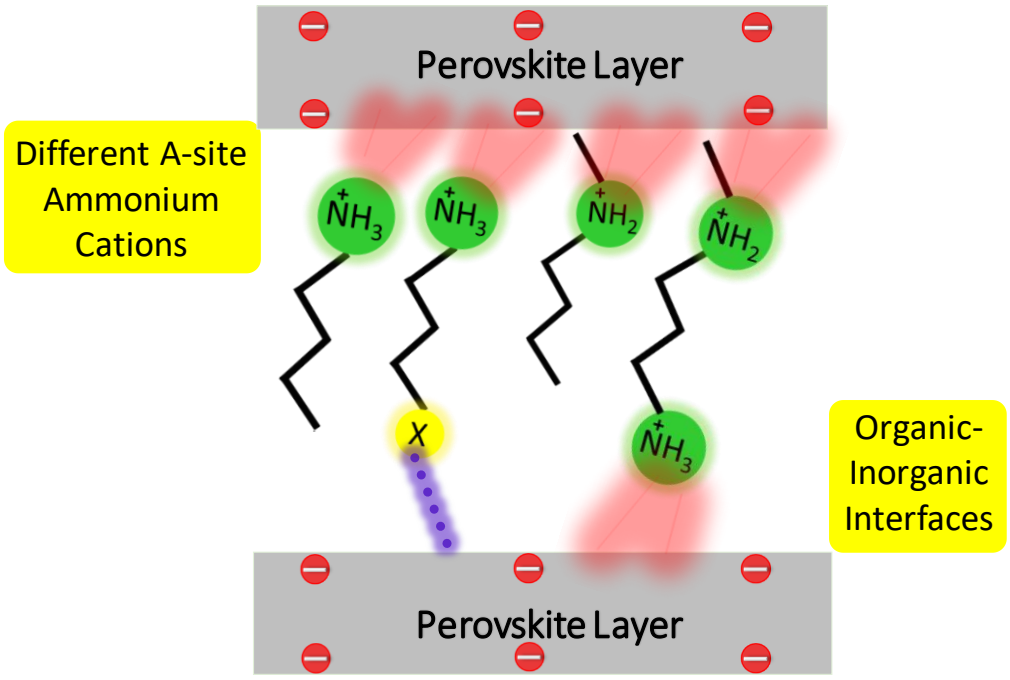

Figure 1.4: Schematic diagram shows different A-site ammonium cations and their interactions with the perovskite layer in lower dimensional hybrid halide perovskites. The interactions are represented by the red shaded region and violet dotted lines, indicating the non-covalent interactions, such as hydrogen bonding, halogen bonding (X = I, Br, Cl), and electrostatic forces, between the ammonium cations and the perovskite layers.

1.3.1 Types of A-Site Ammonium Cations for Lower-Dimensional Hybrid Halide Perovskites

The structural flexibility of hybrid halide perovskites allows for significant variation in the choice of A-site ammonium cations, enabling the introduction of desired functionalities. Simplest monoammonium aliphatic and aromatic A-site cations are butylammonium ($H\text{-}(CH_2)_4\text{-}NH_3^+$) and phenethyl ammonium ($H\text{-}C_6H_4\text{-}(CH_2)_2\text{-}NH_3^+$).[8] But if the hydrogen atom of the last tail carbon in aliphatic or aromatic ammonium cation is replaced with heteroatoms such as fluorine (F), chlorine (Cl),[51] bromine (Br),[51, 52] iodine (I)[52-54] or some functional groups like hydroxyl (OH),[52, 55] cyanide (CN),[56, 57] carboxylic acid (COOH)[58] commonly known as bifunctional monoammonium cations. Similarly, diammonium A-site ammonium cation contains two ammonium heads at both ends of the cation.[8]

Not only tail part but ammonium head also can be modified. Mostly hybrid perovskites have the A-site cations having primary ammonium group that means contain three hydrogen atoms. But these hydrogens can be progressively replaced by methyl groups, transitioning from primary to secondary, tertiary, and quaternary ammonium forms for example [$RNH_3^+ > R_2NH_2^+ > R_3NH^+ > R_4N^+$] (R: aliphatic or aromatic).[11, 59, 60] This substitution introduces steric hindrance, increasing the bulk around the ammonium head.

1.3.2 Interactions in Lower-Dimensional Hybrid Halide Perovskites

Lower-dimensional hybrid halide perovskites consist semiconducting inorganic layers, insulating organic layers, and interfaces where organic and inorganic sublattices interact. A-site ammonium cations establish connections with the inorganic layers primarily through electrostatic forces and hydrogen bonding at the organic-inorganic interfaces, as illustrated in Figure 1.5. In certain cases, interactions between organic layers are also evident.[56, 58, 61] These interactions in lower dimensional halide perovskites lead to affect the physical as well as chemical properties.

For example, in simplest 2D perovskite $(BA)_2PbI_4$, BA cation form three hydrogen bonding interactions (blue, green and red colour) with the Pb-I layer and penetrates in plane (red colour) formed by the axial iodine of the Pb-I layer as shown in Figure 1.5.[35] Cation penetration refers to the perpendicular distance between the nitrogen (N) atoms of the organic cation and the plane formed by the axial halogen atoms in the inorganic perovskite layer. This parameter is critical as

it influences the structural distortion of the inorganic framework.[59] Structural distortion majorly of two types one is the PbX_6 octahedral distortion another one is the global perovskite layer distortion between adjacent octahedra, which can be defined by the Pb-X-Pb bond angles. Deviations in the Pb-X-Pb bond angle from the ideal 180 ° indicate significant distortion in perovskite layer. This distortion, along with the inherent PbX_6 octahedral distortions, critically influences the exciton absorption and photoluminescence (PL) of Pb-based 2D hybrid halide perovskites.

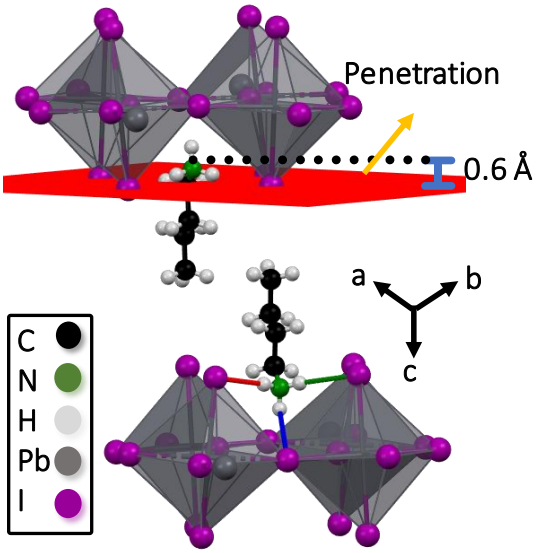

Figure 1.5: Crystal structure of $(BA)_2PbI_4$ 2D perovskite at 296 K. BA cation form hydrogen bonding interactions with the Pb-I layer shown by the green, blue, and red dotted lines. The ammonium head penetrates in the plane (red colour) formed by the axial iodine of Pb-I layer.

The situation changes significantly when the tail hydrogen of the ethyl ammonium spacer is replaced with a bromine group to form $Br(CH_2)_2NH_3^+$, hydrogen bonding interactions between ammonium head and the Br atom, stabilizes the cation in the cis conformation as shown in Figure 1.6a. Cis conformation of ammonium cations resulting in negative penetration depths -0.44 Å for Br substituted cation see Figure 1.6a.[51] Chlorine- and hydroxyl-substituted cations, $Cl(CH_2)_2NH_3^+$ and $HO(CH_2)_2NH_3^+$, experience hydrogen bonding interactions between the amino group and the Cl atom and OH group. The cis conformation of these ammonium cations results in negative penetration depths of -0.39 Å for the $Cl(CH_2)_2NH_3^+$ cation based 2D perovskite[51] and a positive penetration depth of 0.35 Å (lower than typical A-site cation based 2D perovskite like $(BA)_2PbI_4$ for the $HO(CH_2)_2NH_3^+$ cation based 2D perovskite.[52, 55]

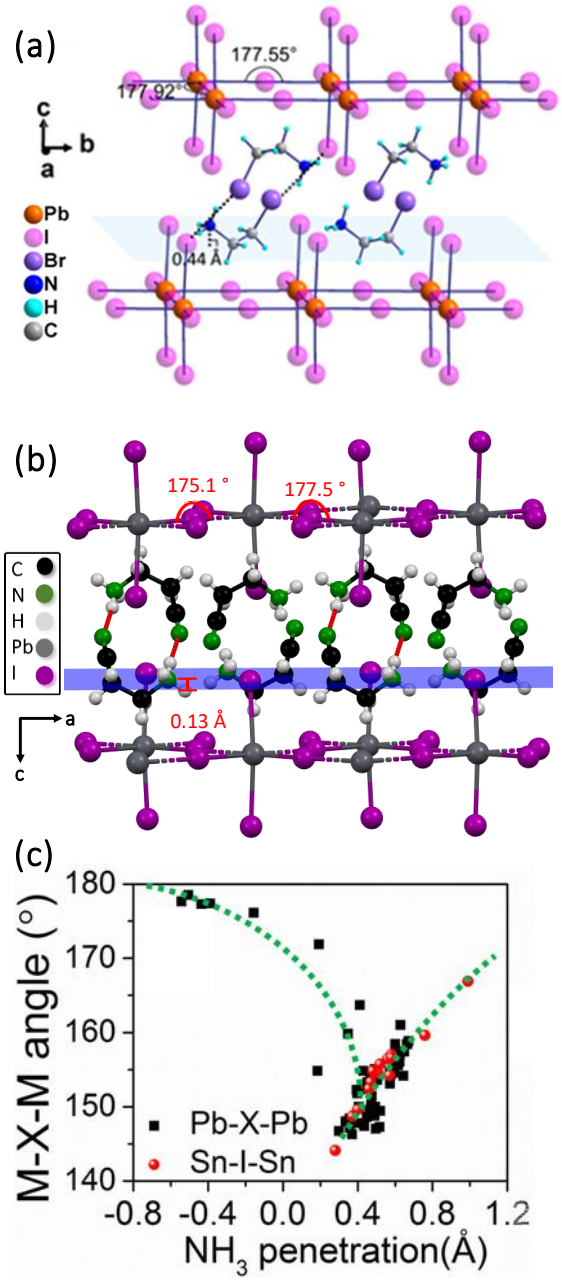

Figure 1.6: Crystal structure of the 2D perovskite (a) $(Br\text{-}(CH_2)_2\text{-}NH_3)_2PbI_4$ and (b) $(CN\text{-}(CH_2)_2\text{-}NH_3)_2PbI_4$ with tilted cation configurations. (c) The Pb–X–Pb and Sn–I–Sn bond angles in literature-reported structures are influenced by organic cation penetration. A negative penetration value indicates that the nitrogen (N) atom is positioned above the plane of the axial X atoms, whereas a positive value signifies that the N atom lies below the plane in different Pb- and Sn-based 2D hybrid perovskites. Figure a is reprinted from reference [8]. Copyright © 2021, American Chemical Society. Figure c is reprinted from reference [59] with permission. Copyright © 2017, American Chemical Society.

In the same line when the hydrogen at the tail of ethyl ammonium is replaced with a cyanide group to form $CN(CH_2)_2NH_3^+$, intermolecular hydrogen bonding interactions are observed between the ammonium head and CN groups, resulting in dimers between the perovskite layers as shown in Figure 1.6b.[56, 57] This reduces the interaction of $CN(CH_2)_2NH_3^+$ cation with the Pb-I framework, making the hydrogen bonding between the amino group and iodide atoms negligible, which results in a reduced penetration depth of 0.13 Å (see Figure 1.6b). In all the cases discussed above the octahedra remain untitled, with Pb-I-Pb bond angles approaching 180 ° (see Figure 1.6c), enabling better orbital overlap between Pb s and I p-orbitals.[35, 36, 52, 59, 62] This structural configuration results in smaller bandgaps compared to n = 1 structures with tilted octahedra.

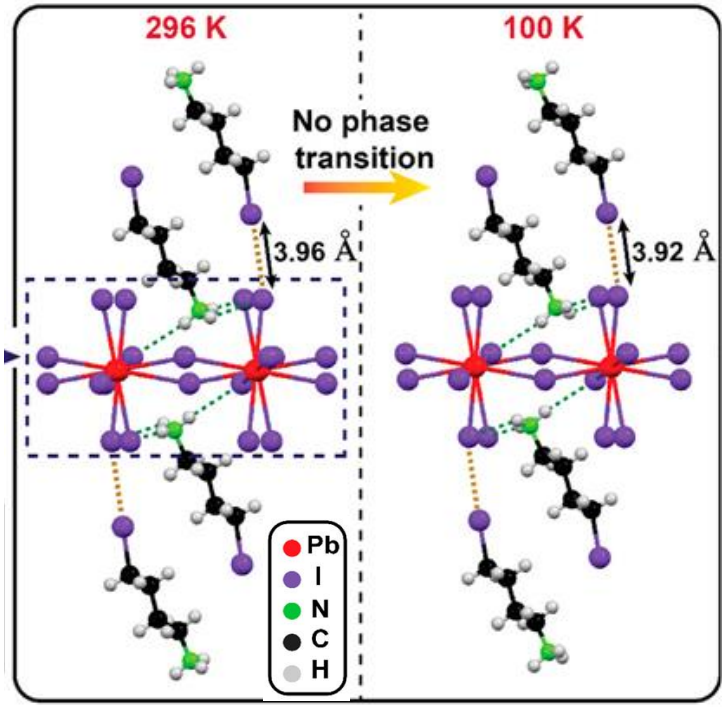

Figure 1.7: Crystal structure of $(I\text{-}(CH_2)_4\text{-}NH_3)_2PbI_4$ at 296 K and 100 K, highlighting non-covalent hydrogen bonding (green dashed lines) and iodine–iodine interactions (yellow dashed lines) between $I\text{-}(CH_2)_4\text{-}NH_3^+$cations and inorganic Pb–I layers. Figure is reprinted from reference [53] with permission. Copyright © 2021, American Chemical Society.

The iodine substituted ethyl ammonium cation, $I(CH_2)_2NH_3^+$, adopts a distinct structure compared to its bromo- and chloro-substituted counterparts.[51, 53] A strong interaction between the iodine atom of the organic cation and the axial iodine atom of the octahedron orients the C-N bond perpendicular to the inorganic layer. This results in the amino group penetrating the octahedral

cavity with a positive penetration depth of +0.44 Å. Consequently, the amino group strongly interacts with the iodine atoms of the octahedron, inducing a heavily tilted structure and a larger bandgap than the Cl- and Br-substituted analogs.[51]

Such halogen-halogen interactions are observed in a series of 2D perovskites with $I(CH_2)_nNH_3^+$ cations (where n = 2 to 6). For example, in $(I(CH_2)_4NH_3^+)_2PbI_4$ 2D perovskite, the shortest iodine-iodine distance is 3.96 Å, is less than the sum of their van der Waals radii (4.3 Å), indicating the presence of non-covalent halogen bonding interactions as shown in Figure 1.7.[53] Such iodine-iodine bonding interactions helps to suppress the structural phase transitions within 10-300 K temperature range, which is very common with $(BA)_2PbI_4$, where no iodine is present at the cation's tail.[63]

1.4 Lower-Dimensional Hybrid Halide Perovskite Single Crystal and Thin Film-Based Photodetectors

As previously highlighted, the structural flexibility of hybrid halide perovskites offers significant advantages in creating multifunctional materials, making them ideal candidates for advanced optoelectronic applications.[64, 65] Compared to their 3D counterparts, lower-dimensional hybrid halide perovskites (2D, 1D, and 0D) exhibit improved environmental stability, minimized ionic migration, and easily tunable electrical properties.[61, 66, 67] However, the higher organic content in lower dimensional hybrid halide perovskite can slightly dilute the optoelectronically active perovskite layers, which can affect the maximum light-to-current conversion efficiency. Nevertheless, lower-dimensional hybrid halide perovskites have shown great promise in emerging applications particularly in fields like lasing and photodetection.[23, 28, 29, 68] Their strong excitonic absorption and emission at room temperature makes them ideal candidates for use in these areas.

As previously discussed, semiconductors exhibit conductive properties in their "on" state, which can be achieved through external stimuli such as light, heat, or doping. When light of sufficient energy, exceeding the semiconductor's bandgap is illuminated, it generates electron-hole pairs, known as excitons. By making proper electrical contacts/connections, the electrons can be directed through an external circuit before recombining with their corresponding holes. Photodetection is possible by different device architectures, such as photoconductors, photodiodes, and

phototransistors.[68] A photoconductor is a planar two-terminal device in which the photoactive layer acts as a conductive channel between the electrodes. When illuminated, photogenerated charge carriers (electrons and holes) travel through this channel, facilitating light detection. This straightforward detection mechanism makes photoconductors ideal for single-crystal-based optoelectronic applications as shown in Figure 1.8a.[69] In comparison, photodiodes leverage a p-n

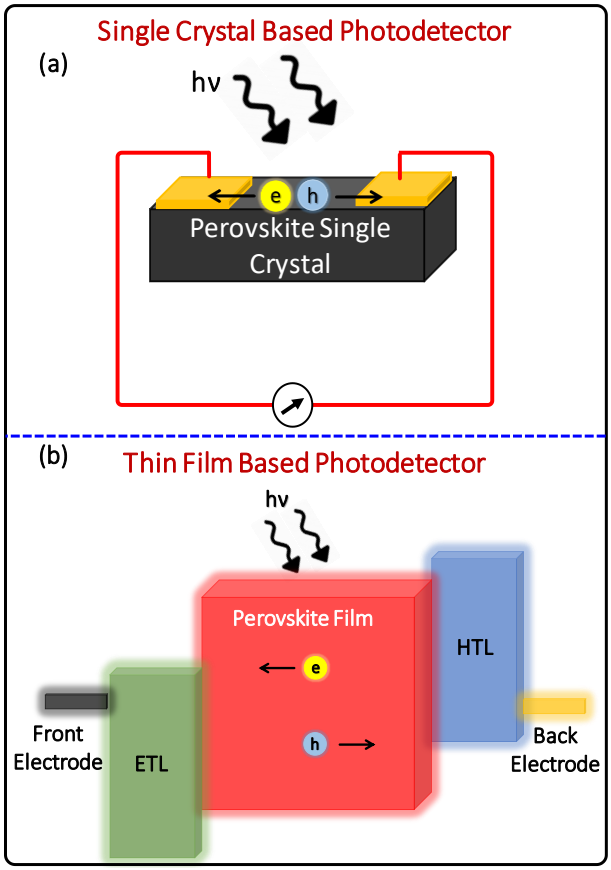

Figure 1.8: (a) The photoconductor configuration, where hybrid perovskite single crystal is directly employed for photodetection. (b) The photodiode architecture, showcasing an active perovskite layer, typically in thin-film form, positioned between an n-type and a p-type transport layer.

junction with a built-in potential to separate photogenerated charge carriers within the active hybrid perovskite layer. Electrons and holes are efficiently directed toward opposite electrodes via specialized electron and hole transport layers, enabling effective charge separation, collection, and detection. The photodiode architecture is particularly well-suited for thin-film-based optoelectronic applications as shown in Figure 1.8b.[70]

1.5 Solvent-Based Single Crystal Synthesis and Thin Film Fabrication of Lower-Dimensional Hybrid Halide Perovskites

Achieving exceptional optoelectronic performance requires the growth of high-quality single crystals and thin films of hybrid halide perovskites.[69, 70] Various synthetic methods have been developed for the preparation of layered hybrid perovskite single crystals. These include solution-based approaches such as acid precipitation,[37] crystallization in organic solvents like dimethylformamide (DMF), dimethyl sulfoxide (DMSO), and gamma-butyrolactone (GBL)[71] as well as vapor diffusion[14] and solvothermal synthesis techniques.[72] Among these, the acid-precipitation method is the most widely employed due to its simplicity (see Figure 1.9).

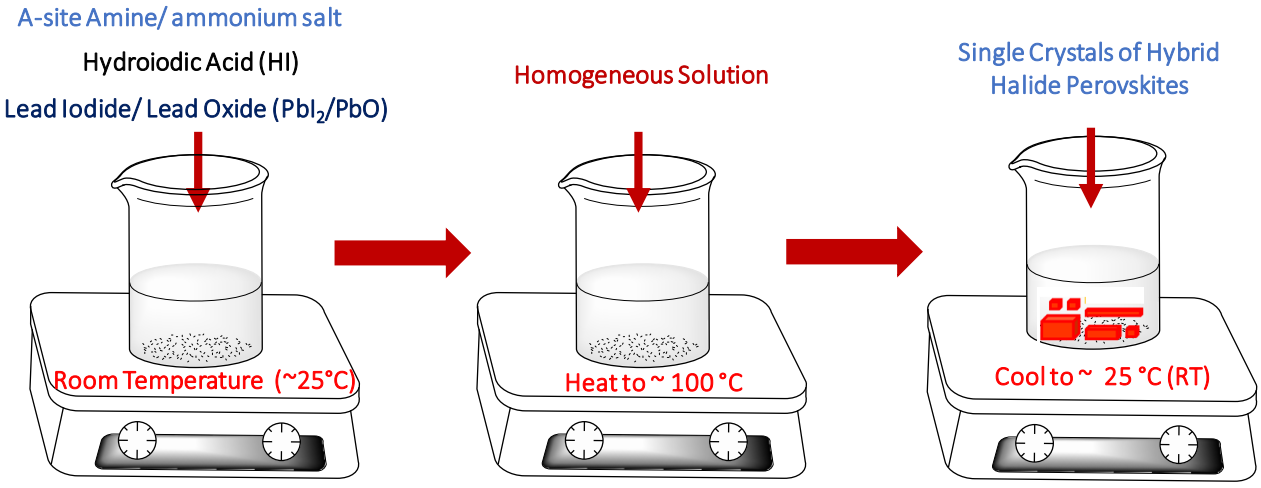

Figure 1.9: Acid precipitation method for the synthesis of lower dimensional hybrid perovskites, demonstrated step by step for lead iodide-based perovskites from left to right.

In the acid-precipitation process, aqueous hydrohalic acid (HX) (where X = Cl, Br, I) is used to dissolve an amine or its corresponding ammonium halide salt (A-site precursor) and metal oxides/halides/acetate [PbO/SnO/PbX_2 (where X = Cl, Br, I)/$Pb(CH_3COO)_2$]. These salts are heated and stirred in the HX solution, usually at boiling conditions, until all the precursors are fully dissolved, forming a clear solution. The solution is then allowed to cool gradually to room temperature, to get the crystals of the 2D, 1D and 0D hybrid halide perovskites.

For the fabrication of high-quality thin films suitable for optical and optoelectronic applications, various methods such as spin coating, slot-die coating, and spray coating are employed.[73, 74]

Among these, spin coating is the most widely used technique for small-scale fabrication. In this method, perovskite precursors are dissolved in organic solvents like GBL, DMF, or DMSO and deposited onto a rotating substrate to form a uniform thin film. Spin coating can be performed using three distinct approaches: the one-step method, hot-casting method, and antisolvent method, as illustrated in Figure 1.10(a-c).[8]

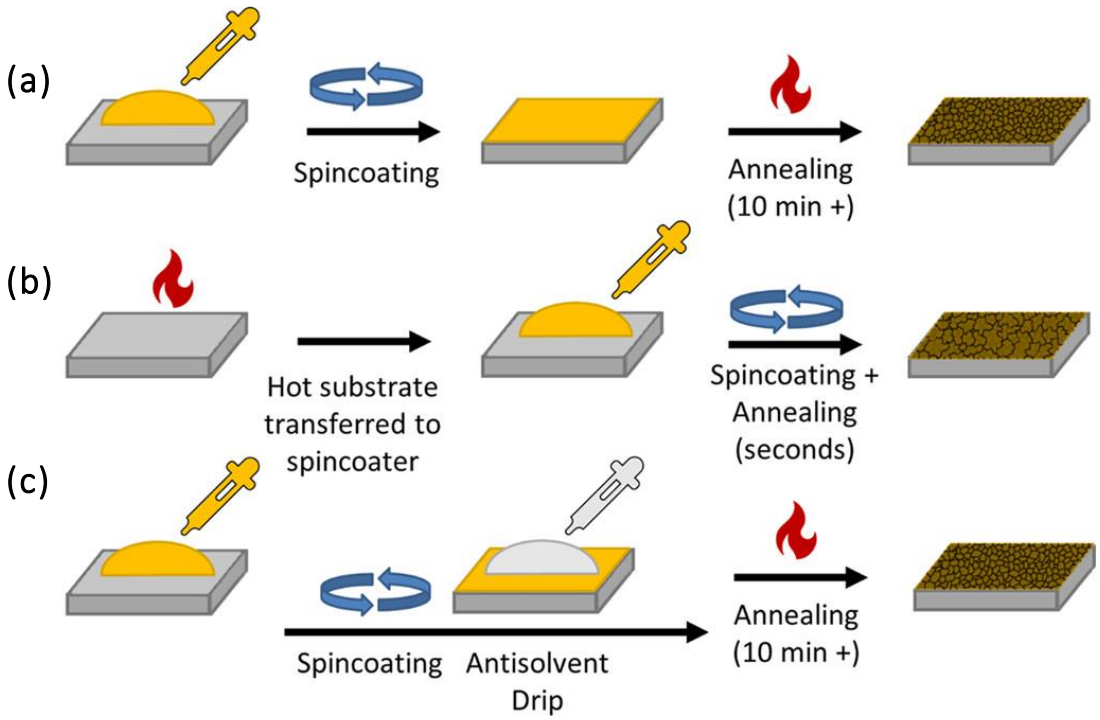

Figure 1.10: Schematics of three commonly used thin-film fabrication methods: (a) the one-step method, where the perovskite precursor is deposited and dried in a single step, (b) the hot-casting method, which involves depositing the precursor solution onto a preheated substrate to promote uniform crystallization, and (c) the antisolvent method, where a non-polar antisolvent is introduced during spin-coating to induce rapid crystallization and achieve high-quality films. Figure is reprinted from reference [8] with permission. Copyright © 2021, American Chemical Society.

1.6 Toxic Solvents: A Major Concern

As discussed above, the synthesis of hybrid halide perovskite single crystals typically involves methods which rely on solvents like hydrohalic acids (HX, where X = Cl, Br, I), dimethylformamide (DMF), dimethyl sulfoxide (DMSO), and gamma-butyrolactone (GBL). [14, 37, 71, 72] All of these solvents are toxic in nature and not good for environment.[75] In addition to single

crystals, the fabrication of perovskite thin films also involves the use of polar solvents like DMF and DMSO to dissolve perovskite precursors efficiently.[69, 70] Therefore, reducing or eliminating the use of toxic solvents in both the synthesis of the single crystals and film preparation of perovskites is critical for improving the environmental sustainability of perovskite-based optoelectronic devices.[76, 77]

Several efforts have been made to reduce or eliminate the use of toxic solvents in perovskite film fabrication.[75, 78] One promising approach being the utilization of the melting property of hybrid halide perovskites to fabricate perovskite films via the melt-pressing method.[79-83] However, challenges remain, as only a limited number of hybrid perovskites possess the ability to melt. Therefore, there is a need to rationally design meltable hybrid halide perovskites. Additionally, optimizing the melt-pressing film fabrication method is crucial, as it currently lacks precise control over the thickness of the perovskite films, a key factor in the design and performance of optoelectronic devices.[84]

1.7 Scope of the Thesis

As discussed above, the specially designed A-site ammonium cations lead to various interactions in lower-dimensional hybrid halide perovskites, significantly influencing their physical and chemical properties. In this thesis, we rationally designed lower dimensional Pb and Bi halide hybrid perovskites and explored various non covalent bonding interactions with single crystal x-ray diffraction (SCXRD). Our objective is to establish structure-property relationships, develop toxic solvent-free synthesis methods, and fabricate solvent- and vacuum-free perovskite films for optoelectronic device applications mainly photodetectors.

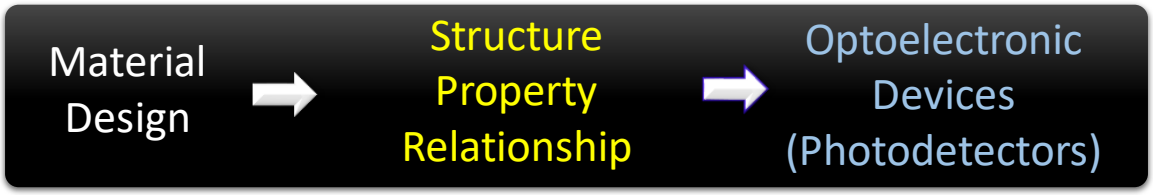

Typically, A_2PbX_4 (A: organic ammonium cation, X: Br, I) hybrid perovskite undergo irreversible decomposition upon heating as shown in Figure 1.11a. In chapter 2 of thesis we have rationally designed the A_2PbX_4 perovskites, which can melt at lower temperatures compared to the

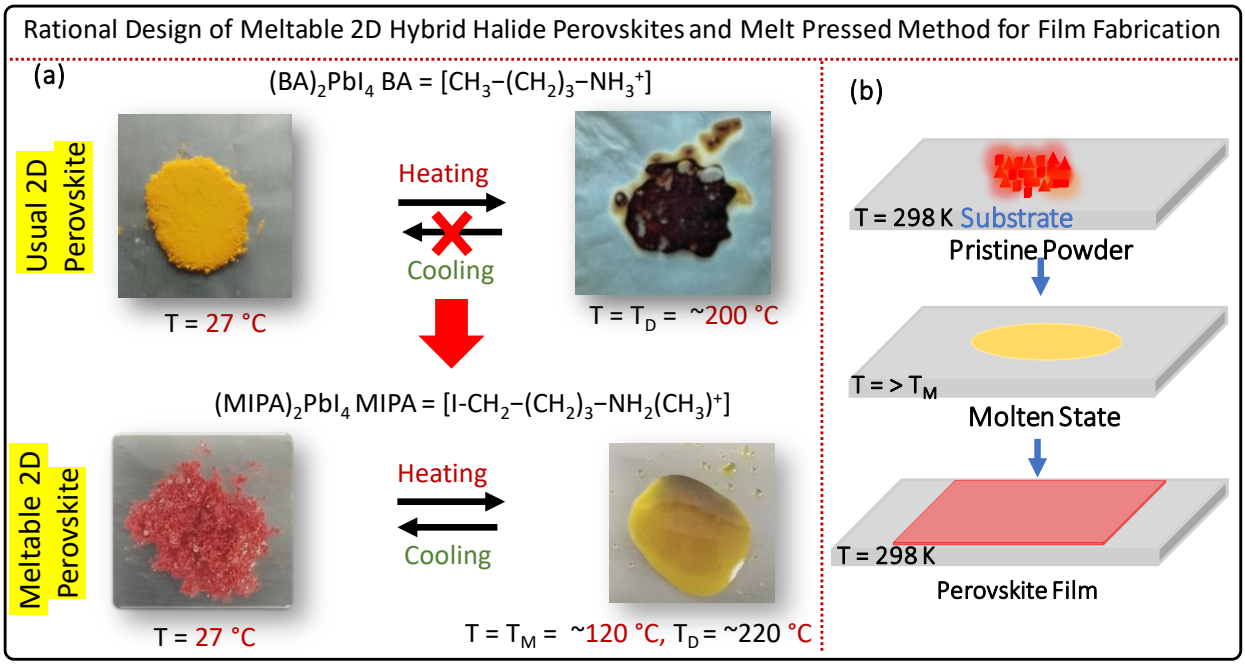

Figure 1.11: (a) Digital photographs demonstrate the contrasting thermal behaviors of the usual 2D perovskite $(BA)_2PbI_4$ and the rationally designed 2D perovskite $(MIPA)_2PbI_4$. Upon heating, the yellowish powder of $(BA)_2PbI_4$ turns dark brown, indicating decomposition, and does not return to its original structure upon cooling. In contrast, $(MIPA)_2PbI_4$ undergoes melting upon heating, forming a yellow liquid. Notably, after cooling, it reverts to its pristine structure, showcasing its reversible melting property. (b) Schematic diagram showing the melt pressed film fabrication method.

decomposition temperature and recrystallizes back to its original crystal structure upon cooling see Figure 1.11a. We tried to established the relation between the crystal structure and the melting phenomenon with the help of thermodynamic parameters like enthalpy of fusion (ΔH_{fus}) and entropy of fusion (ΔS_{fus}). In advancement in this direction we have shown the potential of the melt pressed film fabrication method (see Figure 1.11b) in optoelectronics by fabricating the n-i-p based photodetector in which active perovskite layer is fabricated by the melt pressed method. The melt pressed method of film fabrication does not need any solvent like DMF, DMSO etc.

Solvent-based methods are commonly employed for the synthesis of hybrid halide perovskites; however, these methods often rely on toxic chemicals, posing significant environmental and safety challenges. To overcome these issues, Chapter 3 presents a molten-state synthesis approach as a sustainable alternative. This method utilizes the melting of ammonium iodide salts, where the

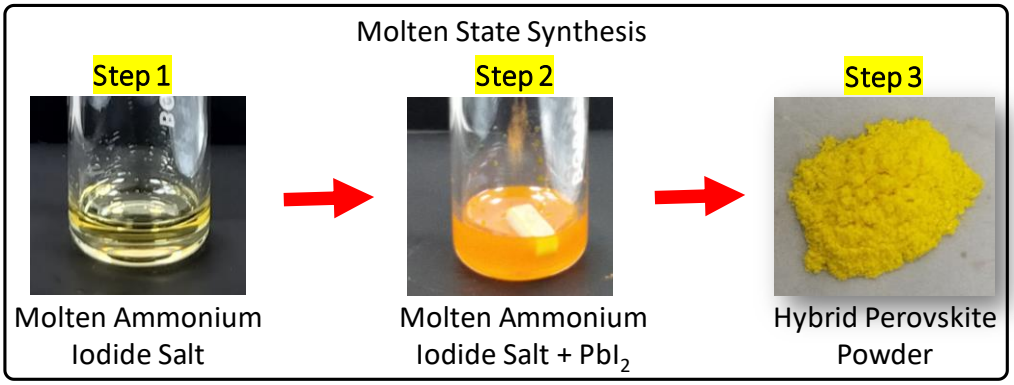

Figure 1.12: Digital photographs depict the stepwise process of the molten-state synthesis method for hybrid halide perovskites. This method differs from the conventional acid-precipitation method discussed in section 1.5 above.

molten salt functions as an ionic liquid to dissolve lead iodide precursors, as illustrated in Figure 1.12. Additionally, a comparative study of the hybrid halide perovskites synthesized through the molten-state method and the conventional acid-precipitation technique highlights the greener and more sustainable nature of this innovative approach.

Structural non-centrosymmetry in semiconducting organic–inorganic hybrid halide perovskites enable unique functionalities, including anomalous photovoltaic effects and nonlinear optical properties. In Chapter 4, we explore these possibilities by introducing mono- and dimethyl-substituted A-site ammonium cations. These substitutions limit the rotational freedom of the ammonium head in the crystal structure, inducing non-centrosymmetry and chirality in the 1D (BMPA)BiI_5 hybrid perovskite derivative. The resulting structural characteristics prompted detailed investigations into the nonlinear optical properties, anomalous bulk photovoltaic effect, and chiroptic responses.

Chirality in hybrid halide perovskites has recently emerged as an exciting area of research, primarily introduced through the use of chiral A-site ammonium cations. Chirality enables new functionalities, such as circular dichroism (CD), circularly polarized emission, circularly polarized photodetectors, and spin selectivity. Despite these advancements, a key question remains: how is chirality induced from the organic cations to the inorganic sublattice? In Chapter 5, we synthesized chiral 0D bismuth-halide hybrid perovskites as to investigate the mechanism of chirality induction. Our analysis revealed that asymmetric hydrogen bonding interaction, play a critical role in

inducing chirality from the organic to the inorganic sublattices. To further explore the chiroptic properties, we used circular dichroism spectroscopy in the transmittance mode on thin films of chiral 0D perovskite derivatives.

1.8 References

1. Kumar, A.; Thorbole, A.; Gupta, R. K. Sustaining The Future: Semiconductor Materials and their Recovery. *Mater. Sci. Semicond. Process.*, **2025,** *185*, 108943.

2. Sze, S. M., Semiconductor Devices: Physics and Technology. *JOHN WILEY & SONS*, **2008**.

3. Hall, R. N.; Fenner, G. E.; Kingsley, J. D.; Soltys, T. J.; Carlson, R. O. Coherent Light Emission From GaAs Junctions. *Phys. Rev. Lett.* **1962,** *9*, 366-368.

4. Weber, D., $CH_3NH_3PbX_3$, a Pb(II)-System with Cubic Perovskite Structure. *Zeitschrift für Naturforschung B* **1978,** *33*, 1443-1445.

5. Weber, D. The Perovskite System $CH_3NH_3[Pb_nSn_{1-n}X_3]$ (X = C1, Br, I). *Zeitschrift für Naturforschung B* **1979,** *34*, 939-941.

6. Mitzi, D. B.; Feild, C. A.; Schlesinger, Z.; Laibowitz, R. B. Transport, Optical, and Magnetic Properties of the Conducting Halide Perovskite $CH_3NH_3SnI_3$. *J. Solid State Chem.* **1995,** *114*, 159-163.

7. Saparov, B.; Mitzi, D. B. Organic–Inorganic Perovskites: Structural Versatility for Functional Materials Design. *Chem. Rev.* **2016,** *116*, 4558-4596.

8. Li, X.; Hoffman, J. M.; Kanatzidis, M. G. The 2D Halide Perovskite Rulebook: How the Spacer Influences Everything from the Structure to Optoelectronic Device Efficiency. *Chem. Rev.* **2021,** *121*, 2230-2291.

9. Sun, S.; Lu, M.; Gao, X.; Shi, Z.; Bai, X.; Yu, W. W.; Zhang, Y. 0D Perovskites: Unique Properties, Synthesis, and Their Applications. *Adv. Sci.* **2021,** *8*, 2102689.

10. Yuan, Z.; Zhou, C.; Tian, Y.; Shu, Y.; Messier, J.; Wang, J. C.; Van de Burgt, L. J.; Kountouriotis, K.; Xin, Y.; Holt, E.; Schanze, K.; Clark, R.; Siegrist, T.; Ma, B. One-Dimensional Organic Lead Halide Perovskites with Efficient Bluish White-Light Emission. *Nat. Commun.* **2017,** *8*, 14051.

11. Mao, L.; Guo, P.; Kepenekian, M.; Hadar, I.; Katan, C.; Even, J.; Schaller, R. D.; Stoumpos, C. C.; Kanatzidis, M. G. Structural Diversity in White-Light-Emitting Hybrid Lead Bromide

Perovskites. *J. Am. Chem. Soc.* **2018,** *140*, 13078-13088.

12. Xing, G.; Mathews, N.; Sun, S.; Lim, S. S.; Lam, Y. M.; Grätzel, M.; Mhaisalkar, S.; Sum, T. C. Long-Range Balanced Electron- and Hole-Transport Lengths in Organic-Inorganic $CH_3NH_3PbI_3$. *Science* **2013,** *342*, 344-347.

13. Stranks, S. D.; Eperon, G. E.; Grancini, G.; Menelaou, C.; Alcocer, M. J. P.; Leijtens, T.; Herz, L. M.; Petrozza, A.; Snaith, H. J. Electron-Hole Diffusion Lengths Exceeding 1 Micrometer in an Organometal Trihalide Perovskite Absorber. *Science* **2013,** *342*, 341-344.

14. Shi, D.; Adinolfi, V.; Comin, R.; Yuan, M.; Alarousu, E.; Buin, A.; Chen, Y.; Hoogland, S.; Rothenberger, A.; Katsiev, K.; Losovyj, Y.; Zhang, X.; Dowben, P. A.; Mohammed, O. F.; Sargent, E. H.; Bakr, O. M. Low Trap-State Density and Long Carrier Diffusion in Organolead Trihalide Perovskite Single Crystals. *Science* **2015,** *347*, 519-522.

15. Egger, D. A.; Rappe, A. M.; Kronik, L. Hybrid Organic–Inorganic Perovskites on the Move. *Acc. Chem. Res.* **2016,** *49*, 573-581.

16. Rosales, B. A.; Hanrahan, M. P.; Boote, B. W.; Rossini, A. J.; Smith, E. A.; Vela, J. Lead Halide Perovskites: Challenges and Opportunities in Advanced Synthesis and Spectroscopy. *ACS Energy Lett.* **2017,** *2*, 906-914.

17. Etgar, L.; Gao, P.; Xue, Z.; Peng, Q.; Chandiran, A. K.; Liu, B.; Nazeeruddin, M. K.; Grätzel, M. Mesoscopic $CH_3NH_3PbI_3/TiO_2$ Heterojunction Solar Cells. *J. Am. Chem. Soc.* **2012,** *134*, 17396-17399.

18. Green, M. A.; Ho-Baillie, A.; Snaith, H. J. The Emergence of Perovskite Solar Cells. *Nat. Photonics* **2014,** *8*, 506-514.

19. Kojima, A.; Teshima, K.; Shirai, Y.; Miyasaka, T. Organometal Halide Perovskites as Visible-Light Sensitizers for Photovoltaic Cells. *J. Am. Chem. Soc.* **2009,** *131*, 6050-6051.

20. Lee, M. M.; Teuscher, J.; Miyasaka, T.; Murakami, T. N.; Snaith, H. J. Efficient Hybrid Solar Cells Based on Meso-Superstructured Organometal Halide Perovskites. *Science* **2012,** *338*, 643-647.

21. Ru, X.; Yang, M.; Yin, S.; Wang, Y.; Hong, C.; Peng, F.; Yuan, Y.; Sun, C.; Xue, C.; Qu, M.; Wang, J.; Lu, J.; Fang, L.; Deng, H.; Xie, T.; Liu, S.; Li, Z.; Xu, X. Silicon heterojunction solar cells achieving 26.6% efficiency on commercial-size p-type silicon wafer. *Joule* **2024,** *8*, 1092-1104.

22. Cao, F.; Bian, L.; Li, L., Perovskite solar cells with high-efficiency exceeding 25%: A review. *Energy Materials and Devices* **2024,** *2*, 9370018.

23. Xian, S.; Hou, S.; Zhang, H.; Yang, J.; Pan, G.; Gao, H.; You, W.; Zhang, Z.; Zhu, B.; Mao, Y. High Quality Quasi-Two-Dimensional Organic–Inorganic Hybrid Halide Perovskite Film for High Performance Photodetector. *Appl. Phys. Lett.* **2023,** *122*, 103503.

24. Geng, X.; Wang, F.; Tian, H.; Feng, Q.; Zhang, H.; Liang, R.; Shen, Y.; Ju, Z.; Gou, G.-Y.; Deng, N.; Li, Y.-t.; Ren, J.; Xie, D.; Yang, Y.; Ren, T.-L. Ultrafast Photodetector by Integrating Perovskite Directly on Silicon Wafer. *ACS Nano* **2020,** *14*, 2860-2868.

25. Fakharuddin, A.; Gangishetty, M. K.; Abdi-Jalebi, M.; Chin, S.-H.; bin Mohd Yusoff, A. R.; Congreve, D. N.; Tress, W.; Deschler, F.; Vasilopoulou, M.; Bolink, H. J. Perovskite Lght-Emitting Diodes. *Nat. Electron.* **2022,** *5*, 203-216.

26. Sun, Y.; Ge, L.; Dai, L.; Cho, C.; Ferrer Orri, J.; Ji, K.; Zelewski, S. J.; Liu, Y.; Mirabelli, A. J.; Zhang, Y.; Huang, J.-Y.; Wang, Y.; Gong, K.; Lai, M. C.; Zhang, L.; Yang, D.; Lin, J.; Tennyson, E. M.; Ducati, C.; Stranks, S. D.; Cui, L.-S.; Greenham, N. C. Bright and Stable Perovskite Light-Emitting Diodes in the Near-Infrared Range. *Nature* **2023,** *615*, 830-835.

27. Temerov, F.; Baghdadi, Y.; Rattner, E.; Eslava, S. A Review on Halide Perovskite-Based Photocatalysts: Key Factors and Challenges. *ACS Appl. Energy Mater.* **2022,** *5*, 14605-14637.

28. Zhang, Q.; Shang, Q.; Su, R.; Do, T. T. H.; Xiong, Q. Halide Perovskite Semiconductor Lasers: Materials, Cavity Design, and Low Threshold. *Nano Lett.* **2021,** *21*, 1903-1914.

29. Stylianakis, M. M.; Maksudov, T.; Panagiotopoulos, A.; Kakavelakis, G.; Petridis, K. Inorganic and Hybrid Perovskite Based Laser Devices: A Review *Materials*, **2019,** 12, 859.

30. Goldschmidt, V. M. Die Gesetze der Krystallochemie. *Naturwissenschaften* **1926,** *14*, 477-485.

31. Liu, X.; Hong, R.; Tian, C., Tolerance Factor and the Stability Discussion of ABO_3-type Ilmenite. *J. Mater. Sci: Mater. Electron.* **2009,** *20*, 323-327.

32. Li, Z.; Yang, M.; Park, J.-S.; Wei, S.-H.; Berry, J. J.; Zhu, K. Stabilizing Perovskite Structures by Tuning Tolerance Factor: Formation of Formamidinium and Cesium Lead Iodide Solid-State Alloys. *Chem. Mater.* **2016,** *28*, 284-292.

33. Katan, C.; Mercier, N.; Even, J. Quantum and Dielectric Confinement Effects in Lower-Dimensional Hybrid Perovskite Semiconductors. *Chem. Revi.* **2019,** *119*, 3140-3192.

34. Billing, D. G.; Lemmerer, A., Synthesis, characterization and phase transitions of the inorganic–organic layered perovskite-type hybrids [$(C_nH_{2n+1}NH_3)_2PbI_4$] (n = 12, 14, 16 and 18). *New J Chem.* **2008,** *32*, 1736-1746.

35. Billing, D. G.; Lemmerer, A. Synthesis, Characterization and Phase Transitions in the Inorganic-Organic Layered Perovskite-Type Hybrids [$(C_nH_{2n+1}NH_3)_2PbI_4$], n = 4, 5 and 6. *Acta Crystallogr., Sect. B: Struct. Sci.* **2007,** *63*, 735.

36. Lemmerer, A.; Billing, D. G., Synthesis, Characterization and Phase Transitions of the Inorganic–Organic Layered Perovskite-Type Hybrids [$(C_nH_{2n+1}NH_3)_2PbI_4$], n = 7, 8, 9 and 10. *Dalton Trans.* **2012,** *41*, 1146-1157.

37. Stoumpos, C. C.; Cao, D. H.; Clark, D. J.; Young, J.; Rondinelli, J. M.; Jang, J. I.; Hupp, J. T.; Kanatzidis, M. G. Ruddlesden–Popper Hybrid Lead Iodide Perovskite 2D Homologous Semiconductors. *Chem. Mater.* **2016,** *28*, 2852-2867.

38. Mao, L.; Ke, W.; Pedesseau, L.; Wu, Y.; Katan, C.; Even, J.; Wasielewski, M. R.; Stoumpos, C. C.; Kanatzidis, M. G. Hybrid Dion–Jacobson 2D Lead Iodide Perovskites. *J. Am. Chem. Soc.* **2018,** *140*, 3775-3783.

39. Cui, B.-B.; Han, Y.; Huang, B.; Zhao, Y.; Wu, X.; Liu, L.; Cao, G.; Du, Q.; Liu, N.; Zou, W.; Sun, M.; Wang, L.; Liu, X.; Wang, J.; Zhou, H.; Chen, Q. Locally Collective Hydrogen Bonding Isolates Lead Octahedra for White Emission Improvement. *Nat. Commun.* **2019,** *10*, 5190.

40. Eckhardt, K.; Bon, V.; Getzschmann, J.; Grothe, J.; Wisser, F. M.; Kaskel, S., Crystallographic insights into $(CH_3NH_3)_3(Bi_2I_9)$: a New Lead-Free Hybrid Organic–Inorganic Material as a Potential Absorber for Photovoltaics. *Chem. Commun.* **2016,** *52*, 3058-3060.

41. Saraswat, A.; Vishnoi, P. 0-D and 1-D Perovskite-like Hybrid Bismuth(III) Iodides. *Chem. Asian J.* **2024,** *19*, e202400048.

42. Rajput, P. K.; Poonia, A. K.; Mukherjee, S.; Sheikh, T.; Shrivastava, M.; Adarsh, K.; Nag, A. Chiral methylbenzylammonium bismuth iodide with zero-dimensional perovskite derivative structure. *J. Phys. Chem. C* **2022,** *126*, 9889-9897.

43. Li, X.; Traoré, B.; Kepenekian, M.; Li, L.; Stoumpos, C. C.; Guo, P.; Even, J.; Katan, C.; Kanatzidis, M. G. Bismuth/Silver-Based Two-Dimensional Iodide Double and One-Dimensional Bi Perovskites: Interplay between Structural and Electronic Dimensions. *Chem. Mater.* **2021,** *33*,

6206-6216.

44. Mitzi, D. B.; Brock, P. Structure and Optical Properties of Several Organic−Inorganic Hybrids Containing Corner-Sharing Chains of Bismuth Iodide Octahedra. *Inorg. Chem.* **2001,** *40*, 2096-2104.

45. Mousdis, G. A.; Papavassiliou, G. C.; Terzis, A.; Raptopoulou, C. P. Notizen: Preparation, Structures and Optical Properties of $[H_3N(CH_2)_6NH_3]BiX_5$ (X = I, Cl) and $[H_3N(CH_2)_6NH_3]SbX_5$ (X = I, Br). *Zeitschrift für Naturforschung B* **1998,** *53*, 927-932.

46. Umebayashi, T.; Asai, K.; Kondo, T.; Nakao, A. Electronic Structures of Lead Iodide Based Low-Dimensional Crystals. *Physical Review B* **2003,** *67* (15), 155405.

47. Filippetti, A.; Mattoni, A. Hybrid Perovskites for Photovoltaics: Insights from First Principles. *Phys. Rev. B* **2014,** *89*, 125203.

48. Xiao, Z.; Meng, W.; Wang, J.; Mitzi, D. B.; Yan, Y. Searching for Promising New Perovskite-Based Photovoltaic Absorbers: The Importance of Electronic Dimensionality. *Mater. Horiz.* **2017,** *4*, 206-216.

49. Mitzi, D. B. Templating and Structural Engineering in Organic–Inorganic Perovskites. *J. Chem. Soc., Dalton Trans.* **2001,** 1, 1-12.

50. Jana, M. K.; Song, R.; Liu, H.; Khanal, D. R.; Janke, S. M.; Zhao, R.; Liu, C.; Valy Vardeny, Z.; Blum, V.; Mitzi, D. B. Organic-to-Inorganic Structural Chirality Transfer in a 2D Hybrid Perovskite and Impact on Rashba-Dresselhaus Spin-Orbit Coupling. *Nat. Commun.* **2020,** *11*, 4699.

51. Sourisseau, S.; Louvain, N.; Bi, W.; Mercier, N.; Rondeau, D.; Boucher, F.; Buzaré, J.-Y.; Legein, C. Reduced Band Gap Hybrid Perovskites Resulting from Combined Hydrogen and Halogen Bonding at the Organic−Inorganic Interface. *Chem. Mater.* **2007,** *19*, 600-607.

52. Lemmerer, A.; Billing, D. G. Effect of Heteroatoms in the Inorganic–Organic Layered Perovskite-Type Hybrids $[(ZC_nH_{2n}NH_3)_2PbI_4]$, n = 2, 3, 4, 5, 6; Z = OH, Br and I; and $[(H_3NC_2H_4S_2C_2H_4NH_3)PbI_4]$. *CrystEngComm* **2010,** *12*, 1290-1301.

53. Chakraborty, R.; Sheikh, T.; Nag, A. Iodine–Iodine Interactions Suppressing Phase Transitions of 2D Layered Hybrid $(I\text{-}(CH_2)_n\text{-}NH_3)_2PbI_4$ (n = 2–6) Perovskites. *Chem. Mater.* **2022,** *34*, 288-296.

54. Chakraborty, R.; Rajput, P. K.; Anilkumar, G. M.; Maqbool, S.; Das, R.; Rahman, A.;

Mandal, P.; Nag, A. Rational Design of Non-Centrosymmetric Hybrid Halide Perovskites. *J. Am. Chem. Soc.* **2023,** *145*, 1378-1388.

55. Mercier, N.; Poiroux, S.; Riou, A.; Batail, P. Unique Hydrogen Bonding Correlating with a Reduced Band Gap and Phase Transition in the Hybrid Perovskites $(HO(CH_2)_2NH_3)_2PbX_4$ (X = I, Br). *Inorg. Chem.* **2004,** *43*, 8361-8366.

56. Mercier, N.; Louvain, N.; Bi, W. Structural Diversity and Retro-Crystal Engineering Analysis of Iodometalate Hybrids. *CrystEngComm* **2009,** *11*, 720-734.

57. Zhao, X.; Ball, M. L.; Kakekhani, A.; Liu, T.; Rappe, A. M.; Loo, Y.-L. A Charge Transfer Framework that Describes Supramolecular Interactions Governing Structure and Properties of 2D Perovskites. *Nat. Commun.* **2022,** *13*, 3970.

58. Mercier, N. $(HO_2C(CH_2)_3NH_3)_2(CH_3NH_3)Pb_2I_7$: a Predicted Non-Centrosymmetrical Structure Built up from Carboxylic Acid Supramolecular Synthons and Bilayer Perovskite Sheets. *CrystEngComm* **2005,** *7*, 429.

59. Du, K.-z.; Tu, Q.; Zhang, X.; Han, Q.; Liu, J.; Zauscher, S.; Mitzi, D. B. Two-Dimensional Lead(II) Halide-Based Hybrid Perovskites Templated by Acene Alkylamines: Crystal Structures, Optical Properties, and Piezoelectricity. *Inorg. Chem.* **2017,** *56*, 9291-9302.

60. Xu, Z.; Mitzi, D. B.; Medeiros, D. R. $[(CH_3)_3NCH_2CH_2NH_3]SnI_4$: A Layered Perovskite with Quaternary/Primary Ammonium Dications and Short Interlayer Iodine−Iodine Contacts. *Inorg. Chem.* **2003,** *42*, 1400-1402.

61. Sheikh, T.; Maqbool, S.; Mandal, P.; Nag, A. Introducing Intermolecular Cation-π Interactions for Water-Stable Low Dimensional Hybrid Lead Halide Perovskites. *Angew. Chem. Int. Ed.* **2021,** *60*, 18265-18271.

62. Knutson, J. L.; Martin, J. D.; Mitzi, D. B. Tuning the Band Gap in Hybrid Tin Iodide Perovskite Semiconductors Using Structural Templating. *Inorg. Chem.* **2005,** *44*, 4699.

63. Sheikh, T.; Shinde, A.; Mahamuni, S.; Nag, A. Possible Dual Bandgap in $(C_4H_9NH_3)_2PbI_4$ 2D Layered Perovskite: Single-Crystal and Exfoliated Few-Layer. *ACS Energy Lett.* **2018,** *3*, 2940-2946.

64. Dong, H.; Ran, C.; Gao, W.; Li, M.; Xia, Y.; Huang, W. Metal Halide Perovskite for Next-Generation Optoelectronics: Progresses and Prospects. *eLight* **2023,** *3*, 3.

65. Zhu, T.; Gong, X. Low-Dimensional Perovskite Materials and Their Optoelectronics. *InfoMat*

2021, *3*, 1039-1069.

66. Sheikh, T.; Anilkumar, G. M.; Das, T.; Rahman, A.; Chakraborty, S.; Nag, A. Combining π-Conjugation and Cation−π Interaction for Water-Stable and Photoconductive One-Dimensional Hybrid Lead Bromide. *J. Phys. Chem. Lett.* **2023,** *14*, 1870-1876.

67. Kim, E.-B.; Akhtar, M. S.; Shin, H.-S.; Ameen, S.; Nazeeruddin, M. K. A Review on Two-Dimensional (2D) and 2D-3D Multidimensional Perovskite Solar Cells: Perovskites Structures, Stability, and Photovoltaic Performances. *J. Photochem. Photobiol. C: Photochem. Rev.* **2021,** *48*, 100405.

68. Wu, D.; Zhang, Y.; Liu, C.; Sun, Z.; Wang, Z.; Lin, Z.; Qiu, M.; Fu, D.; Wang, K. Recent Progress of Narrowband Perovskite Photodetectors: Fundamental Physics and Strategies. *Adv. Devices Instrum.*, **2023,** *4*, 1-23.

69. Yan, J.; Li, H.; Aldamasy, M. H.; Frasca, C.; Abate, A.; Zhao, K.; Hu, Y. Advances in the Synthesis of Halide Perovskite Single Crystals for Optoelectronic Applications. *Chem. Mater.* **2023,** *35*, 2683-2712.

70. Chen, J.; Zhou, Y.; Fu, Y.; Pan, J.; Mohammed, O. F.; Bakr, O. M. Oriented Halide Perovskite Nanostructures and Thin Films for Optoelectronics. *Chem. Rev.* **2021,** *121*, 12112-12180.

71. Liu, Y.; Zhang, Y.; Yang, Z.; Ye, H.; Feng, J.; Xu, Z.; Zhang, X.; Munir, R.; Liu, J.; Zuo, P.; Li, Q.; Hu, M.; Meng, L.; Wang, K.; Smilgies, D.-M.; Zhao, G.; Xu, H.; Yang, Z.; Amassian, A.; Li, J.; Zhao, K.; Liu, S. Multi-inch Single-Crystalline Perovskite Membrane for High-Detectivity Flexible Photosensors. *Nat. Commun.* **2018,** *9*, 5302.

72. Zhang, T.; Yang, M.; Benson, E. E.; Li, Z.; van de Lagemaat, J.; Luther, J. M.; Yan, Y.; Zhu, K.; Zhao, Y. A Facile Solvothermal Growth of Single Crystal Mixed Halide Perovskite $CH_3NH_3Pb(Br_{1-x}Cl_x)_3$. *Chem. Commun.* **2015,** *51*, 7820-7823.

73. Dunlap-Shohl, W. A.; Zhou, Y.; Padture, N. P.; Mitzi, D. B. Synthetic Approaches for Halide Perovskite Thin Films. *Chem Rev* **2019,** *119*, 3193-3295.

74. Dubey, A.; Adhikari, N.; Mabrouk, S.; Wu, F.; Chen, K.; Yang, S.; Qiao, Q. A Strategic Review on Processing Routes Towards Highly Efficient Perovskite Solar Cells. *J. Mater. Chem. A* **2018,** *6*, 2406-2431.

75. Stancu, V.; Tomulescu, A. G.; Leonat, L. N.; Balescu, L. M.; Galca, A. C.; Toma, V.;

Besleaga, C.; Derbali, S.; Pintilie, I. Partial Replacement of Dimethylformamide with Less Toxic Solvents in the Fabrication Process of Mixed-Halide Perovskite Films. *Coatings*, **2023,** 13, 378.

76. Henderson, R. K.; Jiménez-González, C.; Constable, D. J. C.; Alston, S. R.; Inglis, G. G. A.; Fisher, G.; Sherwood, J.; Binks, S. P.; Curzons, A. D. Expanding GSK's Solvent Selection Guide – Embedding Sustainability into Solvent Selection Starting at Medicinal Chemistry. *Green Chem.* **2011,** *13*, 854-862.

77. Käfferlein, H. U.; Ferstl, C.; Burkhart-Reichl, A.; Hennebrüder, K.; Drexler, H.; Brüning, T.; Angerer, J. The Use of Biomarkers of Exposure of Dimethylformamide in Health Risk Assessment and Occupational Hygiene in the Polyacrylic Fibre Industry. *Occup. Environ. Med.* **2005,** *62*, 330.

78. Han, J.; Kim, R. H.; Huang, S.; Kim, J.; Yun, J. S. Green Solution Processing of Halide Perovskite Solar Cells: Status and Future Directions. *Solar RRL* **2024,** *8*, 2400262.

79. Mitzi, D. B.; Dimitrakopoulos, C. D.; Rosner, J.; Medeiros, D. R.; Xu, Z.; Noyan, C. Hybrid Field-Effect Transistor Based on a Low-Temperature Melt-Processed Channel Layer. *Adv. Mater.* **2002,** *14*, 1772-1776.

80. Mitzi, D. B.; Medeiros, D. R.; DeHaven, P. W. Low-Temperature Melt Processing of Organic−Inorganic Hybrid Films. *Chem. Mater.* **2002,** *14*, 2839-2841.

81. Li, T.; Dunlap-Shohl, W. A.; Han, Q.; Mitzi, D. B. Melt Processing of Hybrid Organic–Inorganic Lead Iodide Layered Perovskites. *Chem. Mater.* **2017,** *29*, 6200-6204.

82. Li, T.; Zeidell, A. M.; Findik, G.; Dunlap-Shohl, W. A.; Euvrard, J.; Gundogdu, K.; Jurchescu, O. D.; Mitzi, D. B. Phase-Pure Hybrid Layered Lead Iodide Perovskite Films Based on a Two-Step Melt-Processing Approach. *Chem. Mater.* **2019,** *31*, 4267-4274.

83. Crace, E. J.; Singh, A.; Haley, S.; Claes, B.; Mitzi, D. B. Meltable Hybrid Antimony and Bismuth Iodide One-Dimensional Perovskites. *Inorg. Chem.* **2023,** *62*, 16161-16169.

84. Chaudhary, S.; Yadav, V.; Singh Negi, C. M.; Gupta, S. K. Active Layer Thickness Dependence of Optoelectronic Performance in $CH_3NH_3PbI_3$ Perovskite-Based Planar Heterojunction Photodiodes. *Opt. Mater.* **2020,** *106*, 109960.

Chapter 2

Entropy-Driven Reversible Melting and Recrystallization of Layered Hybrid Perovskites

Graphical Abstract:

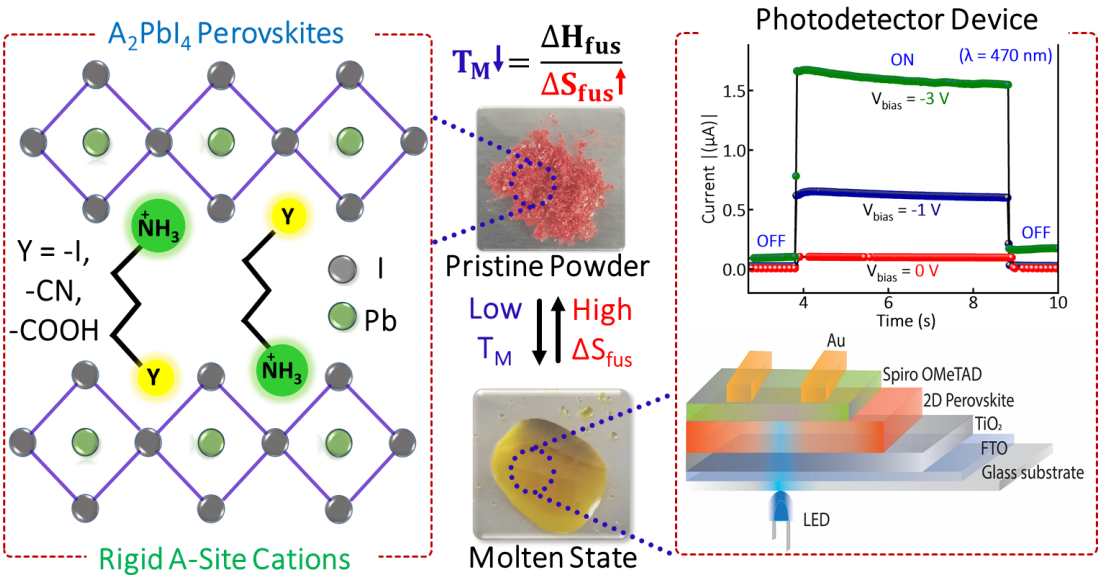

The work of this chapter has been published in the following article:

Rajput, P.K.; Shalunke, P.; Sarma, M.; Basu, M.; Gopal, A.; Joshi, A.; Shingote, A.S.; Saha, S.; Rahman, A; Nag, A. Entropy-Driven Reversible Melting and Recrystallization of Layered hybrid Perovskites. *Small*, **2024,** 20, 240675.

CHAPTER 2: Entropy-Driven Reversible Melting and Recrystallization of Layered Hybrid Perovskites

Abstract

Typical layered two-dimensional A_2PbX_4 (A: organic ammonium cation, X: Br, I) perovskites undergo irreversible decomposition at high temperatures. Can they be designed to melt at lower temperatures without decomposition? Which thermodynamic parameter drive the melting of layered perovskites? We address these questions by considering the melt of A_2PbX_4 as a mixture of ions (like ionic liquids), and hypothesized that the increase in the structural entropy of fusion (ΔS_{fus}) would be the driving force to decrease their melting temperature. Then to increase structural ΔS_{fus}, we designed A-site cations that are rigid in the solid crystal, and become flexible in the molten state. Different tail groups in our A-site cations form hydrogen- and halogen-bonding-interactions, making the cation-layer rigid in the solid form. Additionally, the rotation of $–NH_3^+$ head group is suppressed by replacing –H with $–CH_3$, further enhancing the rigidity. Five A_2PbX_4 crystals with high ΔS_{fus} and low melting temperatures are prepared using this approach. For example, $[I–(CH_2)_3–NH_2(CH_3)]_2PbI_4$ reversibly melts at 388 K (decomposition temperature 500 K), and then recrystallizes back upon cooling. Consequently, melt-pressed films are grown demonstrating the solvent- and vacuum-free perovskite films for future optoelectronic devices.

CHAPTER 2: Entropy-Driven Reversible Melting and Recrystallization of Layered Hybrid Perovskites

2.1 Introduction

Two-dimensional (2D) layered hybrid halide perovskites like A_2PbX_4 (A: organic ammonium cation, X: Br, I) are an improtant class of semiconductor showing interesting optoelectronic properties.[1-6] Typical A_2PbX_4 compounds undergo irreversible decomposition with increasing temperature by forming volatile species. But for a few cases, A_2PbX_4 undergo a reversible melting and recrystallization process, at temperatures lower than the decomposition temperature.[7-15] It is expected that thermodynamics governs such reversible process with melting temperature, $T_M = \Delta H_{fus}/\Delta S_{fus}$, where ΔH_{fus} and ΔS_{fus} are the enthalpy and entropy of fusion, respectively. But which one, ΔH_{fus} or ΔS_{fus} drives the melting of layered perovskites? Understanding such a phenomenon is important for desiging materials, functionilities, and device fabrication methods.

We start with an educated guess that the melt of an ionic compound A_2PbX_4 behaves like an ionic liquid (mixture of cations and anions), where structural ΔS_{fus} is known to determine T_M.[16] In the liquid of ions, the strong long-range ($1/R^2$ dependency, with R as the distance between the two ions) Coulomb electrostatic force will inevitably dominate the inter-ionic interactions, leading to compaction of the liquid.[17] On top, the charge neutrality requirement will ensure clustering or pairing of oppositely charged ions. Both these aspects are expected to suppress the ionic movement in the melt of A_2PbX_4, similar to ionic liquids. Consequently, translation entropy might contribute less in ΔS_{fus}, and instead structural (conformational and configurational) entropy might dominate the ΔS_{fus}. Motivated by these findings of ionic liquids, we hypothesize that in order to reduce T_M of A_2PbX_4, the main strategy should be to increase structural ΔS_{fus}. For that purpose, we rationally design A-site cations that are rigid in the solid form of A_2PbX_4 by introducing suitable intermolecular (or inter-ionic) forces, but becomes flexible in the molten state because of the disruption of intermolecular forces. Figure 2.1 depicts our strategy to design such A-site cation. For a typical layered perovskites like $(BA)_2PbI_4$, the $–NH_3^+$ end of butylammonium (BA) interact with $[PbI_4]^{2-}$ through electrostatic and hydrogen bonding, as shown in Figure 2.1a.

The hydrocarbon tail part remains unbound (or weak van-der-Waals interaction) and flexible, increasing entropy of the solid. In difference, for $(MIPA)_2PbI_4$ (Figure 2.1b, MIPA = $I–(CH_2)_3–NH_2(CH_3)^+$, 3-methyliodopropyl ammonium), in addition to interaction of $–NH_3^+$ head

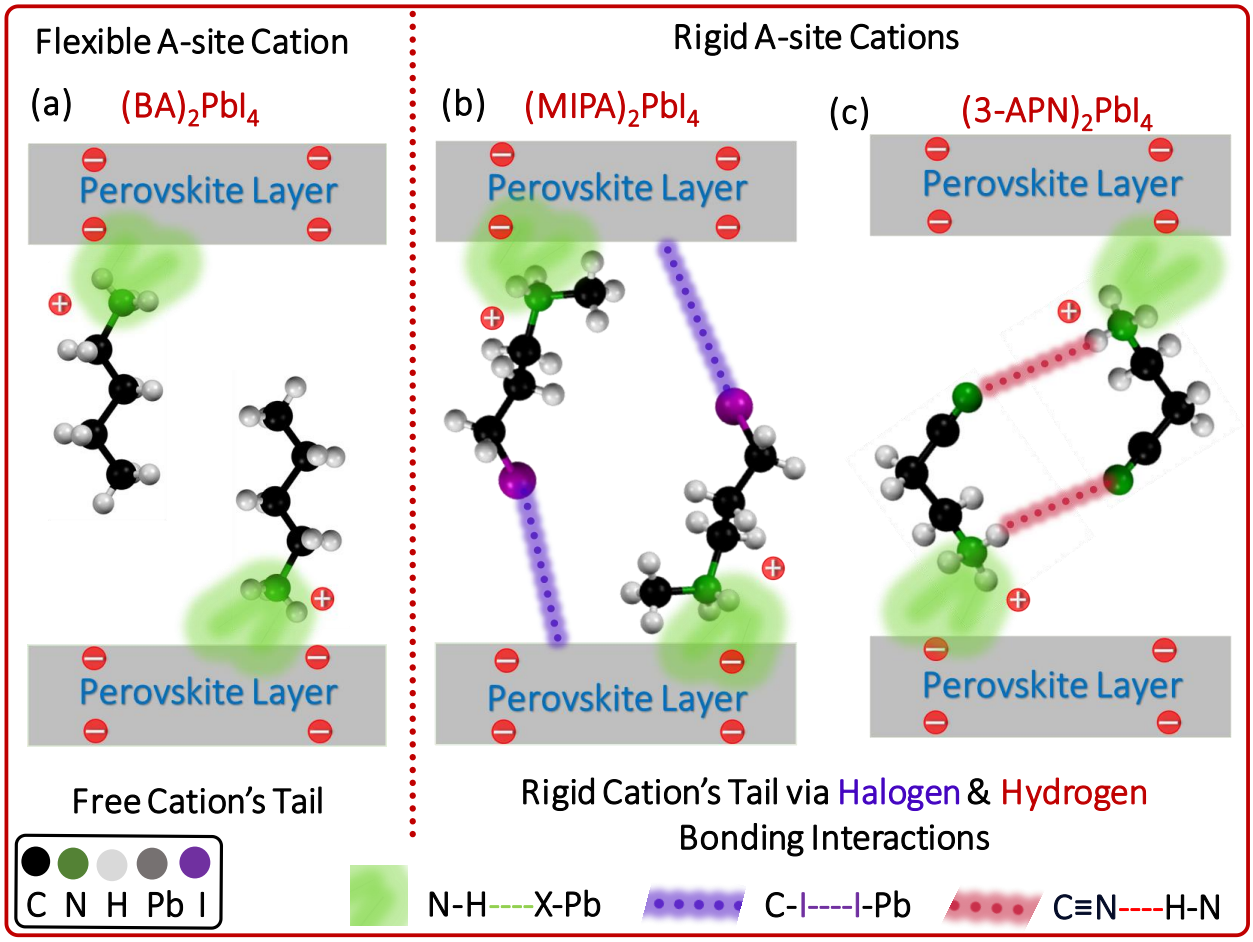

Figure 2.1: Schematic representations of our design principles of rigid A-site cations for A_2PbI_4 perovskite crystal. We hypothesize that the structurally rigid A-site cation in the solid state will become flexible in the molten state, yielding high ΔS_{fus}, and therefore, lower melting temperature T_M. The strategy to increase the rigidity of A-site cation in the solid form is by tailoring its tail part, while retaining the electrostatic and hydrogen bonding interactions (green shaded region) of $–NH_3^+$ head group with the $[PbI_4]^{2-}$ perovskite layers. (a) The $–CH_3$ tail part of BA cation in $(BA)_2PbI_4$ perovskite is flexible. (b) Replacing the $–CH_3$ tail with $–CH_2I$ leads to I---I halogen bonding interactions (purple dotted line) between the MIPA and $[PbI_4]^{2-}$ perovskite layer, imparting rigidity in the A-site layer. (c) The –CN tail group of one 3-APN cation forms hydrogen bond (red dotted lines) with the $–NH_3^+$ head of another 3-APN cation, imparting rigidity in the A-site layer of $(3\text{-APN})_2PbI_4$.

with $[PbI_4]^{2-}$, the –I tail of MIPA interact with $[PbI_4]^{2-}$ through halogen bonding.[18, 19] The halogen bonding interaction at the tail is supposed to increase rigidity of the A-site cations, decreasing the entropy of the crystal. The rigidity of A-site cations can be increased in other ways as well. For

example, in $(3\text{-APN})_2PbI_4$ (Figure 2.1c), the head ($–NH_3^+$) and tail (–CN) of two 3-APN ($CN–(CH_2)_2–NH_3^+$, 3-ammonium-propionitrile) cations interact between themselves,[20] providing rigidity to the A-site cation, and therefore, reducing the entropy of the crystal. Upon melting, the intermolecular forces can be disrupted making the A-site cation flexible, and thereby significantly increasing the ΔS_{fus}.

Table 2.1: Structural details like hydrogen and halogen interactions obtained from single crystal XRD data at 296 K. Melting (T_M), recrystallization (T_C), and decomposition (T_D) temperatures were measured from DSC and TGA data.

A_2PbX_4 compositions (X: Br, I)	**Hydrogen bonding between ammonium head group and $[PbX_4]^{2-}$: H--X distance (Å) / N–H--X angle (°)**	**Hydrogen bonding between organic tails: H--X distance (Å) / hydrogen bond angle (°)**	**Halogen bonding between organic tail and $[PbX_4]^{2-}$: X--X distance (Å)**	**T_M / T_C (K)**	**T_D (K)**	**$\Delta T = T_D - T_M$ (K)**
$(IPA)_2PbI_4$	2.828 / 159.08 2.701 / 165.06 2.846 / 157.26	--	3.862	522 / --	~522	~0
$(MIPA)_2PbI_4$	2.684 / 165.81	--	3.822	388 / 339	500	112
$(DMIPA)_2PbI_4$	2.511 / 170.52	--	3.863	372 / ---	473	101
$(GABA)_2PbI_4$	2.998 / 145.93 3.041 / 146.83	1.763 / 173.23 [-CO---HO-] 2.269 / 158.12 [-NH--OH-]	--	413 / 354	463	50
$(3\text{-APN})_2PbI_4$	2.953 / 137.72 2.907 / 149.81	1.945/166.32 [-CN--HN]	--	472 / 458	483	11
$(MBPA)_2PbBr_4$	2.468 / 163	--	3.708	386 / 358	492	106

Interestingly, all the A_2PbX_4 crystals with rigid A-site cations shown in Figure 2.1 undergo the desired reversible melting at temperatures lower than their irreversible decomposition temperatures. The design hypothesis can be applied to other A-site cations, showing about five layered hybrid perovskite samples (see Table 2.1) exhibiting reversible melting and recrystallization processes. Some of those A_2PbX_4 perovskite samples show T_M ~ 388 K (115 ^oC), which is suitable for film growth from the melt of the hybrid perovskite on both glass and flexible polymer substrate. Consequently, we demonstarted n-i-p-based photodetector using melt-processed $(MIPA)_2PbI_4$ films as an active layer, that operates both in self-powered[21] mode (at 0 V bias) and at applied bias voltages.

2.2 Experimental Section

2.2.1 Chemicals

Lead oxide (PbO, 99.9%, Sigma Aldrich), hydroiodic acid (HI, 57% w/w in water, Sigma Aldrich), hydrobromic acid (HBr, 48% w/w in water, Sigma Aldrich), hypophosphorous acid (H_3PO_2, 50% w/w in water, Avra chemicals), propanolamine ($HO\text{-}(CH_2)_3\text{-}NH_2$, >99%, Sigma Aldrich), 3-methylamino 1-propanol ($HO\text{-}(CH_2)_3\text{-}N(CH_3)H$, 96%, Sigma Aldrich), 3-dimethylamino 1-propanol ($HO\text{-}(CH_2)_3\text{-}N(CH_3)_2$, 99%, TCI chemicals), 3-amino-propionitrile ($CN\text{-}(CH_2)_2\text{-}NH_2$, >98.0%, TCI chemicals), 4-amino butyric acid ($COOH\text{-}(CH_2)_3\text{-}NH_2$, >99.0%, TCI chemicals), titanium diisopropoxide bis(acetylacetonate) (75 wt% in isopropanol, Sigma Aldrich), acetylacetone (>99%, Sigma Aldrich),2,2',7,7'-tetrakis (N,N-di-pme-thoxyphenylamine)−9,9'-spirobifluorene (Spiro-OMeTAD, >99.8%, Sigma Aldrich), lithiumbis (trifluoromethanesulfonyl) imide salt (Li-TFSI, ≥99%, Sigma Aldrich), acetonitrile (anhydrous, 99.8%, Sigma Aldrich), 4-tert-butyl-pyridine (TBP, >96.0%, Sigma Aldrich), chlorobenzene (CB, >98.0%, Sigma Aldrich) and absolute ethanol.

2.2.2 Synthesis of $(IPA)_2PbI_4$ [IPA: $I\text{–}(CH_2)_3\text{–}NH_3^+$], and $(MIPA)_2PbI_4$ [MIPA: $I\text{–}(CH_2)_3\text{–}NH_2(CH_3)^+$]

1 mmol lead oxide (PbO) was dissolved into 3 mL HI and 300 µL H_3PO_2 in a glass beaker by sonication, yielding a transparent yellow colored solution. Then 2 mmol $OH\text{-}(CH_2)_3\text{-}NH_2$ (for IPA)

or 2 mmol OH-$(CH_2)_3$- $NH(CH_3)$ (for MIPA) were added dropwise. The alcohol group (-OH) gets substituted by the iodine group (-I) in situ during heating and stirring the precursor mixture at 110 °C for 30 minutes using an oil bath placed on a hot plate with a magnetic stirrer.[22] After 30 minutes, the hot plate temperature was reduced to room temperature, stirring was stopped. After ~3 to 4 hours, yellow plate-like crystals of $(IPA)_2PbI_4$ or orange plate like crystals of $(MIPA)_2PbI_4$ precipitated at the bottom of the beaker. Crystals were washed with diethyl ether and dried in the air.

2.2.3 Synthesis of $(DMIPA)_2PbI_4$ [DMIPA: $I–(CH_2)_3–NH(CH_3)_2^+$]

1 mmol lead oxide (PbO) was dissolved into 3 mL HI and 300 µL H_3PO_2 in a glass beaker after sonication for 10 minutes. Then 2.8 mmol of $OH–(CH_2)_3–N(CH_3)_2$ was added dropwise. Then, the glass beaker was heated and stirred at 110 °C for 30 minutes using an oil bath placed on a hot plate with a magnetic stirrer, the alcohol group (–OH) gets substituted by the iodine group (–I) in situ during heating.[22] The hot plate temperature was reduced to room temperature, and stirring was stopped. After ~ 6 hours, orange plate-like crystals of $(DMIPA)_2PbI_4$ precipitated at the bottom of the beaker. Crystals were then washed with diethyl ether and dried in air.

2.2.4 Synthesis of $(3\text{-}APN)_2PbI_4$ [3-APN: $CN–(CH_2)_2–NH_3^+$]

1 mmol lead oxide (PbO) was dissolved in 6 mL HI and 600 µL H_3PO_2 in a glass beaker by sonication for 10 minutes, yielding a clear yellow colored solution. Then, dropwise, 2 mmol of $CN– (CH_2)_2–NH_2$ was added to the PbO solution. Immediately, a red precipitate was observed. Then, the glass beaker was placed in an oil bath on a hot plate with magnetic stirrer at 70 °C for 30 minutes to dissolve the red precipitate. The hot plate temperature was reduced to room temperature, stirring was stopped, and then the glass beaker was placed in a freezer, maintaining a 5 °C temperature for crystallization. After 2 days, red colored plate-like crystals were precipitated at the bottom of the beaker. Crystals were collected, washed with diethyl ether and dried in air.

2.2.5 Synthesis of $(GABA)_2PbI_4$ [GABA: $COOH–(CH_2)_3–NH_3^+$]

1 mmol lead oxide (PbO) was dissolved in 3 mL HI and 300 µL H_3PO_2 in a glass beaker by sonication for 10 minutes. Then, 2 mmol of $COOH–(CH_2)_3–NH_2$ was added to PbO solution. Then,

the glass beaker was heated and stirred at 90 °C for 30 minutes using an oil bath placed on a hot plate with a magnetic stirrer. The temperature of the hot plate was reduced to room temperature. After 3 to 4 hours, orange colored crystals were precipitated at the bottom of the beaker. Crystals were washed with diethyl ether and dried in air.

2.2.6 Synthesis of $(MBPA)_2PbBr_4$ [MBPA: $Br–(CH_2)_3–NH_2(CH_3)^+$]

1 mmol PbO was dissolved in 3 mL HBr in a glass beaker after sonication. Then, 2 mmol $OH–(CH_2)_3–NH(CH_3)$ was added dropwise to the PbO solution. The alcohol group (–OH) gets substituted by the bromide group (-Br) in situ during heating and stirring of the precursor mixture at 110 °C for 30 minutes using an oil bath placed on a hot plate with a magnetic stirrer. The temperature of the hot plate was reduced to room temperature, and then the glass beaker was placed in a freezer (~5 °C) for crystallization. The yellowish-white plate-like crystals precipitated at the bottom of the beaker. Crystals were washed with diethyl ether and dried in air.

2.2.7 Structural Characterization

Single crystal X-ray diffraction frames are collected in a Bruker Apex Duo diffractometer using Mo Kα radiation (λ = 0.71 Å). Constant liquid nitrogen flow was maintained towards the mounted crystal to collect data at 100 K and 296 K. The integrations of the collected data and numerical absorption corrections are done using APEX4 software. The structures are solved by the direct method using SHELXS and refined by full-matrix least-squares on F^2 using the SHELXL, as implemented in Olex2.[23]

Powder X-ray diffraction patterns at room and at high temperature are recorded on a Bruker D8 Advance diffractometer in Bragg−Brentano geometry and operating with Cu Kα radiation (1.54 Å). The thermal stability of the samples was checked by thermogravimetric analysis (TGA) under a nitrogen atmosphere, using a Perkin-Elmer STA6000 system at a rate of 5 K per minute. Differential scanning calorimetry (DSC) measurements were performed on the powder samples to determine the phase transition temperatures. A TA instrument DSC250 system was used for the measurements. About 15 mg powder sample and a reference were heated from 298 K (RT) to a suitable temperature (less than the decomposition temperature of each sample). A similar

measurement was also carried out while cooling the sample to 298 K (RT). Field emission scanning electron microscopy (FESEM) images were recorded using a FEI Nova Nano SEM 450 FESEM instrument.

The phonon dynamics were studied using a lab RAM-HR Evolution Raman spectrometer in the backscattering geometry coupled with a Peltier-cooled (CCD) detector. The measurements were performed on the crystals with Nd-YAG laser (532 nm) and He-Ne gas laser (633 nm). The temperature-dependent measurements were performed using the Linkam heating stage (model no. HFS600E-PB4) attached to the spectrometer.

2.2.8 Optical Properties

Optical diffused reflectance spectra were collected at room temperature using Shimadzu UV3600 plus UV-vis-NIR spectrophotometer. $BaSO_4$ powder is used for these measurements to reference 100% reflectance. The diffused reflectance signal was converted to absorbance using the Kubelka−Munk transformation.[24] Steady-state photoluminescence (PL) measurements were carried out using FLS 980 (Edinburgh Instruments). A 405 nm (3.06 eV) and 375 nm (3.37 eV) picosecond pulsed diode lasers are the excitation source for recording the PL.

2.2.9 Preparation of $(MIPA)_2PbI_4$ Films by Melt Pressed Method

The glass substrates (2 cm × 2 cm) were washed first with soap solution, then distilled water, then with acetone and 2-propanol for 15 minutes each in an ultrasonic bath sonicator. Glass substrates were then dried in N_2 flow. Then, placed in a UV ozone cleaner for 30 minutes. After that, 5 mg powder of $(MIPA)_2PbI_4$ was placed on the glass substrate and heated from room temperature (~298 K) to 403 K (130 °C) on a hot plate, slightly above the melting temperature (T_M = 388 K). Once the sample melted, a kapton sheet was placed on top of the yellow melted liquid and pressed with a preheated glass substrate until the perovskite melt spread. The temperature of the hot plate was reduced to room temperature. Complete material recrystallization was indicated by the color change from yellow to red. The upper glass substrate and kapton sheet were removed easily without affecting the perovskite film. The complete process of film preparation was performed in air (ambient conditions).

The melting temperature $(MIPA)_2PbI_4$ around 115 ^oC, along with its degradation temperature of 227 ^oC is desired for both film growth and device operation. A lower melting temperature will risk device stability which can heated up to up to 60-70 ^oC during prolonged operation. A higher melting temperature will reduce the difference between the melting and decomposition temperature, therefore, reducing the stability of the melt. High stability of the melt is required for melt-pressed film growth with somewhat variable temperatures above the melting point. Also, melt-pressed film growth at moderate temperatures (~130 ^oC) is suitable for flexible polymeric substrates.

2.2.10 Device Fabrication

The fluorine-doped tin oxide (FTO) substrates were cleaned first with soap solution, then distilled water, then with acetone and 2-propanol for 15 minutes each in an ultrasonic bath sonicator. The FTO substrates were dried in N_2 flow and exposed to UV ozone cleaner for 30 minutes. The electron transporting layer was fabricated by depositing 60 µL as-prepared TiO_2 solution (see detailed procedure below) at 3000 rpm for 60 seconds and annealed at 450 °C for 60 minutes. After cooling, the $(MIPA)_2PbI_4$ film was fabricated over the compact-TiO_2 (c-TiO_2) layer using the above-mentioned method. Then, the substrates were transferred to the N_2-filled glove box to fabricate the hole-transporting layer. The 30 µL of spiro-OMeTAD solution (see detailed procedure below) was coated at 3000 rpm for 30 seconds inside the N_2-filled glove box. Finally, 70 nm thick gold top electrode was deposited by sputtering using circular shadow mask (300 µm diameter) at a base pressure of ~ 1×10^{-5} mbar.

2.2.11 Electron Transporting Layer (ETL) [compact TiO_2] Solution Preparation

The electron transporting solution was prepared by dissolving 150 µL titanium diisopropoxide bis(acetylacetonate) in 2.25 mL ethanol and 100 µL acetylacetone and stirrer for 30 minutes at room temperature.

2.2.12 Hole Transporting Layer (HTL) [spiro-OMeTAD] Solution Preparation

The hole-transporting layer solution was prepared by dissolving 30 µL TBP, 17 µL Li-TFSI solution (prepared by dissolving 520 mg Li-TFSI in 1 mL acetonitrile), and 70 mg Spiro-OMeTAD

in 1 mL chlorobenzene.

2.2.13 Device Characterization

The electrical measurements were carried out at room temperature in a probe station using a Keithley 2636B dual channel source measure unit (SMU). All the connections were made using triaxial cable to reduce the background current. We have used 470 nm LED having 6.10 mW/cm^2 of power density as the light source for photo response measurements. The LED switching on/off and intensity were controlled with the help of Arduino and a potentiometer. The rise and fall times were measured with Tektronix (TBS 1102B-EDU) digital oscilloscope attached to low noise current amplifier (Stanford Research Systems) (MODEL SR570). The photocurrent (I_{photo}) was estimated from the following equation, $I_{photo} = I_{illuminated} - I_{dark}$ where, $I_{illuminated}$ is the current recorded under light, I_{dark} is the dark current. Generally, the performance of any photodetector is estimated based on the few key parameters such as response time, responsivity and detectivity. The Responsivity can be expressed as the following equation,

$$\boldsymbol{R} = \frac{\boldsymbol{I_{illuminated} - I_{dark}}}{\boldsymbol{P.\ A}} \ \text{(A/W)} \qquad \text{(equation 1)}$$

where, *P* is the optical power and A is illuminated area. Detectivity can be represented as the photodetector's capability of detecting the faintest light signal, and it is expressed as the following equation:

$$\mathbf{D^* = R/\sqrt{2eJ_d}\ (Jones)} \qquad \text{(equation 2)}$$

Where, e is the electronic charge
J_d is the current density

The ideality factor of the n-i-p diode was estimated by using the thermionic emission equation:

$$\mathbf{I} = \boldsymbol{I_s}\left[\mathbf{exp}\left(\frac{\boldsymbol{qV}}{\boldsymbol{\eta kT}}\right) - \mathbf{1}\right] \qquad \text{(equation 3)}$$

Where, *T* represents the temperature
η is the ideality factor
k the Boltzmann constant.

2.3 Result and Discussion

2.3.1 Tailoring the Rigidity of A-site Cations by their Tail Group and its Effect on Thermodynamic Parameters

We show the results of three different bifunctional A-site cations having one ammonium terminus, and another terminus with tail groups like –I, –CN, and –COOH in MIPA, 3-APN, and GABA [$COOH{-}(CH_2)_3{-}NH_3^+$] respectively.

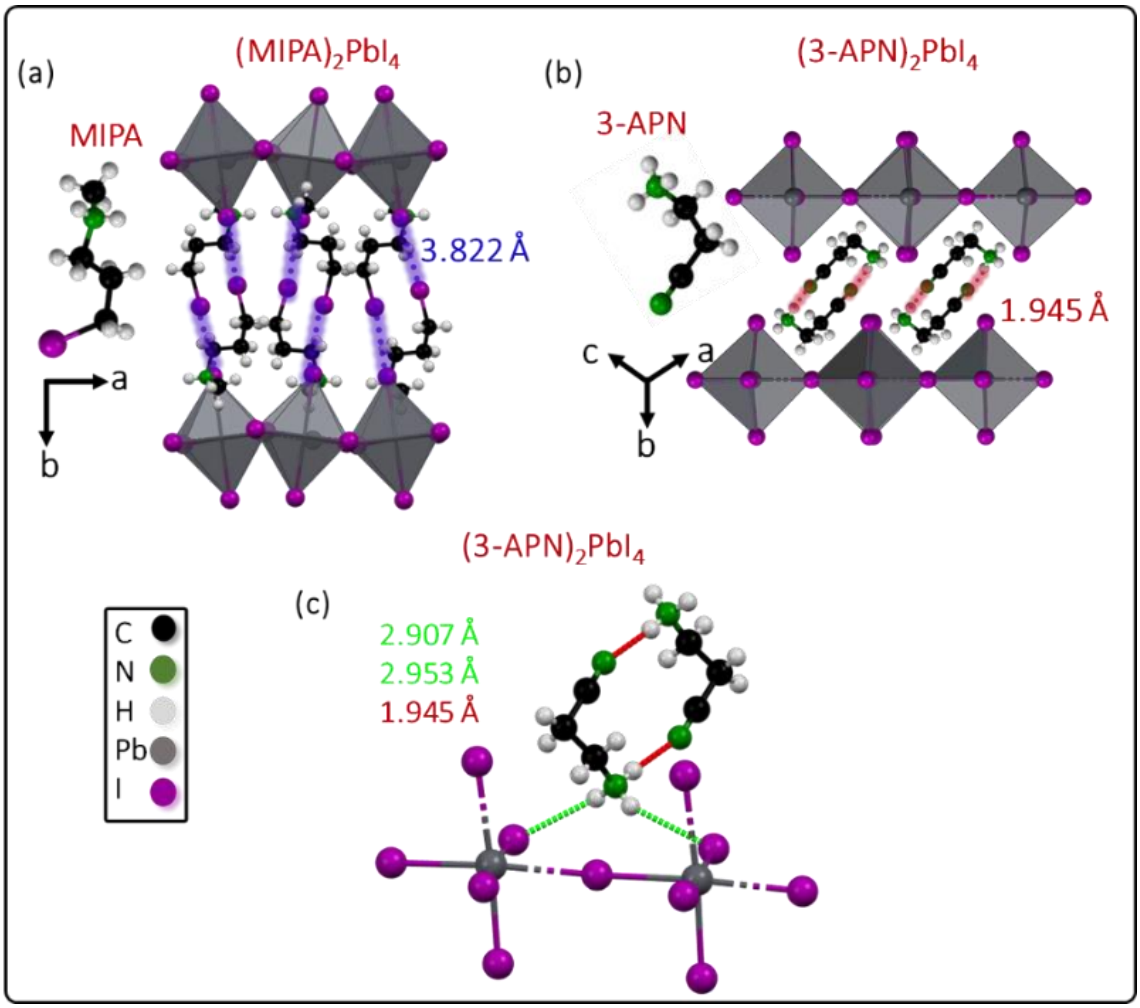

Figure 2.2: Crystal Structures obtained from single crystal XRD data. (a) $(MIPA)_2PbI_4$, iodine at the tail of MIPA cation form I---I interaction (violet dotted line) with the iodine of $[PbI_4]^{2-}$. (b) $(3\text{-}APN)_2PbI_4$, the –CN group at the tail of one 3-APN cation interacts with $–NH_3^+$ of another 3-APN cation, forming a dimer (red dotted lines). (c) Two hydrogens of $–NH_3^+$ of one 3-APN cation form two hydrogen bonding interactions with $[PbI_4]^{2-}$ shown by green dotted lines.

For the synthesis of $(MIPA)_2PbI_4$, PbO and OH-$(CH_2)_3$-$NH(CH_3)$ were dissolved in a 1:2 ratio in HI solution with a small amount of H_3PO_2, following ref.[19] A similar protocol is used for the synthesis of $(3\text{-}APN)_2PbI_4$ and $(GABA)_2PbI_4$, where 3-amino-propionitirle and 4- aminobutyric acid were used respectively, in place if OH-$(CH_2)_3$-$NH(CH_3)$.[12, 20, 25]

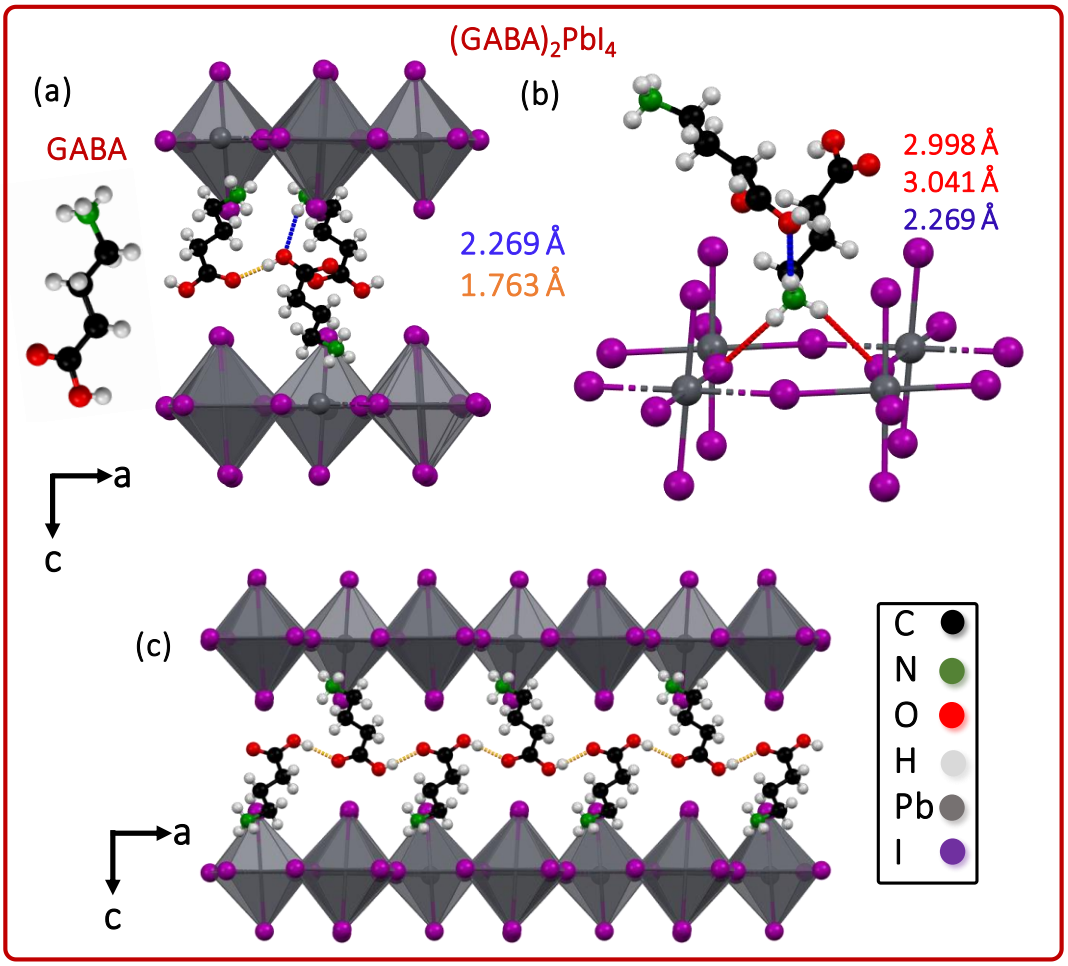

Figure 2.3: Crystal structure obtained from the single crystal XRD (a) $(GABA)_2PbI_4$, the –OH (hydroxyl group) of one GABA cation interacts with the oxygen of –CO (carboxyl group) and –NH_3^+ group of other two GABA cations (orange and blue dotted lines). (b) Two hydrogens of –NH_3^+ of GABA cation form two hydrogen bonding interactions with the $[PbI_4]^{2-}$ and one hydrogen bonding with the oxygen of hydroxyl group of another GABA cation. (c) The –OH (hydroxyl group) at the tails of one GABA cation interacts with the –CO (carboxyl group) of another GABA cation (shown by orange line). Such interactions between the GABA cations are present throughout the crystal between the $[PbI_4]^{2-}$ layers interact with each other, forming a 1D network.

Single crystal X-ray diffraction (XRD) data for all the samples are recorded at both 100 K and 296 K. The structural refinement data of $(3\text{-APN})_2PbI_4$ and $(GABA)_2PbI_4$ are shown in Table 2.2, and 2.3, respectively. Similar structural data for $(MIPA)_2PbI_4$ was reported in our earlier papers.[19] All the samples show 2D layered hybrid perovskite structure.

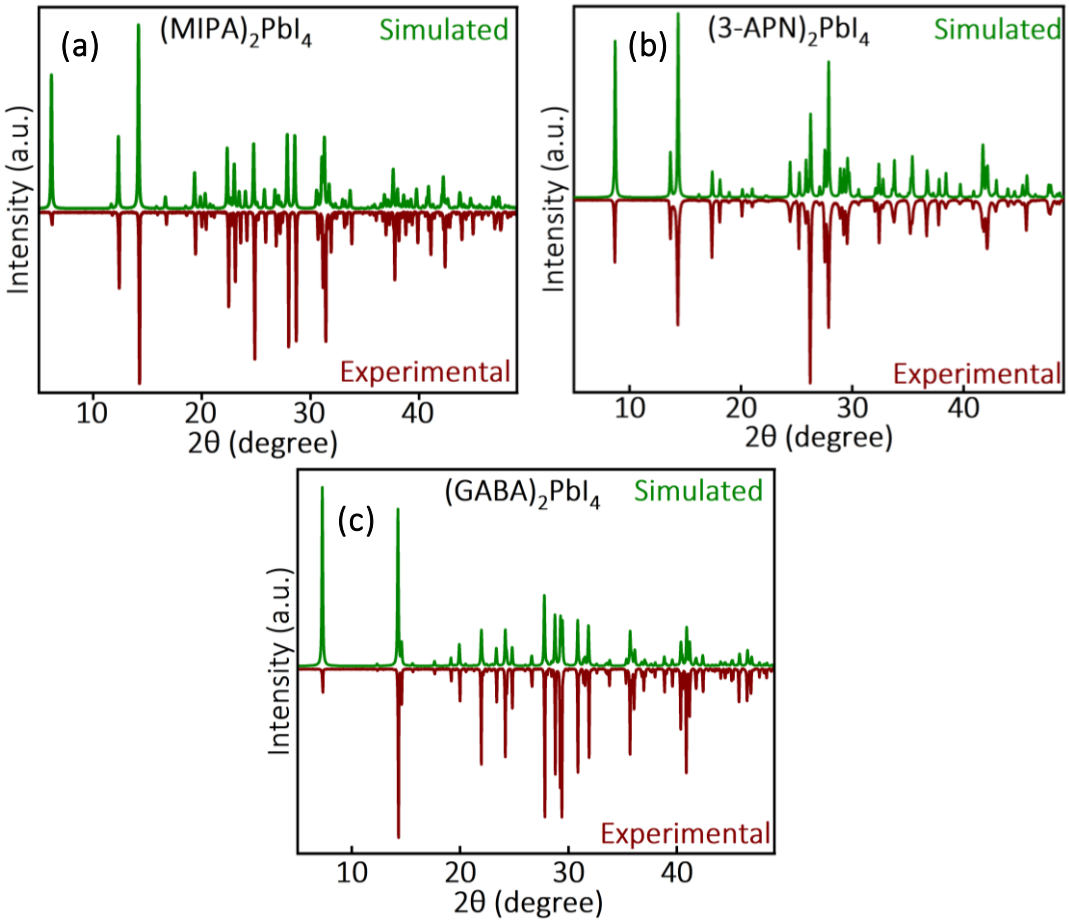

Figure 2.4: Powder XRD patterns of (a) $(MIPA)_2PbI_4$, (b) $(3\text{-APN})_2PbI_4$, and (c) $(GABA)_2PbI_4$ match well with the corresponding simulated patterns obtained from single crystal XRD. All the patterns are recorded at room temperature.

The single crystal XRD data also confirms the non-covalent hydrogen and halogen bonding of the tail groups of A-site cations that are discussed through schematics in Figure 2.1 (b-c). The structure obtained from the single crystal XRD along with quantitative information on the specific tail group interactions are presented in Figure 2.2 and 2.3. Powder XRD patterns recorded on the powders of $(MIPA)_2PbI_4$, $(3\text{-APN})_2PbI_4$, and $(GABA)_2PbI_4$ also match well with their respective simulated

Table 2.2: Crystallographic data and structural refinement details for $(GABA)_2PbI_4$ at 100 K and 296 K.

Sample	**$(GABA)_2PbI_4$**	
CCDC Number	2354551	2354552
Temperature	100 K	296 K
Chemical formula	$C_8H_{20}N_2O_4PbI_4$	
Formula weight	923.05 g/mol	
Wavelength	0.71073 Å	
Crystal system	Orthorhombic	
Space group	*Pbca*	
Unit cell dimensions	a = 8.852(14) Å b = 9.241(14) Å c = 23.922(4) Å	a = 8.916(3) Å b = 9.276(3) Å c = 24.328(9) Å
Volume	1957.1(5) $Å^3$	2012.0(11) $Å^3$
Z	4	4
Density(calculated)	3.133 g/cm^3	3.047 g/cm^3
Absorption coefficient	14.939	14.531
F(000)	1632	1632
Theta range for data collection	2.863° to 24.998°	3.278° to 24.983°
Index ranges	-10<=h<=10 -10<=k<=10 -27<=l<=28	-10<=h<=10 -11<=k<=11 -28<=l<=27
Reflections collected	16418	23594
Independent reflections	1727	1757
Coverage of independent reflections	99.9%	99.2%
Absorption correction	Multi-scan	
Structure solution technique	Direct methods	
Structure solution program	SHELXT 2014/5 (Sheldrick, 2014)	
Refinement method	Full-matrix least-squares on F^2	
Refinement program	SHELXL-2018/3 (Sheldrick, 2018)	
Function minimized	$\Sigma\ w\ (F_o^2 - F_c^2)^2$	
Data/restraints/parameters	1727/0/91	1757/0/91
Goodness of fit on F^2	1.089	1.106
Final R indices; $I>2\sigma(I)$ All data	R1 = 0.0197 wR2 = 0.0589 R1 = 0.0224 wR2 = 0.0607	R1 = 0.0245 wR2 = 0.0535 R1 = 0.0288 wR2 = 0.0556
Weighting scheme	$w = 1/[\sigma^2 (Fo^2)+ (0.1000P)^2]$; $P=(Fo^2+2Fc^2)/3$	

Table 2.3: Crystallographic data and structural refinement details for $(3\text{-APN})_2PbI_4$ at 100 K and 296 K.

Sample	**$(3\text{-APN})_2PbI_4$**	
CCDC Number	2354553	2354554
Temperature	100 K	296 K
Chemical formula	$C_6H_{14}N_2PbI_4$	
Formula weight	857.01 g/mol	
Wavelength	0.71073 Å	
Crystal system	Orthorhombic	
Space group	*Pnma*	
Unit cell dimensions	a = 8.607(10) Å b = 19.976(3) Å c = 9.796(10) Å	a = 8.644(10) Å b = 20.378(3) Å c = 9.818(13) Å
Volume	1684.45(4) $Å^3$	1729.5(4) $Å^3$
Z	4	4
Density(calculated)	3.379 g/cm^3	3.291 g/cm^3
Absorption coefficient	17.329	16.878
F(000)	1488	1488
Theta range for data collection	3.148° to 31.495°	1.946° to 27.007°
Index ranges	-10<=h<=8 -23<=k<=23 -11<=l<=11	-10<=h<=10 -24<=k<=24 -11<=l<=11
Reflections collected	14285	42944
Independent reflections	1531	1576
Coverage of independent reflections	99.8%	100%
Absorption correction	Multi-scan	
Structure solution technique	Direct methods	
Structure solution program	SHELXT 2014/5 (Sheldrick, 2014)	
Refinement method	Full-matrix least-squares on F^2	
Refinement program	SHELXL-2018/3 (Sheldrick, 2018)	
Function minimized	$\Sigma\ w\ (F_o^2 - F_c^2)^2$	
Data/restraints/parameters	1531/0/75	1576/0/75
Goodness of fit on F^2	1.053	1.131
Final R indices; I>2σ(I) All data	R1 = 0.0237 wR2 = 0.0578 R1 = 0.0269 wR2 = 0.0603	R1 = 0.0430 wR2 = 0.1178 R1 = 0.0545 wR2 = 0.1297
Weighting scheme	$w = 1/[\sigma^2 (Fo^2) + (0.1000P)^2]$; $P=(Fo^2+2Fc^2)/3$	

patterns Figure 2.4, confirming the phase purity of the entire sample. The structural data (Figure 2.2 and 2.3) confirm that all four samples $(MIPA)_2PbI_4$, $(3\text{-}APN)_2PbI_4$, and $(GABA)_2PbI_4$ have a rigid A-site cation, because of the interactions of the tail groups of the A-site cations. The same interactions also increase the molar density (see Table 2.4) of hybrid perovskites.

Table 2.4: Molar density of A_2PbX_4 perovskites obtained from crystal structures at 296 K. Molar density of the six samples studied here with rigid A-site cation is significantly higher compared to the non-rigid $(BA)_2PbI_4$, BA: butyl ammonium.

A_2PbX_4 compositions	**Molar density (g/cm^3)**	**Reference**
$(IPA)_2PbI_4$	3.369	This work
$(MIPA)_2PbI_4$	3.141	
$(DMIPA)_2PbI_4$	3.112	
$(GABA)_2PbI_4$	3.047	
$(3\text{-}APN)_2PbI_4$	3.291	
$(MBPA)_2PbBr_4$	2.755	
$(BA)_2PbI_4$	2.690	[26]

Therefore, we anticipate a decrease in entropy of the solid crystals because of these tail group interactions, which is expected to increase ΔS_{fus} and decrease T_M. To verify that, we carried out differential scanning calorimetry (DSC) and thermogravimetry analysis (TGA) measurements on all the samples. Figure 2.5a shows an endothermic peak in DSC data (blue line) of $(MIPA)_2PbI_4$ during the heating cycle. The peak corresponds to melting of the crystal at T_M = 388 K, as shown

by the photographs of the sample in the inset of the Figure 2.5a. But TGA does not show any weight loss at this T_M. The $(MIPA)_2PbI_4$ degrades at a higher temperature of 500 K forming volatile species. So, for DSC measurements, we started cooling down the sample from a temperature lower than the degradation temperature, and then an exothermic peak is observed at 339 K for recrystallization of $(MIPA)_2PbI_4$. From the DSC data, we estimated the value ΔH_{fus}. $(MIPA)_2PbI_4$ shows ΔH_{fus} = 34.8 kJ/mol, and for T_M = 388 K, ΔS_{fus} is calculated as 89.7 J/(mol. K).

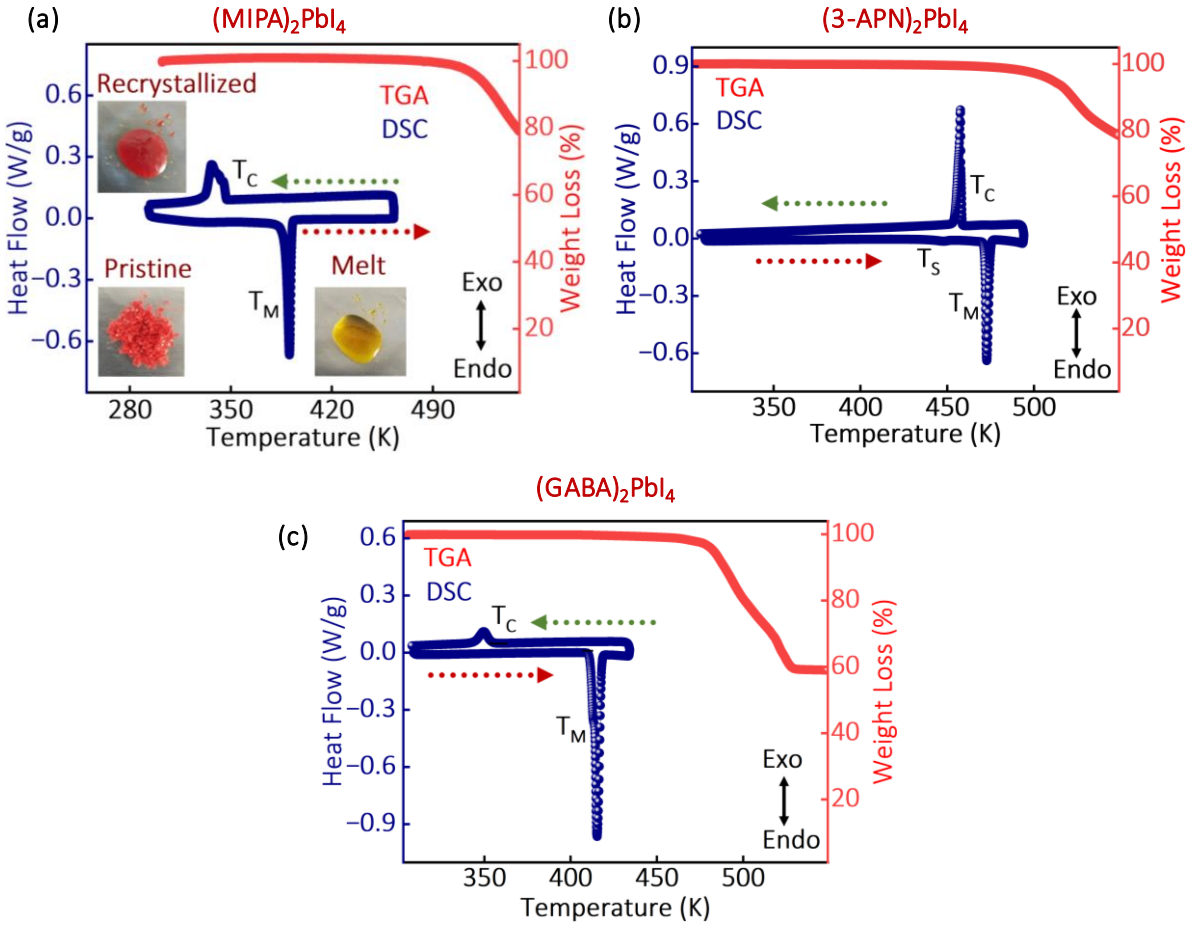

Figure 2.5: DSC (blue color) and TGA (red color) data of (a) $(MIPA)_2PbI_4$, (b) $(3\text{-}APN)_2PbI_4$, and (c) $(GABA)_2PbI_4$ at a ramp rate of 5 K/minute. Melting and recrystallization temperatures are represented by the T_M and T_C, respectively. Reversible melting and recrystallization processes are observed for all three samples. Note that $(3\text{-}APN)_2PbI_4$ shows a small solid-to-solid phase transition indicated by T_S in (b). Photographs in the insets of (a) show the appearance of pristine, molten, and recrystallized $(MIPA)_2PbI_4$. (Note: The DSC experiments were performed in NCL Pune by Mr. Animesh Gopal from Dr. Kadhiravan Shanmuganathan's lab)

Similarly, DSC and TGA data of $(3\text{-APN})_2PbI_4$, and $(GABA)_2PbI_4$ layered perovskites are shown in Figure 2.5b, and 2.5c respectively. Reversible melting and recrystallization process are observed for all three samples, suggesting that the hypothesis of rigid A-site cation increasing the ΔS_{fus} is working. $(3\text{-APN})_2PbI_4$ melts at 472 K [ΔH_{fus} of 13.9 kJ/mol and ΔS_{fus} of 29.5 J/(mol. K)], recrystallizes at 458 K, and no weight loss is observed till 483 K. In $(GABA)_2PbI_4$, the two hydrogens at $–NH_3^+$ of GABA cation form two weak hydrogen bonding interactions (see Figure 2.3b) with $[PbI_4]^{2-}$. A blue dotted line shows the third hydrogen at the ammonium head interacting with the oxygen of the –COOH group at the tail of the cation. All GABA cations in between the $[PbI_4]^{2-}$ layers interact with each other through –CO and –OH groups at the tails of cations, forming a 1D network (see Figure 2.3b and 2.3c). $(GABA)_2PbI_4$ melts at 413 K [ΔH_{fus} of 43.6 kJ/mol and ΔS_{fus} of 105.7 J/(mol. K)], recrystallization at 354 K, and no weight loss is observed till 463 K as shown in Figure 2.5c.

2.3.2 Tailoring the Rigidity of A-site Cations by Substituting –H with $–CH_3$ in the $–NH_3^+$ Head Group, and its Effect on Thermodynamic Parameters

In the above section, we designed rigid A-site cations through non-covalent interactions in the tail part of the cation. Interestingly, the rigidity of A-site cation and T_M can be controlled by tailoring the $–NH_3^+$ terminus as well. Mono- and di-substitution of –H with $–CH_3$ from $–NH_3^+$ of $I–(CH_2)_3–NH_3^+$ (3-iodopropylammonium = IPA), lead to the formation of $I–(CH_2)_3–NH_2(CH_3)^+$ (MIPA) and $I–(CH_2)_3–N(CH_3)_2H^+$ (DMIPA, 3-dimethyliodopropyl ammonium) cations, respectively. Figure 3 shows the structural analysis of $(IPA)_2PbI_4$, $(MIPA)_2PbI_4$ and $(DMIPA)_2PbI_4$ based on the data reported in our prior paper. Details of synthesis and powder XRD patterns are provided in the experimental section and in Figure 2.6(a-b) respectively.

The substitution –H with $–CH_3$ at the ammonium head increases the steric hindrance. Consequently, the penetration depth of ammonium heads of IPA, MIPA, and DMIPA cation in the $[PbI_4]^{2-}$ layer systematically decreases from 0.429 Å to 0.175 Å to -0.259 Å, as shown in Figures 2.7a, 2.7b, and 2.7c, respectively. This increased distance between the A^+ and $[PbI_4]^{2-}$ is expected to reduce the electrostatic attraction, reducing the enthalpy of the crystal. Furthermore, the number of N–H----I hydrogen bonds decreases from three for $(IPA)_2PbI_4$ to one for $(MIPA)_2PbI_4$ and

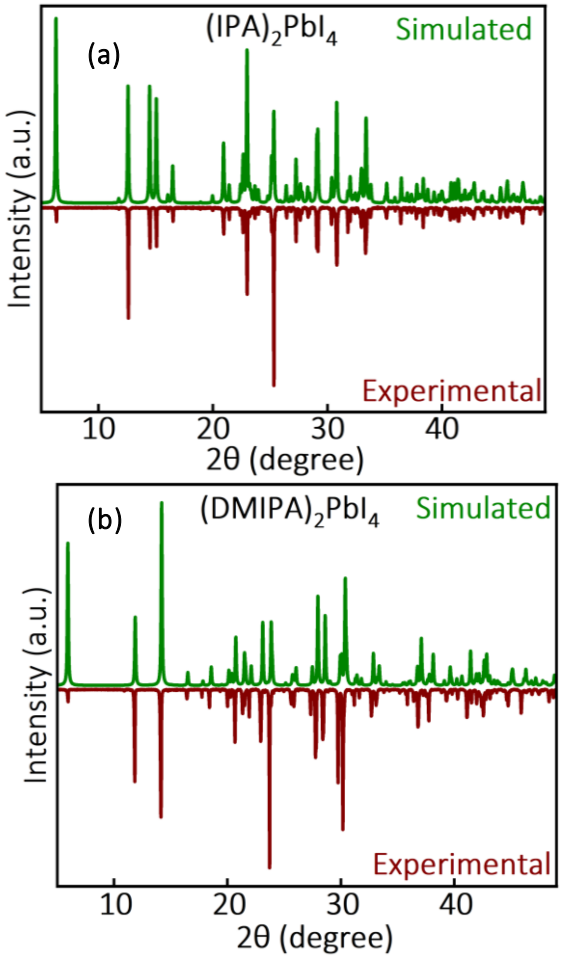

Figure 2.6: Powder XRD patterns of (a) $(IPA)_2PbI_4$ and (b) $(DMIPA)_2PbI_4$ match well with the corresponding simulated patterns obtained from single crystal XRD data. All the patterns are recorded at room temperature.

$(DMIPA)_2PbI_4$, as shown in Figure 2.6. This decrease in number of N−H----I hydrogen bonding is also expected to decrease the enthalpy of crystal. Intuitively, one might think that the decrease in enthalpy of solid is expected to decrease ΔH_{fus}. But Figure 2.8c shows the ΔH_{fus} values obtained from DSC data exhibit a reverse trend, where ΔH_{fus} increases from 20.1 kJ/mol for $(IPA)_2PbI_4$ to 34.8 kJ/mol for $(MIPA)_2PbI_4$ to 37.7 kJ/mol for $(DMIPA)_2PbI_4$. This reverse trend suggest that the substitution of –H with $–CH_3$ also significantly alters the enthalpy of the molten state, which in turn controls the ΔH_{fus}. Suprisingly, though ΔH_{fus} increases, the T_M decreases from 522 K for $(IPA)_2PbI_4$ to 388 K for $(MIPA)_2PbI_4$ to 372 K for $(DMIPA)_2PbI_4$. This decrease in T_M again emphasizes on the role of structural entropy on increasing the ΔS_{fus}.

In $(IPA)_2PbI_4$, the three N–H----I hydrogen bonds have similar strength (see Figure 2.7a), which means rotation (C_3-rotational axis for the C-N bond) of the $–NH_3^+$ head is possible. But with substitution of –H with bulky $–CH_3$, the rotation of the ammonium head is expected to get suppressed in both the crystals of $(MIPA)_2PbI_4$ and $(DMIPA)_2PbI_4$, reducing their structural entropy. In the molten state, the molar density will decrease, which is expected to make the rotations of the substituted ammonium heads feasible, increasing the ΔS_{fus}. Indeed, the DSC datain Figure 2.8c show that the increase in ΔS_{fus} is the main cause of decreasing T_M from $(IPA)_2PbI_4$ to $(MIPA)_2PbI_4$ to $(DMIPA)_2PbI_4$.

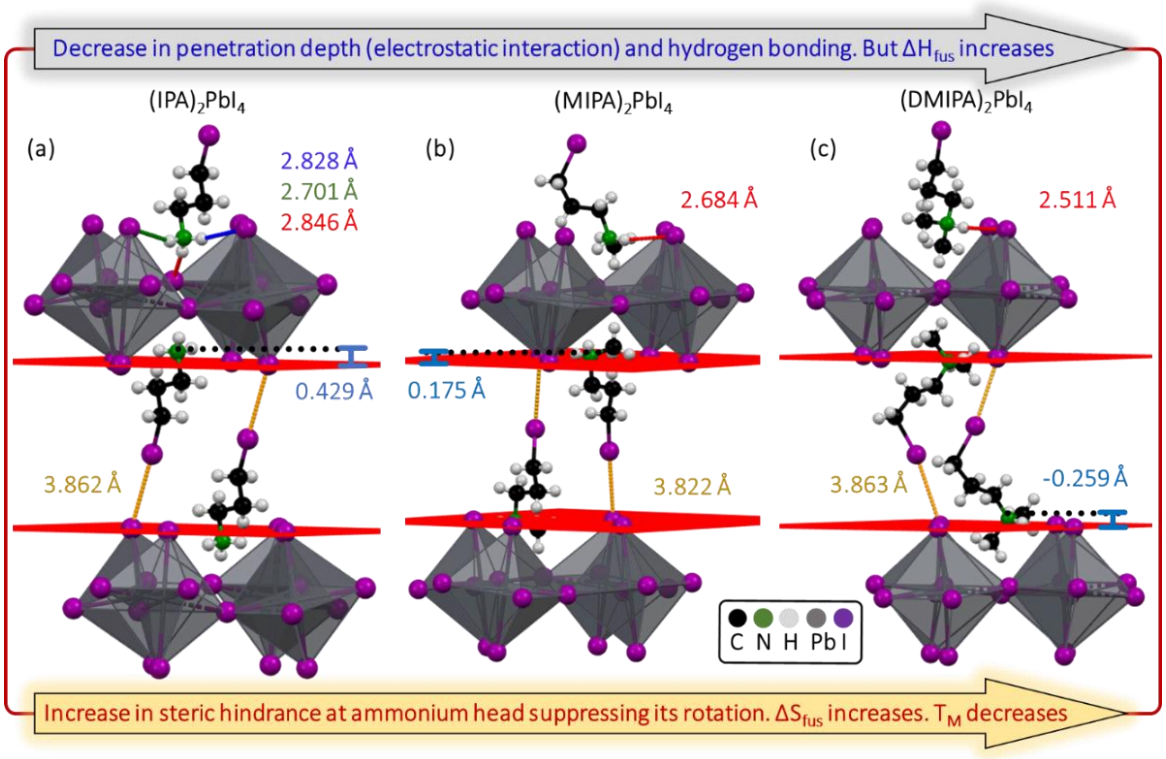

Figure 2.7: (a) Crystal structure of $(IPA)_2PbI_4$ obtained from single crystal XRD data, where IPA cation forms three hydrogen bonding interactions (blue, red, and green lines) with $[PbI_4]^{2-}$ and the ammonium head of the IPA cation penetrates 0.429 Å in the plane (red color) formed by axial iodine atoms of $[PbI_4]^{2-}$. (b) Crystal structure of $(MIPA)_2PbI_4$, where MIPA cation forms only one hydrogen bonding interaction (red line), and the penetration depth of ammonium head reduced to 0.175 Å. (c) Crystal structure of $(DMIPA)_2PbI_4$ with one hydrogen bonding interaction (red line), and a negative value of penetration of -0.259 Å indicates the ammonium head does not penetrate through the axial iodine atom plane (red color).

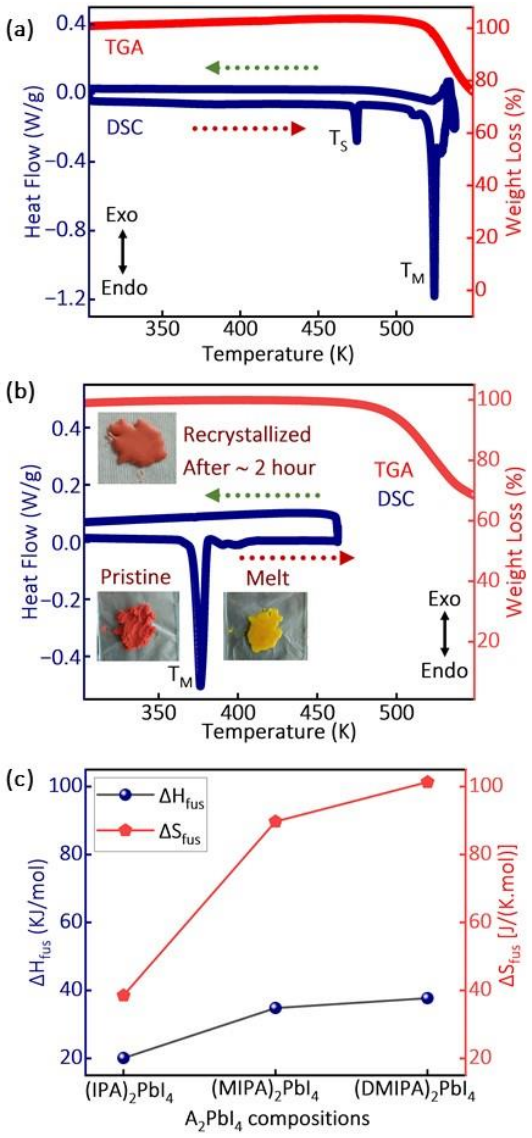

Figure 2.8: DSC (blue line) and TGA (red line) data of (a) $(IPA)_2PbI_4$ shows irreversible melting. Melting temperature of $(IPA)_2PbI_4$ is just below the decomposition temperature. Therefore, melting of $(IPA)_2PbI_4$ is also accompanied with formation minor volatile components (see the TGA), which inhibits the reversible recrystallization process upon cooling the melt. (b) $(DMIPA)_2PbI_4$ shows reversible melting and recrystallization, as indicated by the photographs in the inset. Solid-to-solid structural transition, melting, and recrystallization temperatures are represented by T_S, T_M, and T_C, respectively. (c) Comparison of the ΔH_{fus} and ΔS_{fus} of $(IPA)_2PbI_4$, $(MIPA)_2PbI_4$, and $(DMIPA)_2PbI_4$ calculated from the DSC data shown in Figure 2.5a and Figure 2.8a-b. Both ΔH_{fus} and ΔS_{fus} increase from $(IPA)_2PbI_4$ to $(MIPA)_2PbI_4$ to $(DMIPA)_2PbI_4$. (Note: The DSC experiments were performed in NCL Pune by Mr. Animesh Gopal from Dr. Kadhiravan Shanmuganathan's lab)

It is to be noted that for all the samples, the tail end of A-site cations is also rigid because of the I----I halogen bonding, as shown in both Figure 2.1b and Figure 2.7(a-c). It is to be noted that for all the samples, the tail end of A-site cations is also rigid because of the I----I halogen bonding, as shown in both Figure 2.1b and Figure 2.7(a-c).

2.3.3 Comparison of ΔH_{fus}, ΔS_{fus}, and T_M of A_2PbX_4 with Ionic Liquid and Alkali Halide

Thermodynamic parameters like ΔH_{fus} and ΔS_{fus}, and therefore T_M, depend on many aspects of constituent ions like their size, shape, mass, flexibility, polarizability, charge asymmetry, and hydrogen bonding.[16] When we change the chemical compositions of the cation and anion, multiple such parameters changes together, making it difficult to predict the trends of ΔH_{fus} and ΔS_{fus}. There is a strong interplay between electrostatics, dispersion, hydrogen bonding, and entropic contributions that sometimes lead to counterintuitive experimental observations. For example, (i) a decrease in enthalpy in the solid state of A_2PbI_4 in Figure 2.7 does not decrease the ΔH_{fus}, or (ii) decrease in hydrogen bonding in certain ionic liquids increases their viscosity.[27]

In this complex situation, in order to derive any possible generic trend, we compare here the experimental values of T_M, ΔH_{fus}, and ΔS_{fus} of previously published ionic liquids,[28] alkali halide,[29, 30] and our A_2PbX_4 perovskites. The average values of T_M for about 20 alkali halides and 257 ionic liquids are 983 K (710 ^oC) and 304 K (31 ^oC),[17] respectively, as shown in Figure 2.9a. The average T_M for 11 A_2PbX_4 perovskites is obtained from our results and also from prior reports (see Table 2.5) is 436 K (163 ^oC).

Likewise, Figures 2.9b and 2.9c compare the average values of ΔH_{fus}, and ΔS_{fus}, respectively. The average T_M of alkali halides is about 2.3 times higher than that of A_2PbX_4 perovskites and 3.2 times higher than that of ionic liquids. In contrast, the average ΔH_{fus} for alkali halides, A_2PbX_4 perovskites, and ionic liquids are very similar. This comparison clearly shows that ΔH_{fus} is not the primary reason for the observed 2.3 to 3.2 times decrease in T_M for A_2PbX_4 perovskites and ionic liquids, respectively. Interestingly, the increase in ΔS_{fus} for the A_2PbX_4 perovskites is about 3 times as compared to the alkali halides. Thus, it becomes evident that the increase in ΔS_{fus} for the A_2PbX_4 perovskite scales well with extent of decrease in T_M. This finding suggests that the major strategy

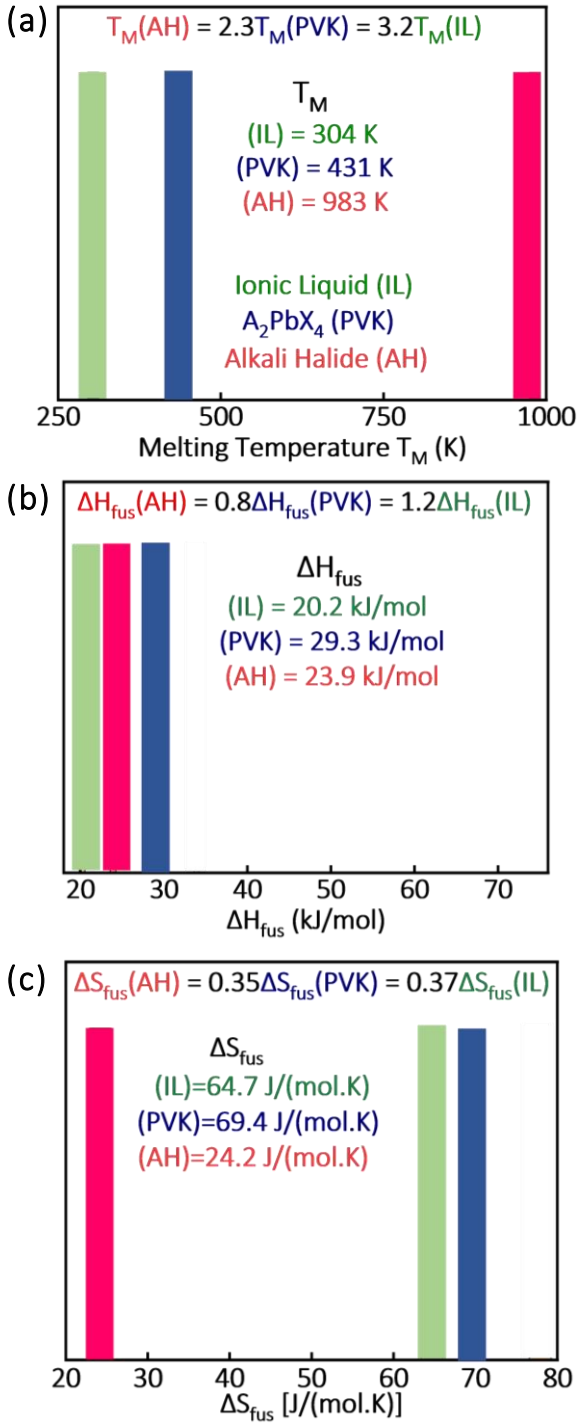

Figure 2.9: Comparison of average (a) melting temperature (T_M), (b) enthalpy of fusion (ΔH_{fus}), and (c) entropy of fusion (ΔS_{fus}) of alkali halides (AH),[17, 28] meltable A_2PbX_4 perovskites (PVK), and ionic liquids (IL).[17, 29, 30]

to control the T_M of A_2PbX_4 hybrid perovskite should be by controlling the ΔS_{fus}, which can be controlled mainly by tuning the flexibility, shape, and size (steric) of the A-site cation.

Table 2.5: Melting temperature (T_M), enthalpy of fusion (ΔH_{fus}), and entropy of fusion (ΔS_{fus}) of A_2PbX_4 perovskites used in this work and $A_2(Pb/Sn)X_4$ perovskites reported in prior literature.

$A_2(Pb/Sn)X_4$ compositions	**Melting temperature T_M (K)**	**Integration range (K)**	**ΔH_{fus} (kJ/mol)**	**ΔS_{fus} [J/(mol. K)]**	**Reference**
$(IPA)_2PbI_4$	522	520.2-525.8	20.1	38.5	This Work
$(MIPA)_2PbI_4$	388	384.9-394.1	34.8	89.7	
$(DMIPA)_2PbI_4$	372	354.3-381.8	37.7	101.3	
$(GABA)_2PbI_4$	413	403-419.7	43.6	105.7	
$(3\text{-}APN)_2PbI_4$	472	465.3-475.1	13.9	29.5	
$(MBPA)_2PbBr_4$	386	375.3-391.4	8.19	21.2	
$(MIBA)_2PbI_4$	409	401.5-424.7	37.1	90	[15]
$(MIPTA)_2PbI_4$	411	389.4-437.8	33.9	82.6	[15]
$(R\text{-}NEA)_2PbBr_4$	441	--	30.6	69.3	[31]
$(S\text{-}NEA)_2PbBr_4$	448	--	37.7	84.1	[31]
$(2F\text{-}PEA)_2SnI_4$	474	--	24.2	51.1	[32]

MIBA: N-methyliodo butylammonium, MIPTA: N-methyliodo pentyammonium, R-NEA: R-(+)-1-(1-naphthyl)ethylammonium, S-NEA: S-(-)-1-(1-naphthyl)ethylammonium, 2F-PEA: 2-fluorophenethylammonium.

2.3.4 Structural and Optical Characterization of Reversible Melting and Recrystallization of $(MIPA)_2PbI_4$

Among the list of six A_2PbX_4 samples (see Table 2.1) studied here, $(MIPA)_2PbI_4$ shows the largest difference (112 K) between melting and decomposition temperature. This large difference suggests the stability of the molten state, which is desired for the fabrication of melt-processed devices. So, as a case study, we present here the structure-property relationships of $(MIPA)_2PbI_4$ during the reversible melting-recrystallization process. At 303 K, the powder XRD pattern matches well with the simulated pattern of $(MIPA)_2PbI_4$, as shown in Figure 2.4a.

The powder XRD patterns (Figure 2.10a) remain very similar with increasing the temperature up to 373 K. Expectedly, a slight shift in XRD peaks is observed towards lower 2θ values because of the thermal expansion of the lattice (see Figure 2.11). But at 393 K, i.e. just above the melting temperature, most of the XRD peaks disappear because of the crystal melting. Further increase in the temperature to 393 K ensures the melting process with absence of XRD peaks from the yellow-colored melt (amorphous). The observed XRD peaks marked by "*" are because of the Pt substrate used for the temperature-dependent XRD measurements. Upon cooling, the melt recrystallizes back to $(MIPA)_2PbI_4$, as shown by the powder XRD pattern of the recrystallized sample.

Interestingly, this reversible melting-recrystallization process can be carried out for unlimited number of cycles. The top-most powder XRD pattern in Figure 2.10a shows the XRD pattern of $(MIPA)_2PbI_4$ after 50 cycles of melting and recrystallization in ambient conditions. Figure 2.10b shows temperature-dependent Raman Spectra of $(MIPA)_2PbI_4$. The peak at ~ 40 cm^{-1} corresponds to the twisting/rocking motions of the octahedral network,[33, 34] and is present at all temperatures below the melting point. But above the melting point, at 393 K, the Raman peak disappears suggesting breakdown of the inorganic octahedral network in the molten state. Again, cooling the melt brings back the 40 cm^{-1} Raman mode because of the recrystallization of $(MIPA)_2PbI_4$. The Raman data further corroborate the reversible melting and recrystallization of $(MIPA)_2PbI_4$.

After verifying the structural and chemical reversibility of the melting-recrystallization process, we check the reversibility of the optical properties. Figure 2.10c compares the optical absorption and emission of the as-prepared pristine $(MIPA)_2PbI_4$ sample with the sample obtained after

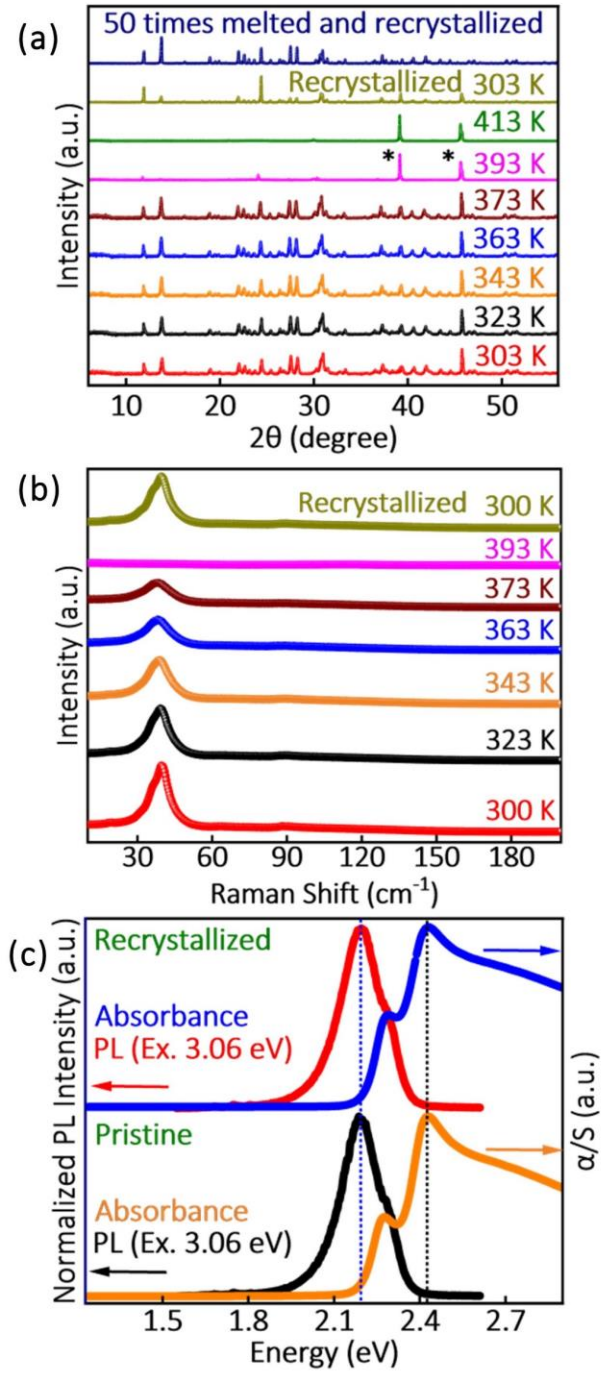

Figure 2.10: (a) Variable temperature (303-413 K) powder XRD patterns of $(MIPA)_2PbI_4$. Also, the powder XRD pattern of the sample obtained after 50 cycles of melted and recrystallization process is shown at the top. Peaks marked with "*" are due to the Pt substrate. (b) Variable temperature (300-393 K) Raman spectra of $(MIPA)_2PbI_4$. (c) Optical absorption and emission of pristine and recrystallized $(MIPA)_2PbI_4$, measured at room temperature.

melting and recrystallization process. Both the pristine and recrystallized powder samples show very similar optical absorption and emission spectra. The absorption and emission features correspond to the excitonic processes, similar to prior reports,[35, 36] of the 2D layered hybrid perovskite semiconductors. It is noteworthy that the excitonic emission in the recrystallized sample is intact, implying good quality of the recrystallized $(MIPA)_2PbI_4$, which might be suitable for optoelectronic device applications.

The bromide counterpart of $(MIPA)_2PbI_4$ is $(MBPA)_2PbBr_4$, where MBPA is 3-methylbromopropyl ammonium, $Br–(CH_2)_3–NH_2(CH_3)^+$. $(MBPA)_2PbBr_4$ also shows low melting temperature of 386 K, which is 106 K lower than its decomposition temperature (Table 2.1). The structural and optical changes of $(MBPA)_2PbBr_4$ during the reversible melting and recrystallization

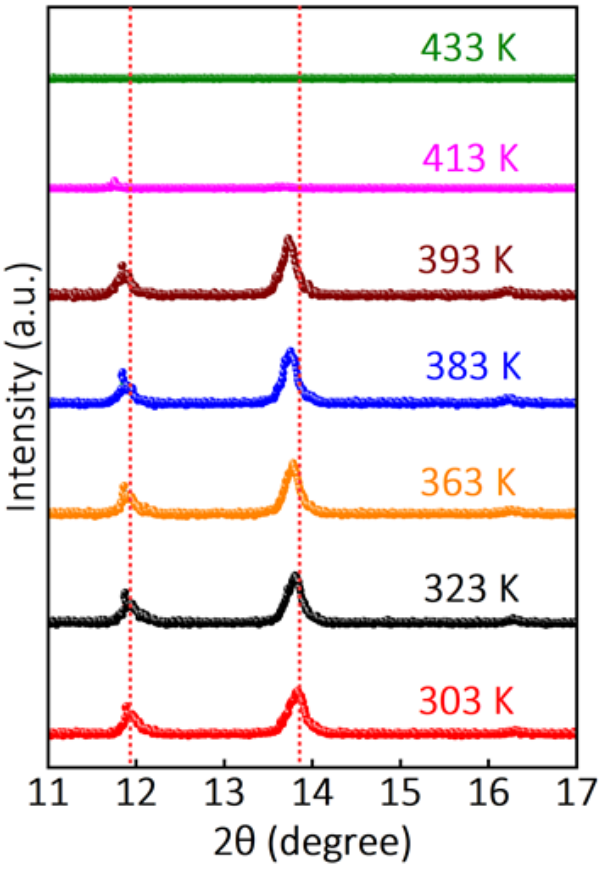

Figure 2.11: Enlarged view of the powder XRD patterns of $(MIPA)_2PbI_4$, showing peaks shift toward lower 2θ values with the increase of temperature (before melting at 388 K) due to lattice expansion.

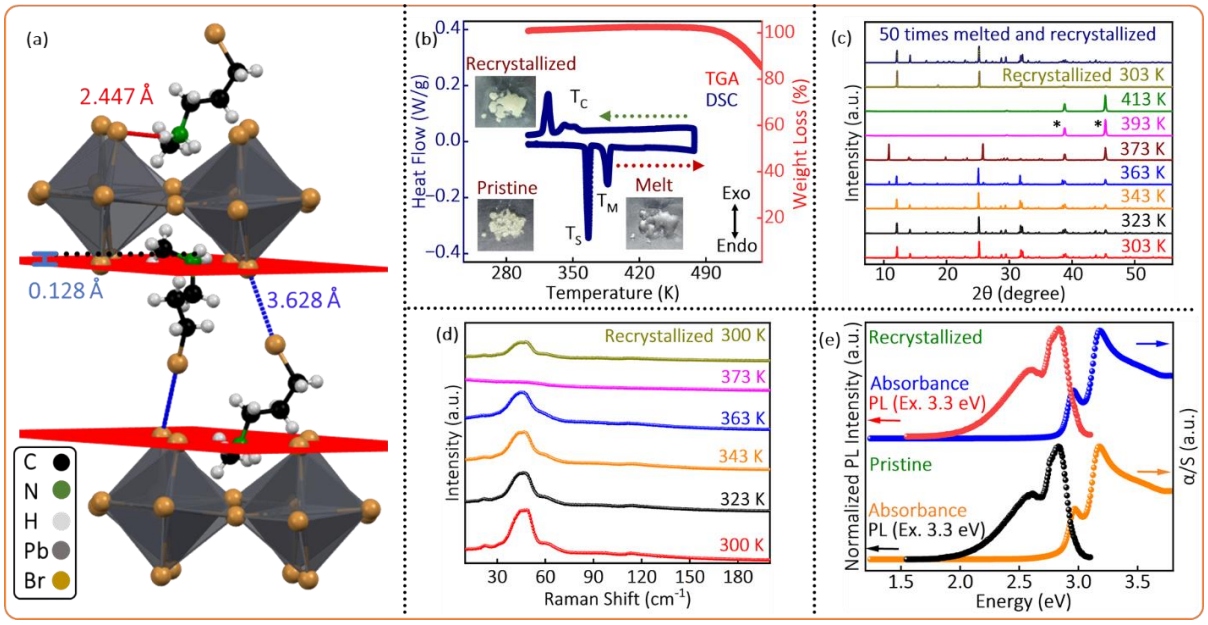

Figure 2.12: (a) Crystal structure of $(MBPA)_2PbBr_4$ obtained from single crystal XRD data, where MBPA cation forms only one hydrogen bonding interaction (red lines) with $[PbBr_4]^{2-}$ and the ammonium head of the MBPA cation penetrates 0.128 Å in the plane (red color) formed by axial bromide atoms of $[PbBr_4]^{2-}$. (b) DSC (blue color) and TGA (red color) data of $(MBPA)_2PbBr_4$ at a ramp rate of 5 K/minute. At 363 K, just before melting, solid-to-solid structure transition is present, which is further confirmed with the help of variable temperature powder XRD. Solid-to-solid structural transition, melting, and recrystallization temperatures are represented by the T_S, T_M, and T_C, respectively. Reversible melting and recrystallization processes are observed for $(MBPA)_2PbBr_4$. Photographs in the insets of (b) show the appearance of pristine, molten, and recrystallized $(MBPA)_2PbBr_4$. (c) Variable temperature (303-413 K) powder XRD patterns of $(MBPA)_2PbBr_4$. A few new peaks started appearing along with the pristine sample peaks in the at 363 K and 374 K, just before the melting of $(MBPA)_2PbBr_4$. At 393 K, most of the XRD peaks disappear because of the crystal melting. Also, the powder XRD pattern of the sample obtained after 50 cycles of melted and recrystallization process is shown at the top. Peaks marked with "*" are due to the Pt substrate. (d) Variable temperature (300-393 K) Raman spectra of $(MBPA)_2PbBr_4$. The Raman peak at ~ 47 cm^{-1} corresponds to the twisting/rocking motions of the octahedral network.[33, 34] Disappearance of Raman peak in the molten state suggests breakdown of the inorganic octahedral network. Again, cooling the melt brings back the 47 cm^{-1} Raman mode because of the recrystallization of $(MBPA)_2PbBr_4$. (e) Optical absorption and emission of pristine and recrystallized $(MBPA)_2PbBr_4$, measured at room temperature. Both the pristine and recrystallized powder samples show very similar optical absorption and emission spectra. (Note: The DSC experiments were performed in NCL Pune by Mr. Animesh Gopal from Dr. Kadhiravan Shanmuganathan's lab)

process (see Figure 2.12) are also similar to that of $(MIPA)_2PbI_4$. We note that $(MBPA)_2PbBr_4$ undergoes a solid-to-solid phase transition (Ts = 363 K) just before the melting at 386 K as shown in Figure 2.12(b-c).

Such a high-temperature-phase solid-to-liquid transition of $(MBPA)_2PbBr_4$ has a different nature compared to the room-temperature-phase solid-to-liquid transition of $(MIPA)_2PbI_4$. Therefore, the absolute values of ΔH_{fus}, and subsequently the ΔS_{fus}, differe for both samples. Interestingly, for both samples the ration $\Delta H_{fus}/\Delta S_{fus}$ remains similar yielding similar values of melting temperatures.

2.3.5 Solvent- and Vacuum-Free Melt-Processed $(MIPA)_2PbI_4$ Films and Photodetector Dvice

Typical hybrid perovskite films are prepared either through solution processed or through vacuum routes.[37, 38] While such perovskite films are the best ones right now in terms of their optoelectronic device performance, but use of large amount of toxic solvents in solution processed method and power-intensive methodology in the vapor route are not desired. Alternatively, melt-pressed film deposition is free from both solvents and vacuum systems. Therefore, there is immense interest to grow melt-processed perovskite films exhibiting good optoelectronic properties.[13, 14] Figure 2.13a schematically shows our method of melt-pressed growth of perovskite films. In this method $(MIPA)_2PbI_4$ powder (~5 mg) is placed on a glass substrate (2 cm × 2 cm) and heated on a hot plate upto ~403 K, which is 5-10 K higher than the melting temperature of the sample lowering down the viscosity. The melt is very stable at this temperature (see Figure 2.5a). A kapton sheet was placed over the melted yellow liquid and pressed with a preheated glass substrate till the melted liquid uniformly spread. The hot plate temperature is then reduced to room temperature. After a complete recrystallization (yellow to red colour conversion), the upper glass substrate and the kapton sheet are removed gently, leaving behind the $(MIPA)_2PbI_4$ film (see the inset of Figure 2.14b). The FESEM image in Figure 2.13b shows the melt-processed film has a uniform thickness of about 4.5 μm. The thickness can be controlled in the range of a few μm (see Figure 2.14c and 2.14d), but it is challenging to get thinner films using this method. Figure 2.14e and 2.14f shows large grain size (more than 100 μm) and absence of pin-holes, which are preferred for good charge

transport through the film. The powder XRD pattern of the film in Figure 2.14a confirms the formation of $(MIPA)_2PbI_4$ after recrystallization of the melt.

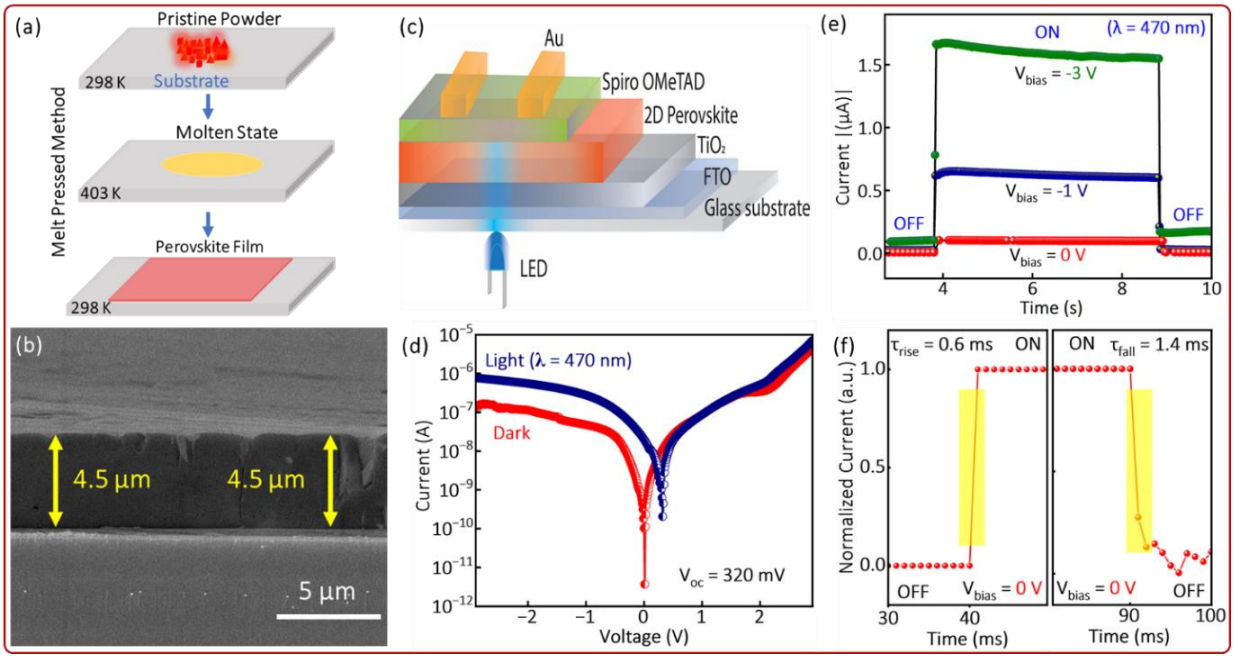

Figure 2.13: (a) Schematic diagrams showing our melt-pressed method for preparing $(MIPA)_2PbI_4$ film. (b) Cross-sectional FESEM images of the prepared film. (c) Schematic diagram of the photodetector device with n-i-p geometry. (d) Current-voltage (I-V) characteristics of the device under dark and 470 nm (power density of 6.10 mW/cm^2) LED illumination. (e) The on-off states of the device during different bias conditions from 0V to -3V. (f) Calculated rise and fall time of a self-powered (V_{bias} = 0 V) photodetector. (Note: Photodetector data in Figure 2.13d, 2.13e, and 2.13f was recorded by Meghasree Basu in Prof. Atikur Rahman's Lab at IISER Pune)

The melt-processed $(MIPA)_2PbI_4$ films also show excitonic photoluminescence (Figure 2.14b) similar to their powder form. After confirming the thickness, morphology, crystal structure, and optical properties of melt-processed $(MIPA)_2PbI_4$ films, we fabricate photodetector devices with n-i-p geometry, as shown by the schematic in Figure 2.13c.

In Figure 2.15, the FESEM cross sectional view of a photodiode is presented. The $(MIPA)_2PbI_4$ film is the active light-absorbing layer. This is coupled with TiO_2 serving as the electron-transporting layer and spiro-OMeTAD as the hole-transporting layer. More details about the device fabrication is presented in the experimental section Figure 2.13d compares the current-voltage

(I-V) characteristics of the $(MIPA)_2PbI_4$ photodiode under both dark and 470 nm (power density of 6.10 mW/cm^2) light illumination at room temperature. In the reverse-biased region, the photo-current is about 7.4 times higher than the dark current.

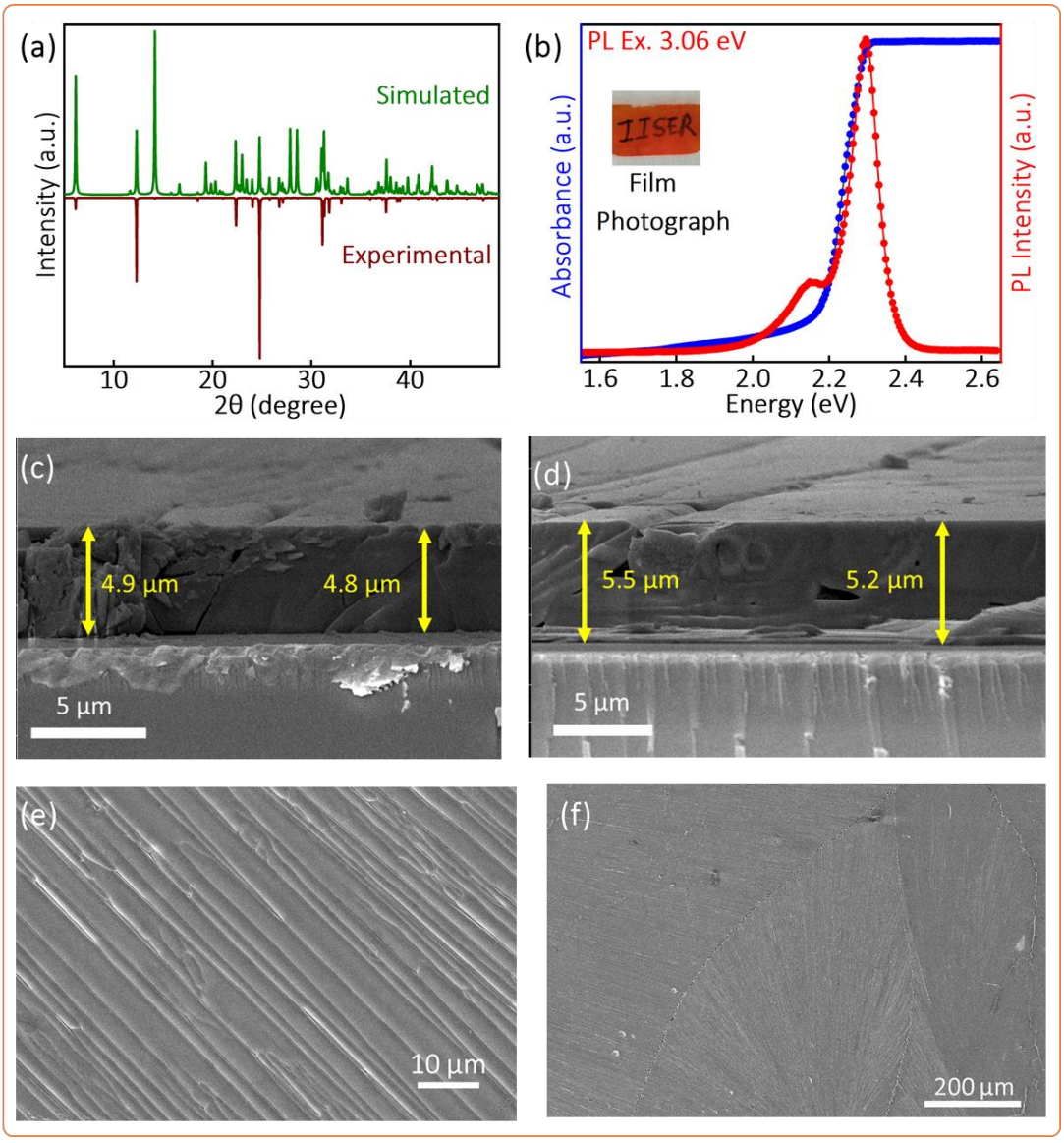

Figure 2.14: (a) Powder XRD pattern of melt-pressed $(MIPA)_2PbI_4$ films confirms its formation after recrystallization. (b) Melt-pressed film of $(MIPA)_2PbI_4$ shows absorbance and excitonic photoluminescence. Inset shows a photograph of a melt-pressed film. (c-d) Cross-section images of the melt-pressed films (on glass substrate) of $(MIPA)_2PbI_4$ at different regions show similar thickness of the films. FESEM images (e-f) of the surface of melt-pressed films of $(MIPA)_2PbI_4$, shows textured growth with large grain sizes (more than 100 µm).

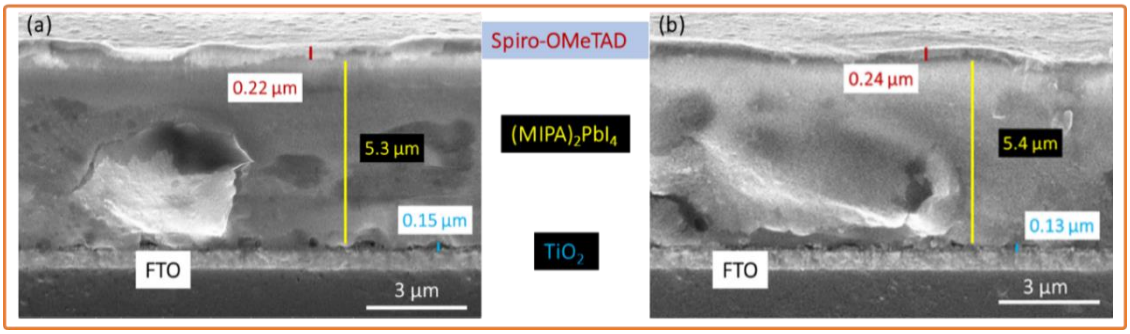

Figure 2.15: (a-b) FESEM cross-section images of the fabricated n-i-p structured photodiode, with the configuration of FTO/c-TiO_2/$(MIPA)_2PbI_4$/Spiro-OMeTAD.

Interestingly, a photovoltaic effect is also observed under illumination with an open-circuit voltage (V_{OC}) of 320 mV, due to the photogenerated carriers at the n-TiO_2/$(MIPA)_2PbI_4$/p-Spiro-OMeTAD interface. This built-in electric field leads to the asymmetric rectifying I-V behavior. The estimated photodiode ideality factor (see Figure 2.16) under both dark and illuminated conditions are 2.3 and 2.2, respectively.

Overall, the I-V characteristics suggest the fabrication of a reasonably good quality photodiode using melt-pressed films of $(MIPA)_2PbI_4$ layered perovskite. Figure 2.13e shows transient photocurrent response of $(MIPA)_2PbI_4$ based photodiode with different applied biases from 0 V to -3 V. A sharp switching of photocurrent during the light on−off cycles is observed. The on-off cycles repeat over many times without a loss of photocurrent as shown in Figures 2.17 and 2.18(a-d). Expectedly, an increase in the applied bias voltage from 0 V to -3 V increases the photocurrent. The photocurrent is directly proportional to the responsivity and detectivity, which are key parameters of the photodiode.

The responsivity increases from 23 mA/W at 0 V, to 145 mA/W at -1 V, to 362 mA/W at -3 V. Likewise, detectivity increases 1.6×10^{10} Jones at 0 V, to 4.6×10^{10} Jones at -1 V, to 5.8×10^{10} Jones at -3 V. The obtained values are reasonably good compared to previously reported devices of layered hybrid perovskites (see Table 2.6). Response time, i.e., photocurrent rise and decay time, is another important photodetector parameter. Figure 2.13f shows that at 0 V bias, the rise and fall time are estimated as 0.6 ms and 1.4 ms. Similar response times are also observed at other bias voltages, as shown in Figure 2.18.

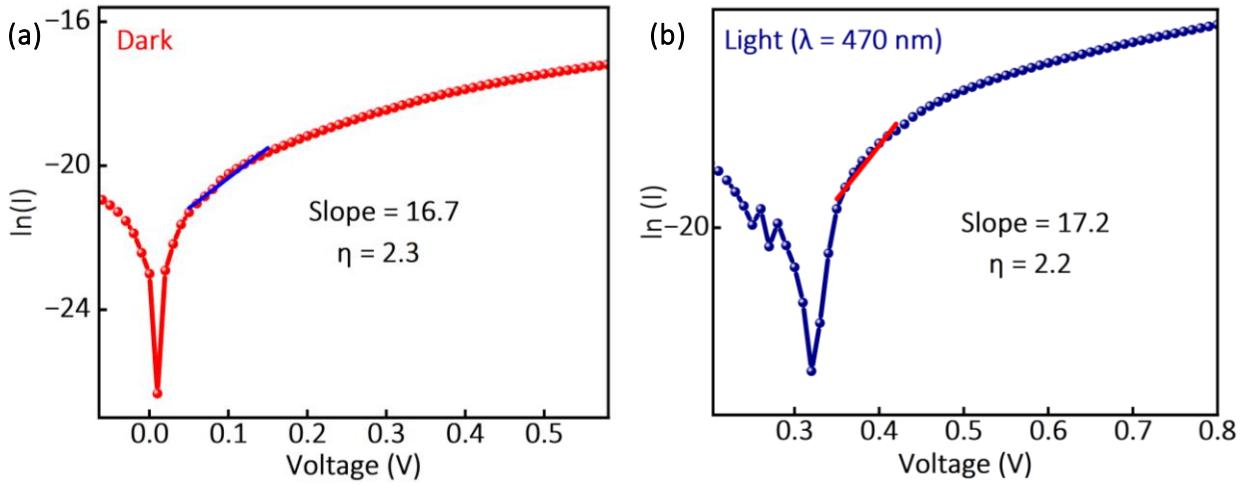

Figure 2.16: I-V characteristic under dark and light conditions of n-i-p structured self-powered photodiode's ideality factor (η) extracted from the ln(I) vs V plot.

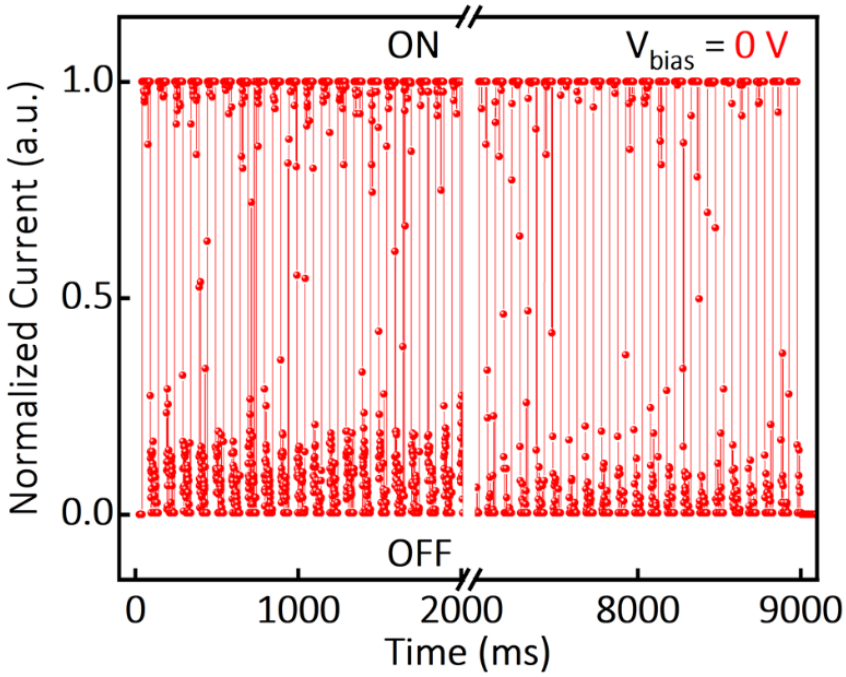

Figure 2.17: Multiple on-off cycles of the melt-pressed $(MIPA)_2PbI_4$ based photodetector device in the self-powered mode, i.e., without applying any bias voltage. (Note: This I-T data was recorded by Meghasree Basu in Dr. Atikur Rahman's Lab at IISER Pune)

The obtained response time is reasonably fast compared to other 2D perovskite photodetectors (see Table 2.6),[39, 40] and remains largely stable (see Figure 2.19) even after many days from the fabrication of devices.

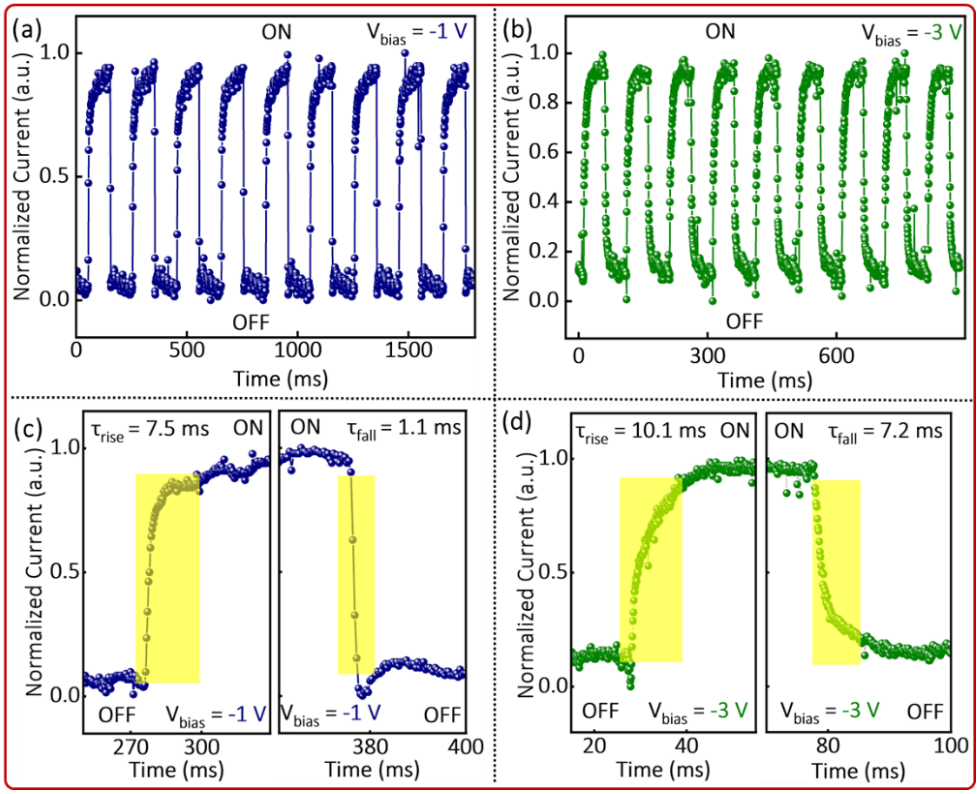

Figure 2.18: (a-b) Multiple on-off cycles of the melt-pressed $(MIPA)_2PbI_4$ based photodetector device at -1V bias and -3 V bias. (c-d) Response (rise / fall) time calculated at -1 V bias and -3 V bias. (Note: This I-t data was recorded by Meghasree Basu in Dr. Atikur Rahman's Lab at IISER Pune)

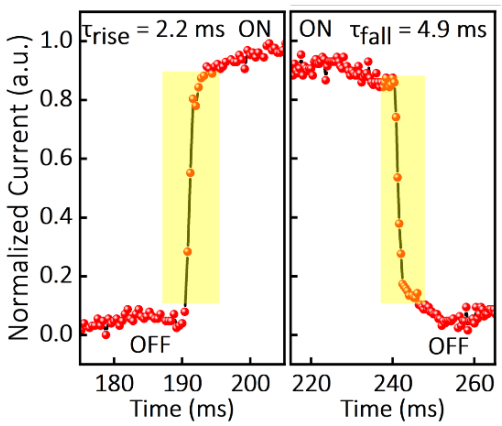

Figure 2.19: Rise and fall time of a self-powered (at V_{bias} = 0 V) photodetector after 40 days from the date of fabrication. The measurements are done in ambient conditions, though the device was stored in nitrogen environment. (Note: This I-t data was recorded by Meghasree Basu in Dr. Atikur Rahman's Lab at IISER Pune)

Table 2.6: Comparison of reported critical device parameters of photodetectors of A_2PbX_4 perovskites with our fabricated photodetector.

A_2PbX_4 composition	**Morphology**	**Light (nm)/ Power (mW/cm^2)**	**Bias (V)**	**Responsivity (mA/W)**	**Detectivity (Jones)**	**Rise/ fall time (ms)**	**Reference**
$(MIPA)_2PbI_4$	Melt pressed film	470/6.1	0	23	1.6×10^{10}	0.6 / 1.4	This Work
			-1	145	4.6×10^{10}	7.5 / 1.1	
			-3	362	5.8×10^{10}	10.1 / 7.2	
$(OA)_2PbI_4$	Spin coated film	470	----	2.89	----	200 / 500	[41]
$(iBA)_2PbI_4$	Spin coated film	532 / 60	1.5	4.78	----	49 / 61	[42]
$(iBA)_2(MA)_3Pb_4I_{13}$				117.09	----	16 / 15	
$(BA)_2PbI_4$	Spin coated film	White light / 3.0	30	3	----	28.4 / 27.5	[43]
$(BA)_2(MA)Pb_2I_7$					----	8.4 / 7.5	
$(BA)_2(MA)_2Pb_3I_{10}$					----	10.0 / 7.5	
$(PEA)_2PbI_4$	Spin coated film	475 / 1.45	10	0.75	2.8×10^8	82.6 / 20.7	[44]
$BDAPbI_4$	Single crystal	462 / 8.8 $\mu W/cm^2$	4	930	1.2×10^{11}	0.19 / 0.16	[45]
$(BA)_2PbI_4$	Spin coating film	--- / 40	5	----	----	500 / 200	[46]
$(HA)_2PbI_4$				----	----	200 / 100	
$(OA)_2PbI_4$				----	----	300 / 100	
$(BA)_2(MA)_4Pb_5I_{16}$	Spin coated film	565 / 830 $\mu W/cm^2$	10	0.01	6.8×10^{12}	14 / 31	[47]

OA: octylammonium, iBA: isobutlyammonium, BA: butylammonium, PEA: phenethylammonium, BDA: 1,4-butanediammonium, HA: hexylammonium, MA: methylammonium

2.4 Conclusions

We show that a series of layered hybrid perovskite samples, $(MIPA)_2PbI_4$, $(DMIPA)_2PbI_4$, $(GABA)_2PbI_4$, $(3\text{-}APN)_2PbI_4$, and $(MBPA)_2PbBr_4$ undergo melting at temperatures lower than the decomposition temperature. Majority of them form stable melts, and upon cooling, recrystallize back to its perovskite form. The control over reversible melting process is achieved by discovering that the structural entropy dominates the ΔS_{fus} and melting temperature. All the A-site cations used here have functional tail groups like –I, –Br, –CN, and –COOH which undergoes non-covalent interactions yielding rigid A-site layer in the crystal. The structural rigidity is increased further by suppressing the rotation of the ammonium head group, by replacing $–NH_3^+$ with $–NH_2(CH_3)^+$ and $–NH(CH_3)_2^+$. Upon melting, the mentioned tail group interactions probably diminish, and the rotation of head group becomes allowed, leading to a substantial increase in ΔS_{fus}, and, subsequently, a decrease in melting temperature. $(MIPA)_2PbI_4$ shows one of the lowest melting temperatures of 388 K (115 ^oC), which is about 112 K lower than its decomposition temperature 500 K. For such a sample, the stable melt can be easily processed into solvent- and vacuum-free perovskite films on both glass and flexible polymer substrates. The melt-pressed films are optoelectronically active forming self-powered n-i-p photodiodes with sub-millisecond response time. This work establishes a new structure-property relationship connecting structural ΔS_{fus} with melting temperature of A_2PbX_4 perovskites, and subsequently demonstrates the feasibility of melt-pressed perovskite films for optoelectronic applications. These generic findings pave the way for designing new functional hybrid perovskite crystals and films.

2.5 References

1. Mitzi, D. B. Synthesis, Crystal Structure, and Optical and Thermal Properties of $(C_4H_9NH_3)_2MI_4$ (M = Ge, Sn, Pb). *Chem. Mater.* **1996,** *8*, 791-800.

2. Smith, I. C.; Hoke, E. T.; Solis-Ibarra, D.; McGehee, M. D.; Karunadasa, H. I. A Layered Hybrid Perovskite Solar-Cell Absorber with Enhanced Moisture Stability. *Angew. Chem. Int. Ed.* **2014,** *53*, 11232-11235.

3. Soe, C. M. M.; Stoumpos, C. C.; Kepenekian, M.; Traoré, B.; Tsai, H.; Nie, W.; Wang, B.; Katan, C.; Seshadri, R.; Mohite, A. D.; Even, J.; Marks, T. J.; Kanatzidis, M. G. New Type of

2D Perovskites with Alternating Cations in the Interlayer Space, $(C(NH_2)_3)(CH_3NH_3)_nPb_nI_{3n+1}$: Structure, Properties, and Photovoltaic Performance. *J. Am. Chem. Soc.* **2017,** *139*, 16297-16309.

4. Dey, A.; Ye, J.; De, A.; Debroye, E.; Ha, S. K.; Bladt, E.; Kshirsagar, A. S.; Wang, Z.; Yin, J.; Wang, Y.; Quan, L. N.; Yan, F.; Gao, M.; Li, X.; Shamsi, J.; Debnath, T.; Cao, M.; Scheel, M. A.; Kumar, S.; Steele, J. A.; Gerhard, M.; Chouhan, L.; Xu, K.; Wu, X. G.; Li, Y.; Zhang, Y.; Dutta, A.; Han, C.; Vincon, I.; Rogach, A. L.; Nag, A.; Samanta, A.; Korgel, B. A.; Shih, C. J.; Gamelin, D. R.; Son, D. H.; Zeng, H.; Zhong, H.; Sun, H.; Demir, H. V.; Scheblykin, I. G.; Mora-Seró, I.; Stolarczyk, J. K.; Zhang, J. Z.; Feldmann, J.; Hofkens, J.; Luther, J. M.; Pérez-Prieto, J.; Li, L.; Manna, L.; Bodnarchuk, M. I.; Kovalenko, M. V.; Roeffaers, M. B. J.; Pradhan, N.; Mohammed, O. F.; Bakr, O. M.; Yang, P.; Müller-Buschbaum, P.; Kamat, P. V.; Bao, Q.; Zhang, Q.; Krahne, R.; Galian, R. E.; Stranks, S. D.; Bals, S.; Biju, V.; Tisdale, W. A.; Yan, Y.; Hoye, R. L. Z.; Polavarapu, L. State of the Art and Prospects for Halide Perovskite Nanocrystals. *ACS Nano* **2021,** *15*, 10775.

5. Li, J.; Matheu, R.; Ke, F.; Liu, Z.; Lin, Y.; Karunadasa, H. I. Mosaic CuI−CuII−InIII 2D Perovskites: Pressure-Dependence of the Intervalence Charge Transfer and a Mechanochemical Alloying Method. *Angew. Chem. Int. Ed.* **2023,** *62*, e202300957.

6. Zhang, H.; Wang, R.; Yang, L.; Hu, Z.; Liu, H.; Liu, Y. Modulating the Dipole Moment of Secondary Ammonium Spacers for Efficient 2D Ruddlesden-Popper Perovskite Solar Cells. *Angew. Chem. Int. Ed.* **2024,** *63*, e202318206.

7. Mitzi, D. B.; Dimitrakopoulos, C. D.; Rosner, J.; Medeiros, D. R.; Xu, Z.; Noyan, C. Hybrid Field-Effect Transistor Based on a Low-Temperature Melt-Processed Channel Layer. *Adv. Mater.* **2002,** *14*, 1772-1776.

8. Mitzi, D. B.; Medeiros, D. R.; DeHaven, P. W. Low-Temperature Melt Processing of Organic−Inorganic Hybrid Films. *Chem. Mater.* **2002,** *14*, 2839-2841.

9. Li, T.; Dunlap-Shohl, W. A.; Han, Q.; Mitzi, D. B. Melt Processing of Hybrid Organic–Inorganic Lead Iodide Layered Perovskites. *Chem. Mater.* **2017,** *29*, 6200-6204.

10. Li, T.; Zeidell, A. M.; Findik, G.; Dunlap-Shohl, W. A.; Euvrard, J.; Gundogdu, K.; Jurchescu, O. D.; Mitzi, D. B. Phase-Pure Hybrid Layered Lead Iodide Perovskite Films Based on a Two-Step Melt-Processing Approach. *Chem. Mater.* **2019,** *31*, 4267-4274.

11. Singh, A.; Jana, M. K.; Mitzi, D. B. Reversible Crystal–Glass Transition in a Metal Halide Perovskite. *Adv. Mater.* **2021,** *33*, 2005868.

12. Salah, M. B. H.; Mercier, N.; Dabos-Seignon, S.; Botta, C. Solvent-Free Preparation and Moderate Congruent Melting Temperature of Layered Lead Iodide Perovskites for Thin-Film Formation. *Angew. Chem. Int. Ed.* **2022,** *61*, e202206665.

13. Singh, A.; Crace, E.; Xie, Y.; Mitzi, D. B. A two-dimensional lead-free hybrid perovskite semiconductor with reduced melting temperature. *Chem. Commun.* **2023,** *59*, 8302-8305.

14. Crace, E. J.; Singh, A.; Haley, S.; Claes, B.; Mitzi, D. B. Meltable Hybrid Antimony and Bismuth Iodide One-Dimensional Perovskites. *Inorg. Chem.* **2023,** *62*, 16161-16169.

15. Wang, W.; Liu, C.-D.; Fan, C.-C.; Fu, X.-B.; Jing, C.-Q.; Jin, M.-L.; You, Y.-M.; Zhang, W. Rational Design of 2D Metal Halide Perovskites with Low Congruent Melting Temperature and Large Melt-Processable Window. *J. Am. Chem. Soc.* **2024,** *146*, 9272-9284.

16. Endo, T.; Sunada, K.; Sumida, H.; Kimura, Y. Origin of low melting point of ionic liquids: dominant role of entropy. *Chem. Sci.* **2022,** *13*, 7560-7565.

17. Philippi, F.; Welton, T. Targeted modifications in ionic liquids – from understanding to design. *Phys. Chem. Chem. Phys.* **2021,** *23*, 6993-7021.

18. Chakraborty, R.; Sheikh, T.; Nag, A. Iodine–iodine interactions suppressing phase transitions of 2D layered hybrid $(I\text{-}(CH_2)_n\text{-}NH_3)_2PbI_4$ (n= 2–6) perovskites. *Chem. Mater.* **2021,** *34*, 288-296.

19. Chakraborty, R.; Rajput, P. K.; Anilkumar, G. M.; Maqbool, S.; Das, R.; Rahman, A.; Mandal, P.; Nag, A. Rational Design of Non-Centrosymmetric Hybrid Halide Perovskites. *J. Am. Chem. Soc.* **2023,** *145*, 1378-1388.

20. Mercier, N.; Louvain, N.; Bi, W. Structural diversity and retro-crystal engineering analysis of iodometalate hybrids. *CrystEngComm* **2009,** *11*, 720-734.

21. Huang, Y.-H.; Wang, X.-D.; Li, W.-G.; Zou, S.-Y.; Yang, X.; Kuang, D.-B. Band Structure Optimized by Electron-Acceptor Cations for Sensitive Perovskite Single Crystal Self-Powered Photodetectors. *Small* **2024,** *20*, 2306821.

22. Lemmerer, A.; Billing, D. G. Effect of heteroatoms in the inorganic–organic layered perovskite-type hybrids $[(ZC_nH_{2n}NH_3)_2PbI_4]$, n= 2, 3, 4, 5, 6; Z= OH, Br and I; and $[(H_3NC_2H_4S_2C_2H_4NH_3)PbI_4]$. *CrystEngComm* **2010,** *12*, 1290-1301.

23. Dolomanov, O. V.; Bourhis, L. J.; Gildea, R. J.; Howard, J. A. K.; Puschmann, H. OLEX2: a complete structure solution, refinement and analysis program. *J. Appl. Crystallogr.* **2009,** *42*, 339-341.

24. Eickhoff, T.; Grosse, P.; Theiss, W. Diffuse reflectance spectroscopy of powders. *Vib. Spectrosc.* **1990,** *1*, 229-233.

25. Mercier, N. $(HO_2C(CH_2)_3NH_3)_2(CH_3NH_3)Pb_2I_7$: a predicted non-centrosymmetrical structure built up from carboxylic acid supramolecular synthons and bilayer perovskite sheets. *CrystEngComm* **2005,** *7* , 429-432.

26. Billing, D. G.; Lemmerer, A. Synthesis, characterization and phase transitions in the inorganic-organic layered perovskite-type hybrids $[(C_nH_{2n+1}NH_3)_2PbI_4]$, n = 4, 5 and 6. *Acta Crystallogr., Sect. B: Struct. Sci.* **2007,** *63*, 735.

27. Hunt, P. A., Why Does a Reduction in Hydrogen Bonding Lead to an Increase in Viscosity for the 1-Butyl-2,3-dimethyl-imidazolium-Based Ionic Liquids? *J. Phys. Chem. B* **2007,** *111*, 4844-4853.

28. Haase, R., G. J. Janz. Molten Salts Handbook. Academic Press, New York-London. *Berichte der Bunsengesellschaft für physikalische Chemie* **1968,** *72*, 358-358.

29. Qian, D.; Chris, M.; Andrei, K.; Vladimir, D.; Joe, M.; Jason, W.; Robert, C.; Kenneth, M.; Michael, F. ILThermo: A Free-Access Web Database for Thermodynamic Properties of Ionic Liquids. **2007,** 52, 1151.

30. Andrei, K.; Joe, M.; Robert, C.; Vladimir, D.; Kenneth, K.; Chris, M.; Michael, F. Ionic Liquids Database - ILThermo (v2.0). Ionic Liquids Database - ILThermo (v2.0): **2013**, 2, 20899.

31. Singh, A.; Jana, M. K.; Mitzi, D. B. Reversible Crystal-Glass Transition in a Metal Halide Perovskite. *Adv. Mater.* **2021,** *33*, e2005868.

32. Mitzi, D. B.; Medeiros, D. R.; DeHaven, P. W. Low-Temperature Melt Processing of Organic–Inorganic Hybrid Films. *Chem. Mater.* **2002,** *14*, 2839.

33. Dhanabalan, B.; Leng, Y.-C.; Biffi, G.; Lin, M.-L.; Tan, P.-H.; Infante, I.; Manna, L.; Arciniegas, M. P.; Krahne, R. Directional Anisotropy of the Vibrational Modes in 2D-Layered Perovskites. *ACS Nano* **2020,** *14*, 4689-4697.

34. Spirito, D.; Asensio, Y.; Hueso, L. E.; Martín-García, B., Raman spectroscopy in layered

hybrid organic-inorganic metal halide perovskites. *J. Phys. Mater.* **2022,** *5*, 034004.

35. Sheikh, T.; Nawale, V.; Pathoor, N.; Phadnis, C.; Chowdhury, A.; Nag, A. Molecular Intercalation and Electronic Two Dimensionality in Layered Hybrid Perovskites. *Angew. Chem. Int. Ed.* **2020,** *59*, 11653.

36. Nag, A. "Plenty of Room" at the Interface of Hybrid Metal Halide Perovskite Single Crystals. *Nano Lett.* **2021,** *21*, 8529-8531.

37. Dunlap-Shohl, W. A.; Zhou, Y.; Padture, N. P.; Mitzi, D. B. Synthetic Approaches for Halide Perovskite Thin Films. *Chem. Rev.* **2019,** *119*, 3193.

38. Li, H.; Zhou, J.; Tan, L.; Li, M.; Jiang, C.; Wang, S.; Zhao, X.; Liu, Y.; Zhang, Y.; Ye, Y.; Tress, W.; Yi, C. Sequential vacuum-evaporated perovskite solar cells with more than 24% efficiency. *Sci. Adv.* **2022,** *8*, eabo7422.

39. Ramasamy, P.; Lim, D.-H.; Kim, B.; Lee, S.-H.; Lee, M.-S.; Lee, J.-S. All-inorganic cesium lead halide perovskite nanocrystals for photodetector applications. *Chem. Commun.* **2016,** *52*, 2067-2070.

40. Hsiao, Y.-W.; Cheng, B. S.; Hsu, H.-C.; Wu, S.-H.; Wu, H.-T.; Leu, C.-C.; Shih, C.-F. Vertical-type 3D/Quasi-2D n-p Heterojunction Perovskite Photodetector. *Adv. Funct. Mater.* **2023,** *33*, 2300169.

41. Perumallapelli, G. R.; Tsuda, T.; Formanek, P.; Kiriy, N.; Bakulev, V.; Simon, F.; Voit, B.; Mannsfeld, S. C. B.; Kiriy, A. New insights into the structure of two-dimensional lead iodide-based perovskites. *Org. Electron.* **2020,** *87*, 105935.

42. Dong, R.; Lan, C.; Xu, X.; Liang, X.; Hu, X.; Li, D.; Zhou, Z.; Shu, L.; Yip, S.; Li, C.; Tsang, S.-W.; Ho, J. C. Novel Series of Quasi-2D Ruddlesden–Popper Perovskites Based on Short-Chained Spacer Cation for Enhanced Photodetection. *ACS Appl. Mater. Interfaces* **2018,** *10*, 19019-19026.

43. Zhou, J.; Chu, Y.; Huang, J. Photodetectors Based on Two-Dimensional Layer-Structured Hybrid Lead Iodide Perovskite Semiconductors. *ACS Appl. Mater. Interfaces* **2016,** *8*, 25660-25666.

44. Yue, Y.; Li, M.; Li, H.; Chai, N.; Dong, Y.; Li, Z.; Chen, X.; Wang, X. One-step anti-solvent associated method for high performance two-dimensional perovskite photodetectors

fabrication at low temperature. *Chem. Eng. J.* **2022,** *441*, 135997.

45. Zhang, Y.; Liu, Y.; Xu, Z.; Yang, Z.; Liu, S. 2D Perovskite Single Crystals with Suppressed Ion Migration for High-Performance Planar-Type Photodetectors. *Small* **2020,** *16*, 2003145.

46. Liu, G.; Qiu, C.; Tian, B.; Pan, X.; Ding, D.; Chen, Y.; Ren, C.; He, T.; Shi, Y.; Su, C.; Li, Y.; Gao, Y.; Fan, D. Influence of the Organic Chain on the Optical Properties of Two-Dimensional Organic–Inorganic Hybrid Lead Iodide Perovskites. *ACS Appl. Electron. Mater.* **2019,** *1*, 2253-2259.

47. Pan, Y.; Wang, H.; Wang, Y.; Wang, Y.; Li, X.; Liu, Y.; Deng, L.; Liu, K.; Hu, T.; Liu, F.; Shi, Z.; Li, C.; Wang, J.; Yu, A.; Zhang, X.; Zhan, Y. An Ultrasensitive Sandwiched Heterostructure Planar Photodetector with Gradient Quasi-2D Perovskite. *Adv. Electron. Mater.* **2023,** *9*, 2201028.

Chapter 3

Molten State Synthesis of Lead-Halide Hybrid Perovskite Derivative

Graphical Abstract:

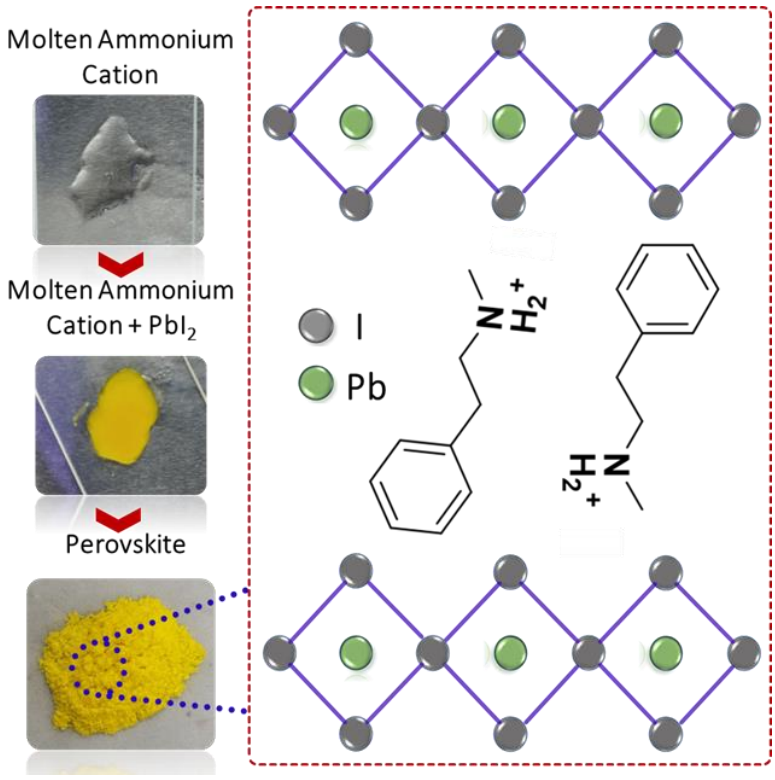

Abstract

In this work, we present a novel solvent-free molten state method for the synthesis of hybrid lead-halide perovskites, specifically targeting the reduction of toxic solvent use typically associated with the conventional methods. Traditional synthesis methods involve hydrohalic acids such as hydroiodic acid (HI) and organic solvents like dimethylformamide (DMF), dimethyl sulfoxide (DMSO), and gamma-butyrolactone (GBL). Our alternative method involves melting an A-site organic ammonium cation precursor, N-methyl phenethyl ammonium iodide [$(C_6H_5\text{-}(CH_2)_2\text{-}NH_2^+(CH_3)\ I^-$] (MPEAI), which melts at ~100 °C. This molten precursor effectively dissolves lead iodide (PbI_2), forming a stable molten mixture. Upon cooling, the $(MPEA)_5Pb_3I_{11}$ perovskite derivative structure crystallizes. We compared the structural and optical properties of $(MPEA)_5Pb_3I_{11}$ synthesized by the molten state and acid precipitation method. In addition, we successfully fabricated films of $(MPEA)_5Pb_3I_{11}$ using this solvent-free approach. Our findings demonstrate that the molten state method offers a solvent free alternative for synthesizing lead-halide perovskites without compromising on structural and optical properties.

3.1 Introduction

Layered hybrid halide perovskite semiconductors are known for their excellent optoelectronic properties.[1-6] Synthesis of hybrid halide perovskite single crystals and polycrystalline powder involve commonly used solvents hydrohalic acid (HX, where X = I, Cl, Br), dimethylformamide (DMF), dimethyl sulfoxide (DMSO), and gamma-butyrolactone (GBL).[7, 8] Thin films of hybrid halide perovskites are typically fabricated using polar solvents like DMF and DMSO through simple techniques such as spin-coating, slot-die coating, and blade-coating, for optoelectronic applications.[9-11] Overall from synthesis (single crystals and polycrystalline powder) to processing (thin films) of hybrid halide perovskites involves the use of toxic solvents. Therefore, reducing or eliminating the use of toxic solvents in the synthesis of perovskites is crucial. Several efforts have been made to reduce the use of toxic solvents, with one promising approach being the melt pressing method for film fabrication.[12-15] Films fabricated via this solvent- and vacuum-free technique have demonstrated reasonably good performance in optoelectronic applications.[12, 14]

Can one think of to reduce the usage of toxic solvent in the synthesis of hybrid halide perovskites in different forms polycrystalline powder, single crystals and films? Yes, it is possible. We have introduced a molten state method for synthesizing lead-halide hybrid perovskites in any desired forms. In this method, one of the precursors is melted, and the molten state acts as a solvent for the other precursors of the hybrid halide perovskite. Hybrid halide perovskites consist of both organic and inorganic sublattices, and the melting temperature of organic components can be adjusted by introducing specific functionalities. Ammonium halide salts, which act as A-site ammonium cation precursors, should form a stable melt that effectively dissolves lead halides (PbX_2), enabling the efficient synthesis of perovskites. We anticipate that the melt of ammonium halide salts behaves similarly to ionic liquids, as they consist of ammonium cations and halide anions. Ionic liquids are well-known as green solvents for chemical reactions and the preparation of functional materials.[16-18]

Using the molten-state approach discussed above, we successfully prepared polycrystalline powder, single crystals and films of $(MPEA)_5Pb_3I_{11}$ perovskite, where MPEA is $[(C_6H_5\text{-}(CH_2)_2\text{-}NH_2^+(CH_3)]$. A detailed structural study using single crystal X-ray diffraction (XRD) and related techniques, conducted over the temperature range of 296-453 K, provided valuable insights into

the non-covalent interactions and the melting phenomenon. For comparison, $(MPEA)_5Pb_3I_{11}$ was also synthesized using the acid precipitation method.

3.2 Experimental Section

3.2.1 Chemicals

Lead iodide (PbI_2, 99.98%, Sigma Aldrich), hydroiodic acid (HI, 57% w/w in water, Sigma Aldrich), hypophosphorous acid (H_3PO_2, 50% w/w in water, Avra chemicals), N-methylphenethylamine (C_6H_5-$(CH_2)_2$-$NH(CH_3)$), 96%, Sigma Aldrich), absolute ethanol.

3.2.2 Synthesis of Single Crystals of $(MPEA)_5Pb_3I_{11}$ [MPEA: $(C_6H_5)–(CH_2)_2–NH_2(CH_3)^+$] by Acid Precipitation Method

1 mmol lead iodide (PbI_2) was dissolved into 3 mL HI and 300 µL H_3PO_2 in a glass beaker by sonication, yielding a transparent yellow colored solution. Then 1.7 mmol N-methyl phenethylamine (C_6H_5-$(CH_2)_2$-$NH(CH_3)$) was added dropwise. This solution then heated to 100 °C for 40 minutes. After that the hot plate temperature was reduced to room temperature, stirring was stopped. After 3 to 4 hours, yellow plate-like crystals of $(MPEA)_5Pb_3I_{11}$ precipitated at the bottom of the beaker. Crystals were washed with diethyl ether and dried in the air.

3.2.3 Synthesis of N-methyl Phenethyl Ammonium Iodide Salt [MPEAI: $(C_6H_5)–(CH_2)_2$-$NH_2(CH_3)^+I^-$)]

5 mmol of N-methyl phenethylamine was added dropwise to 10 ml of ethanol in a beaker while stirring continuously for 20 minutes. The solution was then placed in an ice bath, and 5 mmol of hydroiodic acid (HI) was added dropwise with constant stirring for 1 hour. Afterward, the solution was removed from the ice bath and heated on a hot plate at 70 °C to evaporate the excess ethanol. After 20 minutes, the beaker was taken off the hot plate and left at room temperature. After a few hours, white crystals formed at the bottom of the beaker. These crystals were collected, washed with diethyl ether, and dried at room temperature.

3.2.4 Synthesis of Powder of $(MPEA)_5Pb_3I_{11}$ [MPEA: $(C_6H_5)–(CH_2)_2–NH_2(CH_3)^+$] by Molten State Method

For molten state synthesis, 1.7 mmol (447.3 mg) of N-methyl phenethylammonium iodide (MPEAI) was placed in a glass vial and heated on a hot plate with a magnetic stirrer at 120 °C.

Once the MPEAI melted, 1 mmol of PbI_2 (461.01 mg) was added while stirring continuously. After 5 minutes, the PbI_2 fully dissolved and yellow colour solution formed. The hot plate and stirring were then turned off, and the solution were allowed to cool to room temperature. Upon cooling, a yellow powder was obtained.

3.2.5 Synthesis of Single Crystals of $(MPEA)_5Pb_3I_{11}$ [MPEA: $(C_6H_5)–(CH_2)_2–NH_2(CH_3)^+$] by Molten State Method

For single crystal synthesis using this method, 0.2 mmol of N-methyl phenethylammonium iodide (MPEAI) was heated on a glass slide until it melted. Then, 0.1 mmol of PbI_2 was added and fully dissolved in the molten MPEAI, forming a homogeneous yellow solution. The glass slide was then immediately placed on a cold metal plate at 12 °C to cool the solution, which was subsequently left at room temperature to promote crystallization. Initially, dark red crystals began to form, which eventually transformed into yellow tiny crystals. These crystals, measuring a few micrometers in size, are suitable for single crystal X-ray diffraction analysis.

3.2.6 Films of $(MPEA)_5Pb_3I_{11}$ by Molten State Method

The glass and quartz substrates were initially cleaned with a soap solution, followed by thorough rinsing with distilled water. Subsequently, they were immersed in acetone and 2-propanol for 15 minutes each in an ultrasonic bath sonicator. Afterward, the substrates were dried using nitrogen (N_2) flow and then treated in a UV ozone cleaner for 30 minutes. For the perovskite film preparation, 0.042 mmol (10.8 mg) of MPEAI powder was placed on the glass and quartz substrate and heated on a hot plate from room temperature (~298 K) to 403 K (130 °C), slightly above its melting point (T_M = 390 K). Once the MPEAI melted, 0.025 mmol (11.5 mg) of PbI_2 was added and thoroughly mixed, forming a yellow-colored liquid. This liquid was spread evenly by placing a kapton sheet over it and pressing with a preheated glass substrate. The hot plate temperature was then gradually lowered to room temperature. The kapton sheet and top glass substrate were easily removed without disturbing the perovskite film. The entire film preparation process was conducted in ambient conditions (in air).

3.2.7 Structural Characterization

Single-crystal X-ray diffraction (SCXRD) frames were collected using a Bruker Apex Duo

diffractometer with Mo Kα radiation (λ = 0.71 Å). The single crystals were mounted on a glass-tip sample holder and maintained under a constant flow of nitrogen during the entire experiment. Data integration and numerical absorption corrections were processed using APEX3 software. The structures were solved by the direct method via SHELXS and refined by full-matrix least-squares on F^2 using SHELXL, as implemented in Olex2.4.[19]

Powder X-ray diffraction (PXRD) patterns were recorded on a Bruker D8 Advance diffractometer in Bragg−Brentano geometry and operating with Cu Kα radiation.

Differential scanning calorimetry (DSC) measurement was performed on the polycrystalline sample to determine the phase transition temperatures. A Mettler Toledo DSC823 system was used for this measurement. About 10 mg of a powder sample and a reference were heated from 296 K to 443 K in a nitrogen atmosphere at a rate of 5 °C per minute. A similar measurement was also carried out while cooling the sample from 443 K to 296 K.

3.2.8 Optical properties

Optical diffuse reflectance spectra were collected at room temperature using a Shimadzu UV3600 Plus UV-vis-NIR spectrophotometer, with $BaSO_4$ powder as the 100 % reflectance reference. The diffuse reflectance signal was converted to absorbance using the Kubelka-Munk transformation.[20] Steady-state photoluminescence (PL) measurements were conducted using an FLS 980 spectrometer (Edinburgh Instruments), with a 405 nm (3.06 eV) picosecond pulsed diode laser as the excitation source for recording the PL.

3.3 Results and Discussion

3.3.1 Synthesis of $(MPEA)_5Pb_3I_{11}$ by Molten State Method

From our previous study on meltable 2D hybrid perovskites[14], we anticipate that the melting of any 2D (A_2PbX_4, where A: organic ammonium cation, X: I, Br) perovskite might be possible due to the melting behavior of its A-site organic ammonium cation precursors. However, we encountered challenges in crystallizing the ammonium halide salts utilized in our previous studies. A key observation was that replacing the hydrogen atom of the amine functional group with either one and two methyl groups (-CH_3) significantly reduced the melting temperatures of the

corresponding 2D perovskites. This led us to focus on methyl-substituted amines, ultimately, we have selected N-methyl phenethylamine, a methylated derivative of phenethylamine. To proceed with the synthesis, N-methyl phenethylamine is first converted into its N-methyl phenethyl ammonium iodide salt by following the reaction scheme illustrated in Figure 3.1a. The detailed procedure for this conversion is available in the experimental section. Upon completion of the reaction, a white powder is obtained, as shown in Figure 3.1a.

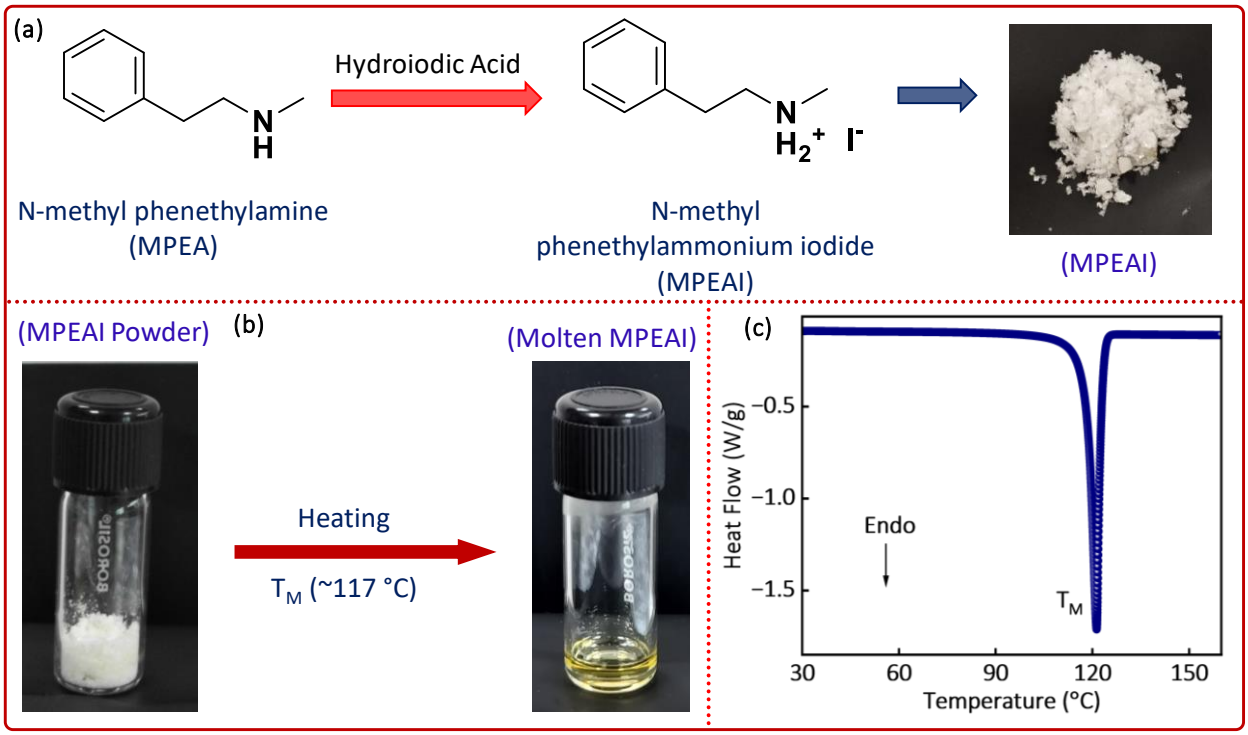

Figure 3.1: (a) Reaction scheme for the synthesis of N-methyl phenethyl ammonium iodide (MPEAI) from N-methyl phenethylamine. Photograph shows the white polycrystalline powder of MPEAI. (b) Polycrystalline MPEAI powder shows melting upon heating to 117 °C. (c) Differential scanning calorimetry (DSC) of MPEAI at a ramp rate of 5 °C/minute. Melting temperature is represented by T_M.

As our synthesis method involve melting of ammonium iodide precursor, the melting of as obtained MPEAI white colour powder is checked on heat plate. Upon heating, the powder converted into a liquid state, as shown in Figure 3.1b. Differential scanning calorimetry (DSC) was then conducted on the MPEAI powder to precisely measure the melting temperature, which was found to be approximately 117 °C, as shown in Figure 3.1c. We hypothesize that the

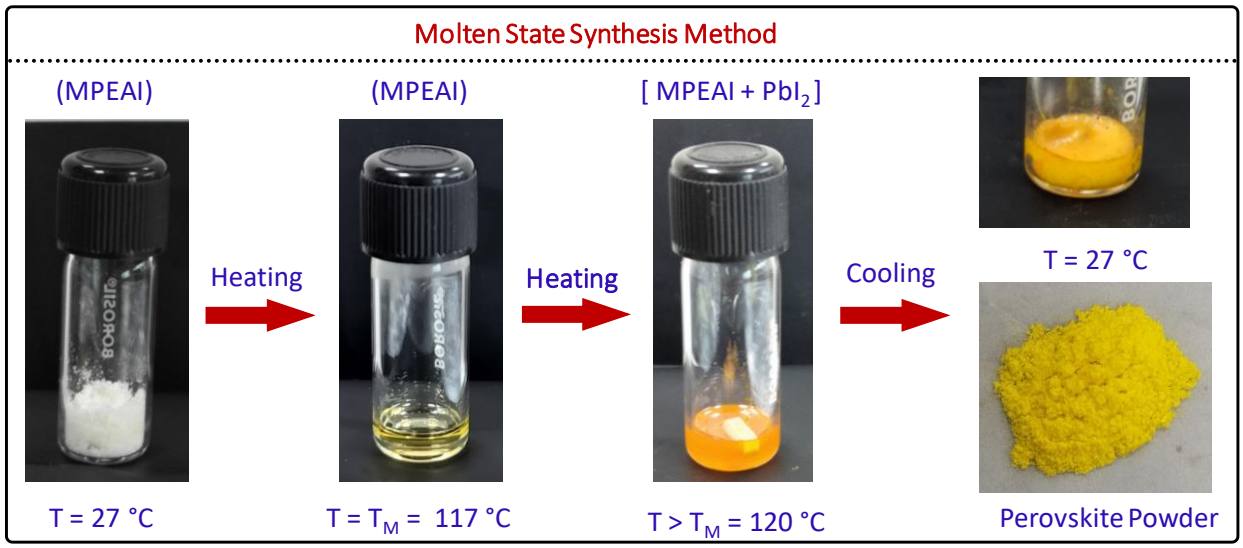

Figure 3.2: Digital photographs of step by step synthesis of hybrid halide perovskites by molten state method, heating of MPEAI powder at melting temperature (T_M) and in molten MPEAI, PbI_2 dissolved under constant stirring and upon cooling yellow colour polycrystalline powder obtained.

ammonium iodide salt in its molten state behaves similarly to an ionic liquid. For any chemical reaction, it is crucial that the precursors are fully dissolved to form a homogenous medium to facilitate interaction and product formation. In this molten state synthesis method, we began by heating 1.7 mmol of MPEAI powder until it melted. After achieving the molten state, 1 mmol of PbI_2 was added to the molten MPEAI under constant stirring to ensure complete dissolution and mixing. This process resulted in a uniform, homogenous mixture of MPEAI and PbI_2. After thorough mixing, the molten solution was allowed to cool to room temperature. As the mixture is cooled, a yellow colored powder product is formed. The final step involved grinding the solidified material to obtain a fine polycrystalline powder of $(MPEA)_5Pb_3I_{11}$. The step-by-step process is illustrated with digital photographs in Figure 3.2.

3.3.2 Acid Precipitations vs. Molten State Synthesis of $(MPEA)_5Pb_3I_{11}$

Hybrid halide perovskites are typically synthesized using the acid precipitation method, where hydrohalic acid (HX, X = I, Br, Cl) acts as a solvent. The quantity of hydrohalic acid used depends on the solubility of the precursors. In the case of $(MPEA)_5Pb_3I_{11}$, the synthesis details via the acid precipitation method are discussed in the experimental section above. Table 3.1 presents the quantities of the precursors and the amount of hydroiodic acid (HI) used. In the acid precipitation

method, approximately 2-3 ml (for 1 mmol of PbI_2) of HI is typically required.

In contrast, the molten state method, a more solvent-efficient alternative, uses one of the precursors, MPEAI, in its molten form, serving as a solvent for the reaction. Notably, the molten state method only requires 0.13 ml of HI, used in the conversion of N-methyl phenethylamine to its iodide form, MPEAI. This significantly reduces the amount of hydroiodic acid needed, offering a notable advantage over the traditional acid precipitation method.

Table 3.1: Comparison of the precursors used in acid precipitation and molten state synthesis method

Perovskite Precursors	Acid Precipitation Method	Molten State Method
Lead Iodide (PbI_2)	1 mmol	1 mmol
Amine / Ammonium Iodide Salt	1.6 mmol	1.6 mmol
Hydroiodic Acid (HI)	2 - 3 ml	0.13 ml

We have successfully synthesized single crystals and polycrystalline powder of $(MPEA)_5Pb_3I_{11}$ using both the acid precipitation and molten state methods. To further compare the crystal structure of the materials obtained by both methods, SCXRD data were recorded for single crystals obtained from each approach. Table 3.2 summarizes the structural refinement parameters, indicating that the single crystals produced via both methods exhibit similar structure. Both crystallize in the monoclinic crystal system with $P2_1/c$ space group and show very similar lattice parameters.

The phase purity of the $(MPEA)_5Pb_3I_{11}$ powder was also verified by powder XRD. Figure 3.3a displays the XRD pattern of the polycrystalline powder obtained by the molten state method, which matched with the simulated pattern generated from the single crystal data at 296 K. This confirms the phase purity of the material synthesized via molten state method. Optical absorption spectra for the powder synthesized by both the acid precipitation and molten state methods is shown in Figure 3.3b. The absorption profiles for both samples are nearly identical, further highlighting that

the molten state method does not compromise the material's optical characteristics. With all such advantages of molten state synthesis, it is difficult to get the large size crystals, which was easy by acid precipitation method.

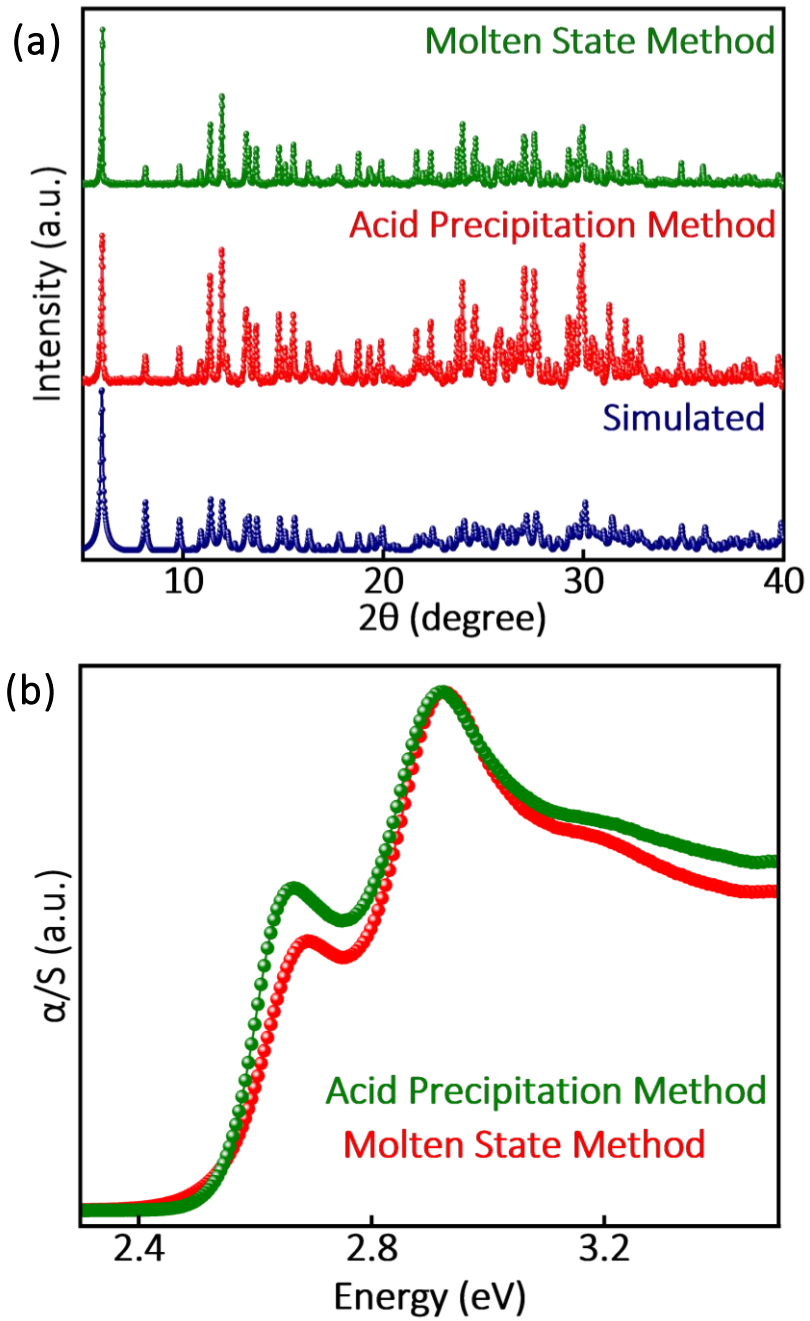

Figure 3.3: (a) Powder XRD patterns of $(MPEA)_5Pb_3I_{11}$ synthesized by acid precipitation and molten state methods. Simulated PXRD pattern matches well with the experimental data. (b) The optical absorption spectra of $(MPEA)_5Pb_3I_{11}$ powder at room temperature.

Table 3.2: Crystallographic data and structural refinement details for $(MPEA)_5Pb_3I_{11}$ crystals obtained by molten state and acid precipitation method at 296 K (near room temperature)

Sample	**$(MPEA)_5Pb_3I_{11}$**	
Synthesis Method	Acid Precipitation	Molten State
Temperature	296 K	296 K
Chemical formula	$C_{45}H_{70}N_4Pb_3I_{11}$	
Formula weight	2682.9 g/mol	
Wavelength	0.71073 Å	
Crystal system	Monoclinic	
Space group	$P2_1/c$	
Unit cell dimensions	a = 9.039(11) Å b = 15.944(2) Å c = 29.873(4) Å β = 96.57(4) °	a = 9.130(16) Å b = 15.940(3) Å c = 30.321(5) Å β = 97.24(4) °
Volume	4277.3(9) $Å^3$	4377(13) $Å^3$
Z	4	4
Density(calculated)	2.658 g/cm^3	2.600 g/cm^3
Absorption coefficient	14.939	12.639
F(000)	1632	3048
Theta range for data collection	2.863° to 24.998°	1.446 ° to 24.996 °
Index ranges	-10<=h<=12 -21<=k<=20 -39<=l<=39	-10<=h<=10 -18<=k<=18 -35<=l<=35
Reflections collected	624274	30844
Independent reflections	7524	7611
Coverage of independent reflections	99.9%	98.9%
Absorption correction	Multi-scan	
Structure solution technique	Direct methods	
Structure solution program	SHELXT 2014/5 (Sheldrick, 2014)	
Refinement method	Full-matrix least-squares on F^2	
Refinement program	SHELXL-2018/3 (Sheldrick, 2018)	
Function minimized	$\Sigma w (F_o^2 - F_c^2)^2$	
Data/restraints/parameters	7524/274/390	7611/273/358
Goodness of fit on F^2	1.059	1.001
Final R indices; I>2σ(I) All data	R1 = 0.0466 wR2 = 0.089 R1 = 0.0814 wR2 = 0.1029	R1 = 0.0757 wR2 = 0.1493 R1 = 0.2012 wR2 = 0.2099
Weighting scheme	$w = 1/[\sigma^2 (Fo^2)+ (0.1000P)^2]$; $P=(Fo^2+2Fc^2)/3$	

3.3.3 Crystal Structure of $(MPEA)_5Pb_3I_{11}$

Single crystals of $(MPEA)_5Pb_3I_{11}$ were successfully synthesized with slight modifications to the molten state synthesis method detailed in the experimental section above. After preparing the crystals, one high-quality single crystal was selected for single crystal X-ray diffraction (XRD) analysis at 296 K. The refinement parameters for this crystal are summarized in Table 3.2.

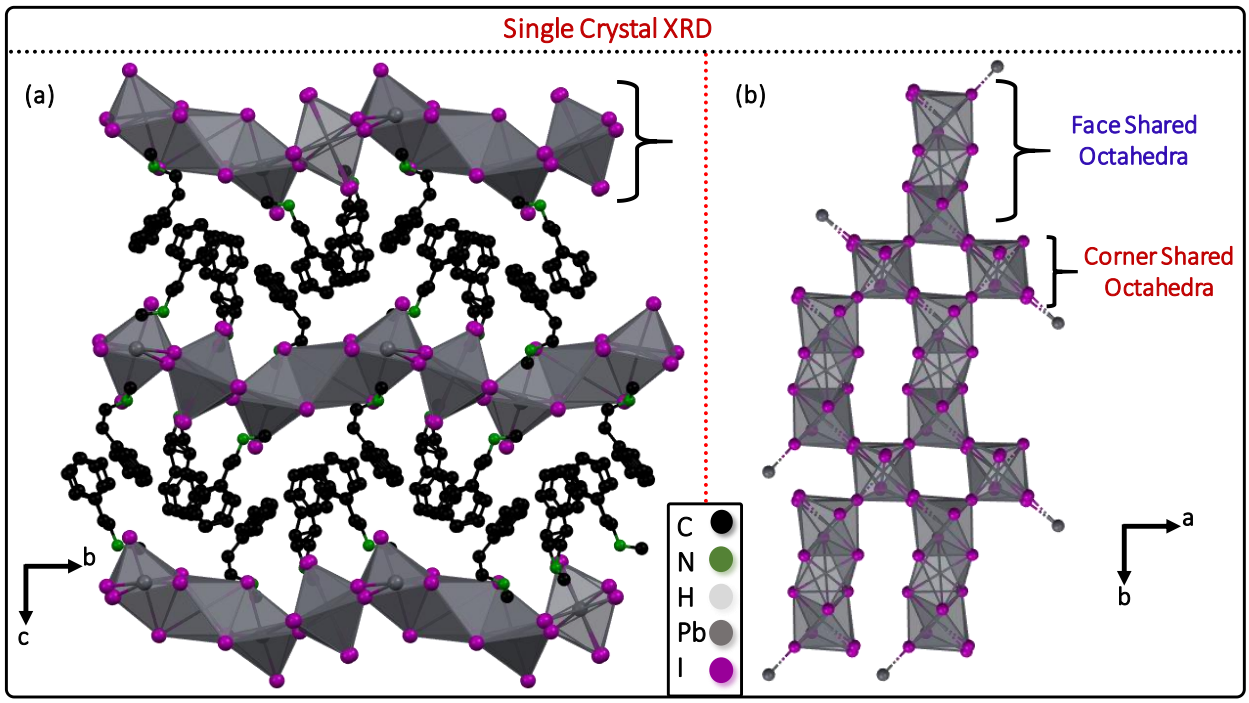

Figure 3.4: Crystal structure of $(MPEA)_5Pb_3I_{11}$ obtained from single crystal XRD at 296 K on the crystals obtained from molten state synthesis method (a) Inorganic layer $[Pb_3I_{11}]^{5-}$ separated by bilayer of organic MPEA cations. (b) The inorganic sublattices contains corner as well as phase shared octahedra connected with each other.

The results indicate that $(MPEA)_5Pb_3I_{11}$ crystallizes in the monoclinic crystal system with $P2_1/c$ space group. Structure of $(MPEA)_5Pb_3I_{11}$ features a layered configuration in which inorganic sheets, consisting of lead-iodide (Pb-I) octahedra, are separated by bilayers of organic N-methyl phenethylammonium (MPEA) cations. As shown in Figure 3.4a, these MPEA cations occupy the spaces between the inorganic $[Pb_3I_{11}]^{5-}$ layers, contributing to the formation of a distinctive layered hybrid perovskite derivative structure. Close examination of the single inorganic sheet in $(MPEA)_5Pb_3I_{11}$, we found that both face-sharing and corner-sharing Pb-I octahedra are present.

Specifically, the inorganic layer contains chains of Pb-I octahedra that share faces and are interconnected by additional Pb-I octahedra via corner-sharing, as shown in Figure 3.4b. This configuration of octahedra is distinct from the more common arrangements seen in traditional 2D perovskites like A_2PbI_4, where only corner-sharing Pb-I octahedra present. Weak hydrogen bonding interactions between the MPEA and Pb-I octahedra present. Similar Pb-I based hybrid halide perovskite derivative structures are reported in literature where both face and corner shared Pb-I octahedral networks are present.[21-23]

3.3.4 Melting and Recrystallization of $(MPEA)_5Pb_3I_{11}$

The polycrystalline powder of $(MPEA)_5Pb_3I_{11}$ synthesized by the molten state method exhibits melting behavior when heated, as confirmed by visual inspection on a hot plate. This observation suggests that if the organic sublattices within the hybrid halide perovskite can melt without decomposition, the entire perovskite structure may also melt. However, this behavior is not universally true for all hybrid halide perovskites. In the case of $(MPEA)_5Pb_3I_{11}$, Figure 3.5a illustrates the melting and subsequent recrystallization of the material, with melting occurring at 141°C during heating and recrystallization at 80°C during cooling cycles.

Interestingly, the melting temperature of $(MPEA)_5Pb_3I_{11}$ is higher than that of the organic sublattice alone, which melts at approximately 117°C see Figure 3.1c. This difference is attributed to the non-covalent interactions, such as hydrogen bonding, between the organic and inorganic sublattices within the hybrid halide perovskite derivative structure. These interactions strengthen the overall lattice, raising the melting point of the perovskite beyond that of the organic ammonium precursor used.

After heating and cooling cycles, the recrystallized $(MPEA)_5Pb_3I_{11}$ powder was analyzed using powder X-ray diffraction (XRD). The PXRD pattern matched well with the simulated patterns from single crystal XRD refinement data at 296 K as shown in Figure 3.5b. This confirms that the perovskite structure remains intact following melting and recrystallization. Additionally, the optical properties were preserved, as the recrystallized powder showed a similar absorption profile to the fresh powder, as seen in Figure 3.5c. Thus, $(MPEA)_5Pb_3I_{11}$ is suitable for film fabrication via the molten state method.

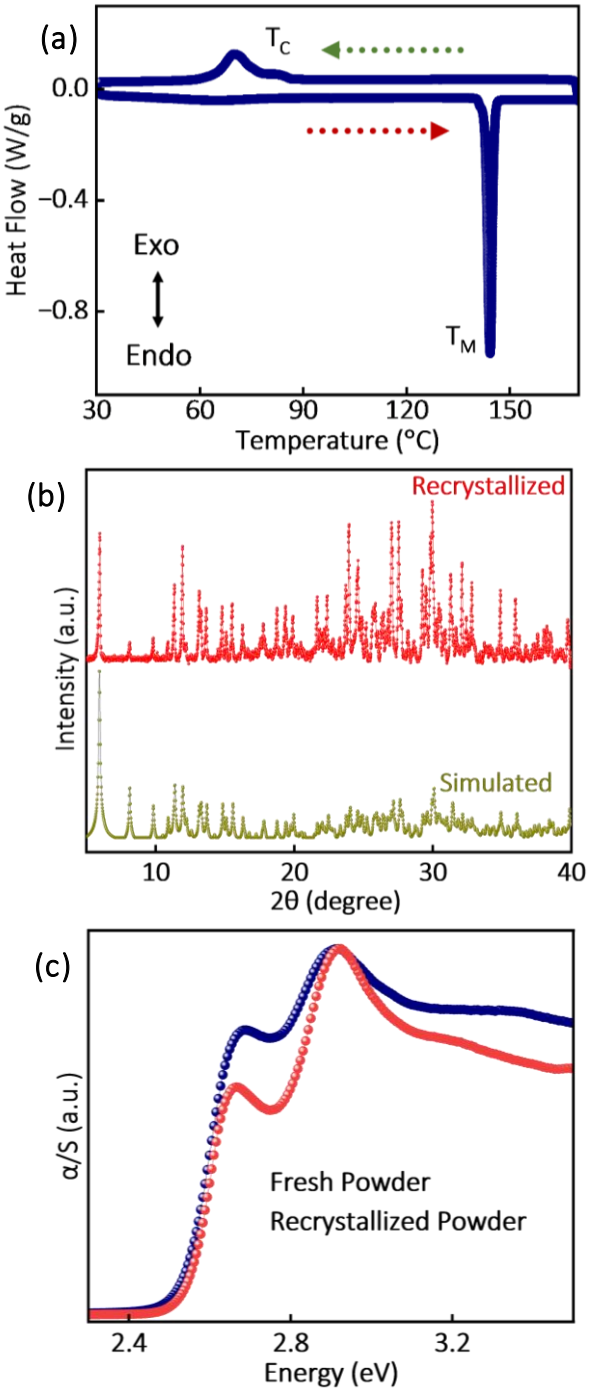

Figure 3.5: (a) Differential scanning calorimetry (DSC) shows the melting and recrystallization of $(MPEA)_5Pb_3I_{11}$ at a rate of 5 °C/min. Melting and recrystallization temperatures are represented by the T_M and T_C, respectively. (b) Powder XRD patterns of the recrystallized $(MPEA)_5Pb_3I_{11}$ matches well with the simulated patterns. (c) The optical absorption spectra of fresh and recrystallized powder were recorded at room temperature.

3.3.5 Films of $(MPEA)_5Pb_3I_{11}$ by Molten State Method

Typical hybrid perovskite films are prepared using either solution-based methods or vacuum deposition techniques.[16, 24] Although these films currently offer the best performance in optoelectronic devices. Solution-based approach involves the use of large amounts of toxic solvents, while the vacuum-based method requires high energy consumption. As an alternative, melt-pressed film deposition provides a solvent-free and vacuum-free route, making it an attractive method. Melt pressed films are performing well as an active layer in optoelectronic devices.[12, 14] For melt pressing pre synthesized (by solvent based methods) perovskite powder required.

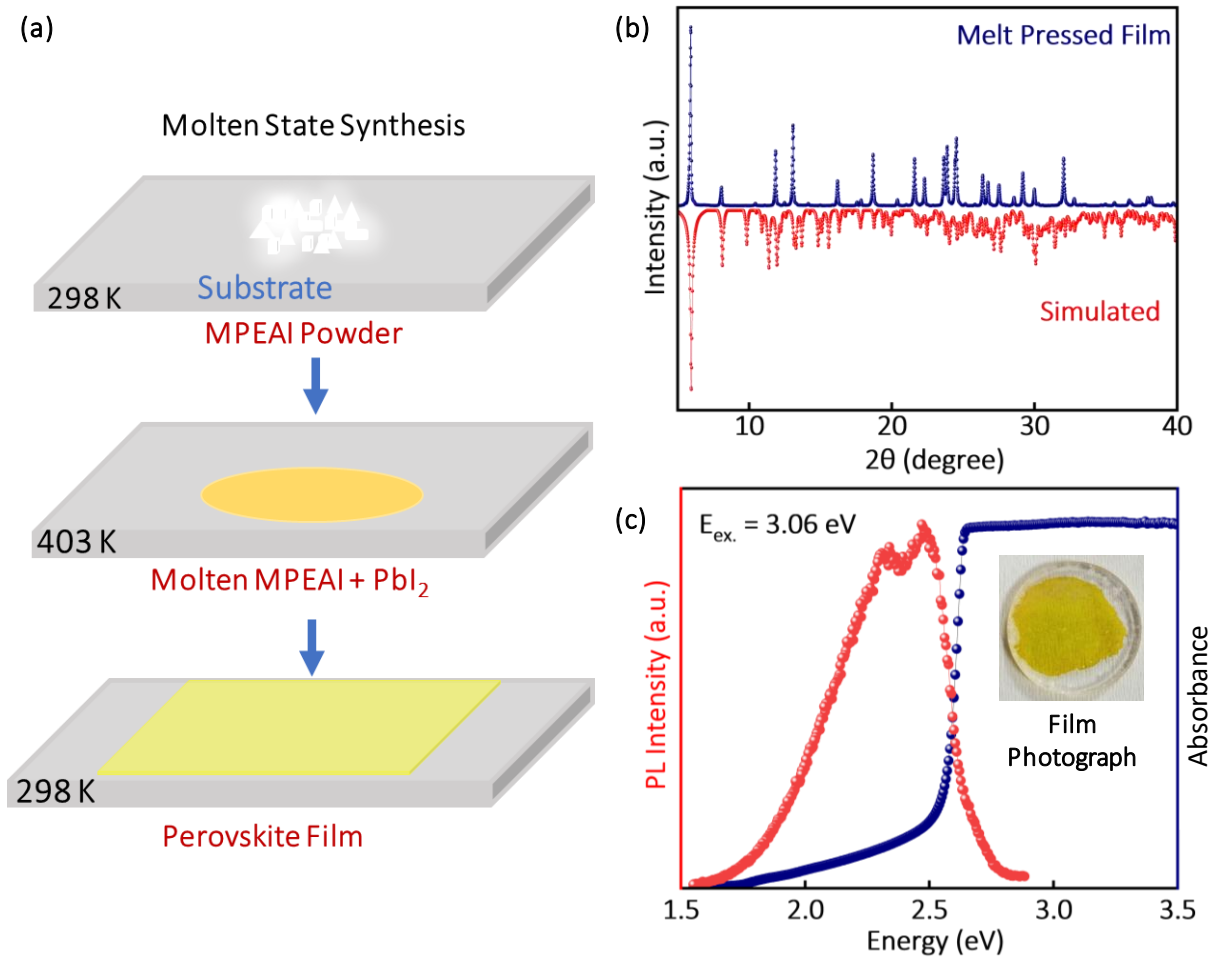

Figure 3.6: (a) Schematic shows the formation of molten state method for film preparation. (b) Powder XRD pattern of the films of $(MPEA)_5Pb_3I_{11}$ by molten state method confirms the formation of the perovskite structure. (c) Film of $(MPEA)_5Pb_3I_{11}$ shows absorbance and photoluminescence. Inset photograph shows film of $(MPEA)_5Pb_3I_{11}$ on quartz substrate.

Here we tried to direct the perovskite film fabrication by using the precursors following the molten state synthesis method as shown by schematic diagram in Figure 3.6a. Details of film synthesis are available in the experimental section above. In this method we took MPEAI powder and PbI_2 is dissolved in molten MPEAI as the molten state of MPEAI is very stable near melting or 5-10 K above the melting temperature. Then this yellow liquid is pressed with the kapton sheet and temperature of hot plate reduced to the room temperature. After recrystallization kapton sheet is removed easily. Digital photograph of the film is shown in the inset of Figure 3.6c. Powder XRD patterns on the films synthesized by molten state method confirms the crystallinity as shown by Figure 3.6b. Films of $(MPEA)_5Pb_3I_{11}$ shows absorbance and photoluminescence see Figure 3.6c.

3.4 Conclusions

We have successfully synthesized the $(MPEA)_5Pb_3I_{11}$ perovskite derivative structures using a novel molten state method. This approach relies on melting the ammonium iodide salt before decomposition, it behaves like a solvent to dissolve PbI_2. Both single crystals and polycrystalline powder were produced using this method. To compare structural and optical properties, we also synthesized the same perovskite derivative via the conventional acid precipitation method. The findings indicate that both methods yield similar structural and optical characteristics. Importantly, the molten state method drastically reduces the amount of hydroiodic acid (HI) required compared to the acid precipitation process, making it a more environmentally friendly alternative. This method has broad applicability, as it can be extended to other meltable ammonium halide salts, facilitating the synthesis of a wide variety of hybrid halide perovskites.

3.5 References

1. Saparov, B.; Mitzi, D. B. Organic–inorganic perovskites: structural versatility for functional materials design. *Chem. Rev.* **2016,** *116*, 4558-4596.

2. Manser, J. S.; Christians, J. A.; Kamat, P. V. Intriguing Optoelectronic Properties of Metal Halide Perovskites. *Chem. Rev.* **2016,** *116*, 12956-13008.

3. Mao, L.; Stoumpos, C. C.; Kanatzidis, M. G. Two-Dimensional Hybrid Halide Perovskites: Principles and Promises. *J. Am. Chem. Soc.* **2018,** *141*, 1171-1190.

4. Chakraborty, R.; Rajput, P. K.; Anilkumar, G. M.; Maqbool, S.; Das, R.; Rahman, A.;

Mandal, P.; Nag, A. Rational Design of Non-Centrosymmetric Hybrid Halide Perovskites. *J. Am. Chem. Soc.* **2023,** *145*, 1378-1388.

5. Smith, M. D.; Karunadasa, H. I. White-Light Emission from Layered Halide Perovskites. *Acc. Chem. Res.* **2018,** *51*, 619-627.

6. Dey, A.; Ye, J.; De, A.; Debroye, E.; Ha, S. K.; Bladt, E.; Kshirsagar, A. S.; Wang, Z.; Yin, J.; Wang, Y.; Quan, L. N.; Yan, F.; Gao, M.; Li, X.; Shamsi, J.; Debnath, T.; Cao, M.; Scheel, M. A.; Kumar, S.; Steele, J. A.; Gerhard, M.; Chouhan, L.; Xu, K.; Wu, X. G.; Li, Y.; Zhang, Y.; Dutta, A.; Han, C.; Vincon, I.; Rogach, A. L.; Nag, A.; Samanta, A.; Korgel, B. A.; Shih, C. J.; Gamelin, D. R.; Son, D. H.; Zeng, H.; Zhong, H.; Sun, H.; Demir, H. V.; Scheblykin, I. G.; Mora-Seró, I.; Stolarczyk, J. K.; Zhang, J. Z.; Feldmann, J.; Hofkens, J.; Luther, J. M.; Pérez-Prieto, J.; Li, L.; Manna, L.; Bodnarchuk, M. I.; Kovalenko, M. V.; Roeffaers, M. B. J.; Pradhan, N.; Mohammed, O. F.; Bakr, O. M.; Yang, P.; Müller-Buschbaum, P.; Kamat, P. V.; Bao, Q.; Zhang, Q.; Krahne, R.; Galian, R. E.; Stranks, S. D.; Bals, S.; Biju, V.; Tisdale, W. A.; Yan, Y.; Hoye, R. L. Z.; Polavarapu, L. State of the Art and Prospects for Halide Perovskite Nanocrystals. *ACS Nano* **2021,** *15*, 10775-10981.

7. Stoumpos, C. C.; Cao, D. H.; Clark, D. J.; Young, J.; Rondinelli, J. M.; Jang, J. I.; Hupp, J. T.; Kanatzidis, M. G. Ruddlesden–Popper Hybrid Lead Iodide Perovskite 2D Homologous Semiconductors. *Chem. Mater.* **2016,** *28*, 2852-2867.

8. Liu, Y.; Zhang, Y.; Yang, Z.; Ye, H.; Feng, J.; Xu, Z.; Zhang, X.; Munir, R.; Liu, J.; Zuo, P.; Li, Q.; Hu, M.; Meng, L.; Wang, K.; Smilgies, D.-M.; Zhao, G.; Xu, H.; Yang, Z.; Amassian, A.; Li, J.; Zhao, K.; Liu, S., Multi-inch single-crystalline perovskite membrane for high-detectivity flexible photosensors. *Nat. Commun.* **2018,** *9*, 5302.

9. Zhang, Z.; Kim, W.; Ko, M. J.; Li, Y., Perovskite single-crystal thin films: preparation, surface engineering, and application. *Nano Converg* **2023,** *10*, 23.

10. Soto-Montero, T.; Soltanpoor, W.; Morales-Masis, M., Pressing challenges of halide perovskite thin film growth. *APL Mater.* **2020,** *8*, 110903.

11. Petrov, A. A.; Ordinartsev, A. A.; Fateev, S. A.; Goodilin, E. A.; Tarasov, A. B. Solubility of Hybrid Halide Perovskites in DMF and DMSO. *Molecules* **2021,** *26*, 7541.

12. Mitzi, D. B.; Dimitrakopoulos, C. D.; Rosner, J.; Medeiros, D. R.; Xu, Z. T.; Noyan, C. Hybrid field-effect transistor based on a low-temperature melt-processed channel layer. *Adv.*

Mater. **2002,** *14*, 1772-1776.

13. Li, T.; Dunlap-Shohl, W. A.; Han, Q.; Mitzi, D. B., Melt Processing of Hybrid Organic–Inorganic Lead Iodide Layered Perovskites. *Chem. Mater.* **2017,** *29*, 6200-6204.

14. Rajput, P. K.; Salunkhe, P.; Sarma, M.; Basu, M.; Gopal, A.; Joshi, A.; Shingote, A. S.; Saha, S.; Rahman, A.; Nag, A. Entropy-Driven Reversible Melting and Recrystallization of Layered Hybrid Perovskites. *Small* **2024,** 2406735.

15. Crace, E. J.; Singh, A.; Haley, S.; Claes, B.; Mitzi, D. B. Meltable Hybrid Antimony and Bismuth Iodide One-Dimensional Perovskites. *Inorg. Chem.* **2023,** *62*, 16161-16169.

16. Li, H.; Zhou, J.; Tan, L.; Li, M.; Jiang, C.; Wang, S.; Zhao, X.; Liu, Y.; Zhang, Y.; Ye, Y. Sequential vacuum-evaporated perovskite solar cells with more than 24% efficiency. *Sci. Adv.* **2022,** *8*, eabo7422.

17. Hallett, J. P.; Welton, T., Room-Temperature Ionic Liquids: Solvents for Synthesis and Catalysis. 2. *Chem. Rev.* **2011,** *111*, 3508-3576.

18. Kubisa, P., Application of ionic liquids as solvents for polymerization processes. *Progress in Polym. Sci.* **2004,** *29*, 3-12.

19. Dolomanov, O. V.; Bourhis, L. J.; Gildea, R. J.; Howard, J. A.; Puschmann, H., OLEX2: a complete structure solution, refinement and analysis program. *J. appl. Crystallogr.* **2009,** *42*, 339-341.

20. Eickhoff, T.; Grosse, P.; Theiss, W., Diffuse reflectance spectroscopy of powders. *Vib. Spectrosc.* **1990,** *1*, 229-233.

21. Kamminga, M. E.; Fang, H.-H.; Filip, M. R.; Giustino, F.; Baas, J.; Blake, G. R.; Loi, M. A.; Palstra, T. T., Confinement effects in low-dimensional lead iodide perovskite hybrids. *Chem. Mater.* **2016,** *28*, 4554-4562.

22. Wang, W.; Liu, C. D.; Fan, C. C.; Zhang, W., Reversible Glass-Crystal Transition in a New Type of 2D Metal Halide Perovskites. *Adv. Funct. Mater.* **2024**, 2407143.

23. Smith, M. D.; Watson, B. L.; Dauskardt, R. H.; Karunadasa, H. I., Broadband emission with a massive stokes shift from sulfonium Pb–Br hybrids. *Chem. Mater.* **2017,** *29*, 7083-7087.

24. Dunlap-Shohl, W. A.; Zhou, Y.; Padture, N. P.; Mitzi, D. B. Synthetic Approaches for Halide Perovskite Thin Films. *Chem. Rev.* **2019,** *119*, 3193-3295.

Chapter 4

Rational Design of Non-Centrosymmetric 1D Bi-I Perovskite Derivatives

Graphical Abstract:

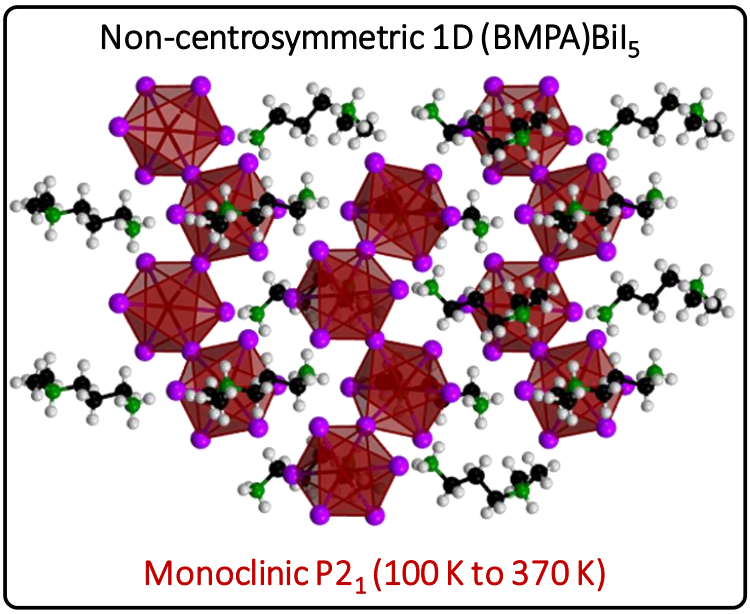

The work of this chapter has been published in the following article:

Chakraborty, R.; **Rajput, P.K.;** Anilkumar, G.M.; Maqbool, S.; Das, R.; Rahman, A.; Mandal, P.; Nag, A. Rational Design of Non-centrosymmetric Hybrid Halide Perovskites. *J. Am. Chem. Soc.*, **2023**, *145*, 1378-1388.

Abstract

Structural non-centrosymmetry in semiconducting organic–inorganic hybrid halide perovskites can introduce functionalities like anomalous photovoltaics and nonlinear optical properties. Here we introduce a design principle to make Bi-I one-dimensional hybrid perovskites with polar non-centrosymmetric space groups. The design principle relies on creating dissimilar hydrogen bonding non-covalent interactions at the organic–inorganic interface. For example, in organic diammonium cations like NH_3^+–$(CH_2)_3$–$NH(CH_3)_2^+$ (BMPA), at one end $-NH_3^+$ is substituted by $-NH(CH_3)_2^+$. These substitutions of two −H atoms by two $-CH_3$ groups reduce the rotational symmetry of BMPA at one end, compared to an unsubstituted cation, NH_3^+–$(CH_2)_3$–NH_3^+. Consequently, the dissimilar hydrogen–iodine interactions at the organic–inorganic interfaces of (BMPA)BiI_5 1D perovskite break the local inversion symmetries of Bi–I octahedra. Owing to this non-centrosymmetry, (BMPA)BiI_5 displays visible to infrared tunable nonlinear optical properties showing second and third harmonic generation. Also, the single crystal shows signature of anomalous photovoltaic effect. Interestingly, (BMPA)BiI_5 also shows the chiral response without any chiral organic counterpart.

4.1 Introduction

Two-dimensional (2D) halide perovskites have attracted significant research interest due to their enhanced stability and greater structural diversity compared to their three-dimensional (3D) counterparts.[1-3] They have been extensively studied for various optoelectronic applications, including solar cells[4-6], light-emitting diodes (LEDs)[7], and detectors.[8] In efforts to expand this material family and reduce the toxicity associated with lead (Pb), Pb^{2+} was replaced with isoelectronic Bi^{3+}.[9-11] However, the trivalent nature of Bi^{3+} often results in the formation of lower-dimensional perovskite derivatives compared to the Pb^{2+} based 2D hybrid perovskites. This shift in dimensionality impacts the structure and properties of the resulting bismuth-based hybrid materials. In addition, can these materials show ferroelectricity, anomalous photovoltaics, and nonlinear optical properties like second harmonic generation (SHG)? The answer to this question is yes, provided Bi-halide hybrid perovskites crystallize in a non-centrosymmetric polar space group at room temperature.[12-15] This chapter deals with the rational design of such non-centrosymmetric hybrid perovskite semiconductors.

We selected $ABiX_5$ (X = I) to achieve lower band gaps compared to other halides (X = Cl or Br), enhancing the material's potential for optoelectronic applications. For the A-site cations, using chiral ammonium molecules can induce non-centrosymmetry in hybrid Bi-I perovskites, promoting ferroelectricity and SHG.[16, 17] However, enantiomerically pure chiral ammonium cations are often rare or expensive due to the complexities involved in asymmetric synthesis and chiral separation techniques. As an alternative, selecting achiral cations that can still induce non-centrosymmetry and polarity in the hybrid perovskite structure becomes a crucial challenge in the material design process. By focusing on achiral cations capable of introducing non-centrosymmetry in 1D Bi-I hybrid perovskites, we can achieve materials with tunable band gaps, self-powered photodetection, and enhanced nonlinear optical properties like SHG, without the limitations of relying on expensive or rare chiral cations.

If $NH_3^+–(CH_2)_n–NH_3^+$ is the A-site cation, then it can form three non-covalent (N–H···I) hydrogen bonds with the $(BiI_5)^{2–}$ sublattice. If the strengths of three H···I interactions are similar, then the C–N bond can have a three-fold rotational symmetry, making the non-covalent H···I interactions

and the overall structure more symmetric. Similar situation at another end of cation. To achieve the non-centrosymmetric structure, we hypothesize reducing the rotational symmetry first at one end of the A-site cations, for example, NH_3^+–$(CH_2)_3$–$NH(CH_3)_2^+$ (BMPA), at one end $-NH_3^+$ is substituted by $-NH(CH_3)_2^+$ which in turn is expected to yield structural asymmetry through the non-covalent interactions. This is expected to reduce the tilting of BiI_6 octahedra, implying a larger Bi–I–Bi bond angle, reduced band gap, and increased carrier mobility.[18] We note that a similar strategy to restrict molecular rotations by hetero-atom substitution to achieve structural non-centrosymmetry has been discussed earlier in the literature on molecular ferroelectrics and is often termed as "quasi-spherical theory".[19]

By employing the hypothesis discussed above, we have prepared two one-dimensional (1D) Bi–I based hybrid perovskites. A detailed structural study using single crystal X-ray diffraction (XRD) and related techniques in the temperature range of 100-450 K provided insights into the nature of non-covalent interactions and structural phase transitions. The structural asymmetry leads to intense SHG signals that depend strongly on the polarization of the incident light. Additionally, $(BMPA)BiI_5$ single crystals show a significant, second (SHG) and third harmonic generation (THG) response from the same excitation pulses. Thus, a spectrally resolved non-linear behavior is observed over the entire visible region. Interestingly, the non-centrosymmetric polar structure leads to an anomalous photovoltaic effect in our single crystals, which dissociates charge carriers without requiring a bias voltage or a p–n junction. Consequently, self-powered photo-detection is also observed.

4.2 Experimental Section

4.2.1 Chemicals

Bismuth oxide (Sigma Aldrich, Bi_2O_3, 99.8%), hydroiodic acid (Sigma Aldrich, HI, 57% w/w in water), hypophosphorous acid (Avra chemicals, H_3PO_2, 50% w/w in water), N-methyl 1,3-diamino propane (Sigma Aldrich, $(CH_3)NH$-$(CH_2)_3$-NH_2, 98%), 3-(dimethylamino)-1-propylamine(Sigma Aldrich, $(CH_3)_2N$-$(CH_2)_3$-NH_2, 99%), N,N-dimethylformamide (Sigma Aldrich, DMF, 99.8%), BBO crystal (EKSMA optics), and butylammonium lead iodide (synthesized following reference[20]).

4.2.2 Synthesis of 1D Bi-I Perovskite Single Crystals

The single crystals of $(BMPA)BiI_5$ and $(NMPA)BiI_5$ (NMPA: H_3N^+-$(CH_2)_3$-$N(CH_3)H_2^+$) were synthesized using acid precipitation method as followed by the Pb-I based hybrid perovskites. 2 mmol of Bismuth (III) oxide (Bi_2O_3) was dissolved in a mixture 20 mL HI and 4 mL H_3PO_2 in a glass beaker at room temperature with stirring, resulting a clear dark-red solution. In the same solution, 2 mmol of the organic amine H_2N-$(CH_2)_3$-$N(CH_3)_2$ or H_2N-$(CH_2)_3$-$NH(CH_3)$ was added dropwise. The mixture was heated and stirred at 110 ^oC for 30 minutes using an oil bath placed on a heater and magnetic stirrer. After 30 minutes, the heating and stirring were stopped, and the dark-red colour solution was allowed to cool to room temperature with a cooling rate of 3 ^oC per hour to get the millimeter-sized crystals. During this process, dark brown crystals of $(BMPA)BiI_5$ or $(NMPA)BiI_5$ precipitated at the bottom of the beaker. The crystals were filtered off and washed with diethyl ether.

4.2.3 Preparation of Thin Films of $(BMPA)BiI_5$

Circular quartz substrates were washed with soap solution then acetone in a sonicator for 20 min, followed by the same treatment with isopropanol. The substrates were then dried with air and treated with oxygen plasma for 10 min using a plasma cleaner. Then 20 mg $(BMPA)BiI_5$ crystals were dissolved in DMF at room temperature under constant stirring. The solution was then spin-coated onto the quartz substrates using a spin rate of 3500 rpm for 30 s. Finally, the films were annealed at 110 °C for 10 minutes on a hotplate to induce crystallization.

4.2.4 Structural Characterization

Frames of single crystal X-ray diffraction **(**SCXRD) were collected in a Bruker Apex Duo diffractometer using Mo Kα radiation (λ = 0.71 Å). The single crystals were mounted on the glass-tip sample holder. They were kept under a constant flow of nitrogen throughout the experiment. The integrations of the collected data and numerical absorption corrections were done using APEX3 software. The structures were solved by the direct method using SHELXS and refined by full-matrix least-squares on F^2 using the SHELXL, as implemented in Olex2.[21] Symmetry analyses of all structures were also performed using PLATON's ADDSYM tool on both the inorganic framework and the hybrid structure. The CIF files, containing the atomic positions, and the

anisotropic displacement parameters, obtained from the refinement, are available via CCDC with accession codes 2217820 – 2217823.

Powder X-ray diffraction (PXRD) patterns were recorded on a Bruker D8 Advance diffractometer in Bragg-Brentano geometry and operating with Cu Kα radiation. Field emission scanning electron microscopy (FESEM) images are collected using the Zeiss Ultra Plus FESEM instrument. Differential scanning calorimetry (DSC) measurement was performed on the polycrystalline sample to determine the phase transition temperatures. A Mettler Toledo DSC823 system was used for this measurement. About 10 mg of a powder sample and a reference were heated from 133 K to 458 K in a nitrogen atmosphere at a rate of 3 °C per minute. A similar measurement was also carried out while cooling the sample from 458 K to 133 K. The thermal stability of sample was checked by thermogravimetric analysis (TGA) under N_2 atmosphere using Mettler Toledo System.

4.2.5 Linear Optical Absorption and Circular Dichroism

Optical diffused reflectance spectra were collected at room temperature using an integrating sphere in a Shimadzu UV3600 plus UV−vis−NIR spectrophotometer. $BaSO_4$ powder was used for these measurements to reference 100% reflectance. The diffused reflectance signal is converted to absorbance using the Kubelka−Munk function.[21] Absorbance of thin films were recorded in transmission mode using a Cary 300 UV–vis spectrometer.

Circular dichroism (CD) measurements were carried out using a Jasco J-1500 spectropolarimeter at a scan speed of 50 nm/minute.

4.3. Results and Discussion

4.3.1 Crystal Structure and Non-Centrosymmetry

The reaction scheme to synthesize (BMPA)BiI_5 and (NMPA)BiI_5 is shown in Figure 4.1a. Dark brown colored crystals are formed. Figure 4.1b and 4.1c shows the digital photographs of (BMPA)BiI_5 and (NMPA)BiI_5 crystals respectively. The crystals of (BMPA)BiI_5 are then used for SCXRD measurements at 100 K and 296 K (near room temperature) (Table 4.1 and 4.2). (BMPA)BiI_5 crystallizes in a 1D hybrid perovskite derivative structure with a corner-shared Bi–I octahedral network as shown in Figure 4.2a.

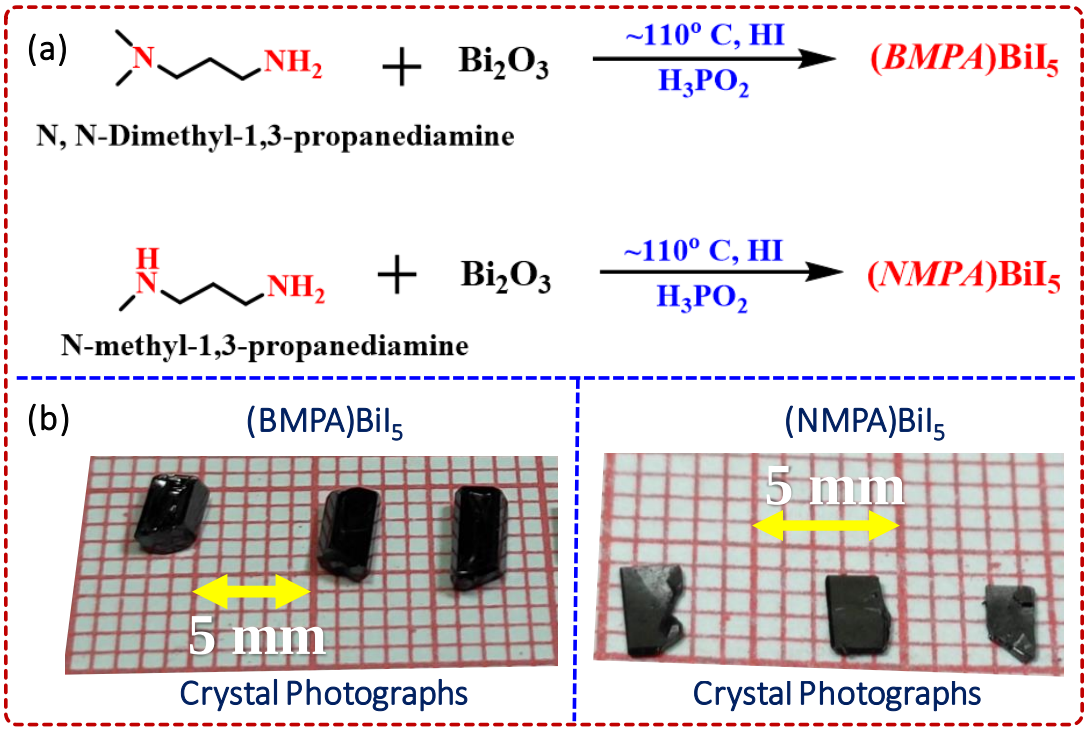

Figure 4.1: (a) Reaction scheme for the synthesis of (BMPA)BiI_5 and (NMPA)BiI_5. Digital photographs of (b) (BMPA)BiI_5 and (c) (NMPA)BiI_5 crystals.

The obtained space group is monoclinic ($P2_1$) non-centrosymmetric, chiral and polar at both measurement temperatures. Figure 4.2b shows the non-covalent H···I interactions present in (BMPA)BiI_5. Since there are two ammonium groups present at the tails of each BMPA cation, they can interact with two separate Bi–I chains as shown in Figure 4.2b. The dimethyl-substituted ammonium head forms only one hydrogen bond with the iodine in the Bi-I octahedra, whereas the unsubstituted ammonium head forms two hydrogen bonds, as shown in Figure 4.2b. The orientation of the ammonium groups of the cations between the two 1D chains of Bi-I octahedra is such that the bridging bi-coordinated iodine atoms remain undisturbed, resulting in minimal in-plane distortion and large Bi–I–Bi angles (see Table 4.3). This suggests a smaller band gap for (BMPA)BiI_5. Indeed, (BMPA)BiI_5 shows an absorption edge at 1.94 eV (639 nm), as shown in Figure 4.7c. This is one of the smallest reported band gaps for hybrid Bi–I based perovskites. Absence of the inversion symmetry also observed in one Bi-I octahedra as shown in Figure 4.2c.

A similar A-site cation NMPA, was earlier found to result in non-centrosymmetric 1D (NMPA)BiI_5 with $Pna2_1$ space group at 200 K.[15] Though the absolute configuration of this

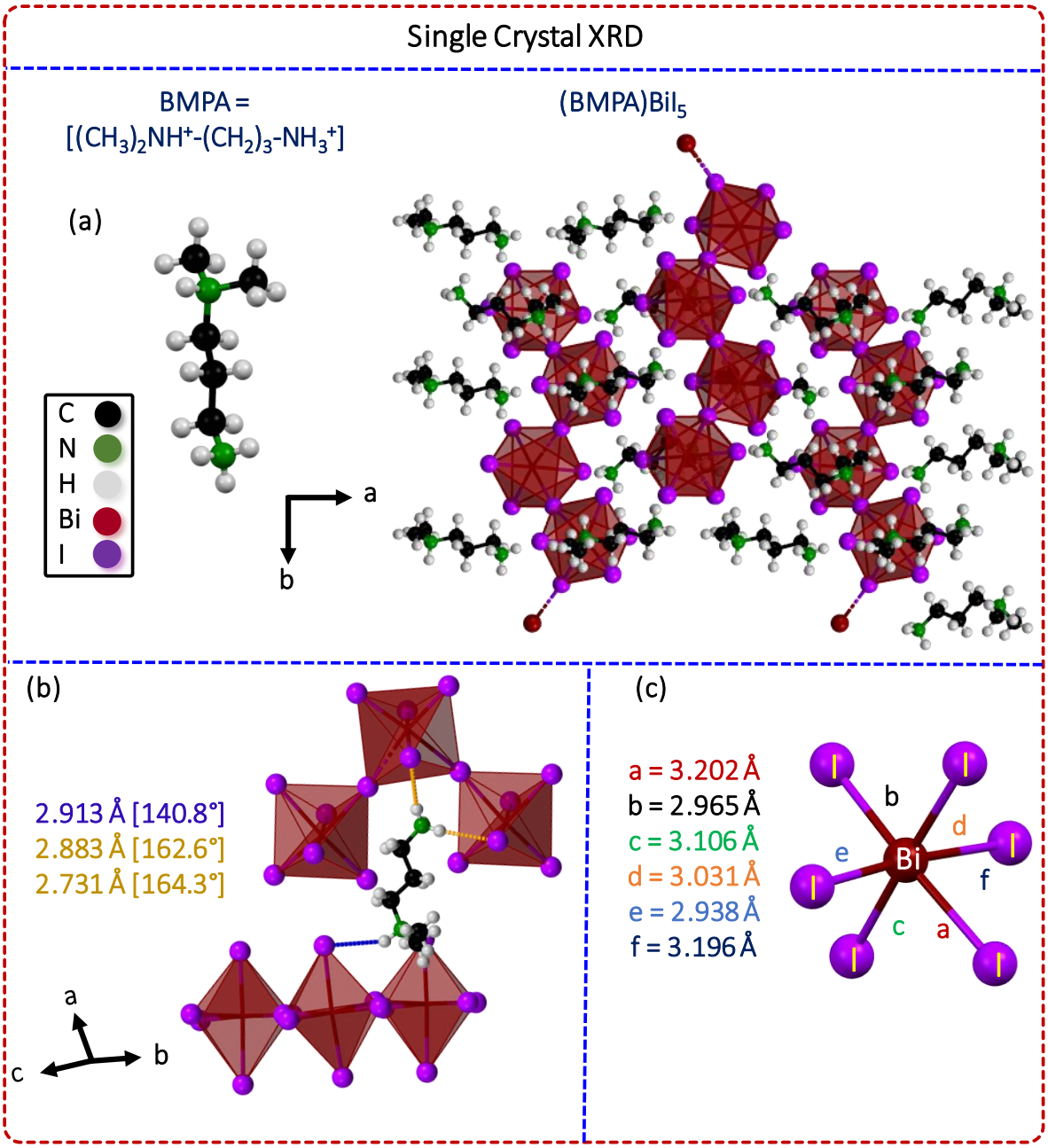

Figure 4.2: (a) Crystal structure of $(BMPA)BiI_5$ at 100 K, obtained using SCXRD. (b) Non-covalent H···I interactions in the $(BMPA)BiI_5$ structure between ammonium groups and mono-coordinated iodines are shown as blue and orange dashed lines. (c) $(BiI)_6$ octahedra shows the absence of the local inversion center.

structure remains a bit ambiguous, the structural analysis at 100 K (Table 4.2 and Figure 4.3) suggests the same non-centrosymmetric structure. Since we were unable to obtain absolute crystal structure information for $(NMPA)BiI_5$, we did not proceed with a detailed study of $(NMPA)BiI_5$.

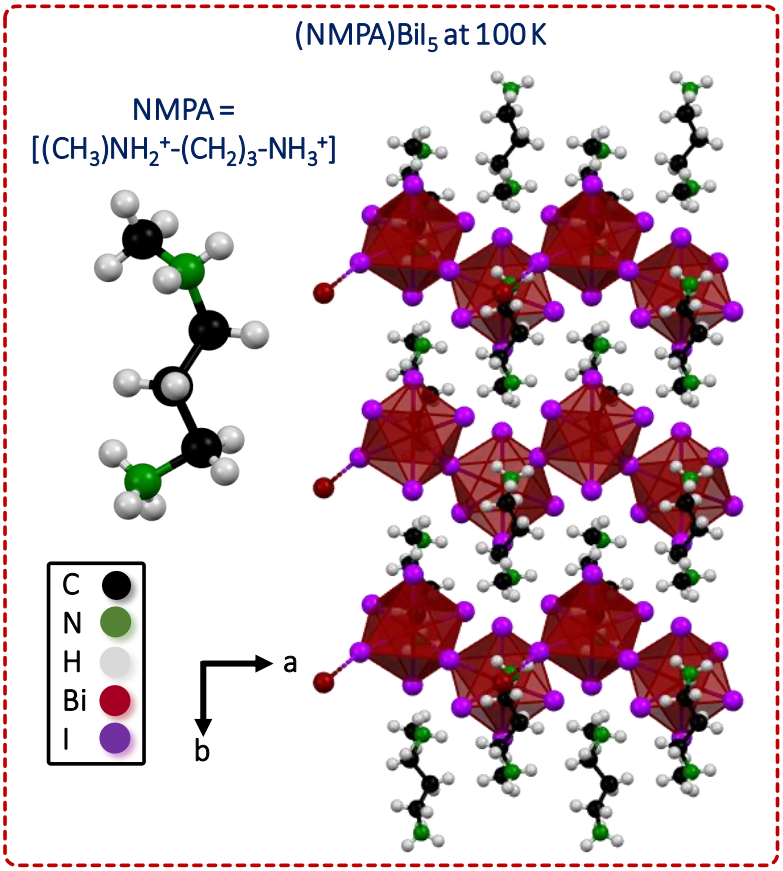

Figure 4.3: Crystal structure of (NMPA)BiI_5 at 100 K, obtained using SCXRD.

As obtained crystals of (BMPA)BiI_5 were grounded and the powder XRD patterns were recorded on the powder samples, the experimentally obtained PXRD pattern matches well with the corresponding simulated pattern see Figure 4.4a. Even after 180 days, the powder pattern matches well with the simulated pattern, demonstrating the stability of (BMPA)BiI_5 under ambient conditions (see Figure 4.4a). Thermal stability of (BMPA)BiI_5 confirms with the help of thermogravimetry analysis (TGA) measurement as negligible weight loss up to ~570 K (~297 °C). Such hybrid halide perovskites are known for their structural phase transition with temperature as shown in Figure 4.4b. Differential scanning calorimetry (DSC) performed on the powder sample to confirm the existence of the non-centrosymmetric structure in the temperature range of 140-500 K (see Figure 4.4c). A single reversible transition at 374 K during heating and 372 K during cooling cycle observed (see Figure 4.4c). This reversible phase transition is corresponding to solid-to-solid structural phase transition.

Table 4.1 Structure refinement data of (BMPA)BiI_5 at 100 K, 296 K (near room temperature), and 394 K (above structural phase transition).

CCDC deposition id	2217820	2217821	2217822
Chemical formula	$C_5H_{16}BiI_5N_2$	$C_5H_{16}BiI_5N_2$	$C_5H_{16}BiI_5N_2$
Formula weight	947.68 g/mol	947.68 g/mol	947.68 g/mol
Temperature	100(2) K	296(2) K	394(2) K
Wavelength	0.71073 Å	0.71073 Å	0.71073 Å
Crystal system	monoclinic	monoclinic	orthorhombic
Space group	$P2_1$	$P2_1$	*Pmcn*
Unit cell dimensions	a = 8.478(2) Å b = 16.701(4) Å c = 12.570(3) Å β = 92.665(7)°	a = 8.513(4) Å b = 16.766(8) Å c = 12.603(6) Å β = 92.402(14)°	a = 8.6134(16) Å b = 12.639(2) Å c = 16.896(3) Å
Volume	1778.0(7) $Å^3$	1797.2(15) $Å^3$	1839.4(5) $Å^3$
Z	4	4	4
Density (calculated)	3.540 g/cm^3	3.502 g/cm^3	3.422 g/cm^3
Absorption coefficient	18.573 mm^{-1}	18.374 mm^{-1}	17.953 mm^{-}
F (000)	1632	1632	1632
Theta range (For data collection)	2.03 to 28.66°	2.02 to 25.00°	2.01 to 27.62°
Index ranges	-11<=h<=10 -22<=k<=22 -16<=l<=16	-10<=h<=10 -19<=k<=18 -14<=l<=14	-11<=h<=11 -16<=k<=16 -21<=l<=21
Reflection collected	16420	29598	24009
Independent reflections	8424 [R_{int} = 0.0558, R_{sigma} = 0.0906]	5883 [R_{int} = 0.0755, R_{sigma} = 0.0622]	2269 [R_{int} = 0.1159, R_{sigma} = 0.0682]
Absorption correction	Numerical Mu Calculated	Multi-Scan	Multi-Scan
Structure solution technique	direct methods	direct methods	direct methods
Data / restraints / parameters	8424 / 4 / 243	5883 / 10 / 243	2269/ 9 /80
Goodness-of-fit on F^2	0.883	1.080	1.123
Final R indices; I>2σ(I)	R1 = 0.0363, wR2 = 0.0829	R1 = 0.0419, wR2 = 0.1016	R1 = 0.0669, wR2 = 0.1620
All data	R1 = 0.0387, wR2 =0.0840	R1 = 0.0507, wR2 = 0.1075	R1 = 0.0857, wR2 = 0.1723
Flack parameter	0.095(6)	0.298(10)	-----
Hooft parameter	0.042(6)	0.006(5)	-----

Table 4.2 Structure refinement data of (NMPA)BiI_5 at 100 K.

CCDC deposition id	2217823
Chemical formula	$C_4H_{14}BiI_5N_2$
Formula weight	933.65 g/mol
Temperature	100(2) K
Wavelength	0.71073 Å
Crystal system	orthorhombic
Space group	*Pna*2_1
Unit cell dimensions	a = 18.242(5) Å b = 10.830(3) Å c = 8.401(2) Å
Volume	1659.7(7) $Å^3$
Z	4
Density (calculated)	3.736 g/cm^3
Absorption coefficient	19.893 mm^{-1}
F (000)	1600
Theta range	2.18° to 25.5°
(For data collection)	
Index ranges	-22<=h<=21 -13<=k<=13 -10<=l<=10
Reflection collected	19147
Independent reflections	3088 [R_{int} = 0.0816, R_{sigma} = 0.0527]
Absorption correction	Multi-Scan
Structure solution technique	direct methods
Data / restraints / parameters	3088 / 26 / 113
Goodness-of-fit on F^2	1.063
Final R indices; I>2σ(I)	R1 = 0.0434, wR2 = 0.0994
All data	R1 = 0.0471, wR2 = 0.1012
Flack parameter	0.495(13)
Hooft parameter	0.022(4)

Table 4.3 Comparison of band gap and Bi–I–Bi angles in different Bi-I based perovskite-like compositions. The following abbreviations are used: MBA: methylbenzylammonium, (4-F)PEA: 4-fluoro phenyl ethyl ammonium, AMP: (aminomethyl)piperidinium, AMPY: (aminomethyl)pyridinium.

Composition	Dimensionality	Bi–I–Bi angle (°)	Band gap (eV)	Ref.
$(Rac\text{-}MBA)_4Bi_2I_{10}$	0D (edge shared $[Bi_2I_{10}]^{4-}$ dimer)	95.23°	2.48	17
$(R\text{-}MBA)_4Bi_2I_{10}$		95.17° & 94.85°		
$(S\text{-}MBA)_4Bi_2I_{10}$		95.18° & 94.86°		
$[(R)\text{-}1\text{-}(4\text{-}F)PEA]_4[Bi_2I_{10}]$	0D (edge shared $[Bi_2I_{10}]^{4-}$ dimer)	92.89° & 92.21° (100 K)	2.09	22
$(1,3propanediammonium)_2Bi_2I_{10}.2H_2O$	0D (edge shared $[Bi_2I_{10}]^{4-}$ dimer)	93.16° & 95.72°	2.3	23
$(Benzylammonium)_3Bi_2I_9$	0D (face shared $[Bi_2I_9]^{3-}$ dimer)	80.51°, 80.46° & 80.51° (180 K)	2.34	24
$(Biphenylbis(methylammonium))_{1.5}BiI_6.2H_2O$	0D (isolated $[BiI_6]^{3-}$ octahedra)	---	2.06	25
$(Naphthalenediimidebis(ethylammonium))_{1.5}BiI_6.2H_2O$		---	1.82	
$(R\text{-}MBA)BiI_4$	1D (edge-shared $[BiI_4]^{1-}$ octahedra)	93.74°	2.36	16
$(S\text{-}MBA)BiI_4$	1D (edge-shared $[BiI_4]^{1-}$ octahedra)	93.75°		
$(3\text{-}AMP)BiI_5$	1D (corner-shared $[BiI_5]^{2-}$ octahedra)	178.98°	1.8 - 1.95	26
$(4\text{-}AMP)BiI_5$		160.93°		
$(3\text{-}AMPY)BiI_5$		179.50°		
$(4\text{-}AMPY)BiI_5$		157.58°		
$(BMPA)BiI_5$	1D (corner-shared $[BiI_5]^{2-}$ octahedra)	171.51°	1.94	This Work

To verify the structural phase transition, single crystal XRD data recorded at 394 K (~ 20 K above the transition temperature) suggest an orthorhombic unit cell in a centrosymmetric (non-polar) *Pmcn* space group (see Figure 4.5).

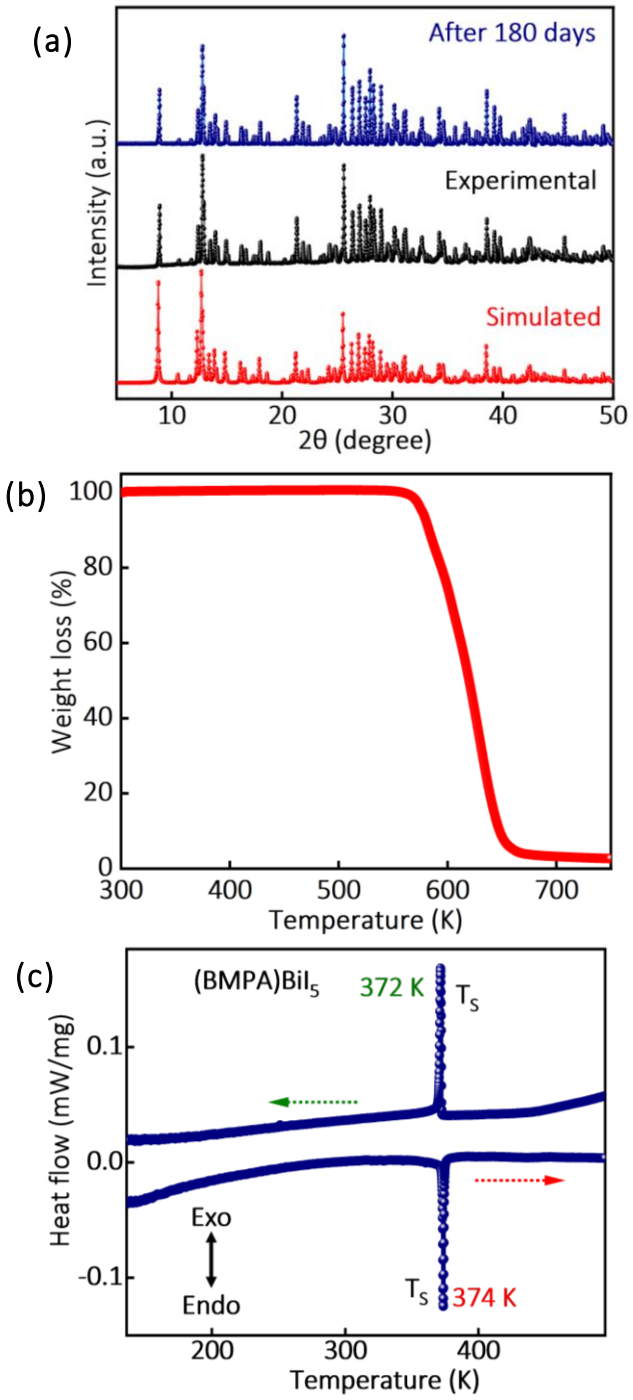

Figure 4.4: (a) PXRD data of (BMPA)BiI_5 fresh powder and after storing it under ambient conditions for 180 days matched well with the simulated pattern. (b) Thermogravimetry Analysis (TGA) data of (BMPA)BiI_5. (c) Differential scanning calorimetry (DSC) data of (BMPA)BiI_5 shows solid-to-solid structural phase transition at 372 K. (Note: DSC and TGA experiments were performed by Ranjan Das at IISC Bangalore)

The structural refinement parameters are given in Table 4.1. The broad range of phase stability for the polar phase might be a consequence of the non-covalent hydrogen bonding interactions present at both ends of the BMPA cation, providing structural rigidity (see Figure 4.2b).

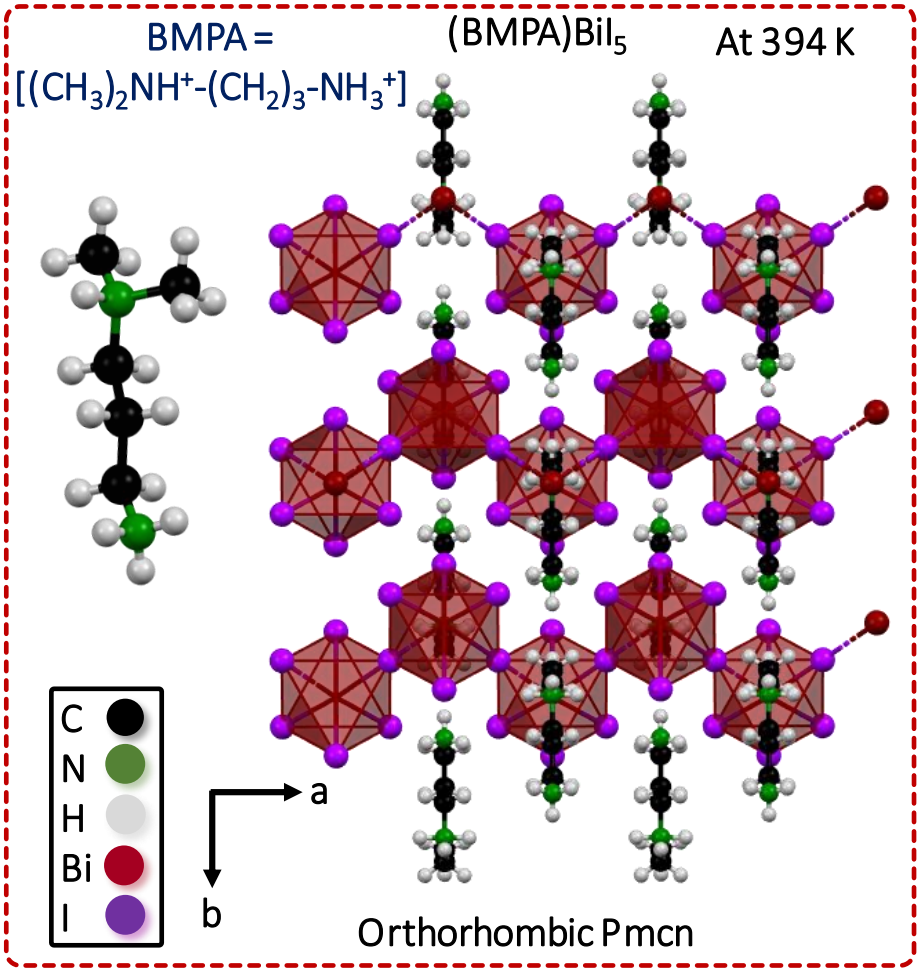

Figure 4.5: Crystal structure of (BMPA)BiI_5 at 394 K (above the transition temperature 372 K), refined from SCXRD data.

4.3.2 Nonlinear Optical Properties of Non-Centrosymmetric (BMPA)BiI_5 1D Perovskite

Nonlinear optical materials with responses in the visible region of the electromagnetic spectrum are important for applications in lasing, quantum optics, and communications.[27-29] Importantly, a non-cetrosymmetric structure is required for even-order non-linear optical properties like SHG. Consequently, we explored the spectrally-resolved harmonic generation spectra of the (BMPA)BiI_5 single crystals which possesses a non-centrosymmetric structure. A point charge

analysis of the crystal structure of (BMPA)BiI_5 also suggests a large polarization in the crystal unit cell (see calculation in section 4.3.3). The sample was excited with pump pulses ranging from 1165 to 1580 nm, and wavelength-tunable NLO emissions were collected in transmission mode[30, 31] as shown in Figure 4.6a. Experimental details for these measurements are provided in reference[30, 31]. Figure 4.6b indicate that the second order nonlinear susceptibility of (BMPA)BiI_5 is significantly high than the BBO but third-order nonlinear susceptibility is slightly lower compared to $(BA)_2PbI_4$.

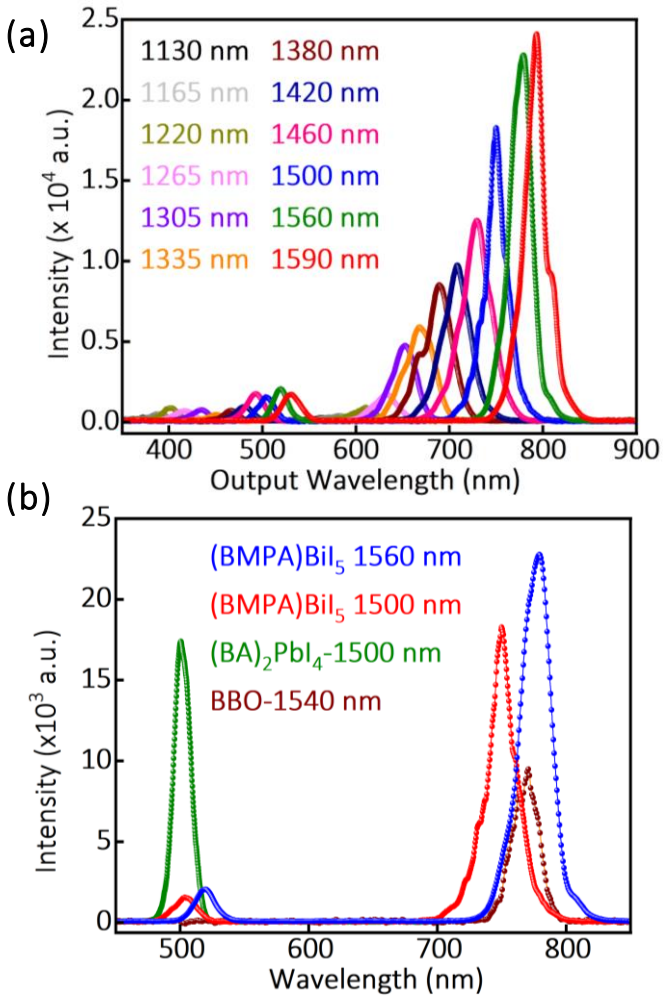

Figure 4.6: (a) Wavelength-dependent SHG and THG responses from (BMPA)BiI_5 single crystals at constant excitation power of 1.8 mW. (b) Comparison of SHG and THG response of (BMPA)BiI_5 single crystals with BBO and $(BA)_2PbI_4$ single crystals, respectively, at 1.8 mW excitation to calculate the second and third order nonlinear susceptibilities, respectively. (Note: This experiment was performed by Shabnum Maqbool in Dr. Pankaj Mondal's Lab at IISER Pune).

4.3.3 Calculation of Polarization Using a Point-Charge Model for (BMPA)BiI_5

In the refined room temperature crystal structure of (BMPA)BiI_5, we assume that the centers of the positive charges of the BMPA cation and the negative charges of the $(BiI_5)^{2-}$ are located on the N atoms and Bi atoms, respectively.

Atom	Atomic co-ordinate			Charge center co-ordinate		
	x	y	z	x	y	z
Bi	0.9664	0.9812	0.0982	0.5	0.644	0.5
	0.5033	0.3075	0.5927			
	0.0336	0.4812	0.9018			
	0.4968	0.8075	0.4073			
N	0.514	0.811	0.919	0.5	0.521	0.5
	0.591	0.583	0.680			
	0.077	0.464	0.389			
	0.923	0.964	0.611			
	0.925	0.726	0.233			
	0.486	0.311	0.081			
	0.075	0.226	0.767			
	0.409	0.082	0.320			

$$\text{Polarization, } P_s = \left|[\{(-3e \times 0.644) \times 4\} + \{(e \times 0.521) \times 8\}] \times {}^{b}/_{V}\right| \quad (1)$$

; here, b and V are the lattice vector in the y-direction, and the lattice volume, respectively, and e is the elementary charge.[32]

$$= \left|\frac{-3.56 \times 1.602 \times 10^{-19}\, C \times 16.77 \times 10^{-10}\, m}{1797.23 \times 10^{-30}\, m^3}\right|$$

$$= 53.2\ \mu C\ cm^{-2}$$

4.3.4 Anomalous Photovoltaics and Self-Powered Photodetector from Non-Centrosymmetric (BMPA)BiI_5 1D Perovskite

The observed polar non-centrosymmetry structure and strong SHG response motivated us to explore the anomalous photovoltaic effect of (BMPA)BiI_5 single crystals where the semiconducting nature might be more beneficial. A schematic of the device is shown in Figure 4.7a. Owing to the 1D perovskite crystal structure, (BMPA)BiI_5 is more insulating than the 2D perovskites. Therefore, to make better contact on (BMPA)BiI_5, a layer of 65 nm gold was sputter deposited (see Figure 4.7a), and further contacts using silver paint were made on top of these gold pads.

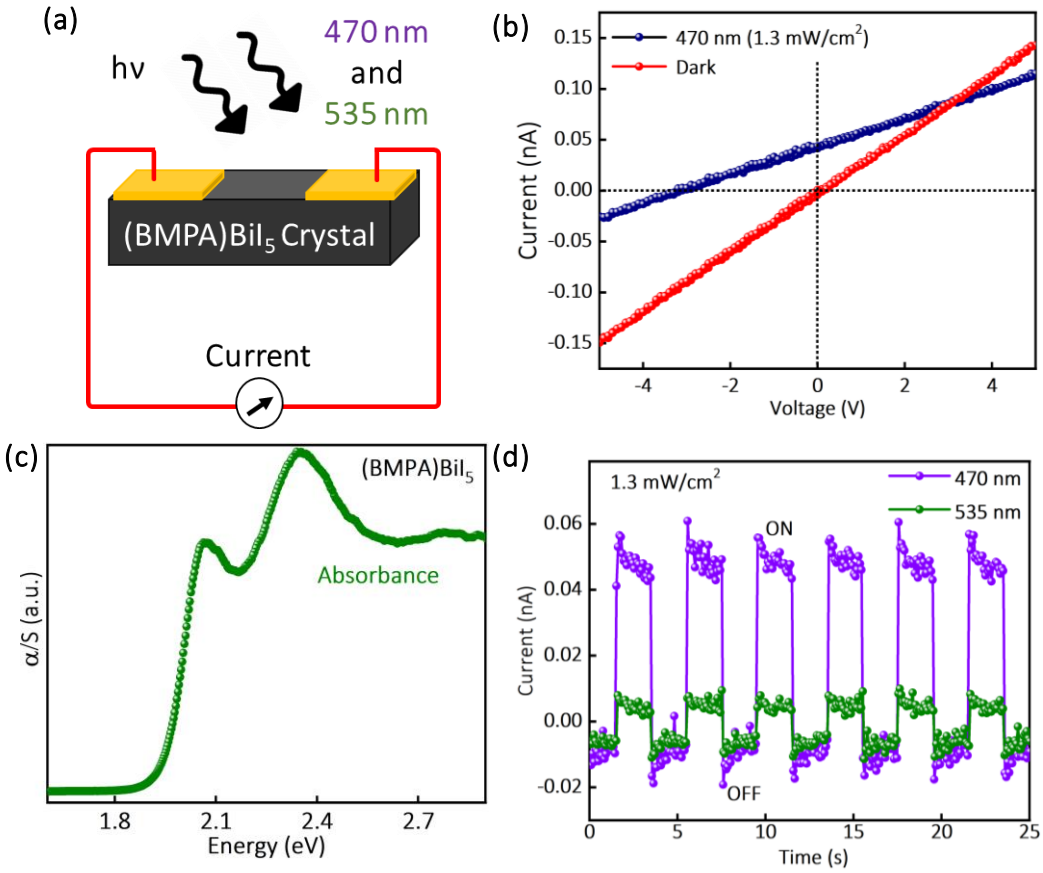

Figure 4.7: (a) Schematic of the device made by (BMPA)BiI_5 crystals. (b) I–V plot under dark and 470 nm light illumination. (c) The optical absorption spectra, recorded using single crystals at room temperature. (d) Photocurrent response of the prototype (BMPA)BiI_5 crystal device at on–off states at 0 V external bias under 470 nm and 535 nm light illumination . (Note: This experiment was performed by Gokul M. Anilkumar in Dr. Atikur Rahman's Lab at IISER Pune)

Figure 4.7d shows the temporal response of the device to lights of two different wavelengths (45 nm and 535 nm) at 4 mW/cm^2 intensity. The response was stronger for illumination with 470 nm LED, which has higher photon energy than the band gap (1.98 eV, 626 nm) of (BMPA)BiI_5 (see Figure 4.7c). The device, upon illumination, showed the generation of current in the absence of an external field. Figure 4.7b shows a V_{OC} of 3.1 V at 1.3 mW/cm^2 intensity of incident light (470 nm). Such a high V_{OC} is a signature of the anomalous photovoltaic effect.

4.3.5 Chiroptical Properties of (BMPA)BiI_5

As discussed above (BMPA)BiI_5 crystallizes in the non-centrosymmetric, polar, and chiral $P2_1$ space group. Interestingly, its synthesis does not involve the use of any chiral organic molecules.

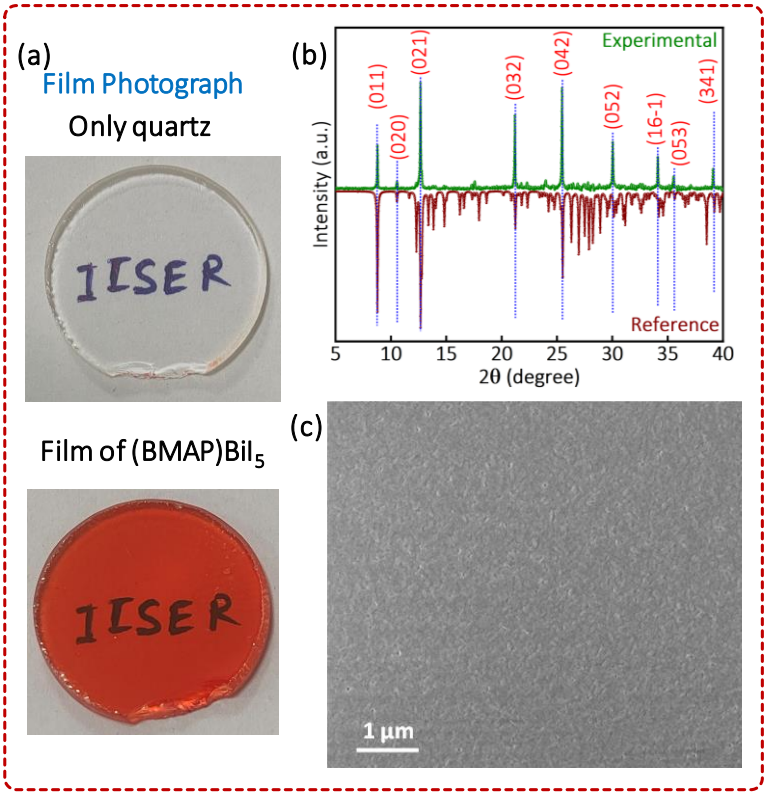

Figure 4.8: Characterization of spin-coated (BMPA)BiI_5 films. (a) Digital photographs of films of (BMPA)BiI_5 on the quartz substrate. (b) PXRD pattern of the film agrees with the simulated reference pattern of the crystal. The relative intensity of the peaks depends on the orientation of the hkl planes on the substrate. Therefore, intensity ratio of PXRD peaks of the films somewhat differs with that of the reference pattern. (c) Field emission scanning electron microscopy (FESEM) image shows the formation of a homogeneous film.

To confirm the chirality of the (BMPA)BiI_5, circular dichroism (CD) measurements were performed at room temperature on thin films of (BMPA)BiI_5. The detailed fabrication method for thin films are described in the experimental section above. Figure 4.8a displays photographs of only quartz and (BMPA)BiI_5 thin film on a quartz substrate. The powder X-ray diffraction (PXRD) patterns of the (BMPA)BiI_5 films matched well with the simulated reference pattern of the crystal, as shown in Figure 4.8b. The relative intensity of the peaks depends on the orientation of the hkl planes on the substrate. Therefore, intensity ratio of PXRD peaks of the films somewhat differs with that of the reference pattern. Further examination of the (BMPA)BiI_5 films using field emission scanning electron microscopy (FESEM) confirmed their homogeneity, as depicted in Figure 4.8c.

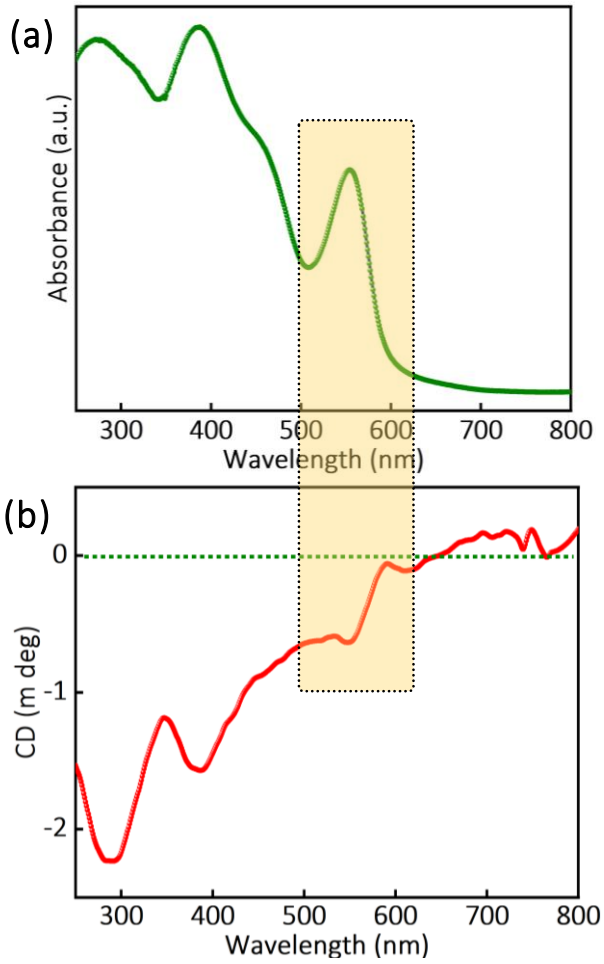

Figure 4.9: (a) UV-visible absorption and (b) circular dichroism (CD) spectra of (BMPA)BiI_5 recorded at room temperature.

Interestingly, the CD spectra of the (BMPA)BiI_5 films show signals corresponding to the absorption features, as shown in Figures 4.9a and 4.9b. It is fascinating to observe a chiroptic response from a hybrid structure that lacks a chiral molecule, though it remains challenging to determine the exact origin of the chirality in this case.

4.4 Conclusions

We have synthesized (BMPA)BiI_5 and (NMPA)BiI_5 non-centrosymmetric hybrid perovskites. The appearance (or disappearance) of non-centrosymmetry in (BMPA)BiI_5 and (NMPA)BiI_5 hybrid perovskites is driven by the nature of non-covalent hydrogen bonding interactions at the interface of organic and inorganic sublattices. Substitution of −H atoms with $-CH_3$ groups, at one end of diammonium A-site organic cations results in cations like (BMAP) and (NMPA). This reduces the rotational symmetry, inducing dissimilar hydrogen bonding interactions. The dissimilar interactions break the local octahedral centrosymmetry of the perovskite network. Then, the preferential arrangement of those octahedra in 1D networks determines whether the global centrosymmetry will be broken or not. The correlation is discussed above in detail. Owing to the structural non-centrosymmetry, 1D (BMPA)BiI_5 show visible to NIR wavelength tunable non-linear optical output, and anomalous photovoltaic effect yielding self-powered photodetection. The chiroptic response shown by the thin films of 1D (BMPA)BiI_5. The design strategy outlined in this work will guide researchers to synthesize newer non-centrosymmetric polar and chiral hybrid perovskites, and therefore, realize the full potential of their structure-driven properties.

4.5 References

1. Saparov, B.; Mitzi, D. B. Organic–inorganic perovskites: structural versatility for functional materials design. *Chem. Rev.* **2016,** *116*, 4558-4596.

2. Smith, M. D.; Karunadasa, H. I. White-light emission from layered halide perovskites. *Acc. Chem. Res.* **2018,** *51*, 619-627.

3. Mao, L.; Stoumpos, C. C.; Kanatzidis, M. G. Two-dimensional hybrid halide perovskites: principles and promises. *J. Am. Chem. Soc.* **2018,** *141*, 1171-1190.

4. Smith, I. C.; Hoke, E. T.; Solis-Ibarra, D.; McGehee, M. D.; Karunadasa, H. I. A layered hybrid perovskite solar-cell absorber with enhanced moisture stability. *Angew. Chem. Int. Ed.*

2014, *53*, 11232-11235.

5. Cao, D. H.; Stoumpos, C. C.; Farha, O. K.; Hupp, J. T.; Kanatzidis, M. G. 2D homologous perovskites as light-absorbing materials for solar cell applications. *J. Am. Chem. Soc.* **2015,** *137*, 7843-7850.

6. Tsai, H.; Nie, W.; Blancon, J.-C.; Stoumpos, C. C.; Asadpour, R.; Harutyunyan, B.; Neukirch, A. J.; Verduzco, R.; Crochet, J. J.; Tretiak, S. High-efficiency two-dimensional Ruddlesden–Popper perovskite solar cells. *Nature* **2016,** *536*, 312-316.

7. Yuan, M.; Quan, L. N.; Comin, R.; Walters, G.; Sabatini, R.; Voznyy, O.; Hoogland, S.; Zhao, Y.; Beauregard, E. M.; Kanjanaboos, P. Perovskite energy funnels for efficient light-emitting diodes. *Nat. Nanotechnol.* **2016,** *11*, 872-877.

8. Liu, Y.; Zhang, Y.; Yang, Z.; Ye, H.; Feng, J.; Xu, Z.; Zhang, X.; Munir, R.; Liu, J.; Zuo, P. Multi-inch single-crystalline perovskite membrane for high-detectivity flexible photosensors. *Nat. Commun.* **2018,** *9*, 5302.

9. Slavney, A. H.; Hu, T.; Lindenberg, A. M.; Karunadasa, H. I. A bismuth-halide double perovskite with long carrier recombination lifetime for photovoltaic applications. *J. Am. Chem. Soc.* **2016,** *138*, 2138-2141.

10. McClure, E. T.; Ball, M. R.; Windl, W.; Woodward, P. M. Cs_2AgBiX_6 (X= Br, Cl): new visible light absorbing, lead-free halide perovskite semiconductors. *Chem. Mater.* **2016,** *28*, 1348-1354.

11. Wolf, N. R.; Connor, B. A.; Slavney, A. H.; Karunadasa, H. I. Doubling the stakes: the promise of halide double perovskites. *Angew. Chem. Int. Ed.* **2021,** *133*, 16400-16414.

12. Zhao, W.-P.; Shi, C.; Stroppa, A.; Di Sante, D.; Cimpoesu, F.; Zhang, W. Lone-pair-electron-driven ionic displacements in a ferroelectric metal–organic hybrid. *Inorg. Chem.* **2016,** *55*, 10337-10342.

13. Wang, Y.; Shi, C.; Han, X.-B. Organic–inorganic hybrid $[H_2mdap][BiCl_5]$ showing an above-room-temperature ferroelectric transition with combined order–disorder and displacive origins. *Polyhedron* **2017,** *133*, 132-136.

14. Wang, Y.; Shi, C.; Han, X. B. Mixed Bromine–Chlorine Induced Great Dielectric and Second-Order Nonlinear Optical Properties Changes in Phase Transitions Compounds $[H_2mdap][BiBr_{5(1-x)}Cl_{5x}]$(x= 0.00–1.00). *J. Phys. Chem. C* **2017,** *121*, 23039-23044.

15. Tao, K.; Li, Y.; Ji, C.; Liu, X.; Wu, Z.; Han, S.; Sun, Z.; Luo, J. A lead-free hybrid iodide with quantitative response to X-ray radiation. *Chem. Mater.* **2019,** *31*, 5927-5932.

16. Yao, L.; Zeng, Z.; Cai, C.; Xu, P.; Gu, H.; Gao, L.; Han, J.; Zhang, X.; Wang, X.; Wang, X. Strong second-and third-harmonic generation in 1D chiral hybrid bismuth halides. *J. Am. Chem. Soc.* **2021,** *143*, 16095-16104.

17. Rajput, P. K.; Poonia, A. K.; Mukherjee, S.; Sheikh, T.; Shrivastava, M.; Adarsh, K.; Nag, A. Chiral methylbenzylammonium bismuth iodide with zero-dimensional perovskite derivative structure. *J. Phys. Chem. C* **2022,** *126*, 9889-9897.

18. Knutson, J. L.; Martin, J. D.; Mitzi, D. B. Tuning the band gap in hybrid tin iodide perovskite semiconductors using structural templating. *Inorg. Chem.* **2005,** *44*, 4699-4705.

19. Zhang, H.-Y.; Tang, Y.-Y.; Shi, P.-P.; Xiong, R.-G. Toward the targeted design of molecular ferroelectrics: modifying molecular symmetries and homochirality. *Acc. Chem. Res.* **2019,** *52*, 1928-1938.

20. Sheikh, T.; Shinde, A.; Mahamuni, S.; Nag, A. Possible dual bandgap in $(C_4H_9NH_3)_2PbI_4$ 2D layered perovskite: single-crystal and exfoliated few-layer. *ACS Energy Lett.* **2018,** *3*, 2940-2946.

21. Eickhoff, T.; Grosse, P.; Theiss, W. Diffuse reflectance spectroscopy of powders. *Vib. Spectrosc.* **1990,** *1*, 229-233.

22. Dehnhardt, N.; Axt, M.; Zimmermann, J.; Yang, M.; Mette, G.; Heine, J. Band gap-tunable, chiral hybrid metal halides displaying second-harmonic generation. *Chem. Mater.* **2020,** *32*, 4801-4807.

23. Pious, J. K.; Katre, A.; Muthu, C.; Chakraborty, S.; Krishna, S.; Vijayakumar, C. Zero-dimensional lead-free hybrid perovskite-like material with a quantum-well structure. *Chem. Mater.* **2019,** *31*, 1941-1945.

24. Pious, J. K.; Muthu, C.; Dani, S.; Saeki, A.; Vijayakumar, C. Bismuth-based zero-dimensional perovskite-like materials: effect of benzylammonium on dielectric confinement and photoconductivity. *Chem. Mater.* **2020,** *32*, 2647-2652.

25. Pious, J. K.; Basavarajappa, M. G.; Muthu, C.; Nishikubo, R.; Saeki, A.; Chakraborty, S.; Takai, A.; Takeuchi, M.; Vijayakumar, C. Self-Assembled Organic Cations-Assisted Band-Edge Tailoring in Bismuth-Based Perovskites for Enhanced Visible Light Absorption and Photoconductivity. *J. Phys. Chem. Lett.* **2021,** *12*, 5758-5764.

26. Li, X.; Traore, B.; Kepenekian, M.; Li, L.; Stoumpos, C. C.; Guo, P.; Even, J.; Katan, C.; Kanatzidis, M. G. Bismuth/silver-based two-dimensional iodide double and one-dimensional Bi perovskites: interplay between structural and electronic dimensions. *Chem. Mater.* **2021,** *33*, 6206-6216.

27. Boyd, R. W.; Shin, H.; Malik, M.; O'Sullivan, C.; Chan, K. W. C.; Chang, H. J.; Gauthier, D. J.; Jha, A.; Leach, J.; Murugkar, S; Rodenburg, B. *Applications of nonlinear optics in quantum imaging and quantum communication, Nonlinear Optics, Kauai, Hawai, 2011/07/17,* Optica Publishing Group: 2011; p NWC2.

28. Braune, M.; Maiwald, M.; Eppich, B.; Brox, O.; Ginolas, A.; Sumpf, B.; Tränkle, G. Design and Realization of a Miniaturized DFB Diode Laser-based SHG Light Source with a 2-nm Tunable Emission at 488 nm. *IEEE Trans. Compon., Packag. Manuf. Technol.* **2017,** *7*, 720-725.

29. Li, G.; Chen, Y.; Jiang, H.; Chen, X. Broadband sum-frequency generation using d33 in periodically poled LiNbO 3 thin film in the telecommunications band. *Opt. Lett.* **2017,** *42*, 939-942.

30. Maqbool, S.; Sheikh, T.; Thekkayil, Z.; Deswal, S.; Boomishankar, R.; Nag, A.; Mandal, P. Third Harmonic Upconversion and Self-Trapped Excitonic Emission in 1D Pyridinium Lead Iodide. *J. Phys. Chem. C* **2021,** *125*, 22674-22683.

31. Sheikh, T.; Maqbool, S.; Rajput, P. K.; Mandal, P.; Nag, A. Effect of chirality on the optical properties of layered hybrid perovskite R- and S-α-methylbenzylammonium lead iodide. *Chem. Commun.* **2022,** *58*, 7650-7653.

32. Li, D.; Liu, X.; Wu, W.; Peng, Y.; Zhao, S.; Li, L.; Hong, M.; Luo, J., Chiral lead-free hybrid perovskites for self-powered circularly polarized light detection. *Angew. Chem. Int. Ed.* **2021,** *133*, 8496-8499.

Chapter 5

Chirality Induction from Organic to Inorganic Sublattices in Chiral 0D Bi-I Hybrid Perovskite Derivatives

Graphical Abstract:

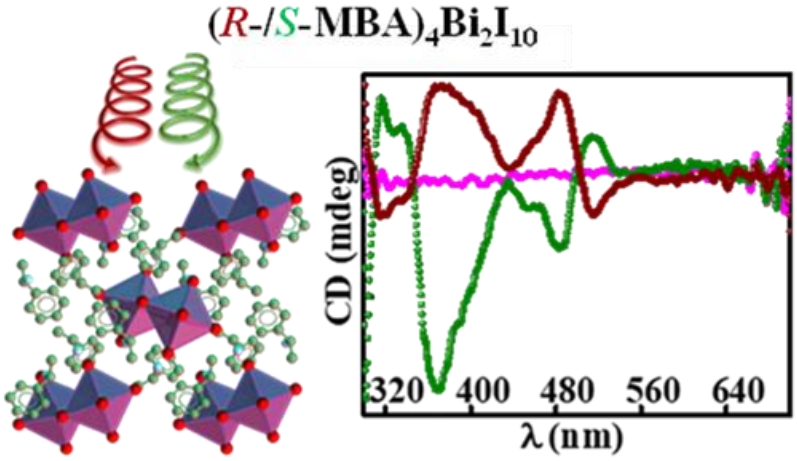

The work of this chapter has been published in the following article:

Rajput, P.K.; Poonia, A.K.; Mukherjee, S.; Sheikh, T.; Shrivastava, M.; Adarsh, K.V.; Nag, A. Chiral Methylbenzylammonium Bismuth Iodide with Zero-Dimensional Perovskite Derivative Structure. *J. Phys. Chem. C* **2022**, *126*, 9889-9897.

CHAPTER 5: Chirality Induction from Organic to Inorganic Sublattices in Chiral 0D Bi-I Hybrid Perovskite Derivatives

Abstract

Chiral hybrid metal halide perovskites provide hopes of combining chirality induced by the organic sublattice with optoelectronic properties arising from the inorganic sublattice. The field is still in its infancy, with material space mainly focused on two-dimensional hybrid lead halide perovskites. Here we report a zero-dimensional Pb-free perovskite derivative structure with chemical composition [(*R*-/*S*-MBA)$_4$Bi$_2$I$_{10}$], where MBA stands for methylbenzylammonium. Single-crystal X-ray diffraction data show that the enantiomerically pure *R*-MBA and *S*-MBA induce chirality in the Bi−I inorganic sublattice. Consequently, chiroptical properties like circular dichroism (CD) is observed for the excitonic transitions of (*R*-/*S*-MBA)$_4$Bi$_2$I$_{10}$. Temperature-dependent (7−300 K) photoluminescence shows excitonic and shallow-defect emissions, indicating fewer deep defect trap states. The material design, structure, and optical properties reported here will be useful to develop next-generation Pb-free perovskites for chiral optoelectronics.

5.1 Introduction

Chiral crystal has a unit cell that does not superimpose with its mirror image. Typical inorganic crystals lack such chirality, whereas many organic molecules exhibit chirality. Can chirality be induced to the usually achiral inorganic sublattice by making hybrid organic−inorganic perovskites containing chiral organic ammonium cation?[1-5] This question becomes more important for hybrid metal halide perovskites that show excellent optical and optoelectronic properties mainly arising from the inorganic sublattice.[6-19] So, if the organic component induces chirality in the inorganic component, then there is a possibility to observe interesting chiroptical and chiral optoelectronic properties. Here we report Pb-free zero-dimensional (0D) perovskite derivative structure with chemical composition (*R*-/*S*-) methylbenzylammonium bismuth iodide [(*R*-/*S*-MBA)$_4$Bi$_2$I$_{10}$], exhibiting excitonic chiroptical properties.

In recent years, chiral organic sublattice has been shown to introduce chirality in the optical, optoelectronic, and spin-based properties of inorganic sublattice of two-dimensional (2D) layered hybrid halide perovskites. Optical properties like circular dichroism (CD), second harmonic generation, and circularly polarized luminescence have been demonstrated.[20-23] Futuristic optoelectronic properties like circularly polarized photodetectors and bulk photovoltaic effect have also been shown to exist.[24-26] Spin filters based on chiral-induced spin selectivity (CISS) effect[27-28] and chiral ferroelectrics[29] have also been demonstrated in chiral 2D hybrid perovskites. Nevertheless, active research on chiral hybrid perovskites has just started recently. A significant improvement in the observed properties, enabled by developing novel materials and methods, is required before such chiral hybrid perovskites become potential candidates for future applications. The explored material space for chiral hybrid perovskites is still mainly limited to (i) layered 2D structures and (ii) Pb halide-based compositions. There are a few reports on Sn-, Sb-, and Bi-based chiral hybrid halide perovskites and their derivative structures.[17, 30-33] Sn-based samples show CD and signature of CISS. Sb- and Bi-based samples show second harmonic generation. None of these Pb-free chiral perovskites show photoluminescence (PL) at room temperature, indicating the dominance of nonradiative decay channels. (*R*-/*S*-MBA)$_2$SnI$_4$ even does not show excitonic absorption, probably because of large structural distortion.[31]

We prepare 0D chiral hybrid perovskite derivative (*R*-/*S*-MBA)$_4$Bi$_2$I$_{10}$. The 0D structure is not really a perovskite structure but has some similarity with hybrid perovskite structures.[14, 34] The 0D structure is expected to increase the exciton binding energy leading to excitonic PL, and nonlinear optical properties but will suffer from poor charge transport. Our (*R*-/*S*-MBA)$_4$Bi$_2$I$_{10}$ show sharp excitonic absorption and PL. CD peaks corresponding to the excitonic transition are observed. Temperature-dependent PL provide insights about the excitonic photophysics. Structural analysis by single-crystal X-ray diffraction (SCXRD) provides mechanistic insights on how the chirality in organic sublattice induces the chirality in inorganic sublattice.

5.2 Experimental Section

5.2.1 Chemicals

Bismuth (III) oxide (Sigma Aldrich, 99.9%), hydroiodic acid (Sigma Aldrich, 57% w/w in H_2O, 99.9%), hypophosphorous acid (Avra, 50% w/w H_2O), racemic-methyl benzylamine (Sigma Aldrich, 98%), *R*-(+)- α- methyl benzylamine (Sigma Aldrich, 99%), *S*- (-)-α-methyl benzylamine (Sigma Aldrich, 99%), N,N-dimethylformaide (Sigma Aldrich, > 99.8%).

5.2.2 Synthesis of 0D (*Rac*-, *R*-, and *S*-MBA)$_4$Bi$_2$I$_{10}$ Single Crystals

Synthesis of 0D (*Rac*-, *R*-, and *S*-MBA)$_4$Bi$_2$I$_{10}$ single crystals are carried out following an acid precipitation method. One millimole of Bismuth (III) oxide is dissolved in a mixture of 10 mL of hydroiodic acid (HI) and 1 mL of hypophosphorous acid (H_3PO_2) at ∼100 °C with constant magnetic stirring. Once a clear transparent solution is obtained, 2 mmol of each *Rac*-, *R*-, or *S*-methylbenzylamine is added to this solution. After 30 min, the heating and stirring are stopped. The solution is allowed to cool to room temperature with a cooling rate of 5 °C per hour. The solution is then kept overnight unperturbed. During this process, orange-red color crystals of (*Rac*-, *R*-, or *S*-MBA)$_4$Bi$_2$I$_{10}$ precipitated out. The crystals are filtered off and washed with diethyl ether and stored in argon filled glove box.

5.2.3 Preparation of (*Rac*-, *R*-, and *S*-MBA)$_4$Bi$_2$I$_{10}$ Thin Films

The glass and sapphire substrates were cleaned first with soap solution, then distilled water, then

with acetone and 2-propanol for 15 minutes each in an ultrasonic bath sonicator. The glass and sapphire substrates were dried in N_2 flow and exposed to oxygen plasma for 10 minutes using a plasma cleaner. The synthesized crystals of (*Rac*-, *R*-, and *S*-MBA)$_4Bi_2I_{10}$ are dissolved in N,N-dimethylformamide to achieve a solution concentration of 0.184 M. Thin films are then prepared by spin coating (Spin NXG-P1, apex instruments) with the solution onto substrates (glass or sapphire) using a spin rate of 3000 rpm for 30 s, followed by annealing at 100 °C for 10 min to induce crystallization. Films on glass substrates are used for powder XRD (PXRD), CD, and UV−visible absorption measurements. Thin films on sapphire substrates are used for temperature-dependent PL measurements.

5.2.4 Structural Characterization

Frames of single crystal X-ray diffraction **(**SCXRD) were collected in a Bruker Apex Duo diffractometer using Mo Kα radiation (λ = 0.71 Å) at 120 and 296 K (near room temperature). Crystals were kept under a constant flow of nitrogen to collect the data at 120 and 296 K. The integrations of the collected data and numerical absorption corrections were done using APEX3 software. The structures were solved by the direct method using SHELXS and refined by full-matrix least-squares on F^2 using the SHELXL, as implemented in APEX3. The CIF files, containing the atomic positions, and the anisotropic displacement parameters, obtained from the refinement are available via CCDC with codes 2142129, 2142130, 2142132, 2142133, 2142135, and 2142136. Powder X-ray diffraction patterns at room temperature are recorded on a Bruker D8 Advance diffractometer in Bragg−Brentano geometry and operating with Cu Kα radiation (1.54 Å).

Field emission scanning electron microscopy (FESEM) images are collected using the Zeiss Ultra Plus FESEM instrument. The thermal stability of the samples is checked by thermogravimetric analysis (TGA) under a nitrogen atmosphere, using a Perkin-Elmer STA6000 system at a rate of 10 K per minute.

5.2.5 Optical Characterization

Optical absorption (transmission mode) spectroscopy is carried out using a Cary series UV−visible

spectrophotometer. CD measurements (transmission mode) are carried out using a JASCO J-815 spectropolarimeter at a scan speed of 50 nm/min with 0.5 nm resolution. Steady-state PL and PL decay dynamics (time- correlated single photon counting) are carried out using FLS 980 (Edinburgh Instruments). Steady-state PL is measured by excitation with a xenon lamp, and PL decay is measured by excitation with a 405 nm diode laser (pulse width is 60 ps). For temperature-dependent PL measurements, thin films of samples on sapphire substrates are mounted on a gold-plated sample holder attached to a closed cycle He cryostat (Advanced Research Systems) with a temperature controller (Lake Shore Cryotronics) to achieve the desired lower temperatures.

5.2.6 Fitting of Photoluminescence Decay

The measured PL decay dynamics have been fitted by the bi-exponential decay function

$$I(t) = A_1 \exp(-t/\tau_1) + A_2 \exp(-t/\tau_2) \qquad (1)$$

where τ_i (i = 1, 2) represents the lifetime of the i^{th} decay component and A_i (i = 1, 2) is the corresponding amplitude.

The average PL decay lifetime τ_{av} has been evaluated by using the expression

$$\tau_{av} = \sum_{i=1}^{2} A_i \tau_i^2 / A_i \tau_i \qquad (2)$$

5.3 Results and Discussion

5.3.1 Structure and Morphology

The reaction scheme to synthesize achiral (*Rac*-MBA)$_4$Bi$_2$I$_{10}$ and chiral (*R*-/*S*-MBA)$_4$Bi$_2$I$_{10}$ is shown in Figure 5.1a. Dark orange-red colored crystals are formed. Figure 5.1b shows the photographs of (*Rac*-, *R*-, and *S*-MBA)$_4$Bi$_2$I$_{10}$ crystals with approximate sizes (length × breadth × height) 13 mm × 8 mm × 4 mm, 4 mm × 3 mm × 1 mm, and 5 mm × 4 mm × 1 mm, respectively. These crystals are then used for SCXRD measurements at 120 and 296 K (near room temperature). The crystallographic structural parameters remain similar for both temperatures, as shown in Table 5.1 and Table 5.2. All three samples crystallize in monoclinic crystal systems with a 0D perovskite derivative structure, as shown in Figure 5.1c.

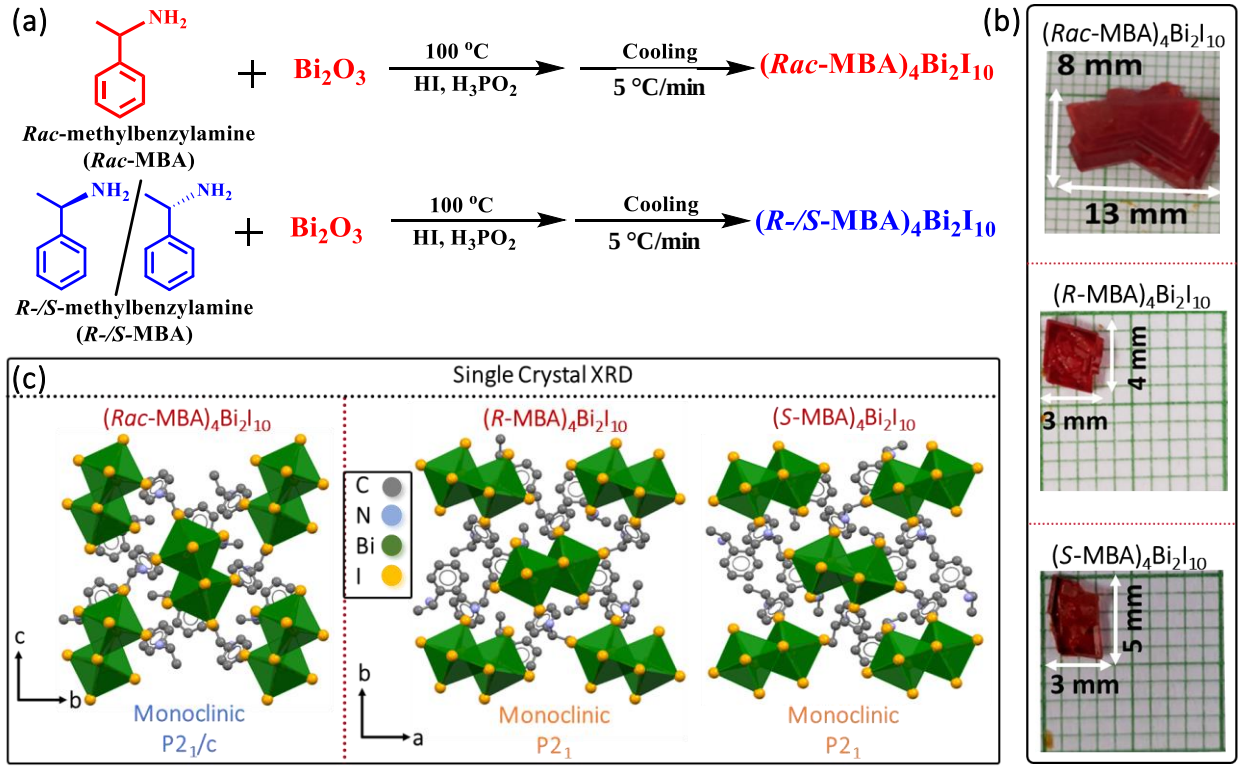

Figure 5.1. (a) Reaction scheme and (b) Digital photographs of (*Rac*-, *R*-, and *S*-MBA)$_4$Bi$_2$I$_{10}$ crystals. (c) Crystal structures of (*Rac*-, *R*- and *S*-MBA)$_4$Bi$_2$I$_{10}$ obtained from single-crystal XRD data measured at 120 K. The 0D perovskite derivative structure with $[Bi_2I_{10}]^{4-}$ dimers separated by organic cations is observed.

Bi–I$_6$ octahedra share their edges through two iodine(I) forming the $[Bi_2I_{10}]^{4-}$ dimers. The voids between the dimers are occupied by four *Rac*-/*R*-/*S*-MBA cations, providing the charge-neutral compositions (*Rac*-, *R*-, and *S*-MBA)$_4$Bi$_2$I$_{10}$.

The same structures of Figure 5.1c, if viewed from a different direction [Figure 5.2 (a-c)], show layers of organic and inorganic sublattice arranged on top of each other. PXRD patterns in Figure 5.7b also show such layered arrangement. Such layered structural arrangement is found to give a layered morphology for all the three samples, as shown by the FESEM images in Figure 5.2 (d-f). The signature of layered morphology is also indicated in the photographs of crystals shown in Figure 5.1b. Also, the PXRD patterns obtained from finely powdered (*Rac*-, *R*-, and *S*-MBA)$_4$Bi$_2$I$_{10}$ samples match well with their corresponding simulated patterns, confirms the phase

purity of all three samples in their bulk phases, as shown in Figure 5.2 (g-i).

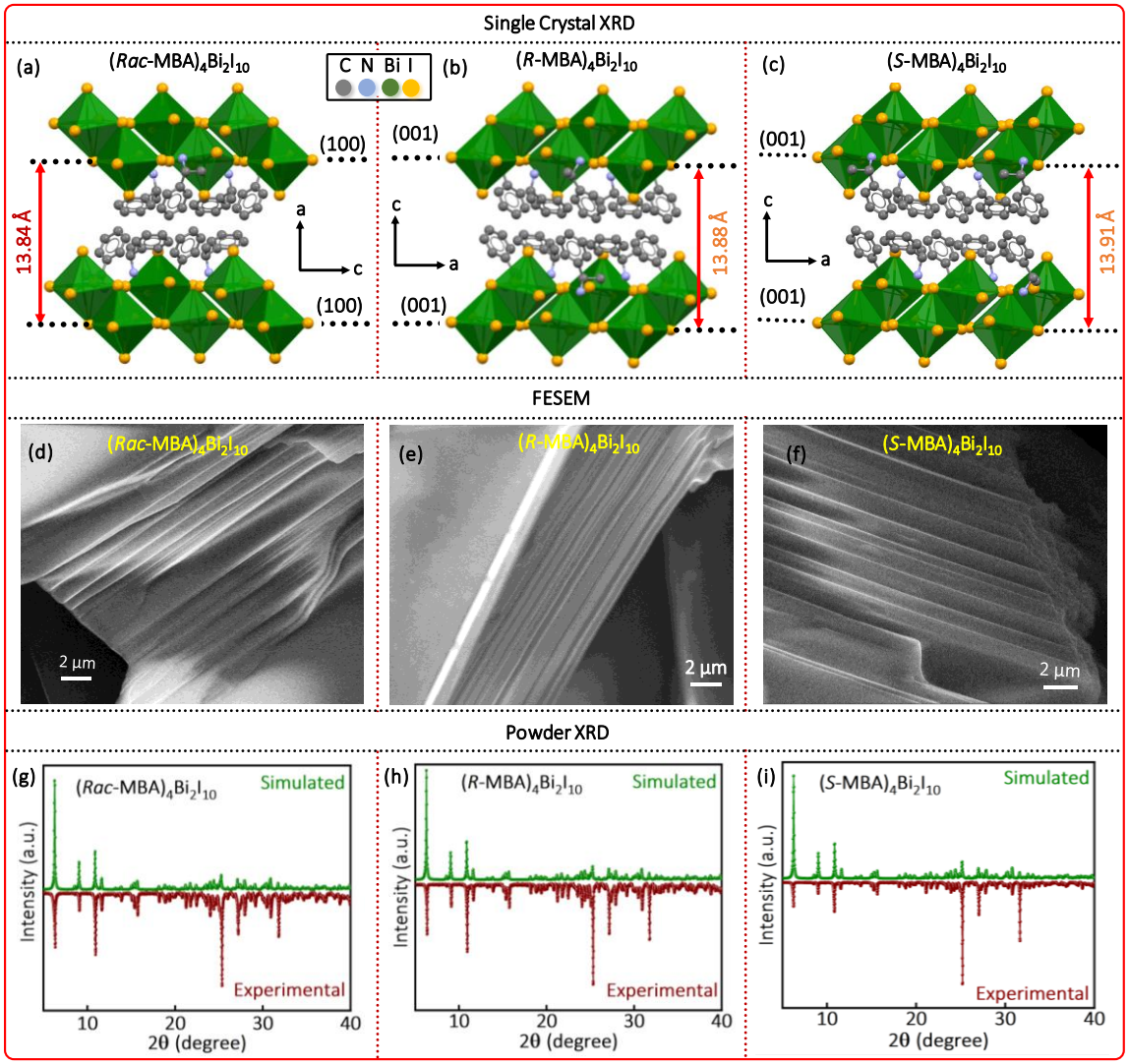

Figure 5.2: The crystal structure of (*Rac*-, *R*-, and *S*-MBA)$_4$Bi$_2$I$_{10}$ if viewed from a different direction shows the layered arrangement of organic and inorganic layers. Crystal growth in (*Rac*-MBA)$_4$Bi$_2$I$_{10}$ is along [h00] direction while in (*R*-, and *S*-MBA)$_4$Bi$_2$I$_{10}$ is along [00l] direction. (e-f) FESEM images of (*Rac*-, *R*-, and *S*-MBA)$_4$Bi$_2$I$_{10}$ crystals showing layered morphology agreeing with the structure shown by the single-crystal [Figure 5.2(a-c)] and powder (Figure 5.7b) XRD measurements. Powder XRD patterns of finely powdered (g) (*Rac*-MBA)$_4$Bi$_2$I$_{10}$, (h) (*R*-MBA)$_4$Bi$_2$I$_{10}$ and (i) (*S*-MBA)$_4$Bi$_2$I$_{10}$, measured at 296 K. The experimental patterns are compared with the simulated patterns obtained from the CIF files of single crystal XRD analysis of the respective samples.

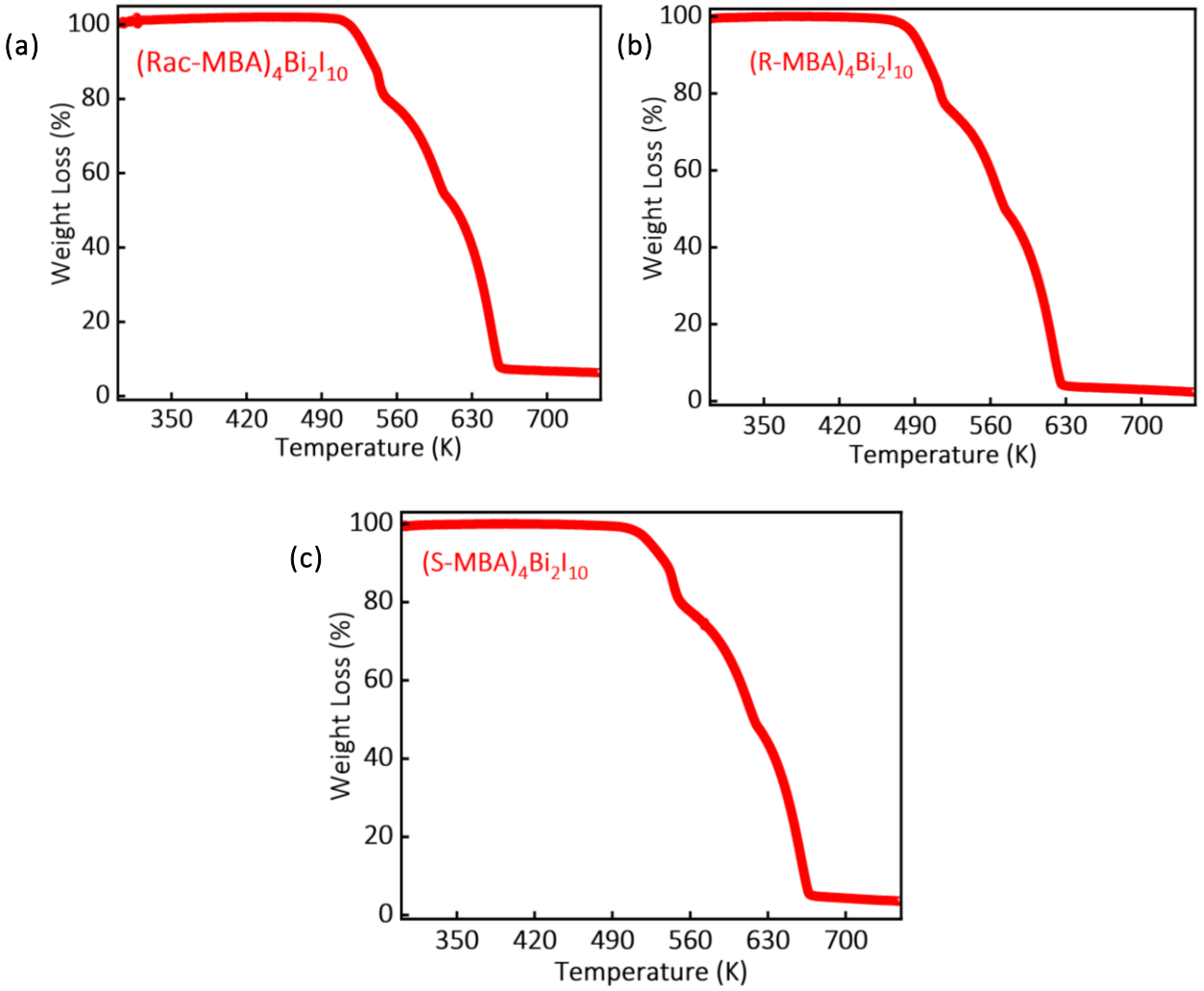

Figure 5.3: Thermogravimetric analysis (TGA) was performed on (a) (Rac-MBA)$_4$Bi$_2$I$_{10}$, (b) (R-MBA)$_4$Bi$_2$I$_{10}$, and (c) (S-MBA)$_4$Bi$_2$I$_{10}$, powdered samples. The data recorded at a heating rate of 10 K per minute. The red line in each TGA plot represents the weight loss percentage as a function of temperature.

The thermal stability of all samples was checked using thermogravimetric analysis (TGA) at a rate of 10 K per minute. The TGA results indicate that all samples (*Rac*-, *R*-, and *S*-MBA)$_4$Bi$_2$I$_{10}$ remained stable up to 475 K, showing no weight loss (see Figure 5.3). After 475 K, all samples (*Rac*-, *R*-, and *S*-MBA)$_4$Bi$_2$I$_{10}$ began to decompose. In such hybrid organic-inorganic perovskite derivatives, the initial decomposition event occurring above ~200 °C, is primarily due to the evaporation of the organic ammonium cations.

Table 5.1: Crystal structure refinement data for (*Rac*-, *R*-, and *S*-MBA)$_4Bi_2I_{10}$ at 120 K

Identification code	**(*Rac*-MBA)$_4Bi_2I_{10}$**	**(*R*-MBA)$_4Bi_2I_{10}$**	**(*S*-MBA)$_4Bi_2I_{10}$**
Chemical formula	$C_{32}H_{48}Bi_2I_{10}N_4$	$C_{32}H_{48}Bi_2I_{10}N_4$	$C_{32}H_{48}Bi_2I_{10}N_4$
Formula weight	2174.96 g/mol	2174.96 g/mol	2174.96 g/mol
Temperature	120(2) K	120(2) K	120(2) K
Wavelength	0.71073 Å	0.71073 Å	0.71073 Å
Crystal system	monoclinic	monoclinic	monoclinic
Space group	$P2_1/c$	$P2_1$	$P2_1$
Unit cell dimensions	a = 13.841(2) Å b = 14.990(2) Å c = 12.7712(17) Å β = 91.565(4)°	a = 12.7941(13) Å b = 15.0038(16) Å c = 13.8876(14) Å β = 91.671(3)°	a = 12.7877(14) Å b = 15.0369(17) Å c = 13.9154(16) Å β = 91.674(3)°
Volume	2648.7(6) Å^3	2663.8(5) Å^3	2674.6(9) Å^3
Z	2	2	2
Density (calculated)	2.728 g/cm^3	2.712 g/cm^3	2.702 g/cm^3
Absorption coefficient	12.487 mm^{-1}	12.416 mm^{-1}	12.369 mm^{-1}
F (000)	1928	1928	1928
Theta range (For data collection)	2.59 to 24.71°	1.59 to 24.99°	1.59 to 26.46°
Index ranges	-16<=h<=16 -17<=k<=16 -15<=l<=14	-15<=h<=15 -13<=k<=17 -16<=l<=16	-15<=h<=15 -18<=k<=18 -17<=l<=17
Reflection collected	37068	25288	67411
Independent reflections	4503	8555	10970
Coverage (Independent reflections)	99.80%	99.90%	99.7%
Absorption correction	Multi-Scan	Multi-Scan	Multi-Scan
Structure solution technique	direct methods	direct methods	direct methods
Structure solution program	SHELXT 2014/5 (Sheldrick, 2014)	SHELXT 2014/5 (Sheldrick, 2014)	SHELXT 2014/5 (Sheldrick, 2014)
Refinement method	Full-matrix least-squares on F^2		
Refinement program	SHELXL-2018/3 (Sheldrick, 2018)	SHELXL-2018/3 (Sheldrick, 2018)	SHELXL-2018/3 (Sheldrick, 2018)
Function minimized	$\Sigma w(F_o^2 - F_c^2)^2$	$\Sigma w(F_o^2 - F_c^2)^2$	$\Sigma w(F_o^2 - F_c^2)^2$
Data / restraints / parameters	4503 / 0 / 221	8555 / 25 / 393	10970 / 1 / 393
Goodness-of-fit on F^2	0.832	1.032	0.714
Final R indices; I>2σ(I)	R1 = 0.0255, wR2 = 0.0908	R1 = 0.0348, wR2 = 0.0746	R1 = 0.0304, wR2 = 0.0907
All data	R1 = 0.0276, wR2 = 0.0950	R1 = 0.0424, wR2 =0.0777	R1 = 0.0426, wR2 = 0.1022
Weighting scheme	$w=1/[\sigma^2(F_o^2)+(0.1000P)^2]$ where $P=(F_o^2+2F_c^2)/3$		
Flack Parameter	---	0.012(8)	0.000(6)
CCDC deposition id	2142129	2142132	2142135

Table 5.2: Crystal structure refinement data for (*Rac*-, *R*-, and *S*-MBA)$_4Bi_2I_{10}$ at 296 K

Identification code	**(*Rac*-MBA)$_4Bi_2I_{10}$**	**(*R*-MBA)$_4Bi_2I_{10}$**	**(*S*-MBA)$_4Bi_2I_{10}$**
Chemical formula	$C_{32}H_{48}Bi_2I_{10}N_4$	$C_{32}H_{48}Bi_2I_{10}N_4$	$C_{32}H_{48}Bi_2I_{10}N_4$
Formula weight	2174.96 g/mol	2174.96 g/mol	2174.96 g/mol
Temperature	296(2) K	296(2) K	296(2) K
Wavelength	0.71073 Å	0.71073 Å	0.71073 Å
Crystal system	monoclinic	monoclinic	monoclinic
Space group	$P2_1/c$	$P2_1$	$P2_1$
Unit cell dimensions	a = 14.0997(11) Å b = 15.2144(11) Å c = 12.7506(9) Å β = 91.958(2)°	a = 12.7502(5) Å b = 15.2408(6) Å c = 14.1032(6) Å β = 91.907(2)°	a = 12.810(4) Å b = 15.214(5) Å c = 14.155(4) Å β = 91.804(9)°
Volume	2733(3) Å^3	2739.06(19) Å^3	2757.2(15) Å^3
Z	2	2	2
Density (calculated)	2.643 g/cm^3	2.637 g/cm^3	2.621 g/cm^3
Absorption coefficient	12.099 mm^{-1}	12.075 mm^{-1}	11.996 mm^{-1}
F (000)	1928	1926	1928
Theta range (For data collection)	1.97 to 24.99°	1.96 to 24.80°	1.59 to 24.99°
Index ranges	-16<=h<=16 -17<=k<=18 -15<=l<=14	-15<=h<=15 -17<=k<=17 -15<=l<=16	-15<=h<=15 -18<=k<=18 -16<=l<=16
Reflection collected	39502	53281	53978
Independent reflections	4798	9392	9731
Coverage (Independent reflections)	99.70%	99.8%	100%
Absorption correction	Multi-Scan	Multi-Scan	Multi-Scan
Structure solution technique	direct methods	direct methods	direct methods
Structure solution program	SHELXT 2014/5 (Sheldrick, 2014)	SHELXT 2014/5 (Sheldrick, 2014)	SHELXT 2014/5 (Sheldrick, 2014)
Refinement method	Full-matrix least-squares on F^2		
Refinement program	SHELXL-2018/3 (Sheldrick, 2018)	SHELXL-2018/3 (Sheldrick, 2018)	SHELXL-2018/3 (Sheldrick, 2018)
Function minimized	$\Sigma\, w(F_o^2 - F_c^2)^2$	$\Sigma\, w(F_o^2 - F_c^2)^2$	$\Sigma\, w(F_o^2 - F_c^2)^2$
Data / restraints / parameters	4798 / 6 / 131	9392 / 355 / 392	9731 / 123 / 393
Goodness-of-fit on F^2	1.033	1.050	1.078
Final R indices; I>2σ(I)	R1 = 0.0365, wR2 = 0.0801	R1 = 0.0484, wR2 = 0.0797	R1 = 0.0409, wR2 = 0.0809
All data	R1 = 0.0473, wR2 = 0.0893	R1 = 0.0990, wR2 =0.0987	R1 = 0.0833, wR2 = 0.1027
Weighting scheme	$w=1/[\sigma^2(F_o^2)+(0.1000P)^2]$	Where	$P=(F_o^2+2F_c^2)/3$
Flack Parameter	----	-0.017(10)	-0.028(10)
CCDC deposition id	2142130	2142133	2142136

5.3.2 Chirality of Organic and Inorganic Sublattice

In spite of similarity of 0D structures and layered morphologies among all the three samples, there are critical structural differences with respect to chirality. The (*R*-/*S*-MBA)$_4$Bi$_2$I$_{10}$ crystals belong to a chiral Sohncke space group of $P2_1$. It is worth mentioning that the chiral space group of (*R*-/*S*-MBA)$_4$Bi$_2$I$_{10}$ remained intact when we remeasured the SCXRD after storing the samples for about 45 days in ambient conditions. In contrast, (*Rac*-MBA)$_4$Bi$_2$I$_{10}$ crystallizes into an achiral space group $P2_1/c$. Does the enantiomerically pure organic sublattice of (*R*-/*S*-MBA)$_4$Bi$_2$I$_{10}$ induce chirality in their inorganic sublattice $[Bi_2I_{10}]^{4-}$? This is an important question because the inorganic sublattice is expected to constitute valence and conduction band edges controlling the electronic and optical properties. Therefore, we explore the chirality aspects of the organic and inorganic sublattices separately, as shown in Figure 5.4 and 5.5. The absence of an improper axis of rotation, which includes planes of symmetry or inversion center, is the essential criterion for chirality.[35-36] The left panel of Figure 5.4a shows that the organic sublattice of (*Rac*-MBA)$_4$Bi$_2$I$_{10}$ crystals has an inversion symmetry. Similarly, the middle panel of Figure 5.4a shows that the inorganic dimer $[Bi_2I_{10}]^{4-}$ also has an inversion symmetry. The opposite pair of Bi–I bonds, like the axial Bi1–I_{up} and Bi1'–I_{down}, have equal bond lengths (3.067 Å), as indicated by the same-colored fonts in Figure 5.4a (middle panel). Similar symmetries of diametrically opposite bond angles are shown in Figure 5.5a. Such symmetry of the inorganic dimer also gets reflected in the unit cell of inorganic sublattice, as shown in the right panel of Figure 5.4a. Therefore, organic sublattice, inorganic sublattice, and the overall hybrid lattice of (*Rac*-MBA)$_4$Bi$_2$I$_{10}$ lack chirality. The situation is pretty different for (*R*-MBA)$_4$Bi$_2$I$_{10}$. The organic sublattice lacks the inversion symmetry, as shown in the left panel of Figure 5.4b. The $[Bi_2I_{10}]^{4-}$ shown in the middle panel of Figure 5.4b is also significantly distorted. The opposite pairs of Bi–I bonds, like Bi1–I_{up} and Bi2–I_{down} bond lengths, are no longer equal. In fact, most of the bond lengths (middle panel of Figure 5.4b) and bond angles (Figure 5.5b) are different from each other.

The organic ammonium cations form hydrogen bonds with the iodine of $[Bi_2I_{10}]^{4-}$ dimers. SCXRD data show that the chiral organic sublattice introduces asymmetry in hydrogen bonding interactions as shown in Figures 5.6b and 5.6c in (*R*-MBA)$_4$Bi$_2$I$_{10}$ and (*S*-MBA)$_4$Bi$_2$I$_{10}$ respectively. Such

asymmetric hydrogen bonding is known to distort the inorganic sublattice.[30-31, 37] Achiral organic sublattices introduces symmetry in hydrogen bonding interactions as shown in Figure 5.6a in (*Rac*-MBA)$_4$Bi$_2$I$_{10}$. More number of H-bonding interactions along with different strengths produce a

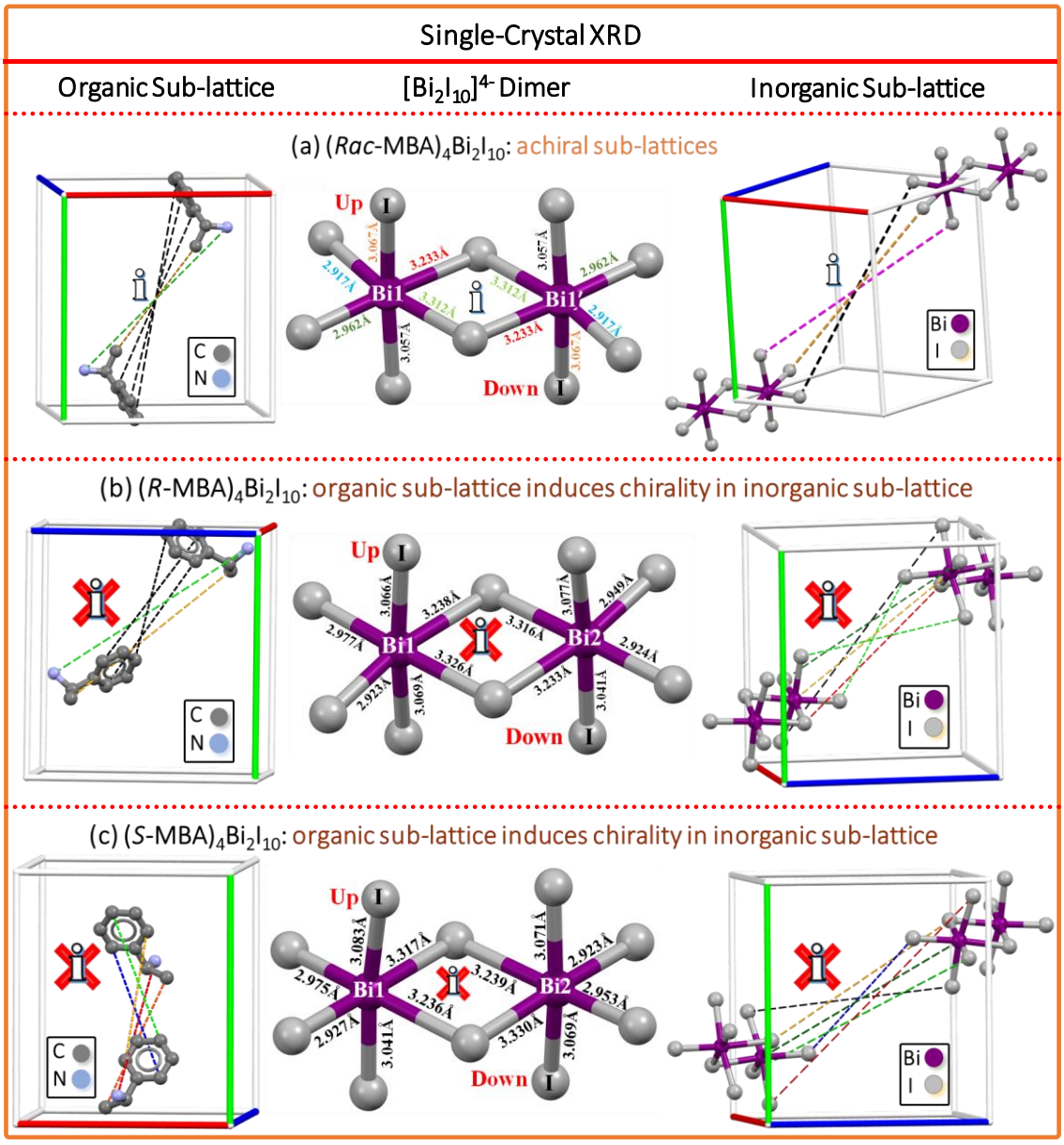

Figure 5.4: Left column: organic sublattices. Middle column: $[Bi_2I_{10}]^{4-}$ dimer. Right column: inorganic sublattices. (a) The crystal of (*Rac*-MBA)$_4$Bi$_2$I$_{10}$ has an inversion center "i". (b) and (c) are the isomers of (*R*- and *S*-MBA)$_4$Bi$_2$I$_{10}$ without a center of inversion. Unit cell axes *a*, *b*, and *c* are shown by green, blue, and red colors, respectively.

significant distortion in $[Bi_2I_{10}]^{4-}$ dimer units of (*R*- and *S*-MBA)$_4Bi_2I_{10}$ crystal compared to (*Rac*-MBA)$_4Bi_2I_{10}$ crystal. These distortions result into the absence of both inversion and mirror symmetry in $[Bi_2I_{10}]^{4-}$ dimer. Lack of these symmetries in the dimer makes the unit cell of inorganic sublattice chiral, as shown in the right panel of Figure 5.4b. We attempted to correlate the bond length distortion index (*D*) and bond angle variance (σ^2) with the extent of chirality, as shown in Table 5.3.

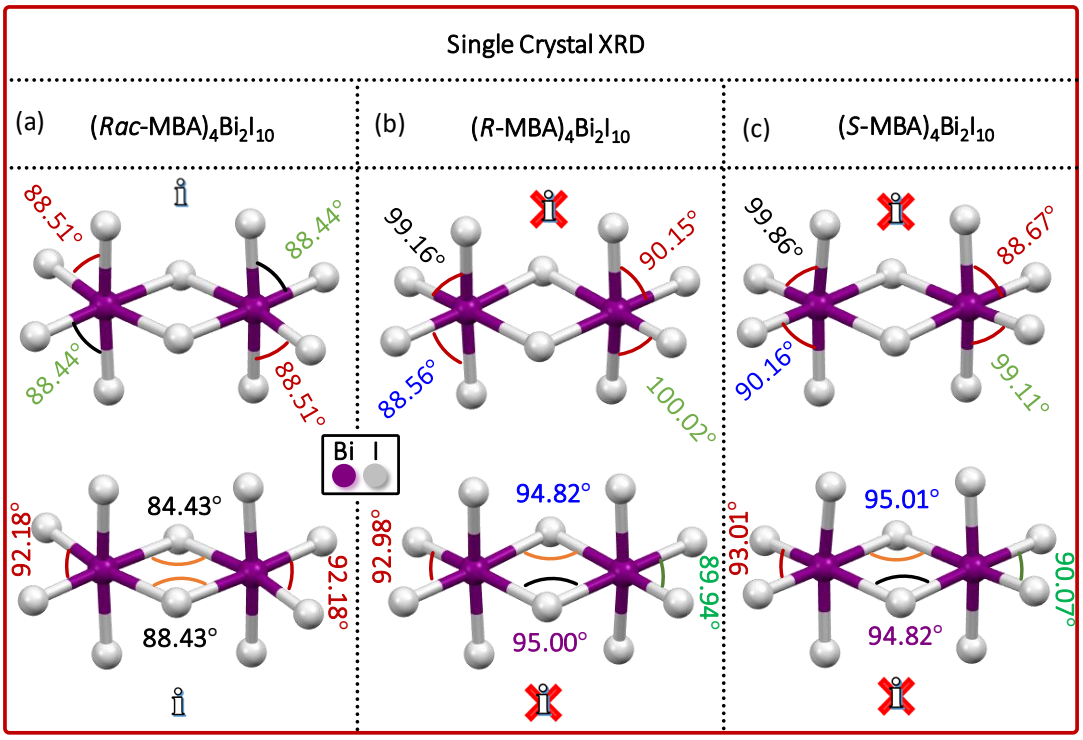

Figure 5.5: Bond angle representation of inorganic dimer $[Bi_2I_{10}]^{4-}$ of (*Rac*-, *R*-, and *S*-MBA)$_4Bi_2I_{10}$, obtained from SCXRD data at 120 K. Diagonally opposite I-Bi-I bond angles of (*Rac*-MBA)$_4Bi_2I_{10}$ are equal, fulfilling a requirement of inversion symmetry "i". Diagonally opposite I-Bi-I bond angles (*R*- and *S*-MBA)$_4Bi_2I_{10}$ are different, indicating the absence of inversion symmetry "i".

However, such a correlation is not satisfactory. A reliable structural descriptor for quantitative estimation of the extent of chirality in 0D structure is still absent, unlike the recent reports[37-38] of 2D layered perovskites. Similar to the case of (*S*-MBA)$_4Bi_2I_{10}$, Figure 5.4c shows that both the organic and inorganic sublattice of (*S*-MBA)$_4Bi_2I_{10}$ are also chiral. Also, most of the bond angles are different from each other as shown in Figure 5.5c.

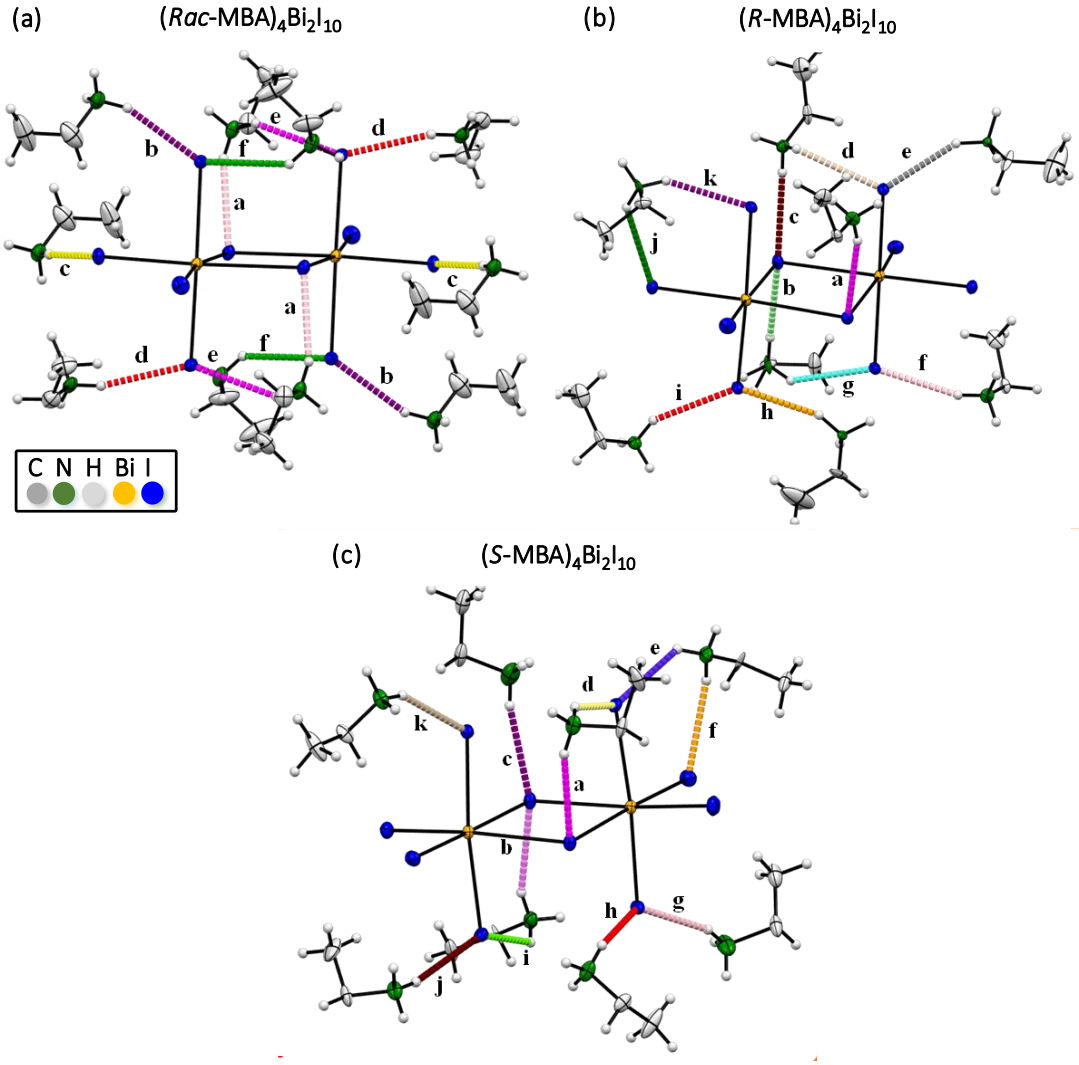

Figure 5.6: Hydrogen bonding interactions between the H-atoms (light gray colour) of organic ammonium cations (to avoid the crowd phenyl group of organic ammonium cations is removed from the figures) and I-atoms (blue colour) of Bi-I of $[Bi_2I_{10}]^{4-}$ dimers are shown by the different colour dotted lines. (a) In (*Rac*-MBA)$_4Bi_2I_{10}$ crystal two I-atoms of Bi-I-Bi bridging units have two such interactions in opposite direction which counterbalance the overall effect represented by same pink color dotted lines also by the symbol "a". In the same manner other H-bonding interactions have same strength but in opposite directions are shown by the purple, yellow, red, magenta and green color dotted lines, which are labeled as b, c, d, e and f, respectively. This shows the symmetry in H-bonding. (b) and (c) In (*R*- and *S*-MBA)$_4Bi_2I_{10}$ crystal all the H-bonds have unequal strengths as labeled by different colours and notations from "a" to "k" respectively. This shows the asymmetry in H-bonding. Compared to the (*Rac*-MBA)$_4Bi_2I_{10}$ crystal a greater number of hydrogen bonding interactions are present in (*R*- and *S*-MBA)$_4Bi_2I_{10}$ crystal.

Table 5.3: Bond length distortion index (D)[39] and bond angle variance (σ^2)[40] for an individual octahedron of (*Rac*-, *R*-, and *S*-MBA)$_4$Bi$_2$I$_{10}$ and reported Bi-iodide 0D structures have been calculated from the deposited crystal information files (CIFs) at room temperature.

$$D = \frac{1}{6}\sum_{i=1}^{6}\frac{|d_i - d_0|}{d_0} \qquad (3)$$

$$\sigma^2 = \frac{1}{11}\sum_{i=1}^{12}(\theta_i - 90)^2 \qquad (4)$$

Where, d_i= individual Bi-I bond lengths,

d_0= mean Bi-I bond distances, and

θ_i = octahedral I-Bi-I bond angles

Sample	Crystal Structure Description	(D)	(σ^2) (deg^2)	Ref.
(*Rac*-MBA)$_4$Bi$_2$I$_{10}$ (Achiral)	0D (edge-shared $[Bi_2I_{10}]^{4-}$ dimer)	0.039	18.03	This Work
(*R*-MBA)$_4$Bi$_2$I$_{10}$ (Chiral)		0.040	17.33	
(*S*-MBA)$_4$Bi$_2$I$_{10}$ (Chiral)		0.040	17.88	
[(*R*)-1-(4-F) phenylethylamine]$_4$[Bi$_2$I$_{10}$] (Chiral)	0D (edge-shared $[Bi_2I_{10}]^{4-}$ dimer)	0.036	13.71	[33]
(1,3propanediammonium)$_2$Bi$_2$I$_{10}$.2 H$_2$O (Achiral)	0D (edge-shared $[Bi_2I_{10}]^{4-}$ dimer)	0.031	13.44	[41]
(Benzylammonium)$_3$Bi$_2$I$_9$ (Achiral)	0D (face-shared $[Bi_2I_9]^{3-}$ dimer)	0.040	21.68	[42]
(Biphenylbis(methylammonium))$_{1.5}$ BiI$_6$.2H$_2$O (Achiral)	0D (isolated $[BiI_6]^{3-}$ octahedra)	0.015	6.86	[43]
(Naphthalenediimidebis(ethylammonium))$_{1.5}$BiI$_6$.2H$_2$O (Achiral)		0.020	6.66	

A few noteworthy observations from Table 5.3: (i) two samples have isolated $[BiI_6]^{3-}$ octahedron and show significantly smaller values of D and σ^2; (ii) all other samples have either edge-shared or face-shared ($[Bi_2I_{10}]^{4-}$ or $[Bi_2I_9]^{3-}$) dimer with much higher values of D and σ^2; (iii) the values D and σ^2 of an octahedron in $[Bi_2I_{10}]^{4-}$ or $[Bi_2I_9]^{3-}$ dimer are not correlated with chirality; and (iv) the face-shared samples show higher D and σ^2 values even compared to the edge-shared ones, irrespective of chirality. Overall, the D and σ^2 values do not predominantly depend on chirality of these system. Instead, the D and σ^2 values of 0D perovskites is governed by whether the octahedra are isolated, or edge-shared or face-shared.

5.3.3 Chiroptical Properties

To explore the effect of chiral structure on optical properties, films of (*Rac*-/*R*-/*S*-MBA)$_4$Bi$_2$I$_{10}$ are used. The photographs of yellow colored (*Rac*-, *R*-, and *S*-MBA)$_4$Bi$_2$I$_{10}$ thin films are shown in Figure 5.7a. UV-visible absorption data of the films are shown in Figure 5.7c manifests a sharp exciton absorption followed by continuum band. Spectra for all three samples are almost identical, suggesting that the structural chirality does not impact the band gap.

An exciton contribution is decoupled from continuum using Elliott equation[44-45] for a hydrogenic Wannier-Mott exciton given by

$$\alpha_T(E) = A \cdot R_{ex} \cdot \sum_{n=1}^{\infty} \frac{4\pi}{n^3} \cdot \delta\left(E - E_c + \frac{R_{ex}}{n^2}\right) + [A \cdot \Theta(E - E_c) \cdot D_{cv}(E)] \cdot \left[\frac{\pi x e^{\pi x}}{Sinh(\pi x)}\right] \qquad (5)$$

where A, E, E_c, R_{ex}, Θ, and δ are dipole transitions across the band gap, the energy of the photon, band gap, Rydberg binding energy of exciton, heaviside unit step function and delta function, respectively. $D_{cv} \propto \sqrt{(E - E_c)}$ is the joint density of states (JDOS) responsible for the continuum states above the bandgap and $x = \sqrt{\frac{R_{ex}}{E - E_c}}$. The first term accounts for the absorption due to the Coulomb interaction bound electron-hole pair known as exciton below bandgap, while the second term accounts for the continuum states absorption above the bandgap (Sommerfeld factor right square bracket). The modeling, accomplished by convolving Equation (5) with a Gaussian function to account for inhomogeneous line broadening (see Figure 5.7c), reveals exciton centered at 2.48 ± 0.01 eV (500 nm) and continuum band at 2.63 ± 0.01 eV (472 nm). This suggests a high exciton binding energy (150 meV) indicating confinement of electron and hole in the inorganic [Bi$_2$I$_{10}$]$^{4-}$ dimers of the 0D perovskite derivative structure. Such confinement might become helpful for non-linear optical properties[17] and light emission, but will be detrimental for charge transport.

Chiral structures are known to interact with left and right circularly polarized light differently. So, we measured CD spectra of (*Rac*-, *R*-/*S*-MBA)$_4$Bi$_2$I$_{10}$ thin films in transmission mode. The CD spectra show distinct features in case of (*R*- and *S*-MBA)$_4$Bi$_2$I$_{10}$ while (*Rac*-MBA)$_4$Bi$_2$I$_{10}$ remains featureless in the whole wavelength range as shown in Figure 5.8b. The CD spectra show exactly opposite signals with peaks at the same wavelengths 315 nm, 369 nm, 485 nm, and 517 nm for

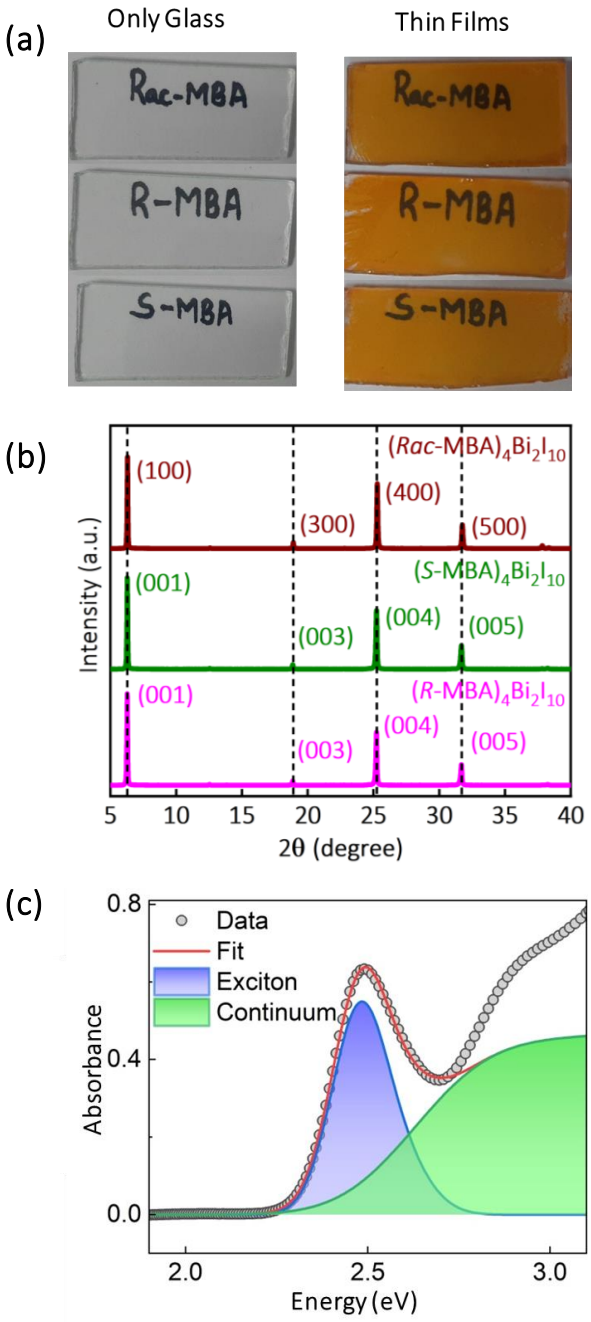

Figure 5.7: (a) Digital photographs of films of (*Rac*-, *R*-, and *S*-MBA)$_4$Bi$_2$I$_{10}$ on the glass substrate. (b) Powder XRD patterns of thin films of (*Rac*-, *R*-, and *S*-MBA)$_4$Bi$_2$I$_{10}$ at room temperature show the layered behavior, in accordance with Figure 5.2 (a-c) and 5.2 (d-f). (c) Ground state optical absorption of (*Rac*-MBA)$_4$Bi$_2$I$_{10}$ with theoretical fit using Elliott model. (Note: Analysis and discussion related to Figure 5.7c was performed by Ajay K. Poonia and Megha Shrivastav from Prof. K. V. Adarsh's Lab at IISER Bhopal)

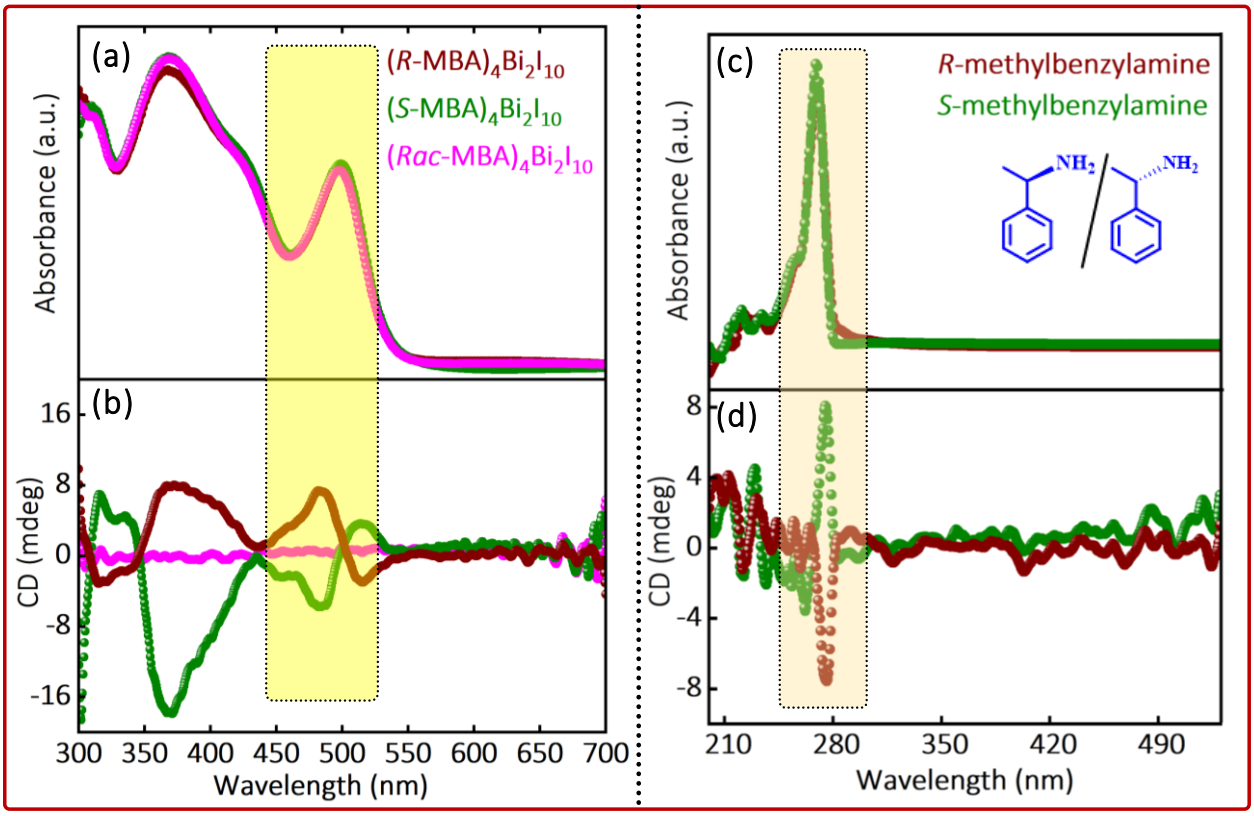

Figure 5.8: (a) Linear optical absorbance and (b) circular dichroism (CD) spectra of (*Rac*-, *R*-, and *S*-MBA)$_4$Bi$_2$I$_{10}$ thin films. CD spectra show the derivative feature close to the excitonic absorption peak (500 nm). The highlighted region shows the excitonic absorption and corresponding derivative like bipolar CD signals of (*R*- and *S*-MBA)$_4$Bi$_2$I$_{10}$. (c) Linear optical absorption and (d) circular dichroism (CD) spectra of (*R*-, and *S*-methylbenzylamine) dissolved in dimethylformamide. The spectra are recorded in the transmission mode.

(*R*- and *S*-MBA)$_4$Bi$_2$I$_{10}$. None of these chiroptical active transitions is from the organic component, which only absorbs in the lower wavelength range of 200–300 nm (Figure 5.8c and 5.8d).

The CD spectra of (*R*- and *S*-MBA)$_4$Bi$_2$I$_{10}$ exhibit a derivative-like bi-polar response close to the excitonic absorption peak of 500 nm. This is indicative of the CD transitions originating from the inorganic sub-lattice, agreeing with the finding of structural chirality of the inorganic sub-lattice. Similar bi-polar CD signals at the excitonic transition have been previously reported in the case of (*R*- and *S*-MBA)$_2$PbI$_4$ and also in chiral semiconductor quantum dots.[2, 27-28, 46] The peak energy splitting is typically attributed to the lifting of the spin degeneracy due to spin-orbit coupling (SOC) within the electronic absorption band. The anisotropy factor (g) is calculated as

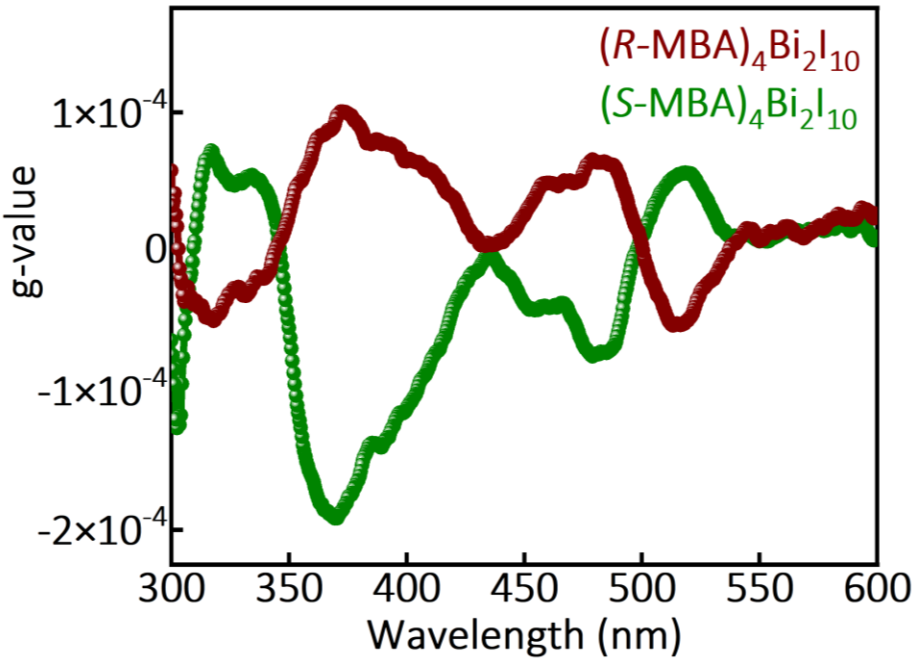

Figure 5.9: The anisotropy factor (g) of (*R*- and *S*-MBA)$_4$Bi$_2$I$_{10}$ thin films calculated from the CD data at room temperature.

CD / (absorbance × 32980), and is plotted in Figure 5.9. The g-factor of (*R*- and *S*-MBA)$_4$Bi$_2$I$_{10}$ is in the order of 10^{-4}, which is slightly lower compared to the reported chiral lead-free perovskite derivative structures (see Table 5.4). To compete with chiral Pb halide perovskites, the g-factor of Pb-free perovskites needs to be increased by more than an order of magnitude.

Table 5.4: The g-factor of chiral (*R*- and *S*-MBA)$_4$Bi$_2$I$_{10}$ and reported chiral lead-free perovskite derivative structures at room temperature.

Sample	g-factor	Ref.
(*R*-MBA)$_4$Bi$_2$I$_{10}$	1.0014×10^{-4}	This work
(*S*-MBA)$_4$Bi$_2$I$_{10}$	1.8892×10^{-4}	
[(I-C$_8$H$_{12}$N)$_4$][Bi$_2$Br$_{10}$]	8.02×10^{-4}	[30]
[((S)-C$_8$H$_{12}$N)$_4$][Bi$_2$Br$_{10}$]	1.28×10^{-3}	

5.3.4 Temperature-Dependent PL

Figure 5.10a shows that (*R*-MBA)$_4$Bi$_2$I$_{10}$ films at 300 K has an emission maximum at 550 nm (2.25 eV), with about 230 meV Stokes shift compared to the excitonic absorption peak as shown in the inset to Figure 5.10a. As the measurement temperature decreases, a PL peak at lower wavelengths dominates (Figure 5.10a). At 7 K, a narrow peak at 512 nm (2.42 eV) dominates the PL spectrum. This sharp peak can be assigned as the excitonic emission. The pseudo colormap in Figure 5.10b indicates PL spectra at multiple temperatures. The intensity of the excitonic emission with a peak ~512 nm increases systematically with decreasing temperatures below 100 K. This increase in intensity is because of the suppression of non-radiative decay channels at lower temperatures. Figure 5.10c shows PL decay of (*R*-MBA)$_4$Bi$_2$I$_{10}$ thin films. The decay profiles are fitted using a bi-exponential decay equation. The best-fit-parameters are shown in Table 5.5. At 7 K, the emission at 512 nm has an average lifetime of 5.5 ns. This fast lifetime agrees with the assignment of excitonic emission. Prior reports of chiral Pb-free hybrid metal halide perovskites do not show excitonic emission. The observed excitonic emission in our samples suggests lesser non-radiative defect channels compared to prior reports.[31]

Table 5.5: The best-fit parameters of bi-exponential PL decay of (*R*-MBA)$_4$Bi$_2$I$_{10}$ shown in Figure 5.10c. τ_i represents the lifetime of the i^{th} decay component and A_i is the corresponding amplitude. The average lifetime is denoted as τ_{av}.

Emission wavelength and temperature	**A_1 (%)**	**A_2 (%)**	**τ_1 (ns)**	**τ_2 (ns)**	$\boldsymbol{\tau_{av} = \sum A_i\tau_i^2 / A_i\,\tau_i}$ **(ns)**
512 nm at 7 K	85	15	1.5	9.2	5.5
550 nm at 7 K	74	26	1.8	12.4	9.3
550 nm at 300 K	70	30	1.8	11.9	9.0

The average lifetimes of the emission of (*R*-MBA)$_4$Bi$_2$I$_{10}$ films at 550 nm have been found to be 9.3 ns and 9.0 ns at 7 K and 300 K (Table 5.5), respectively. The average lifetime of 550 nm emission is slightly longer than that of the excitonic emission (512 nm). But still the observed

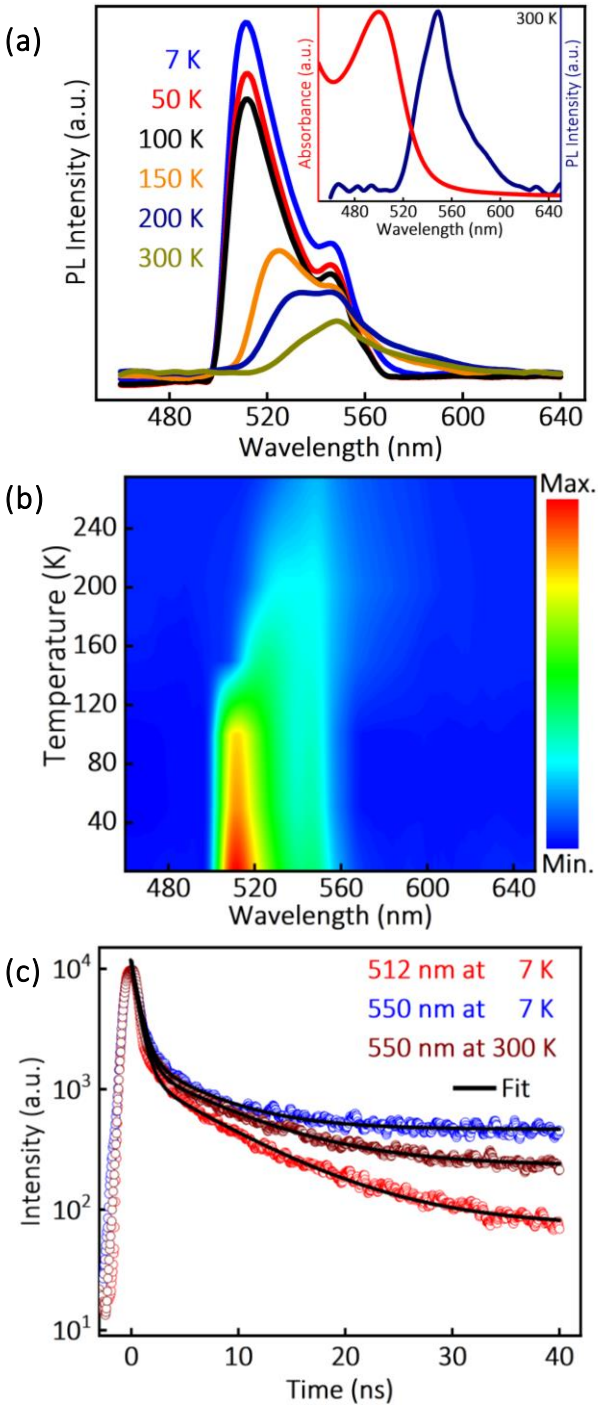

Figure 5.10: (a) Temperature-dependent PL spectra of the (*R*-MBA)$_4$Bi$_2$I$_{10}$ thin film. The inset compares the room temperature optical absorbance and PL. (b) Pseudo colormap of temperature-dependent PL spectra. (c) Temperature-dependent PL decay dynamics of the (*R*-MBA)$_4$Bi$_2$I$_{10}$ thin film.

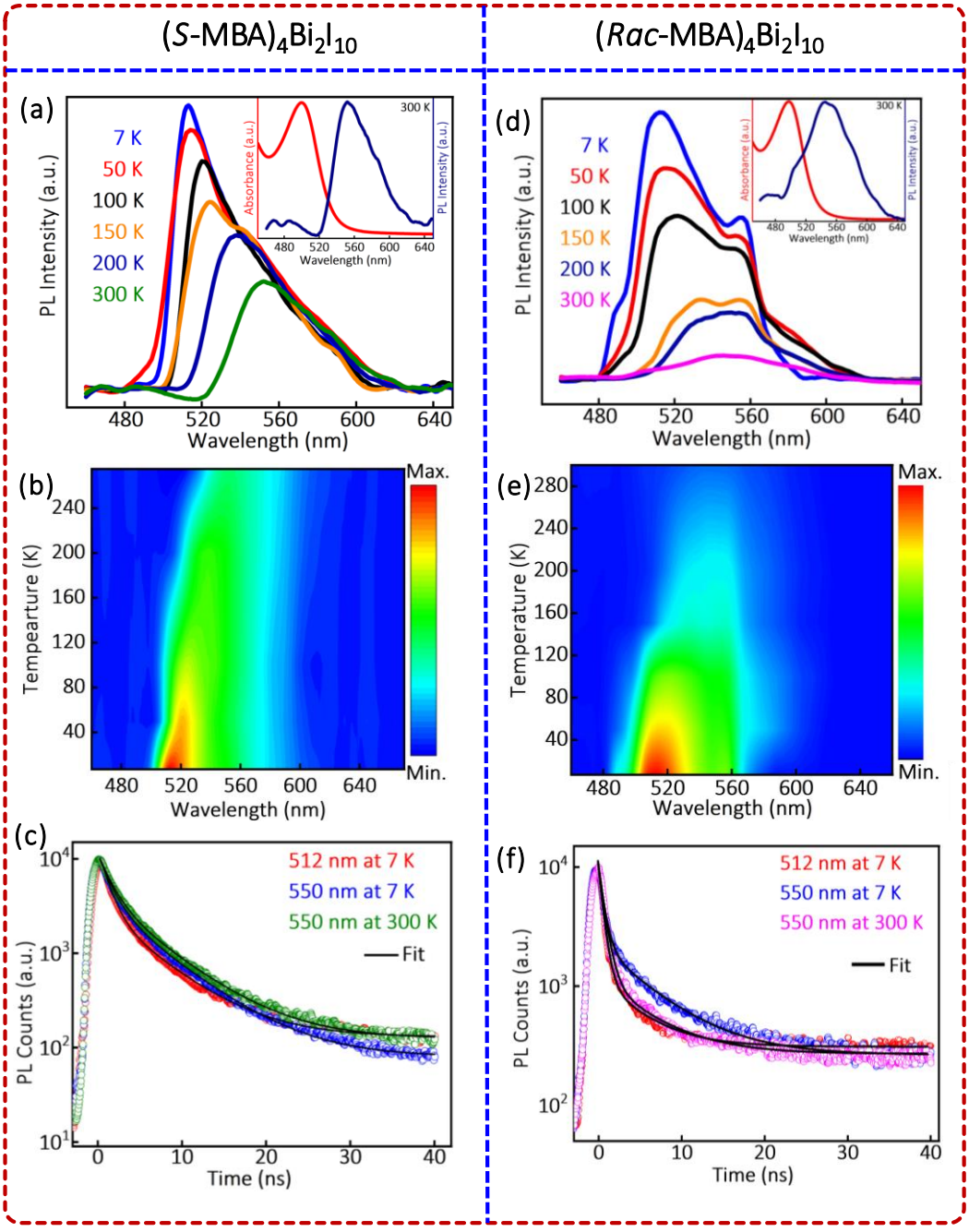

Figure 5.11: (a) Temperature-dependent PL spectra of (*S*-MBA)$_4$Bi$_2$I$_{10}$ thin film. Inset compares the absorption and PL spectra at room temperature. (b) Corresponding pseudo color contour map of temperature-dependent PL. (c) Temperature-dependent PL decay profiles. (d) Temperature-dependent PL spectra of (*Rac*-MBA)$_4$Bi$_2$I$_{10}$ thin film. Inset compares the absorption and PL spectra at room temperature. (e) Corresponding pseudo color contour map of temperature-dependent PL. (f) Temperature-dependent PL decay profiles.

lifetime of 550 nm emission is significantly shorter than a typical deep trap[47] emission or emission originating from $6s^2$ electrons of isolated Bi^{3+} ion,[48] that often has a lifetime around 100 ns or longer. The small Stokes shift (Figure 5.10a) and relatively small lifetime suggest that the 550 nm emission involves shallow defects close to band edges.

Temperature-dependent PL data for (*S*-MBA)$_4$Bi$_2$I$_{10}$ and (*Rac*-MBA)$_4$Bi$_2$I$_{10}$ films are shown in Figures 5.11 (a-c) and 5.11 (d-f), along with their best-fit parameters in Table 5.6 and 5.7, respectively. Overall, the PL data for all the three samples (*Rac*-/*R*-/*S*-MBA)$_4$Bi$_2$I$_{10}$ are similar, suggesting that the chirality does not significantly impact the PL peak positions and dynamics.

Table 5.6: The best-fit parameters of bi-exponential PL decay of (*S*-MBA)$_4$Bi$_2$I$_{10}$ shown in Figure 5.11c. τ_i represents the lifetime of the i_{th} decay component and A_i is the corresponding amplitude. The average lifetime is denoted as τ_{av}.

Emission wavelength and temperature	**A_1 (%)**	**A_2 (%)**	**τ_1 (ns)**	**τ_2 (ns)**	**$\tau_{av} = \sum A_i\tau_i^2/A_i\,\tau_i$ (ns)**
512 nm at 7 K	82	18	1.9	10.2	6.4
550 nm at 7 K	61	29	2	9.9	8.2
550 nm at 300 K	74	26	2.0	11.1	8.1

Table 5.7: The best-fit parameters of bi-exponential PL decay of (*Rac*-MBA)$_4$Bi$_2$I$_{10}$ shown in Figure 5.11f. τ_i represents the lifetime of the i_{th} decay component and A_i is the corresponding amplitude. The average lifetime is denoted as τ_{av}.

Emission wavelength and temperature	**A_1 (%)**	**A_2 (%)**	**τ_1 (ns)**	**τ_2 (ns)**	**$\tau_{av} = \sum A_i\tau_i^2/A_i\,\tau_i$ (ns)**
512 nm at 7 K	78	22	1.6	13.9	10.4
550 nm at 7 K	65	35	1.7	16.9	14.5
550 nm at 300 K	73	27	1.7	14.3	11.9

5.4 Conclusions

We have prepared single crystals and films of (*Rac*-, *R*-, and *S*-MBA)$_4$Bi$_2$I$_{10}$ 0D Pb-free hybrid perovskite derivatives. SCXRD data show that the (*Rac*-MBA)$_4$Bi$_2$I$_{10}$ crystallizes in an achiral space group P2$_1$/c, and both (*R*-, and *S*-MBA)$_4$Bi$_2$I$_{10}$ crystallize in the chiral Sohncke space group of P2$_1$. Importantly, the organic sub-lattice of *R*- and *S*-MBA, induces chirality in the Bi-I inorganic sub-lattice through the hydrogen bonding interactions at the organic-inorganic interface. Consequently, the excitonic transitions arising from the inorganic sub-lattice interacts differently with left and right circularly polarized light, as shown by the CD spectra. Excitonic photophysics of (*Rac*-, *R*-, and *S*-MBA)$_4$Bi$_2$I$_{10}$ is explored by using temperature (7 K to 300 K) dependent PL. The rationally designed structure of (*R*-, and *S*-MBA)$_4$Bi$_2$I$_{10}$ showing excitonic chiroptical properties will motivate future research to develop novel chiral perovskite semiconductors.

5.5 References

1. Billing, D. G.; Lemmerer, A. Synthesis and crystal structures of inorganic–organic hybrids incorporating an aromatic amine with a chiral functional group. *CrystEngComm* **2006,** *8*, 686-695.

2. Ahn, J.; Lee, E.; Tan, J.; Yang, W.; Kim, B.; Moon, J. A new class of chiral semiconductors: chiral-organic-molecule-incorporating organic–inorganic hybrid perovskites. *Mater. Horiz.* **2017,** *4*, 851-856.

3. Gao, X.; Han, B.; Yang, X.; Tang, Z. Perspective of Chiral Colloidal Semiconductor Nanocrystals: Opportunity and Challenge. *J. Am. Chem. Soc.* **2019,** *141*, 13700-13707.

4. Kim, Y.-H.; Zhai, Y.; Gaulding, E. A.; Habisreutinger, S. N.; Moot, T.; Rosales, B. A.; Lu, H.; Hazarika, A.; Brunecky, R.; Wheeler, L. M.; Berry, J. J.; Beard, M. C.; Luther, J. M. Strategies to Achieve High Circularly Polarized Luminescence from Colloidal Organic–Inorganic Hybrid Perovskite Nanocrystals. *ACS Nano* **2020,** *14*, 8816-8825.

5. Long, G.; Sabatini, R.; Saidaminov, M. I.; Lakhwani, G.; Rasmita, A.; Liu, X.; Sargent, E. H.; Gao, W. Chiral-perovskite optoelectronics. *Nat. Rev. Mater.* **2020,** *5*, 423-439.

6. Manser, J. S.; Christians, J. A.; Kamat, P. V. Intriguing Optoelectronic Properties of Metal Halide Perovskites. *Chem. Rev.* **2016,** *116*, 12956-13008.

7. Sheikh, T.; Shinde, A.; Mahamuni, S.; Nag, A. Possible Dual Bandgap in (C$_4$H$_9$NH$_3$)$_2$PbI$_4$ 2D

Layered Perovskite: Single-Crystal and Exfoliated Few-Layer. *ACS Energy Lett.* **2018,** *3*, 2940-2946.

8. Shynkarenko, Y.; Bodnarchuk, M. I.; Bernasconi, C.; Berezovska, Y.; Verteletskyi, V.; Ochsenbein, S. T.; Kovalenko, M. V. Direct Synthesis of Quaternary Alkylammonium-Capped Perovskite Nanocrystals for Efficient Blue and Green Light-Emitting Diodes. *ACS Energy Lett.* **2019,** *4*, 2703-2711.

9. Hamdeh, U. H.; Ryan, B. J.; Nelson, R. D.; Zembrzuski, M.; Slobidsky, J.; Prince, K. J.; Cleveland, I.; Vela-Ramirez, A.; Hillier, A. C.; Panthani, M. G. Solution-Processed Bismuth Halide Perovskite Thin Films: Influence of Deposition Conditions and A-Site Alloying on Morphology and Optical Properties. *J. Phys. Chem. Lett.* **2019,** *10*, 3134-3139.

10. Febriansyah, B.; Borzda, T.; Cortecchia, D.; Neutzner, S.; Folpini, G.; Koh, T. M.; Li, Y.; Mathews, N.; Petrozza, A.; England, J. Metal Coordination Sphere Deformation Induced Highly Stokes-Shifted, Ultra Broadband Emission in 2D Hybrid Lead-Bromide Perovskites and Investigation of Its Origin. *Angew. Chem. Int. Ed.* **2020,** *59*, 10791-10796.

11. Sheikh, T.; Nawale, V.; Pathoor, N.; Phadnis, C.; Chowdhury, A.; Nag, A. Molecular Intercalation and Electronic Two Dimensionality in Layered Hybrid Perovskites. *Angew. Chem. Int. Ed.* **2020,** *59*, 11653-11659.

12. Vargas, B.; Rodríguez-López, G.; Solis-Ibarra, D. The Emergence of Halide Layered Double Perovskites. *ACS Energy Lett.* **2020,** *5*, 3591-3608.

13. Yin, W.; Li, H.; Chesman, A. S. R.; Tadgell, B.; Scully, A. D.; Wang, M.; Huang, W.; McNeill, C. R.; Wong, W. W. H.; Medhekar, N. V.; Mulvaney, P.; Jasieniak, J. J. Detection of Halomethanes Using Cesium Lead Halide Perovskite Nanocrystals. *ACS Nano* **2021,** *15*, 1454-1464.

14. Dey, A.; Ye, J.; De, A.; Debroye, E.; Ha, S. K.; Bladt, E.; Kshirsagar, A. S.; Wang, Z.; Yin, J.; Wang, Y.; Quan, L. N.; Yan, F.; Gao, M.; Li, X.; Shamsi, J.; Debnath, T.; Cao, M.; Scheel, M. A.; Kumar, S.; Steele, J. A.; Gerhard, M.; Chouhan, L.; Xu, K.; Wu, X.-g.; Li, Y.; Zhang, Y.; Dutta, A.; Han, C.; Vincon, I.; Rogach, A. L.; Nag, A.; Samanta, A.; Korgel, B. A.; Shih, C.-J.; Gamelin, D. R.; Son, D. H.; Zeng, H.; Zhong, H.; Sun, H.; Demir, H. V.; Scheblykin, I. G.; Mora-Seró, I.; Stolarczyk, J. K.; Zhang, J. Z.; Feldmann, J.; Hofkens, J.; Luther, J. M.; Pérez-Prieto, J.; Li, L.;

Manna, L.; Bodnarchuk, M. I.; Kovalenko, M. V.; Roeffaers, M. B. J.; Pradhan, N.; Mohammed, O. F.; Bakr, O. M.; Yang, P.; Müller-Buschbaum, P.; Kamat, P. V.; Bao, Q.; Zhang, Q.; Krahne, R.; Galian, R. E.; Stranks, S. D.; Bals, S.; Biju, V.; Tisdale, W. A.; Yan, Y.; Hoye, R. L. Z.; Polavarapu, L. State of the Art and Prospects for Halide Perovskite Nanocrystals. *ACS Nano* **2021,** *15*, 10775-10981.

15. Wang, X.-D.; Huang, Y.-H.; Liao, J.-F.; Wei, Z.-F.; Li, W.-G.; Xu, Y.-F.; Chen, H.-Y.; Kuang, D.-B. Surface passivated halide perovskite single-crystal for efficient photoelectrochemical synthesis of dimethoxydihydrofuran. *Nat. Commun.* **2021,** *12*, 1202.

16. Wang, S.; Kershaw, S. V.; Rogach, A. L. Bright and Stable Dion-Jacobson Tin Bromide Perovskite Microcrystals Realized by Primary Alcohol Dopants. *Chem. Mater.* **2021,** *33*, 5413-5421.

17. Yao, L.; Zeng, Z.; Cai, C.; Xu, P.; Gu, H.; Gao, L.; Han, J.; Zhang, X.; Wang, X.; Wang, X.; Pan, A.; Wang, J.; Liang, W.; Liu, S.; Chen, C.; Tang, J. Strong Second- and Third-Harmonic Generation in 1D Chiral Hybrid Bismuth Halides. *J. Am. Chem. Soc.* **2021,** *143*, 16095-16104.

18. Lin, Y. L.; Blackburn, J. L.; Beard, M. C.; Johnson, J. C. Interlayer Triplet-Sensitized Luminescence in Layered Two-Dimensional Hybrid Metal-Halide Perovskites. *ACS Energy Lett.* **2021,** *6*, 4079-4096.

19. Nag, A. "Plenty of Room" at the Interface of Hybrid Metal Halide Perovskite Single Crystals. *Nano Lett.* **2021,** *21*, 8529-8531.

20. Long, G.; Jiang, C.; Sabatini, R.; Yang, Z.; Wei, M.; Quan, L. N.; Liang, Q.; Rasmita, A.; Askerka, M.; Walters, G.; Gong, X.; Xing, J.; Wen, X.; Quintero-Bermudez, R.; Yuan, H.; Xing, G.; Wang, X. R.; Song, D.; Voznyy, O.; Zhang, M.; Hoogland, S.; Gao, W.; Xiong, Q.; Sargent, E. H. Spin control in reduced-dimensional chiral perovskites. *Nat. Photonics* **2018,** *12*, 528-533.

21. Yuan, C.; Li, X.; Semin, S.; Feng, Y.; Rasing, T.; Xu, J. Chiral Lead Halide Perovskite Nanowires for Second-Order Nonlinear Optics. *Nano Lett.* **2018,** *18*, 5411-5417.

22. Ma, J.; Fang, C.; Chen, C.; Jin, L.; Wang, J.; Wang, S.; Tang, J.; Li, D. Chiral 2D Perovskites with a High Degree of Circularly Polarized Photoluminescence. *ACS Nano* **2019,** *13*, 3659-3665.

23. Ahn, J.; Ma, S.; Kim, J.-Y.; Kyhm, J.; Yang, W.; Lim, J. A.; Kotov, N. A.; Moon, J. Chiral 2D Organic Inorganic Hybrid Perovskite with Circular Dichroism Tunable Over Wide Wavelength

Range. *J. Am. Chem. Soc.* **2020,** *142*, 4206-4212.

24. Huang, P.-J.; Taniguchi, K.; Miyasaka, H. Bulk Photovoltaic Effect in a Pair of Chiral–Polar Layered Perovskite-Type Lead Iodides Altered by Chirality of Organic Cations. *J. Am. Chem. Soc.* **2019,** *141*, 14520-14523.

25. Chen, C.; Gao, L.; Gao, W.; Ge, C.; Du, X.; Li, Z.; Yang, Y.; Niu, G.; Tang, J. Circularly polarized light detection using chiral hybrid perovskite. *Nat. Commun.* **2019,** *10*, 1927. 26. Wang, L.; Xue, Y.; Cui, M.; Huang, Y.; Xu, H.; Qin, C.; Yang, J.; Dai, H.; Yuan, M. A Chiral Reduced-Dimension Perovskite for an Efficient Flexible Circularly Polarized Light Photodetector. *Angew. Chem. Int. Ed.* **2020,** *59*, 6442-6450.

27. Lu, H.; Wang, J.; Xiao, C.; Pan, X.; Chen, X.; Brunecky, R.; Berry, J. J.; Zhu, K.; Beard, M. C.; Vardeny, Z. V., Spin-dependent charge transport through 2D chiral hybrid lead-iodide perovskites. *Sci. Adv. 5*, eaay0571.

28. Kim, Y.-H.; Zhai, Y.; Lu, H.; Pan, X.; Xiao, C.; Gaulding, E. A.; Harvey, S. P.; Berry, J. J.; Vardeny, Z. V.; Luther, J. M.; Beard, M. C. Chiral-induced spin selectivity enables a room-temperature spin light-emitting diode. *Science* **2021,** *371*, 1129-1133.

29. Yang, C.-K.; Chen, W.-N.; Ding, Y.-T.; Wang, J.; Rao, Y.; Liao, W.-Q.; Tang, Y.-Y.; Li, P.-F.; Wang, Z.-X.; Xiong, R.-G. The First 2D Homochiral Lead Iodide Perovskite Ferroelectrics: [R- and S-1-(4-Chlorophenyl)ethylammonium]$_2$PbI$_4$. *Adv. Mater.* **2019,** *31*, 1808088.

30. Moon, T. H.; Oh, S.-J.; Ok, K. M. [((R)-$C_8H_{12}N)_4$][Bi_2Br_{10}] and [((S)-$C_8H_{12}N)_4$][Bi_2Br_{10}]: Chiral Hybrid Bismuth Bromides Templated by Chiral Organic Cations. *ACS Omega* **2018,** *3*, 17895-17903.

31. Lu, H.; Xiao, C.; Song, R.; Li, T.; Maughan, A. E.; Levin, A.; Brunecky, R.; Berry, J. J.; Mitzi, D. B.; Blum, V.; Beard, M. C. Highly Distorted Chiral Two-Dimensional Tin Iodide Perovskites for Spin Polarized Charge Transport. *J. Am. Chem. Soc.* **2020,** *142*, 13030-13040.

32. Li, Y.; Yang, T.; Liu, X.; Han, S.; Wang, J.; Ma, Y.; Guo, W.; Luo, J.; Sun, Z. A chiral lead-free photoactive hybrid material with a narrow bandgap. *Inorg. Chem. Front.* **2020,** *7*, 2770-2777.

33. Dehnhardt, N.; Axt, M.; Zimmermann, J.; Yang, M.; Mette, G.; Heine, J. Band Gap-Tunable, Chiral Hybrid Metal Halides Displaying Second-Harmonic Generation. *Chem. Mater.* **2020,** *32*, 4801-4807.

34. Pious, J. K.; Muthu, C.; Vijayakumar, C. Organic Spacer Cation Assisted Modulation of the Structure and Properties of Bismuth Halide Perovskites. *Acc. Chem. Res.* **2022,** *55*, 275-285.

35. Pidcock, E., Achiral molecules in non-centrosymmetric space groups. *ChemComm* **2005,** 27, 3457-3459.

36. Atkins, P., *Shriver and Atkins' inorganic chemistry*. Oxford University Press, USA: **2010**.

37. Jana, M. K.; Song, R.; Liu, H.; Khanal, D. R.; Janke, S. M.; Zhao, R.; Liu, C.; Valy Vardeny, Z.; Blum, V.; Mitzi, D. B. Organic-to-inorganic structural chirality transfer in a 2D hybrid perovskite and impact on Rashba-Dresselhaus spin-orbit coupling. *Nat. Commun.* **2020,** *11*, 4699.

38. Jana, M. K.; Song, R.; Xie, Y.; Zhao, R.; Sercel, P. C.; Blum, V.; Mitzi, D. B. Structural descriptor for enhanced spin-splitting in 2D hybrid perovskites. *Nat. Commun.* **2021,** *12*, 4982.

39. Baur, W. The geometry of polyhedral distortions. Predictive relationships for the phosphate group. *Acta Crystallogr. Sect. B: Struct. Crystallogr. Cryst. Chem.* **1974,** *30*, 1195-1215.

40. Robinson, K.; Gibbs, G.; Ribbe, P. Quadratic elongation: a quantitative measure of distortion in coordination polyhedra. *Science* **1971,** *172*, 567-570.

41. Pious, J. K.; Katre, A.; Muthu, C.; Chakraborty, S.; Krishna, S.; Vijayakumar, C. Zero-dimensional lead-free hybrid perovskite-like material with a quantum-well structure. *Chem. Mater.* **2019,** *31*, 1941-1945.

42. Pious, J. K.; Muthu, C.; Dani, S.; Saeki, A.; Vijayakumar, C. Bismuth-based zero-dimensional perovskite-like materials: Effect of benzylammonium on dielectric confinement and photoconductivity. *Chemistry of Materials* **2020,** *32*, 2647-2652.

43. Pious, J. K.; Basavarajappa, M. G.; Muthu, C.; Nishikubo, R.; Saeki, A.; Chakraborty, S.; Takai, A.; Takeuchi, M.; Vijayakumar, C. Self-Assembled Organic Cations-Assisted Band-Edge Tailoring in Bismuth-Based Perovskites for Enhanced Visible Light Absorption and Photoconductivity. *J. Phys. Chem. Lett.* **2021,** *12*, 5758-5764.

44. Elliott, R. J., Intensity of Optical Absorption by Excitons. *Phys. Rev.* **1957,** *108* (6), 1384-1389.

45. Mondal, A.; Aneesh, J.; Kumar Ravi, V.; Sharma, R.; Mir, W. J.; Beard, M. C.; Nag, A.; Adarsh, K. V. Ultrafast exciton many-body interactions and hot-phonon bottleneck in colloidal cesium lead halide perovskite nanocrystals. *Phys. Rev. B* **2018,** *98*, 115418.

46. Ben-Moshe, A.; Teitelboim, A.; Oron, D.; Markovich, G. Probing the Interaction of Quantum Dots with Chiral Capping Molecules Using Circular Dichroism Spectroscopy. *Nano Lett.* **2016,** *16*, 7467-7473.

47. Rao, M. J.; Shibata, T.; Chattopadhyay, S.; Nag, A., Origin of Photoluminescence and XAFS Study of $(ZnS)_{1-x}(AgInS_2)_x$ Nanocrystals. *J. Phys. Chem. Lett.* **2014,** *5*, 167-173.

48. Arfin, H.; Nag, A. Origin of Luminescence in Sb^{3+}- and Bi^{3+}-Doped Cs_2SnCl_6 Perovskites: Excited State Relaxation and Spin–Orbit Coupling. *J. Phys. Chem. Lett.* **2021,** *12*, 10002-10008.

Thesis Summary and Future Outlook

Thesis Summary

Lower-dimensional hybrid halide perovskites have negatively charged inorganic sub-lattices and positively charged organic sublattices, attached together with the non-covalent bonding interactions.[1, 2] This thesis explores electrostatic, hydrogen, and halogen bonding non-covalent interactions of novel A-site ammonium cations with the inorganic sublattices in Pb and Bi-based lower dimensional hybrid halide perovskites. Specially designed A-site cations have potential to affect the chemical and physical properties of lower dimensional hybrid halide perovskites.

In Chapter 2, we have rationally designed a series of meltable A_2PbX_4 2D perovskites. By employing experimental techniques like single crystal x-ray diffraction (SCXRD), differential scanning calorimetry (DSC), thermogravimetry analysis (TGA), we have identified that the main thermodynamic parameter driving their melting is the increase in structural entropy of fusion (ΔS_{fus}). This was achieved by carefully engineering the organic A-site cations. By introducing different tail groups that can make the cation layer rigid in the solid-state structure and become flexible in the liquid state. Furthermore, a photodetector based on melt-pressed films of $(MIPA)_2PbI_4$ was developed, showing promising performance in optoelectronic applications.

Solvents used during the synthesis of the hybrid halide perovskite single crystals and thin films are toxic. The use of toxic solvent must be minimized or reduced. In chapter 3 we have developed the molten-state synthesis method for the Pb halide hybrid perovskites to avoid the toxic solvents. In this method, we utilized the melting properties of the A-site ammonium halide salt (MPEAI), which, in its molten state, exhibits ionic liquid-like behavior and dissolves the lead halide precursors. Upon cooling, we obtained the $(MPEA)_5Pb_3I_{11}$ hybrid perovskite structure. The $(MPEA)_5Pb_3I_{11}$ synthesized through both molten-state and acid-precipitation methods exhibited similar optical and structural properties, demonstrating the effectiveness of this new synthesis approach.

We have successfully designed 1D $(BMPA)BiI_5$ non centrosymmetric hybrid halide perovskite by introducing dissimilar hydrogen bonding non-covalent interactions at the organic–inorganic interface. Methyl substitution at ammonium head reduces rotation at ammonium head, leading to dissimilar hydrogen bonding interactions with the Bi-I layers. This breaks the local

centrosymmetry in its perovskite structure and resulting $P2_1$ crystal system which is non-centrosymmetric polar and chiral. (BMPA)BiI_5 shows visible to infrared tunable second harmonic signals and a signature of bulk photovoltaic effect. Thin films of (BMPA)BiI_5 shows the chiroptic response.

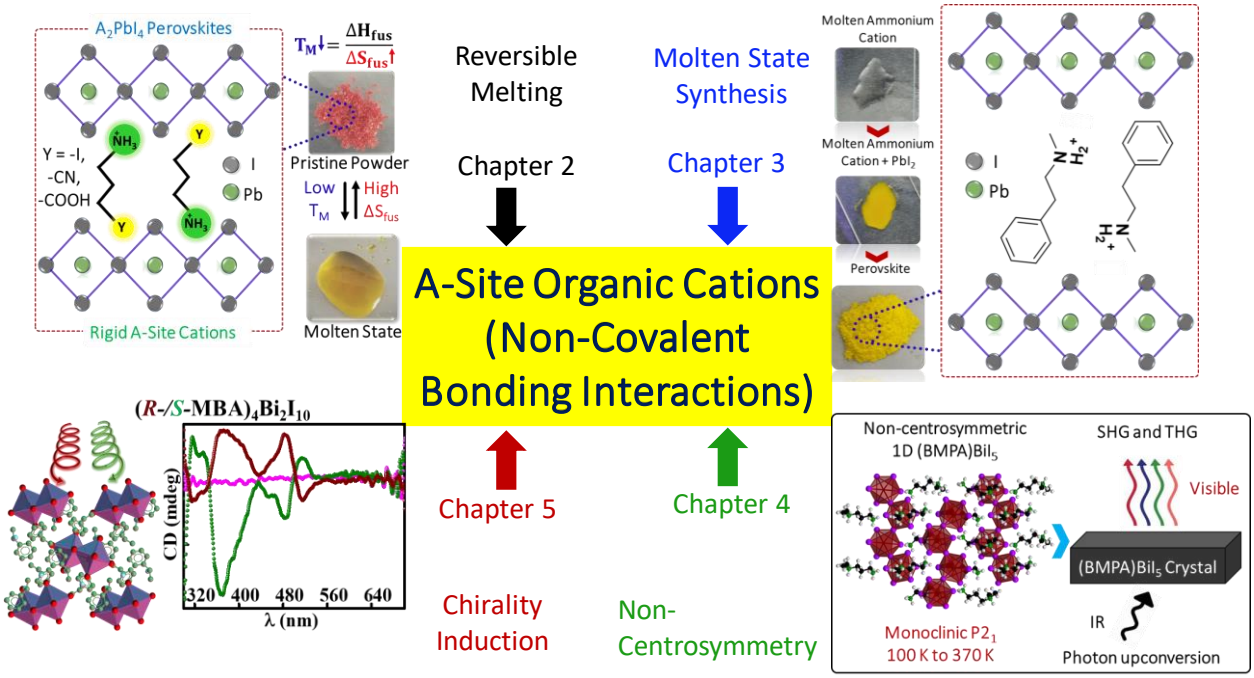

Figure F.1: The graphical summary highlights that functionalities such as reversible melting, molten-state synthesis, non-centrosymmetry, and chirality arise from the non-covalent bonding interactions of specially designed A-site ammonium cations.

In Chapter 5, we investigated the interactions of the chiral ammonium cations (R- and S-MBA) with the inorganic sublattices in 0D (R-/S-MBA)$_4Bi_2I_{10}$ with the help of single crystal x-ray diffraction (SCXRD). (R- and S-MBA) introduce asymmetric hydrogen-bonding interactions with Bi-I dimers in the 0D chiral structure (R-/S-MBA)$_4Bi_2I_{10}$, whereas Rac-MBA induces symmetric hydrogen-bonding interactions with the Bi-I dimers in 0D (Rac-MBA)$_4Bi_2I_{10}$. Finally, we observed chiroptic response from the films of (R-/S-MBA)$_4Bi_2I_{10}$ at excitonic transitions, confirms the chirality. Temperature-dependent (7−300 K) photoluminescence shows excitonic and shallow-defect emissions in (*Rac*-, *R*-, and *S*-MBA)$_4Bi_2I_{10}$.

Overall, the newly introduced functionalities, such as reversible melting, molten state synthesis,

non-centrosymmetry, and chirality in Pb- and Bi-based hybrid halide perovskites are primarily attributed to the hydrogen and halogen bonding non-covalent bonding interactions of newly designed A-site ammonium cations at organic-inorganic interfaces.

Future Outlook

In Chapters 2 and 3, we explore the molten states of perovskites and ammonium salts, which present a fascinating area for further study. These molten materials share notable similarities with ionic liquids,[3, 4] such as (i) low melting temperatures around 100 °C, (ii) a wide liquidus range of approximately 115 °C, and (iii) high viscosity. These characteristics make molten perovskites and ammonium salts promising candidates for further investigations into their unique physical and chemical properties.

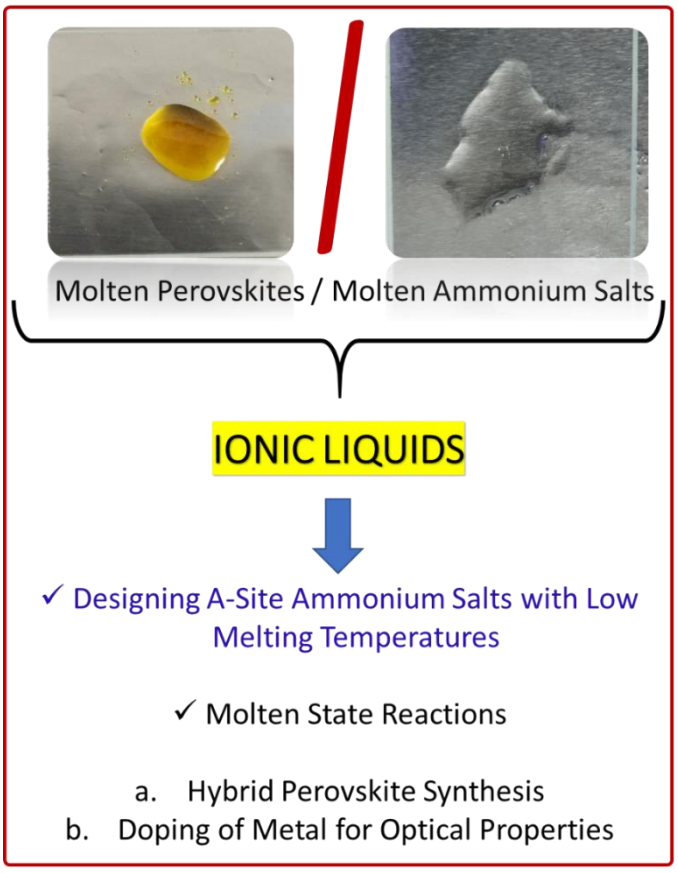

Figure F.2: Molten perovskites and molten ammonium salts are like ionic liquids.

We discovered that some of our A_2PbX_4 perovskites (discussed in Chapter 2) exhibit a melting temperature around 100 °C, with a significant difference of approximately 115 °C between the melting and decomposition temperatures. This satisfies both the criteria of a low melting temperature and a large liquidus range. Although we have not yet measured the exact experimental value of viscosity, one of the 2D perovskites, $(MIPA)_2PbI_4$, forms droplets upon melting without

spreading. This observation suggests that the $(MIPA)_2PbI_4$ in liquid state has a relatively high viscosity. Based upon our observations, we are excited to explore two different directions:

(a) Molten state synthesis of hybrid halide perovskites:

The molten-state method, discussed in Chapter 3, significantly reduces the need for hydrohalic acid (HX, where X: -Br, -I) during the synthesis of hybrid halide perovskites compared to the traditional acid-precipitation method. We applied this method to synthesize hybrid halide perovskites, and it shows great potential. This approach can be applied to synthesize a range of hybrid halide perovskites, as long as the ammonium cation salts used have melting points lower than their decomposition temperatures. We have experimentally measured and summarized the A-site ammonium halide salt's melting temperatures in Table F.1. Furthermore, by careful design, it is possible to create A-site ammonium halide salts that melt at even lower temperatures, potentially below 100 °C.[2]

Table F.1: Containing A-site organic ammonium cations and their melting temperatures

Ammonium Halide Salt (Name and Structures)	Melting Temperature (T_M)
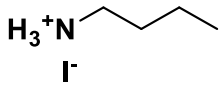 Butyl ammonium iodide	173 °C (446 K)
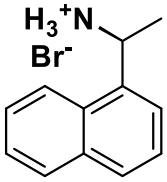 (S)-(−)-1-(1-naphthyl)ethylammonium bromide	194 °C (467 K)

(b) Melt assisted doping in 2D $(MBPA)_2PbBr_4$ perovskite:

New emission centers introduced by doping different metals into hybrid halide perovskites introduces. Metal ion (Mn^{2+}, Yb^{3+} etc.) doping in lower dimensional hybrid halide perovskites is typically achieved through the solvent based method.[5, 6] However, this process often requires a

large amount of dopant precursors, leading to considerable wastage, especially when rare-earth metals like lanthanides are involved. To address this, we explored an alternative approach which involves the meltable hybrid halide perovskites.

To validate this, we have tried to Mn^{2+} doping into 2D $(MBPA)_2PbBr_4$, which resulted in emissions centered at 600 nm. While this is a preliminary attempt, it demonstrates the potential of the molten-state method as a more resource-efficient doping process for hybrid halide perovskites. However, this approach is applicable only to hybrid halide perovskites that form a stable molten state.

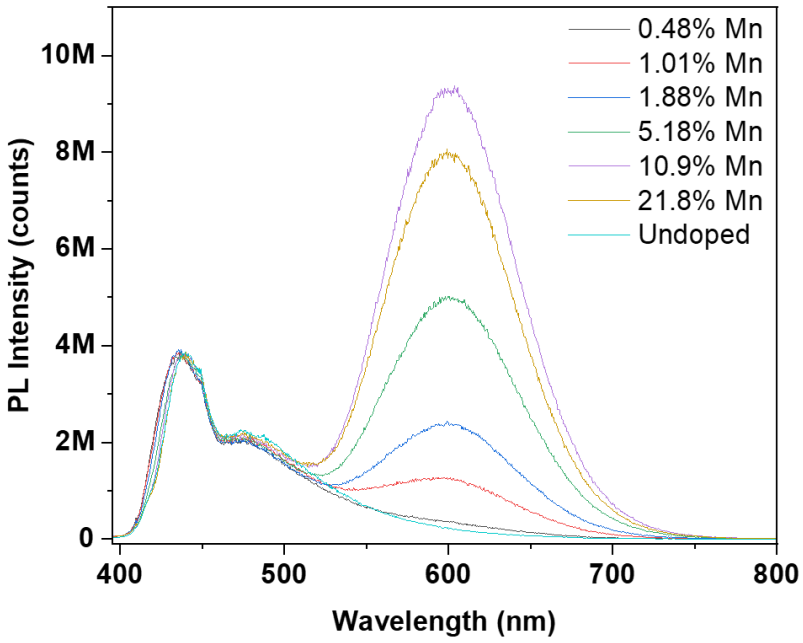

Figure F.3: Emission spectra of Mn doped $(MBPA)_2PbBr_4$. Figure shows that with an increase in $MnBr_2$ content the Mn emission centered at 600 nm increases to 10.9% $MnBr_2$ addition and then decreases.

References

1. Mitzi, D. B. Templating and Structural Engineering in Organic–Inorganic Perovskites. *J. Chem. Soc., Dalton Trans.* **2001,** 1, 1-12.

2. Li, X.; Hoffman, J. M.; Kanatzidis, M. G. The 2D Halide Perovskite Rulebook: How the Spacer Influences Everything from the Structure to Optoelectronic Device Efficiency. *Chem. Rev.* **2021,** *121*, 2230-2291.

3. Introduction: Ionic Liquids. *Chem. Rev.* **2017,** *117*, 6633-6635.

4. Hallett, J. P.; Welton, T. Room-Temperature Ionic Liquids: Solvents for Synthesis and Catalysis. 2. *Chem. Rev.* **2011,** *111*, 3508-3576.

5. Sheikh, T.; Nag, A. Mn Doping in Centimeter-Sized Layered 2D Butylammonium Lead Bromide (BA_2PbBr_4) Single Crystals and Their Optical Properties. *J. Phys. Chem. C* **2019,** *123*, 9420-9427.

6. Mondal, B.; Poovathan, A.; Sheikh, T.; Nag, A. Yb^{3+}-Doped Phenylethylammonium Lead Bromide 2D Layered Hybrid Perovskite for Near-Infrared Emission. *ChemNanoMat* **2022,** *8*, e202200104.

Included in Thesis

1. **Parikshit Kumar Rajput**, Parashurama Salunkhe, Manmayuri Sarma, Meghasree Basu, Animesh Gopal, Aprajita Joshi, Ajinkya Sundarnath Shingote, Surajit Saha, Atikur Rahman, and Angshuman Nag. Entropy-Driven Reversible Melting and Recrystallization of Layered Hybrid Perovskites. *Small* **2024**, 20, 2406735.
2. **Parikshit Kumar Rajput**, Manmayuri Sarma, and Angshuman Nag. Molten State Synthesis of Lead Halide Hybrid Perovskites. Manuscript under preparation.
3. Rayan Chakraborty, **Parikshit Kumar Rajput**, Gokul M. Anilkumar, Shabnum Maqbool, Ranjan Das, Atikur Rahman, Pankaj Mandal, and Angshuman Nag. Rational design of non-centrosymmetric hybrid halide perovskites. *J. Am. Chem. Soc.* **2023**, 145, 1378-1388.
4. **Parikshit Kumar Rajput**, Ajay K. Poonia, Suman Mukherjee, Tariq Sheikh, Megha Shrivastava, K. V. Adarsh, and Angshuman Nag. Chiral methylbenzylammonium bismuth iodide with zero-dimensional perovskite derivative structure. *J. Phys. Chem. C* **2022**, 23, 9889-9897.

Not Included in Thesis

5. Urmila Makhija, **Parikshit Kumar Rajput**, Pavithra Parthiban, and Angshuman Nag. Effect of film morphology on circular dichroism of low-dimensional chiral hybrid perovskites. *J. Chem. Phys.* **2024**, 2, 160.
6. Aparna Shinde, **Parikshit Kumar Rajput**, Urmila Makhija, Riteeka Tanwar, Pankaj Mandal, and Angshuman Nag. Emissive Dark Excitons in Monoclinic Two-Dimensional Hybrid Lead Iodide Perovskites. *Nano Lett.*, **2023**, 23, 6985-6993.
7. Ajinkya Sundarnath Shingote, Taniya Dutta, **Parikshit Kumar Rajput**, and Angshuman Nag. Thermal Evolution of the Structure and Luminescence of the Hybrid-Cation-Stabilized $[(4AMTP)PbBr_2]_2PbBr_4$ Layered Perovskite. *Chem. Mater.* **2024**, 20, 5277-5283.
8. Barnali Mondal, Aparna Shinde, **Parikshit Kumar Rajput**, Habibul Arfin, Riteeka Tanwar, Prasenjit Ghosh, and Angshuman Nag. Vibronically Coupled Near-Infrared Emission and Excitation from d− d Transitions of Cs_2MX_6 (M= Mo/W, X= Cl/Br). *ACS Energy Lett.* **2024**, 9, 819-828.

9. Tariq Sheikh, Shabnum Maqbool, **Parikshit Kumar Rajput**, Pankaj Mandal, and Angshuman Nag. Effect of chirality on the optical properties of layered hybrid perovskite R-and S-α-methylbenzylammonium lead iodide. *Chem. Commun.* **2022,** 58, 7650-7653.

10. Vikash Kumar Ravi, Seong Hoon Yu, **Parikshit Kumar Rajput**, Chandrani Nayak, Dibyendu Bhattacharyya, Dae Sung Chung, and Angshuman Nag. Colloidal $BaZrS_3$ chalcogenide perovskite nanocrystals for thin film device fabrication. *Nanoscale* **2021,** 13, 1616-1623.

Copyrights and Permissions

Quantum and Dielectric Confinement Effects in Lower-Dimensional Hybrid Perovskite Semiconductors

Author: Claudine Katan, Nicolas Mercier, Jacky Even
Publication: Chemical Reviews
Publisher: American Chemical Society
Date: Mar 1, 2019

Bismuth/Silver-Based Two-Dimensional Iodide Double and One-Dimensional Bi Perovskites: Interplay between Structural and Electronic Dimensions

Author: Xiaotong Li, Boubacar Traoré, Mikaël Kepenekian, et al
Publication: Chemistry of Materials
Publisher: American Chemical Society
Date: Aug 1, 2021

The 2D Halide Perovskite Rulebook: How the Spacer Influences Everything from the Structure to Optoelectronic Device Efficiency

Author: Xiaotong Li, Justin M. Hoffman, Mercouri G. Kanatzidis
Publication: Chemical Reviews
Publisher: American Chemical Society
Date: Feb 1, 2021

Two-Dimensional Lead(II) Halide-Based Hybrid Perovskites Templated by Acene Alkylamines: Crystal Structures, Optical Properties, and Piezoelectricity

Author: Ke-zhao Du, Qing Tu, Xu Zhang, et al
Publication: Inorganic Chemistry
Publisher: American Chemical Society
Date: Aug 1, 2017

Iodine–Iodine Interactions Suppressing Phase Transitions of 2D Layered Hybrid (I-(CH2)n-NH3)2PbI4 (n = 2–6) Perovskites

Author: Rayan Chakraborty, Tariq Sheikh, Angshuman Nag

Publication: Chemistry of Materials
Publisher: American Chemical Society
Date: Jan 1, 2022

The 2D Halide Perovskite Rulebook: How the Spacer Influences Everything from the Structure to Optoelectronic Device Efficiency

Author: Xiaotong Li, Justin M. Hoffman, Mercouri G. Kanatzidis
Publication: Chemical Reviews
Publisher: American Chemical Society
Date: Feb 1, 2021

JOHN WILEY AND SONS LICENSE

TERMS AND CONDITIONS

Nov 18, 2024

This Agreement between Parikshit Kumar Rajput ("You") and John Wiley and Sons ("John Wiley and Sons") consists of your license details and the terms and conditions provided by John Wiley and Sons and Copyright Clearance Center.

License Number	5912270249580
License date	Nov 18, 2024
Licensed Content Publisher	John Wiley and Sons
Licensed Content Publication	Small
Licensed Content Title	Entropy-Driven Reversible Melting and Recrystallization of Layered Hybrid Perovskites
Licensed Content Author	Parikshit Kumar Rajput, Parashurama Salunkhe, Manmayuri Sarma, et al
Licensed Content Date	Sep 1, 2024
Licensed Content Volume	0
Licensed Content Issue	0
Licensed Content Pages	9

Type of use	Dissertation/Thesis
Requestor type	Author of this Wiley article
Format	Print and electronic
Portion	Full article
Will you be translating?	No
Title of new work	Designing Organic A-Site Cations for Emerging Optoelectronic Properties of Hybrid Halide Perovskites: Reversible Melting, Non-Centrosymmetry, and Chirality
Institution name	IISER PUNE
Expected presentation date	Jan 2025
The Requesting Person / Organization to Appear on the License	Parikshit Kumar Rajput
Requestor Location	Mr. Parikshit Rajput Hostel 2 Indian Institute of Science Education and Research (IISER) Pune Dr Homi Bhabha Road Pashan Pune, Maharashtra 411008 India
Publisher Tax ID	EU826007151
Total	0.00 USD

Terms and Conditions

TERMS AND CONDITIONS

This copyrighted material is owned by or exclusively licensed to John Wiley & Sons, Inc. or one of its group companies (each a"Wiley Company") or handled on behalf of a society with which a Wiley Company has exclusive publishing rights in relation to a particular work (collectively "WILEY"). By clicking "accept" in connection with completing this licensing transaction, you agree that the following terms and conditions apply to this transaction (along with the billing and payment terms and conditions established by the Copyright Clearance Center Inc., ("CCC's Billing and Payment terms and conditions"), at the time that you opened your RightsLink account (these are available at any time at http://myaccount.copyright.com).

Terms and Conditions

- The materials you have requested permission to reproduce or reuse (the "Wiley Materials") are protected by copyright.

- You are hereby granted a personal, non-exclusive, non-sub licensable (on a standalone basis), non-transferable, worldwide, limited license to reproduce the Wiley Materials for the purpose specified in the licensing process. This license, **and any CONTENT (PDF or image file) purchased as part of your order,** is for a onetime use only and limited to any maximum distribution number specified in the license. The first instance of republication or reuse granted by this license must be completed within two years of the date of the grant of this license (although copies prepared before the end date may be distributed thereafter). The Wiley Materials shall not be used in any other manner or for any other purpose, beyond what is granted in the license. Permission is granted subject to an appropriate acknowledgement given to the author, title of the material/book/journal and the publisher. You shall also duplicate the copyright notice that appears in the Wiley publication in your use of the Wiley Material. Permission is also granted on the understanding that nowhere in the text is a previously published source acknowledged for all or part of this Wiley Material. Any third party content is expressly excluded from this permission.

- With respect to the Wiley Materials, all rights are reserved. Except as expressly granted by the terms of the license, no part of the Wiley Materials may be copied, modified, adapted (except for minor reformatting required by the new Publication), translated, reproduced, transferred or distributed, in any form or by any means, and no derivative works may be made based on the Wiley Materials without the prior permission of the respective copyright owner.**For STM Signatory Publishers clearing permission under the terms of the STM Permissions Guidelines only, the terms of the license are extended to include subsequent editions and for editions in other languages, provided such editions are for the work as a whole in situ and does not involve the separate exploitation of the permitted figures or extracts,** You may not alter, remove or suppress in any manner any copyright, trademark or other notices displayed by the Wiley Materials. You may not license, rent, sell, loan, lease, pledge, offer as security, transfer

or assign the Wiley Materials on a stand-alone basis, or any of the rights granted to you hereunder to any other person.

- The Wiley Materials and all of the intellectual property rights therein shall at all times remain the exclusive property of John Wiley & Sons Inc, the Wiley Companies, or their respective licensors, and your interest therein is only that of having possession of and the right to reproduce the Wiley Materials pursuant to Section 2 herein during the continuance of this Agreement. You agree that you own no right, title or interest in or to the Wiley Materials or any of the intellectual property rights therein. You shall have no rights hereunder other than the license as provided for above in Section 2. No right, license or interest to any trademark, trade name, service mark or other branding ("Marks") of WILEY or its licensors is granted hereunder, and you agree that you shall not assert any such right, license or interest with respect thereto
- NEITHER WILEY NOR ITS LICENSORS MAKES ANY WARRANTY OR

  REPRESENTATION OF ANY KIND TO YOU OR ANY THIRD PARTY,

  EXPRESS, IMPLIED OR STATUTORY, WITH RESPECT TO THE MATERIALS

  OR THE ACCURACY OF ANY INFORMATION CONTAINED IN THE

  MATERIALS, INCLUDING, WITHOUT LIMITATION, ANY IMPLIED

  WARRANTY OF MERCHANTABILITY, ACCURACY, SATISFACTORY

  QUALITY, FITNESS FOR A PARTICULAR PURPOSE, USABILITY,

  INTEGRATION OR NON-INFRINGEMENT AND ALL SUCH WARRANTIES ARE HEREBY EXCLUDED BY WILEY AND ITS LICENSORS AND WAIVED BY YOU.
- WILEY shall have the right to terminate this Agreement immediately upon breach of this Agreement by you.
- You shall indemnify, defend and hold harmless WILEY, its Licensors and their respective directors, officers, agents and employees, from and against any actual or threatened claims, demands, causes of action or proceedings arising from any breach of this Agreement by you.
- IN NO EVENT SHALL WILEY OR ITS LICENSORS BE LIABLE TO YOU OR

  ANY OTHER PARTY OR ANY OTHER PERSON OR ENTITY FOR ANY

  SPECIAL, CONSEQUENTIAL, INCIDENTAL, INDIRECT, EXEMPLARY OR

  PUNITIVE DAMAGES, HOWEVER CAUSED, ARISING OUT OF OR IN

  CONNECTION WITH THE DOWNLOADING, PROVISIONING, VIEWING OR USE OF THE MATERIALS REGARDLESS OF THE FORM OF ACTION,

  WHETHER FOR BREACH OF CONTRACT, BREACH OF WARRANTY, TORT,

  NEGLIGENCE, INFRINGEMENT OR OTHERWISE (INCLUDING, WITHOUT

LIMITATION, DAMAGES BASED ON LOSS OF PROFITS, DATA, FILES, USE,

BUSINESS OPPORTUNITY OR CLAIMS OF THIRD PARTIES), AND

WHETHER OR NOT THE PARTY HAS BEEN ADVISED OF THE

POSSIBILITY OF SUCH DAMAGES. THIS LIMITATION SHALL APPLY NOTWITHSTANDING ANY FAILURE OF ESSENTIAL PURPOSE OF ANY LIMITED REMEDY PROVIDED HEREIN.

- Should any provision of this Agreement be held by a court of competent jurisdiction to be illegal, invalid, or unenforceable, that provision shall be deemed amended to achieve as nearly as possible the same economic effect as the original provision, and the legality, validity and enforceability of the remaining provisions of this Agreement shall not be affected or impaired thereby.

- The failure of either party to enforce any term or condition of this Agreement shall not constitute a waiver of either party's right to enforce each and every term and condition of this Agreement. No breach under this agreement shall be deemed waived or excused by either party unless such waiver or consent is in writing signed by the party granting such waiver or consent. The waiver by or consent of a party to a breach of any provision of this Agreement shall not operate or be construed as a waiver of or consent to any other or subsequent breach by such other party.

- This Agreement may not be assigned (including by operation of law or otherwise) by you without WILEY's prior written consent.

- Any fee required for this permission shall be non-refundable after thirty (30) days from receipt by the CCC.

- These terms and conditions together with CCC's Billing and Payment terms and conditions (which are incorporated herein) form the entire agreement between you and WILEY concerning this licensing transaction and (in the absence of fraud) supersedes all prior agreements and representations of the parties, oral or written. This Agreement may not be amended except in writing signed by both parties. This Agreement shall be binding upon and inure to the benefit of the parties' successors, legal representatives, and authorized assigns.

- In the event of any conflict between your obligations established by these terms and conditions and those established by CCC's Billing and Payment terms and conditions, these terms and conditions shall prevail.

- WILEY expressly reserves all rights not specifically granted in the combination of (i) the license details provided by you and accepted in the course of this licensing transaction, (ii) these terms and conditions and (iii) CCC's Billing and Payment terms and conditions.

- This Agreement will be void if the Type of Use, Format, Circulation, or Requestor Type was misrepresented during the licensing process.

- This Agreement shall be governed by and construed in accordance with the laws of the State of New York, USA, without regards to such state's conflict of law rules.

  Any legal action, suit or proceeding arising out of or relating to these Terms and Conditions or the breach thereof shall be instituted in a court of competent jurisdiction in New York County in the State of New York in the United States of America and each party hereby consents and submits to the personal jurisdiction of such court, waives any objection to venue in such court and consents to service of process by registered or certified mail, return receipt requested, at the last known address of such party.

WILEY OPEN ACCESS TERMS AND CONDITIONS

Wiley Publishes Open Access Articles in fully Open Access Journals and in Subscription journals offering Online Open. Although most of the fully Open Access journals publish open access articles under the terms of the Creative Commons Attribution (CC BY) License only, the subscription journals and a few of the Open Access Journals offer a choice of Creative Commons Licenses. The license type is clearly identified on the article.

The Creative Commons Attribution License

The Creative Commons Attribution License (CC-BY) allows users to copy, distribute and transmit an article, adapt the article and make commercial use of the article. The CC-BY license permits commercial and non-

Creative Commons Attribution Non-Commercial License

The Creative Commons Attribution Non-Commercial (CC-BY-NC)License permits use, distribution and reproduction in any medium, provided the original work is properly cited and is not used for commercial purposes.(see below)

Creative Commons Attribution-Non-Commercial-NoDerivs License

The Creative Commons Attribution Non-Commercial-NoDerivs License (CC-BY-NCND) permits use, distribution and reproduction in any medium, provided the original work is properly cited, is not used for commercial purposes and no modifications or adaptations are made. (see below)

Use by commercial "for-profit" organizations

Use of Wiley Open Access articles for commercial, promotional, or marketing purposes requires further explicit permission from Wiley and will be subject to a fee.

Further details can be found on Wiley Online Library

http://olabout.wiley.com/WileyCDA/Section/id-410895.html **Other Terms**

and Conditions:

v1.10 Last updated September 2015

Questions? customercare@copyright.com.

Rational Design of Non-Centrosymmetric Hybrid Halide Perovskites

Author: Rayan Chakraborty, Parikshit Kumar Rajput, Gokul M. Anilkumar, et al
Publication: Journal of the American Chemical Society
Publisher: American Chemical Society
Date: Jan 1, 2023

Chiral Methylbenzylammonium Bismuth Iodide with Zero-Dimensional Perovskite Derivative Structure

Author: Parikshit Kumar Rajput, Ajay K. Poonia, Suman Mukherjee, et al
Publication: The Journal of Physical Chemistry C
Publisher: American Chemical Society
Date: Jun 1, 2022